University of Arkansas, Fayetteville

ScholarWorks@UARK

5-2021

Si-Based Germanium Tin Photodetectors for Infrared Imaging and High-Speed Detection

Huong Tran
University of Arkansas, Fayetteville

Citation

Si-Based Germanium Tin Photodetectors for Infrared Imaging and High-Speed Detection

A dissertation submitted in partial fulfillment
of the requirements for the degree of
Doctor of Philosophy in Engineering

by

Huong Tran
University of Arkansas
Bachelor of Electrical Engineering, 2014

May 2021
University of Arkansas

This dissertation is approved for recommendation to the Graduate Council.

_____
Shui-Qing (Fisher) Yu, Ph.D.
Dissertation Director

_____
Gregory J. Salamo, Ph.D.
Dissertation Co-Director

_____
Magda O. El-Shenawee, Ph.D.
Committee Member

_____
Hameed A. Naseem, Ph.D.
Committee Member

Abstract

Infrared (IR) radiation spans the wavelengths of the windows: (1) near-IR region ranging from 0.8 to 1.0 µm, (2) shortwave IR (SWIR) ranging from 1.0 to 3.0 µm, (3) mid-wave IR (MWIR) region covering from 3.0 to 5.0 µm, (4) longwave IR (LWIR) spanning from 8.0 to 12.0 µm, and (5) very longwave IR extending beyond 12.0 µm. The MWIR and LWIR regions are important for night vision in the military, and since the atmosphere does not absorb at these wavelengths, they are also used for free-space communications and astronomy. Automotive and defect detection in the food industry and electronic circuits also use IR detection as non-contact inspection methods. IR detection is also applied in the medical field. The market of SWIR and MWIR detectors is primarily dominated by mature technology from III-V systems such as indium gallium arsenide (InGaAs and extended InGaAs), indium antimonide (InSb), from II-VI such as mercury cadmium telluride (MCT), lead sulfide (PbS), and from group IV such as silicon (Si) and germanium (Ge) for shorter wavelength. However, the mature IR photodetector technology is expensive, demands to operate at low temperatures, and has complicated fabrication processes. In order to lower cost by mass production, many approaches have been developed towards the hybrid integration of III-Vs or II-VIs on a Si substrate. At the same time, it is desirable to develop an alternative material to reduce the cost and improve the performance for high-temperature operations. The discovery of group IV (Si)GeSn alloys has opened a route for a new generation of IR detectors.

The work in this dissertation set out to develop Si-based $Ge_{1-x}Sn_x$ photodetectors for low-cost infrared imaging and high-speed detection. A study of effective carrier lifetime and optical properties of $Ge_{1-x}Sn_x$ materials is presented. The carrier lifetime is then applied to model the $Ge_{1-x}Sn_x$ photodetectors. For optical properties of $Ge_{1-x}Sn_x$ materials, two empirical formulae

with extracted constants and coefficients were developed: (1) Absorption coefficient. The absorption regarding Urbach tail, indirect and direct bandgap transitions were comprehensively considered; (2) refractive index. The developed formulae could simplify the optoelectronic device design process due to their parameter-based expressions.

A comprehensive study of Si-based GeSn mid-infrared photodetectors is carried out. A set of photoconductors with Sn compositions ranging from 10.5% to 22.3% show the cutoff wavelength to be extended to 3.65 μm. The devices' peak D* is comparable to that of commercial extended-InGaAs detectors. The GeSn photodiodes are also explored with an in-depth analysis of a dark current. The dark current is suppressed as the photodiode was passivated. Moreover, mid-infrared images were captured using GeSn photodetectors, showing the comparable image quality with that acquired by using commercial PbSe detectors.

The performance of GeSn photodiodes with 6.44 % and 9.24 % Sn is evaluated under high-speed measurements and simulations. The cutoff wavelength is extended up to 2.2 μm and 2.5 μm for 6.44 % and 9.24 % Sn devices, respectively. The photodiodes' bandwidth is 1.78 GHz, and the simulation shows excellent agreement with measurement results.

Acknowledgements

Finally, from the bottom of my heart, I would like to thank my family who is always being understanding and supportive, and friends who make my time living in Fayetteville enjoyable. Their encouragement has been very important as I pursue my dreams.

Table of Contents

List of Figures

List of Tables

Chapter 1.   Introduction

1.1. Motivation

Detecting and sensing infrared (IR) radiation is enormously critical in various applications. IR illumination can be divided into different categories such as short-wave infrared (SWIR) region from 0.8 to 3 µm, mid-infrared (MWIR) region from 3 to 5 µm, and long-wavelength IR (LWIR) region from 8 to 12 µm. The MWIR and LWIR regions are used for free-space communications and astronomy since the atmosphere does not absorb at these wavelengths. The same ranges are also important for night vision in the military. IR detection also allows many non-contact inspection methods such as automotive and defect detection in the food industry and electronic circuits. IR detection is also applied in the medical field. Since the 1960s, the narrow gap III-V semiconductor alloys (for example InGaAs and InSb), IV-VI (PbSnTe), and II-VI (HgCdTe) material systems have enabled an unprecedented degree of freedom in IR detector design due to high absorption coefficient, high electron mobility, and low thermal generation rate together with bandgap engineering capability. However, the mature IR photodetector technology is costly, hard to fabricate, and operates at low temperatures [1]. For the past decades, many approaches have been developed towards the hybrid integration of III-Vs or II-VIs on a Si substrate. Simultaneously, it is desirable to develop an alternative material to reduce the cost and improve the performance for high-temperature operation [2-5]. Recently, GeSn techniques have succeeded to demonstrate GeSn-based optoelectronic devices, which results in the launch of a new generation of infrared detectors. In fact, the GeSn materials have become a decent candidate to develop high-performance GeSn detectors based on their properties. By incorporating Sn in Ge lattice, the bandgap can significantly vary from Ge bandgap around 0.67 eV to less than 0 eV. For 10% Sn, the material can cover the SWIR range, and for 20% Sn, the

1

cutoff wavelength can extend to 5 μm, which covers MWIR. For 26% Sn incorporating in Ge, the operating wavelength can extend to 12 μm, and of course, this detector can operate in the LWIR window[6-9]. With more than 8% Sn, we can achieve a direct gap to enhance absorption [6,7]. Moreover, Si, Ge, and GeSn have lattice mismatches. There is a formation of a defective layer as it is required to grow the thick and relaxed GeSn layers. To avoid the defective layer, the lattice constant needs to be engineered. It is feasible to independently engineer the lattice constant by using the different combinations of Si, Ge, and Sn compositions, and the bandgap can remain unchanged. A key property is that GeSn growth temperature is below 400 ^{0}C. If there is an existing complementary metal-oxide-semiconductor (CMOS) Si readout circuit wafer, it is required to have a material system that is CMOS compatible so that the material can be directly grown on this existing circuit using aspect ratio trapping growth. This growth provides high material quality. Hence, the cost of production is reduced as it is enabled to produce large-scale focal plane arrays (FPAs) monolithically integrated on Si using GeSn. There is also a readily available material growth technique via industrial standard systems [2,5,8-12]. The GeSn 320×256 pixel FPA imaging sensor with 1.6-1.9 μm wavelength spectral response was successfully demonstrated in 2016 [13]. It is reasonable to choose the direct material to build photodetectors as it has a large absorption coefficient. However, direct gap materials have a shorter lifetime comparing with indirect materials. This material has a unique capability of k-space charge separation. The mechanism involves the absorption that happens at gamma valley, and then excited carriers transfer to L valley for transportation, which helps to increase lifetime. To make a diagonal indirect transition, both an appropriate energy photon and an appropriate momentum phonon must be presented together with the electron. This means that electrons and holes of different momenta do not recombine quickly.

2

1.2. Figures of Merit of Photodetectors

1.2.1. Responsivity

Responsivity defines photocurrent in mA that can be generated for signal optical power of 1 mW. If each photon generates a carrier, the responsivity will be $\mathcal{R} = q/h\nu = q\lambda/hc$, where q is the electron charge; $h\nu$ is photon energy; c is the speed of light and λ is the signal wavelength. The photodiode responsivity will be

$$\mathcal{R} = \frac{I(mA)}{P(mW)} = \eta \frac{q}{h\nu} = \eta \frac{q\lambda}{hc} \tag{1.2.1}$$

where η is quantum efficiency [3]. The responsivity is linearly proportional to the wavelength of the optical signal till cutoff wavelength, which is, $\lambda_c = hc/E_g$, where E_g is the bandgap. The surface reflectivity affects the process of the number of photons injected, so in order to increase the responsivity, it is necessary to use an antireflection coating at the surface to reduce the reflectivity.

1.2.2. Detectivity

The detectivity D* can be calculated using:

$$D^* = \frac{R\sqrt{A\Delta f}}{i_{noise}} \tag{1.2.2}$$

where i_{noise} (A) is total noise current, R (A/W) is the responsivity, A (cm^2) is detector area and Δf (Hz) is bandwidth. Generally, the detectivity D* can be normalized to an area of 1 cm^2 and a noise bandwidth of 1 Hz [3].

The total noise current is calculated as:

$$i_{noise} = \sqrt{i_{thermal}^2 + i_{shot\ noise}^2 + i_{G-R}^2 + i_{1/f}^2} \tag{1.2.3}$$

where $i_{thermal}$ (A) is Johnson noise; $i_{shot\ noise}$ (A) is shot noise; i_{G-R} (A) is generation-recombination noise and $i_{1/f}$ (A) is flicker noise.

3

Johnson noise, also known as thermal noise depends on the resistance value, temperature, and bandwidth of the measuring system, and is given by:

$$i_{thermal} = \sqrt{\frac{4kT\Delta f}{R_0}} \qquad (1.2.4)$$

where R_0 (Ω) is the resistance value, k (J/K) is Boltzman constant, and T (K) is device temperature.

Shot noise is related to both photocurrent and dark current, and is considered as:

$$i_{shot\ noise} = \sqrt{2q(I_{dark} + I_{photo})\Delta f} \qquad (1.2.5)$$

where I_{dark} (A) is dark current and I_{photo} (A) is photocurrent.

Generation-recombination noise is caused by the fluctuation in the current generation and recombination rates, and is calculated using:

$$i_{G-R} = 2qG\sqrt{\eta EA\Delta f} \qquad (1.2.6)$$

where G is photoconductive gain, η is quantum efficiency, E is radiance intensity (W/cm^{-2}) and A (cm^2) is device area.

Flicker noise is usually predominant at low frequencies and is given by:

$$i_{1/f} = \sqrt{\frac{C \times I^\alpha \times \Delta f}{f^\beta}} \qquad (1.2.7)$$

where I (A) is dark current, $C, \alpha,$ and β are constants, and f (Hz) is operating frequency [3]. Moreover, the GeSn photodetectors cause the shot noise and thermal noise to become the dominant noise mechanisms amongst all other components due to the large dark currents.

1.3. Progress of GeSn photodetectors

In the last ten years, many GeSn-based photodetectors including photoconductors and photodiodes have been reported, and their performances have been dramatically improved. Moreover, a lot of new quantum-based structures such as double-heterostructure structure (DHS) and quantum well (QW) structure were developed to enhance the carrier confinement. Table 1.1 shows a brief review of GeSn detectors. Ten years ago, only 3% Sn could be grown. It was hard to incorporate Sn in Ge lattice, but recently, a new growth mechanism is discovered. It is known as the spontaneous-relaxation-enhanced Sn incorporation mechanism. It was discovered that Sn incorporation into Ge lattice is limited by high compressive strain. If the thick GeSn layer is grown, the generation of dislocations at Ge/GeSn interface eases the compressive strain, which increases Sn incorporation. As a result, our group owned the highest Sn composition so far with 22 % Sn [58]. However, there are no published reports for GeSn detectors with their spectrum covering the entire MWIR range. It is highly desirable to fully understand the potential of GeSn detectors. Hence, it is needed to perform a comprehensive study regarding Sn-compositional device performance, particularly with higher Sn composition (higher than 10%).

Table 1.1 A brief review of GeSn photodetector development

Year	Sn%	Structure	Responsivity @1.55 μm (A/W)	Cut-off (μm)	Dark current @ -1V	Reference
2009	2%	PIN	0.05	1.75	1 A/cm^2	[14]
2011	0.5%	PIN	0.1	1.65	10 A/cm^2	[15]
2011	2%	PIN	0.12	1.75	1.0 A/cm^2	[16]
2011	3%	PIN	0.23, 0.12 @1.64 μm	1.8	1.8 A/cm^2	[17]

Table 1.1 (Cont.)

Year	Sn%	Structure	Responsivity @1.55 μm (A/W)	Cut-off (μm)	Dark current @ -1V	Reference
2013	3.9%	PIN	0.27, 0.165 @1.6 μm	1.8	400 mA/cm^2	[18]
2012	4%	PIN	0.2, 0.17@1.6 μm	1.95	100 mA/cm^2	[19]
2012	9%	QW/PC	1.0, 0.1 @ 2.2 μm	2.3	0.5 mA	[20]
2013	3.6%	PIN	0.71 @ 1.8μm	2.0	6.1 mA/cm^2	[21]
2013	8%	PN	0.031	1.575	11 μA	[22]
2013	9.8%	PN	Broadband photocurrent 200 μA	2.0	100 μA	[23]
2013	9%	PN	N. A.	No report	1 A/cm^2	[24]
2014	1.8%	PIN	0.18	1.6	50 mA/cm^2	[25]
2014	4.2%	PIN	0.22	N. A.	890 mA/cm^2	[26]
2014	7%	QW/PIN	0.13	1.91	100 mA/cm^2	[27]
2014	*7%*	*PC*	*0.18 @ 10 V*	*2.1*	*37.5 mA/cm^2 @ 10V*	*[28]*
2014	*10%*	*PC*	*1.63 @ 50 V*	*2.4*	*82.5 mA/cm^2*	*[29]*
2014	12%	PN	0.081	2.0 @ 100 K	50 mA	[30]
2015	5%	PIN	0.18, 0.06 @ 1.63 μm	1.85	73 mA/cm^2	[31]
2015	*10%*	*PC*	*2.85 @ 5V*	*2.4*	*7.7 A/cm^2*	*[32]*
2016	2.5%	PIN	0.3	1.9	1 mA/cm^2	[33]

Table 1.1 (Cont.)

Year	Sn%	Structure	Responsivity @1.55 μm (A/W)	Cut-off (μm)	Dark current @-1V	Ref.
2016	2.5%	PIN/Array	0.45 @ 1.7 μm	1.9	0.1 mA/cm^2	[13]
2016	6%	PIN	0.35, 0.09 @ 2 μm	1.985	3 A/cm^2	[34], [35]
2016	*7%*	*PIN*	*0.3*	*2.2 μm*	*1A/cm^2*	*[36]*
2016	*10%*	*PIN*	*0.19*	*2.6 μm*	*4.3 A/cm^2*	*[36]*
2017	2.8%	MQW/PIN	62 mA/W	1.635	59 mA/cm^2	[37]
2017	3%	QW/PIN	80 mA/W	1.65	4 mA/cm^2	[38]
2017	10%	MQW PIN	0.02 @ 2 μm	N. A.	31 mA/cm^2	[39]
2017	6.5%	HPT	1.8, 0.043 @ 2 μm	2.0	147 mA/cm^2	[40]
2018	*11%*	*PIN*	*0.32 @ 2 μm*	*2.65 μm*	*7.9 mA/cm^2 @ -0.1V & 77 K*	*[41]*
2018	8%	MSM	N.A.	N.A.	10 mA/cm^2	[42]
2018	7%	PIN GeSnOI	0.16 @ 2 μm	N.A.	1 μA	[43]
2018	2.5%	PIN	0.376 @ 1.65 μm	1.8	0.3	[44]
2018	8%	MSM	0.1 @ 2 μm	N.A.	65 nA	[45]
2019	10%	APD (Design)	N.A.	N.A.	0.2 nA@ -10V	[46]

Table 1.1 (Cont.)

Year	Sn%	Structure	Responsivity @1.55 µm (A/W)	Cut-off (µm)	Dark current @ -1V	Ref.
2019	9%	HPT (Design)	40 @ 2.1 µm	N.A.	N.A.	[47]
2019	9%	HPT (Design)	50 @ 2 µm	2.125 µm	N.A.	[48]
2019	25%	PC (µbolometer)	N.A.	N.A.	45.46 Ω·cm	[49]
2019	7%	PIN	N.A.	N.A.	0.3 mA/cm^2	[50]
2019	8%	MQW PIN	30 mA/W @ 2 µm	> 2 µm	25 mA/cm^2	[51]
2019	8%	MQW PIN	15 mA/W @ 2 µm	> 2 µm	40 mA/cm^2	[52]
2019	11%	PN	100 mA/W @ 2 µm	N.A.	1mA/cm^2	[53]
2019	16%	GeSn/n-GaAs	0.28 mA/W @1.064 µm	3 µm	59 mA/cm^2	[54]
2019	*9.24%*	*PIN*	*0.19*	*2.5 µm*	*2 A/cm^2 @ -0.1V*	*[55]*
2019	10.4%	GeSn-Graphene PC	220 A/W @ 2 µm	N. A.	1.5 mA	[56]

Table 1.1 (Cont.)

Year	Sn%	Structure	Responsivity @1.55 µm (A/W)	Cut-off (µm)	Dark current @ -1V	Ref.
2019	6%	PIN	0.12 @ 2 µm	2.3 µm	78 mA/cm^2	[57]
2019	*11%*	*PC & PIN*	*0.38 @ 2 µm*	*2.65 µm*	*1 mA/cm^2 @ 0.2 V & 77 K*	*[58]*
2020	3.4%	PC	N.A.	N.A.	20 A/cm^2	[59]
2020	5%	LTLM	N.A.	N.A.	1 mA @ -40 V	[60]
2020	10 %	PIN (DLTS)	N.A.	N.A.	N.A.	[61]
2020	17.9%	Nanocry-stal	100 pA	2.5 µm	1 µA @ -0.1V	[62]
2020	2%	Nano-island	0.2-0.3 @ 0.650 µm	N. A.	2 µA @ -0.5V	[63]
2020	3.2%	Graphene-oxide-GeSn	50 mA/W @ 0.532 µm	N.A.	N.A.	[64]
2020	4.9%	HPT	0.68	1.94 µm	2 A/cm^2	[65]
2020	10%	PIN Theoretical	0.57	2.3 µm	0.17 mA/cm^2 @ -3V	[66]
2020	16%	MQW/PIN (Design)	1 @ 4.3 µm	5 µm	N.A.	[67]
2020	4.5%	WG PIN (Design)	1.25 @ 1.675 µm	1.91 µm	11.1 mA/cm^2	[68]

Table 1.1 (Cont.)

Year	Sn%	Structure	Responsivity @1.55 µm (A/W)	Cut-off (µm)	Dark current @ -1V	Ref.
2020	10%	DBR PIN (Design)	1.02 @ 2 µm	3.7 µm	N.A.	[69]
2020	8%	MQW/PIN	0.11	2.26	45.2 mA/cm^2	[70]
2020	10%	PIN	0.2	N.A.	25.5 mA/cm^2 @ -0.1V	[71]
2020	3.2%	Graphene /doped GeSn	0.2 A/W @ 1.064 µm	1.832 µm	N. A.	[72]
2020	4.7%	PIN	0.1 A/W @ 2 µm	2.1 µm	3 A/cm^2	[73]
2020	4%	MSM	70 mA/W @ 1.51 µm	1.8 µm	0.55 mA	[74]
2020	8%	MSM (mechanical bending)	4 mA/W @ 2 µm	2.1 m	4 µA	[75]
2020	17%	Membrane	0.5 mA/W @ 2 µm	4.6 µm	3.5 mA	[76]
2020	10%	GeSn/Ge dual NW	1.1 @ 2 µm	2.2 µm	N. A.	[77]
2020	3.4%	PIN	0.2	1.675	30 mA/cm^2	[78]

* PC stands for photoconductor; The results in bold and italic are reported by our group.

Particularly, our group reported $Ge_{0.9}Sn_{0.1}$ photoconductors with interdigitated electrodes to achieve photoconductive gain, which presents a high peak responsivity of 2.85 A/W at a wavelength of 1.55 µm. Moreover, *p-i-n* photodiodes with the active layer containing Sn compositions ranging from 7% to 11% were investigated. The cut-off wavelength is extended to 2.65 µm. These results provided a standard for the SWIR detectors. In 2019, we also reported the demonstration of i) a set of GeSn photoconductors with Sn compositions from 10.5% to 22.3% and cut-off wavelengths up to 3.65 µm. The highest specific detectivity (D*) of 1.1×10^{10} $cm \cdot Hz^{1/2} \cdot W^{-1}$ was comparable with that ($\sim 4 \times 10^{10}$ $cm \cdot Hz^{1/2} \cdot W^{-1}$) of commercial extended-InGaAs detectors; and ii) the passivation technique on GeSn photodiode was investigated. Based on the in-depth current-voltage analysis, the significantly reduced dark current was achieved with passivated device. Also, the high-quality mid-infrared images were captured using the GeSn photodetectors. Particularly, the images from the photoconductor were taken without the lock-in technique.

1.4. Organization of the dissertation

The main goal of this dissertation was divided into three objectives: 1) To achieve the GeSn photoconductors whose operating wavelengths extend to mid-infrared; 2) To achieve the GeSn photodiodes which operate at room temperature for imaging system; 3) To obtain high-speed GeSn photodetectors. Following the abovementioned objectives, this dissertation could be organized into 8 chapters. Chapter 1 introduces the background of GeSn as a group IV material for infrared imaging and high-speed detection. Chapter 2 focuses on the carrier lifetime of the GeSn materials from an envelope calculation to an estimation of the lifetime using GeSn photoconductors. Chapter 3 studies optical properties of the GeSn materials to obtain the formulae, so those formulae can be re-used for further simulations and design of the GeSn

detectors. Chapter 4 presents a set of GeSn photoconductors which shows the operating wavelengths extending to mid-infrared. The dark current and effective carrier lifetime are also analyzed to understand the dominant factors for future design. Chapter 5 exhibits the GeSn photodiodes with the exploration of passivation to achieve room-temperature operation. The dark current is analyzed to identify the dominant mechanism affecting the devices' performance. Chapter 6 demonstrates the infrared imaging system, and the devices' performance can be comparable to the commercial camera. Chapter 7 concentrates on developing the GeSn photodetectors for high-speed applications. The simulations and practical characterizations show an agreement. Chapter 8 presents the future work to develop high-performance GeSn photodetectors.

Chapter 2.   Carrier lifetime of GeSn

2.1. Role of carrier lifetime

Generation and recombination processes set up a steady-state concentration of carriers, so they directly affect the performance of photodetectors. The excited carriers can be recombined before they are effectively collected at the contacts, which reduces the quantum efficiency and gain of the devices. The noise can be created by the generation-recombination processes since they fluctuate carriers. The recombination process can be avoided by arranging it to happen in neutral regions of the diodes due to low gain. The generation process with its associated fluctuation cannot be avoided. For the narrow-gap semiconductors, thermal generation noise is dominant, so it is ideal to reduce thermal generation to a level below that of optical generation. The generation-recombination rate due to various processes is the summation of $n_o p_o - np$ multiplied by the term g_k as [3,79]:

$$G - R = \sum_k g_k (n_o p_o - np) \tag{2.1.1}$$

where $p = p_o + \Delta p$ and $n = n_o + \Delta n$ are the majority carrier densities.

For small excess carriers, the summation of net generation rates can be written as

$$G - R = \sum_k -\frac{\Delta n}{\tau_k} \tag{2.1.2}$$

where τ_k are the minority-carrier recombination times for various mechanisms.

The recombination life can be calculated as

$$\frac{1}{\tau} = \sum_k \frac{1}{\tau_k} = \frac{R - G}{\Delta n} \tag{2.1.3}$$

The carrier lifetime is very important because it regulates the responsivity and speed of the detectors. There are two significant recombination processes. Firstly, it is known as a direct

band-to-band process where an electron can directly drop from the conduction band to an unoccupied state in the valence band. Secondly, it is known as an indirect process where an electron initially makes a transition to an energy level lying deep in the bandgap and later captures a hole from the valence band. For the recombination process, there is emitted energy with a value equal to the difference between electron and hole energies. If the energy can be emitted as a photon, the recombination is radiative. If the energy can be dissipated to the lattice as phonons, the recombination is non-radiative. There is the third recombination process, which is called the Auger process as the energy can be imparted as the kinetic energy to a third mobile carrier. This process is also non-radiative. In narrow-gap semiconductors, there are three major generation-recombination mechanisms: Shockley-Read, radiative, and Auger [3,79].

2.2. Envelope calculation of carrier lifetime

2.2.1. Shockley-Read mechanism

Because of native defects and impurities, there is a formation of the energy levels inside the bandgap. The recombination happens via these levels, which is known as the Shockley-Read mechanism. This process can be reduced if the material achieves purer and higher quality. Hence, this mechanism is not intrinsic and fundamental, and the Shockley-Read process does not represent a fundamental limit to photodetector performance.

In the Shockley-Read mechanism, the electrons and holes can be trapped at energy levels by impurities or lattice defects in the bandgap. These energy levels are recombination centers. The electrons and holes can be emitted from energy levels, which are called generation centers. Their occupation state of charge carriers and the local densities of those carriers are factors to establish the rates of generation and recombination. Generally, the transition rates via energy levels for electrons and holes are quite different which leads to different lifetimes. There are

14

shallow traps and deep traps. The shallow traps have a small energy difference from either a conduction band or a valence band, which may be overcome by thermal energy. In other words, the carrier is very likely to be released from the trap, and therefore shallow traps generally do not cause SRH recombination. The deep traps exist near the middle of the bandgap. Since their energy levels are well separated from band edges, carriers are not easily released, and therefore these traps are highly effective at promoting electron-hole pair recombination events. The Fermi energy level becomes a reference to determine if the trap is empty or filled. If the trapped energy is above Fermi level, then the trap is more likely to be empty than full. If the trapped energy is below Fermi level, it is more likely to be filled. To simplify the treatment of traps, it is enabled to consider a trap at the Fermi level [79,80].

The single-level recombination can be explicated by four processes: electron capture, electron emission, hole capture, and hole emission. For different capture cross-sections for electron and hole σ_n and σ_p, respectively, the trap generation rate is defined as [3,79,80]

$$G_{SR} - R_{SR} = \frac{\sigma_n \sigma_p v_{th}(n_o p_o - np)N_t}{\sigma_n(n + n_1) + \sigma_p(p + p_1)} \tag{2.2.1}$$

where $n_1 = N_c exp[-(E_c - E_t)/kT]$ and $p_1 = N_v exp[-(E_t - E_v)/kT]$ are the carrier concentrations for the trap level at the Fermi energy; N_c and N_v are the density of states for conduction and valence band; E_c and E_v are the energy of conduction and valence band edge; v_{th} is the carrier thermal velocity equal to $(8kT/\pi m^*)^{1/2}$; E_t is the trap energy level; and σ_n and σ_p are the capture cross-sections for electrons and holes, respectively. The recombination rate reaches a peak when the energy level is equal to the mid-gap. Hence, the most effective recombination centers are those located near the middle of the bandgap.

Eq. (2.2.1) can be simplified for low carrier injection ($\Delta n \ll \Delta n_o$ or $\Delta p \ll \Delta p_o$) into the material in which the ionization energy of the centers is comparatively deep relative to kT. In

15

other words, the carriers cannot be released by thermal energy. In n-type material, when trapping can be neglected ($\Delta n = \Delta p$) at sufficiently low temperature ($n_o > n_1 > p_o$)

$$R_{SR} - G_{SR} \approx \sigma_n N_t v_{th} \Delta n \qquad (2.2.2)$$

From Eqs. (2.1.3) and (2.2.2), the trap-limited lifetime in doped n-type material is

$$\tau_{po} = \left(\sigma_p v_{th_p} N_t \right)^{-1} \qquad (2.2.3)$$

 Similarly, for p-type material

$$\tau_{no} = \left(\sigma_n v_{th_n} N_t \right)^{-1} \qquad (2.2.4)$$

From Eqs. (2.2.3) and (2.2.4), the SR lifetime can be obtained as

$$\tau_{SR} = \frac{\tau_{po}(n_o + n_1) + \tau_{no}(p_o + p_1)}{n_o + p_o} \qquad (2.2.5)$$

Three distinct ranges of temperature are analyzed in order to show the dependence of the lifetime on temperature for the n-type semiconductor where the trap is located above mid-gap ($E_t > E_i$) and assuming that σ_n and σ_p are constant such as:

- region I (at low temperature, freezeout), in which $E_t < E_F < E_c$; then $n_o > p_o, n_1, p_1$ and the steady-state carrier lifetime is defined by Eq.(2.2.3);

- region II, in which $E_i < E_F < E_t$; then $n_o > p_o, n_1$ and $n_1 > p_o$; the carrier lifetime

$$\tau_{SR} = \frac{N_c}{\sigma_p v_{th} N_t n_o} exp \frac{E_t - E_c}{kT} \qquad (2.2.6)$$

increases exponentially with temperature. The transition between region I and region II happens at the point for which $n_o = n_1$(when $E_F = E_t$);

- region III (the intrinsic range), in which $n_o = p_o = n_i, n_1 > n_i, p_1 < n_i$, and the lifetime

$$\tau_{SR} \propto exp \left(\frac{E_g}{2kT} - \frac{E_c - E_t}{kT} \right) \qquad (2.2.7)$$

decreases exponentially with temperature.

The lifetime of the Shockley-Read mechanism is a function of four parameters such as N_t, E_t, τ_{no}, and τ_{po}. If there is more than a recombination level, each level will have its own parameters. For the case of multiple numbers of recombination levels, the Shockley-Read lifetime becomes

$$\tau_{SR}^{-1} = \sum \tau_i^{-1} \qquad (2.2.8)$$

where τ_i is the lifetime of the ith recombination level.
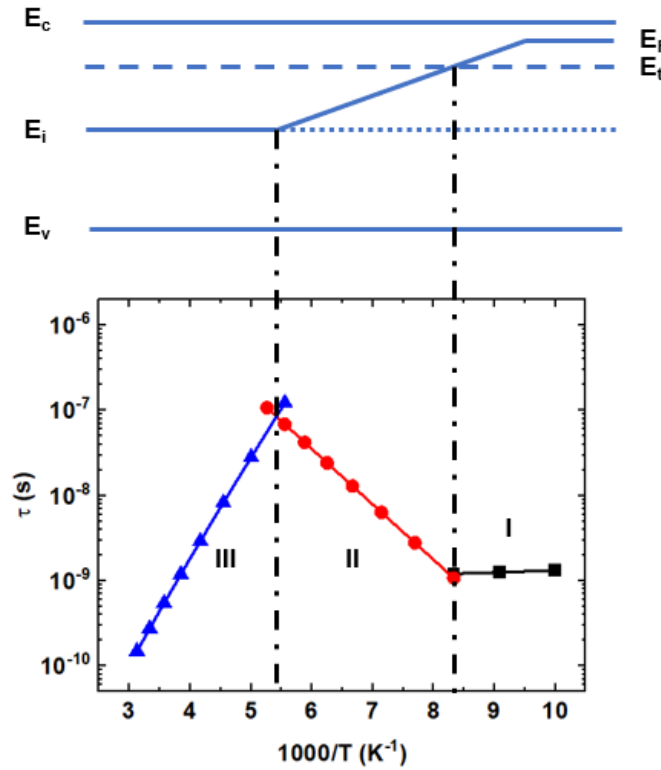
Figure 2.1 Lifetime of minority carriers as a function of temperature for the n-type Ge$_{0.91}$Sn$_{0.09}$ material.

Figure 2.1 shows the calculated SRH lifetime of minority carriers as the function of temperature for the n-type Ge$_{0.91}$Sn$_{0.09}$ material with a doping level of 2×10^{18} cm^{-3} and the capture cross-sections of holes $\sigma_p = 2 \times 10^{-17} cm^2$ as reported in [81]. The trap density is 1×10^{18} cm^{-3}, and the ratio between trap energy and bandgap, E_t/E_g is 20 %. Three distinct ranges

of temperature are to be observed following the above mention. With high trap density, the SRH lifetime is in the range between 0.1 ns to 0.1 μs.

2.2.2. Radiative mechanism

When an electron and a hole recombine, the process which releases the photon with the excess energy is known as the radiative process. This mechanism is determined by the electronic band structure of the semiconductor, which is intrinsic. The radiative recombination is preferred to occur in any direct gap semiconductor. The recombination rate depends on the absorption coefficient through the equations for the spherical symmetry bands [3,79,80]

$$G_R = \frac{8\pi}{h^3 c^3} \int_0^\infty \frac{\varepsilon(E)\alpha(E)E^2 dE}{exp(E/kT) - 1} \tag{2.2.9}$$

where $\alpha(E)$ is the absorption coefficient, $\varepsilon(E)$ is the relative dielectric constant, h is Planck's constant, and c is the speed of light. The high-frequency value, ε_∞ is used instead of $\varepsilon(E)$. For a small deviation from equilibrium, the radiative lifetime is described as

$$\tau_R = \frac{n_i^2}{G_R(n_o + p_o)} \tag{2.2.10}$$

where n_i is the intrinsic carrier concentration. The steady-state radiative lifetimes of excess electrons (τ^e) and holes (τ^h) are equal with a condition of no charge trapping at defects. For an intrinsic semiconductor, the radiative lifetime can be written as

$$\tau_R^i = \frac{n_i}{2G_R} \tag{2.2.11}$$

Eq. (2.2.11) shows that the lifetime achieves the longest possible value. One can obtain the value of G_R by using theoretical expressions for the absorption coefficient in simple semiconductors. The expression for α as a function of E is shown as

$$\alpha(E) = \frac{2^{2/3}mq^2}{3\varepsilon_\infty^{1/2}\hbar^2} \left(\frac{m_e^* m_h^*}{m(m_e^* + m_h^*)}\right)^{3/2} \left(1 + \frac{m}{m_e^*} + \frac{m}{m_h^*}\right) \left(\frac{E - E_g}{mc^2}\right)^{1/2} \tag{2.2.12}$$

18

where m_e^* and m_h^* are the electron and hole effective masses, m is the free electron mass, and E_g is the material bandgap. From Eq. (2.2.9) and (2.2.12) and assuming that $E_g > kT$ and using the high-frequency value, ε_∞, the radiative rate can be calculated as [3]

$$G_R = n_i^2 5.8 \times 10^{-13} \varepsilon_\infty^{1/2} \left(\frac{m}{m_e^* + m_h^*}\right)^{3/2} \left(1 + \frac{m}{m_e^*}\right)\left(\frac{300}{T}\right)^{3/2}$$
$$\times \left(E_g^2 + 3kTE_g + 3.75k^2T^2\right)$$
(2.2.13)

where E_g is in eV.

It is worth noticing that the expression of α is acquired from the assumption of parabolic bands and nondegenerate statistics, which leads to the calculations are only strictly valid for those conditions. However, Eq. (2.2.13) can still apply for a Kane-type band structure employing degenerate statistics and considering only transitions between the conduction band and heavy hole band. While the other two terms in Eq. (2.2.13), $3kT$ and $3.75(kT)^2$ can be ignored for wide bandgap, for the narrow gap, they should be included.

Based on Eq. (2.2.10), the minority carrier lifetimes for radiative recombination are presented as

$$\tau_R^h = \frac{2\tau_R^i}{(n_o/n_i) + (n_i/n_o)} = \frac{n_i^2}{G_R(n_o + n_i^2/n_o)}$$
(2.2.14)

$$\tau_R^e = \frac{2\tau_R^i}{(p_o/n_i) + (n_i/p_o)} = \frac{n_i^2}{G_R(p_o + n_i^2/p_o)}$$
(2.2.15)

Figure 2.2 shows the radiative lifetime as a function of inverse temperature. For carrier concentration ranging from 10^{15} cm^{-3} to 10^{18} cm^{-3}, the lifetime is ranging from 1 μs to 1 nm. For low-temperature ranges, the conductivity of the GeSn materials enters the extrinsic region, which leads to the lifetime is slightly constant in this region. It is worth noticing that most photons emitted in photodetectors from radiative decay are instantaneously reabsorbed so that the observed radiative lifetime shows the escape of photons from the body of the detector. Due to

reabsorption, the radiative lifetime is highly prolonged and depends on the semiconductor geometry, which implies the requirement of exceptionally high material quality, as shown in Fig. 2.2 with low carrier concentration.
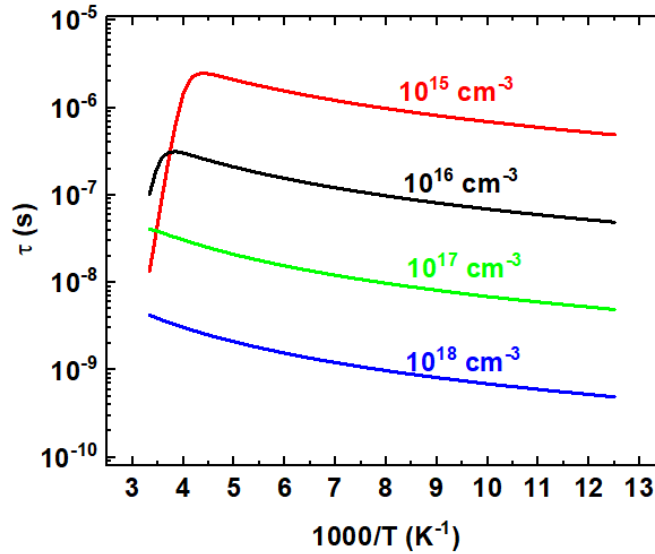
Figure 2.2 Radiative lifetime as the function of 1000/T for the n-type $Ge_{0.91}Sn_{0.09}$ material with different carrier concentration ranging from $10^{15}\,cm^{-3}$ to $10^{18}\,cm^{-3}$

2.2.3. Auger mechanism

The Auger effect is an important mechanism, which affects the performance of infrared detectors made from narrow-gap semiconductors. This effect is also the intrinsic recombination mechanism. The Auger mechanism is the inverse process of impact ionization (Auger generation) where a three-particle Coulomb interaction occurs. Figure 2.3 (a) shows one of the Auger transitions for a simple two-band model of a semiconductor. The Auger mechanism involves three particles: an electron in the conduction band, a hole in the valence band, and a second conduction-band electron. The electron recombines with the hole, and then the energy is released is transferred to the second electron, which is pushed to an excited state. The second electron does not stay in the excited state but returns to its initial state by phonon emission via the electron-lattice interaction.

The Auger process may also take part in a Shockley-Read process, which is a transition from a band to a recombination center level in the energy gap. However, the band-to-band Auger effect represents the most efficient intrinsic recombination process in semiconductors with a small energy gap. In narrow-gap semiconductors, a Shockley-Read process often controls the lifetime of the excess carrier, but this behavior is not dominant if the material quality is high [82].
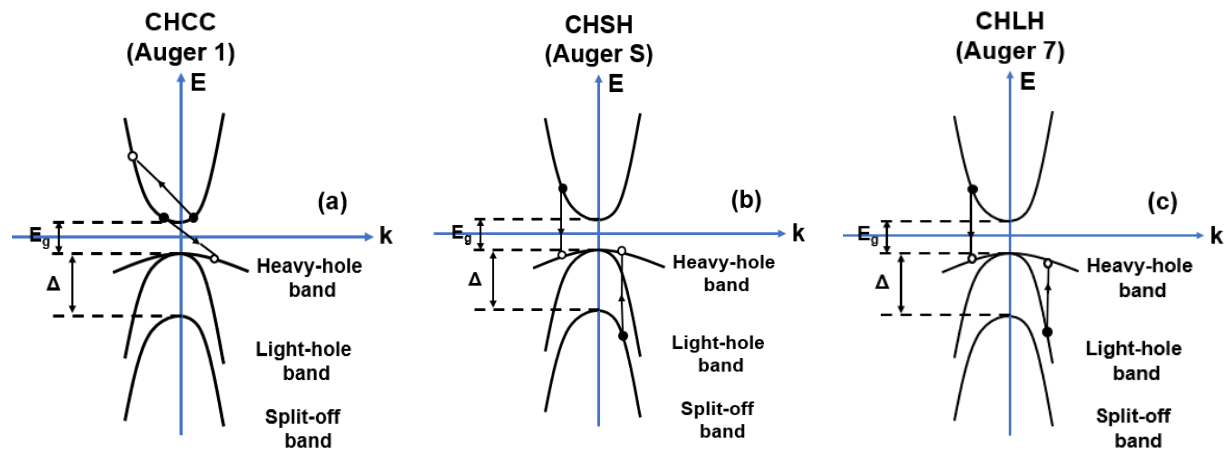
Figure 2.3 The three band-to-band Auger recombination processes.

2.2.3.1. Band-to-band Auger mechanisms

The band-to-band Auger effects are categorized in several processes according to related bands. There are reported ten types of Auger recombination mechanisms with no photon which are possible in a semiconductor with a single conduction band and heavy- and light-hole valence bands. There are two most dominant mechanisms in the case of this type of band structure. They have the smallest threshold $\left(E_T \approx E_g\right)$ and the largest combined density of states. The CHCC recombination mechanism, also known as Auger 1 requires two electrons and a heavy hole and is dominant in n-type material. The CHLH process, as known as Auger 7 involves a heavy hole, a light hole, and an electron. It is dominant in p-type material if the spin split-off

band can be excluded. If the spin-split-off energy Δ is much larger than the bandgap energy E_g, the probability of the Auger transition through the conduction band/heavy-hole band/spin split-off band mechanism, CHSH, may be negligibly small in comparison with that of the CHLH Auger transition. For the direct-bandgap materials, when the bandgap energy E_g approaches the spin-orbit splitting Δ, the spin split-off band is dominant over the light-hole band.

In n-type materials in which $m_e^*/m_h^* \ll 1$, the process involving a hole as the third carrier can be ignored and only electron-electron processes are important. The electron-electron recombination rate in a nondegenerate semiconductor is proportional to $n^2 p$ and is described as

$$R_A = G_{A1} n^2 p \tag{2.2.18}$$

The generation (or impact ionization) rate on the other hand is given by

$$G_A = G_{A1} n_i^2 n \tag{2.2.19}$$

Hence, the net recombination rate is given by

$$R_A - G_A = G_{A1} n(np - n_i^2) \tag{2.2.20}$$

where

$$G_{A1} = \frac{8(2\pi)^{5/2} q^4 m_o}{h^3 (4\pi\varepsilon_o\varepsilon_s)^2} \left(\frac{(m_c^*/m_o)|F_1 F_2|^2}{(1+\mu)^{1/2}(1+2\mu)} \right) \frac{1}{n_i^2} \left(\frac{kT}{E_g} \right)^{3/2}$$

$$\times exp\left[-\left(\frac{1+2\mu}{1+\mu} \right) \frac{E_g}{kT} \right] \tag{2.2.21}$$

In Eq. (2.2.21), μ is the ratio of the conduction to the heavy-hole valence-band effective mass, ε_s is the relative static dielectric constant, and F_1 and F_2 are the overlap integrals of the periodic part of the electron wave functions. The overlap integrals F_1 and F_2 cause the largest uncertainty in the Auger 1 lifetime. The value of $|F_1 F_2|$ was a constant falling in anywhere between 0.1 and 0.3, which can change the lifetime by an order of magnitude.

The carrier lifetime defined by the Auger process $\tau_A = \Delta n/(R_A - G_A)$ is

$$\tau_A = \frac{n_i^4}{G_A^{ee}(n_o + p_o + \Delta n)np_o} \tag{2.2.22}$$

If the hole-hole recombination process is also counted, then

$$\tau_A = \frac{n_i^4}{(n_o + p_o + \Delta n)\big(G_A^{ee}np_o + G_A^{hh}pn_o\big)} \tag{2.2.23}$$

In the calculations of the transition rate of Auger processes, different estimates of overlap integrals have been indicated. These integrals were evaluated for the threshold momentum values of particles participating in the Auger recombination. Generally, these integrals depend on the wave functions, which are not sufficiently understood, and methods of approximation must be used. For the narrow-gap semiconductors considered here, $\mu = m_e^*/m_h^*$ is $\ll 1$, and then in the extrinsic region, the Auger 1 lifetime is estimated by [3, 82]

$$\tau_{A1} = \frac{2n_i^2\tau_{A1}^i}{(n_o + p_o + \Delta n)[(n_o + \Delta n) + \beta(p_o + \Delta n)]} \tag{2.2.24}$$

where Δn is the excess carrier density that can be neglected since the evaluation occurs in the small-signal conditions; the β term equal to

$$\beta = \frac{\mu^{\frac{1}{2}}(1 + 2\mu)}{(2 + \mu)} exp\left[-\left(\frac{1 - \mu}{1 + \mu}\right)\frac{E_g}{kT}\right] \tag{2.2.25}$$

refers to hole-hole collisions and is also usually neglected. For nondegenerated material, the following expression for the Auger 1 recombination lifetime is [3, 82]

$$\tau_{A1} = \frac{2\tau_{A1}^i}{1 + (n_o/n_i)^2} \tag{2.2.26}$$

where τ_{A1}^i is the Auger lifetime for intrinsic material computed by

$$\tau_{A1}^i = \frac{3.8 \times 10^{-18}\varepsilon_s^2(1 + \mu)^{1/2}(1 + 2\mu)exp\left[\left(\frac{1 + 2\mu}{1 + \mu}\right)\frac{E_g}{kT}\right]}{(m_e^*/m)|F_1F_2|^2\big(kT/E_g\big)^{3/2}} \tag{2.2.27}$$

The Auger 7 process requires the recombination between a conduction electron and a heavy hole, while at the same time an electron is excited from the light-hole band to an empty state in the heavy-hole band, absorbing the excess energy and momentum, as shown in Fig. 2.3 (c). The Auger 7 lifetime in the p-type extrinsic region should be of the same order of magnitude as that in the n-type material with the same carrier concentration. Comparable with the Auger 1 process, the lifetime associated with the Auger 7 process is

$$\tau_{A7} = \frac{2n_i^2 \tau_{A7}^i}{(n_o + p_o + \Delta n)(p_o + \Delta n)} \tag{2.2.28}$$

where τ_{A7}^i is the Auger 7 lifetime for intrinsic material

$$\left(\tau_{A7}^i\right)^{-1} = \frac{16q^4 \alpha_{ch}^{(7)} \alpha_{co}^{(7)} m_{co}^{*3/2} \eta_7^{3/2} I_7(\eta_7)}{\pi^{1/2} \hbar^7 \varepsilon^2 [m_l^*(k_7)]^2 a_7^2 (2 + \mu_o)^{3/2} [1 + (m_{lo}^*/m_h^*)^{3/2}]} \tag{2.2.29}$$

where $\eta_7 = E_T/k_B T$, E_T is the Auger 7 threshold energy; m_{co}^* and m_{lo}^* are the conduction- and light-hole band effective masses at $k = 0$; μ_o is the ratio of m_{lo}^*/m_h^*; m_h^* is the heavy-hole mass; $m_l^*(k_7)$ is the light-hole effective mass at the threshold; $a_7 = m_l^*(k_7)/m_{co}^* + (1 + \mu_o/2)^{-1}$; ε is the dielectric constant; and $\hbar$ is Planck's constant. The factors $\alpha_{ch}^{(7)}$ and $\alpha_{lh}^{(7)}$ are overlap integral coefficients proportional to the oscillator strength of a transition between the initial and final states in the conduction band c, heavy-hole valence band h, and light hole valence band l. The factor $I_7(\eta_7)$ is given by

$$I_7(\eta_7) = \int_1^\infty e^{-\eta_7 y} a^2(y) m_l^{*\frac{5}{2}}(y) \left(m_y^*(y) + y \frac{dm_l^*}{dy}\right) y^{1/2}(y - 1)^2 dy \tag{2.2.30}$$

where $y = E/E_T$ and E is energy.

The calculations of Auger 7 carrier lifetime are complicated. It is necessary to simplify the calculations, and it is found that

24

$$\gamma = \frac{\tau_{A7}^i}{\tau_{A1}^i} \approx 2 \frac{m_e^*(E_T)\left[1 - \frac{5}{4\eta_T}\right]}{m_{eo}^*\left[1 - \frac{3}{2\eta_T}\right]} \tag{2.2.31}$$

For the Auger 7 process, the threshold energy $E_T \approx E_g$. From Kane's nonparabolic approximation $m_e^*(E_T)/m_{eo}^* \approx 3$.

The combined lifetime of the two Auger processes (Auger 1 and Auger 7) is given by

$$\tau_A = \frac{2n_i^2\gamma\tau_{A1}^i}{(n_o + p_o + \Delta n)[(n_o + \Delta n)\gamma + (p_o + \Delta n)]}. \tag{2.2.32}$$

In the limit of small modulation

$$\tau_{A7} = \frac{2\tau_{A7}^i}{1 + (p_o/n_i)^2} \tag{2.2.33}$$

and

$$\tau_A = \frac{2\gamma\tau_{A7}^i}{1 + \gamma + \gamma(n_o/n_i)^2 + (p_o/n_i)^2}. \tag{2.2.34}$$

The Auger lifetime decreases very slowly with decreasing temperatures in the extrinsic range since it is proportional to $T^{3/2}exp[\mu E_g/(1+\mu)kT]$. At very low temperatures, τ_A starts increasing due to the exponential term. However, since $\mu \ll 1$ in a narrow-gap semiconductor, this effect should be noticed only at very low temperatures below 10K. The exponential increase in the Auger lifetime is steeper than in the radiative process, since τ_A is inversely proportional to the square of the hole concentration rather than to its first power.

For the case where the bandgap energy E_g approaches the spin-orbit splitting Δ, the Auger S process, as shown in Fig. 2.3 (b), plays an important role in extrinsic p-type material. The Auger S recombination lifetime is expressed as:

$$\tau_{AS} = \frac{2\tau_{AS}^i}{1 + (p_o/n_o)^2} \tag{2.2.35}$$

where

$$\tau_{AS}^i = \frac{n_i}{2G_{AS}}$$

(2.2.36)

For different values of Δ, the Auger S recombination rate is evaluated as

(a) for $\Delta > E_g$

$$G_{AS} = \frac{27}{5}\pi^4 n_i^2 p \frac{q^4 \hbar^3 m_s^{*5/2}(\Delta - E_g)exp\left[-(\Delta - E_g)/kT\right]}{\varepsilon^2 m_h^{*3} m_e^{*3/2} kT\Delta^2(E_g + \Delta)}$$

(2.2.37)

where m_s^* is the split-off band effective mass;

(b) for $\Delta < E_g$

$$G_{AS} = \frac{18\pi q^4 m_e^* \hbar^3 (E_g + \Delta)^2}{\varepsilon^2 m_h^* m_s^{*2} E_g^5} n_i^2 \gamma^2 p[I_1(\gamma) - I_2(\gamma)/2]$$

(2.2.38)

In this equation

$$\gamma = 2\frac{m_s^*}{m_h^*}\frac{E_g^2}{(E_g + \Delta)(3E_g - 2\Delta)}\frac{(E_g - \Delta)}{kT}$$

(2.2.39)

and the functions $I_1(\gamma)$ and $I_2(\gamma)$ are the following integrals

$$I_1(\gamma) = 2\pi^{3/2}\gamma^{1/2}\left[\frac{\pi}{2^{3/2}}\int_1^\infty \left(1 - \frac{1}{2t^2}\right)exp\left(-\frac{\gamma t^2}{2}\right)dt\right.$$

$$\left. + \int_0^{\pi/4} sin\theta \; exp(-\gamma cos^2\theta)\left(\frac{\theta/2 - sin4\theta/8}{cos^2\theta} - 2\theta\right)d\theta\right]$$

(2.2.40)

$$I_2(\gamma) = 4\pi \int_0^\infty q^2(4q^2 - 1)(4q^4 + 1)^{-2}\left[\left(\frac{4q^2 + 1}{4q} + \frac{4q}{4q^2 + 1}\right)ln\left(\frac{2q + 1}{2q - 1}\right)^2\right.$$

$$\left. - 2\right] \times exp[-\gamma(2q^2 + 1/2)]dq.$$

(2.2.41)

It is observed that the band-to-band Auger process is a complex function of the carrier effective mass, the density of state distribution, the bandgap energy, and a steep function of the majority carrier concentration. The band-to-band Auger processes are characterized by a strong temperature dependence arising from a characteristic "threshold energy" for these processes conditioned by the momentum and energy conservation of the four particles.

2.2.3.2. Other Auger recombination mechanisms

There is Auger recombination via traps, which is known as the trap-assisted Auger recombination process. The two relevant trap Auger effects are shown in Fig. 2.4. In process (a) a trapped electron makes a transition to the valence band by giving up its energy to an electron in the conduction band. The rate of this process can be written as $C_{ta}pnn_t$, where n_t represents the concentration of trapped electrons and C_{ta} is the trap coefficient. This process becomes important only in a very heavily doped n-type semiconductor with a high concentration of traps below the Fermi level. Process (b) shows recombination involving two holes and one electron. Here the electron makes a transition to an unoccupied trap level in the bandgap and gives its energy to a hole in the valence band. Like the above, the rate of the process can be expressed as $C_{tb}pnp_t$, and this process may acquire importance in heavily doped p-type semiconductors with a large density of traps located above the Fermi level.

The trap Auger coefficients of processes (a) and (b) by assuming a hydrogen-like wave function and a rigid-parabolic model is estimated as

$$C_{ta} = 2.23 \times 10^{-26} \left(\frac{m}{\varepsilon_s m_e^*} \right)^2 \frac{E_t^{5/2}}{\left(E_g - E_t \right)^{3/2} E_g^4} |F|^2 \qquad cm^6/sec \qquad (2.2.42)$$

$$C_{tb} = 2.23 \times 10^{-26} \left(\frac{m}{\varepsilon_s m_e^*} \right)^2 \frac{1}{E_t^3} |F|^2. \qquad (2.2.43)$$

In these equations m^* is the density of state effective mass E_t is the trapped energy measured from the conduction band edge, and $|F|^2$ accounts for wave-function overlap and, although not precisely known, is estimated to be of the order of 0.1.
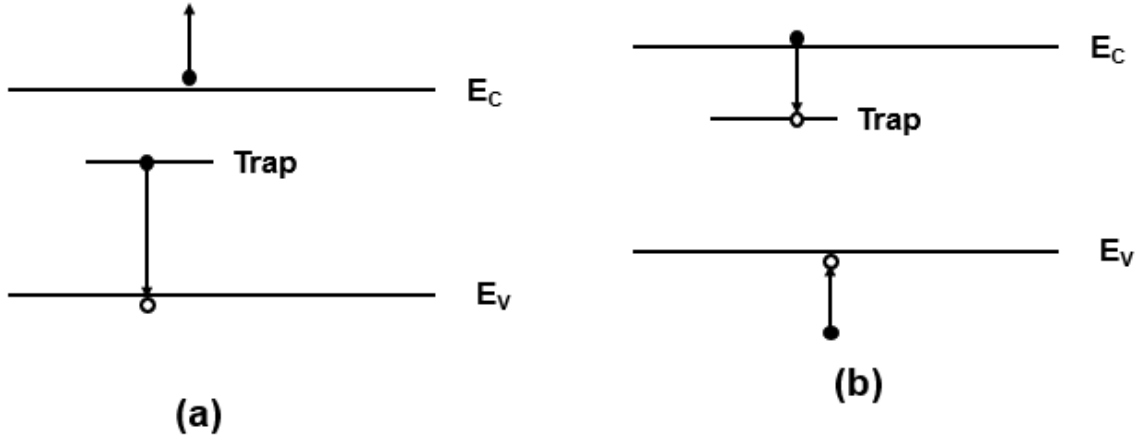
Figure 2.4 Schematic illustration of two possible trap-assisted Auger process.

The effective carrier lifetime is given by [83, 84, 85]

$$\frac{1}{\tau_{ef}} = \frac{1}{\tau_R} + \frac{1}{\tau_{A1}} + \frac{1}{\tau_{A7}} + \frac{1}{\tau_{AS}} + \frac{1}{\tau_{SR}}$$

(2.2.44)

2.2.4. Carrier lifetime in GeSn

The effective carrier lifetimes of the GeSn materials are estimated using Eq. (2.2.8), (2.2.14), and (2.2.26). The parameters are summarized in Appendix A. Figure 2.5 shows the lifetime for the $Ge_{0.89}Sn_{0.11}$ material with n-type doping. The lifetime is ranging from 0.1 µs to 0.01 ns. Both the radiative lifetime and the Auger lifetime have a peak in the transition from the extrinsic to the intrinsic region. At low temperatures and with low impurity concentrations, the lifetime is determined by radiative recombination. When the temperature increase, the Auger recombination becomes dominant and determines the carrier lifetime. For a high impurity concentration of 10^{18} cm^{-3}, the lifetime does not follow the behavior, which reduces as

temperature increases. The lifetimes at 300 K for different Sn compositions incorporating in the materials as the function of various impurity concentrations are shown in Fig. 2.6. The higher the impurity concentrations are, the shorter the lifetime is. The more Sn composition incorporates in the materials, the shorter the lifetime is.
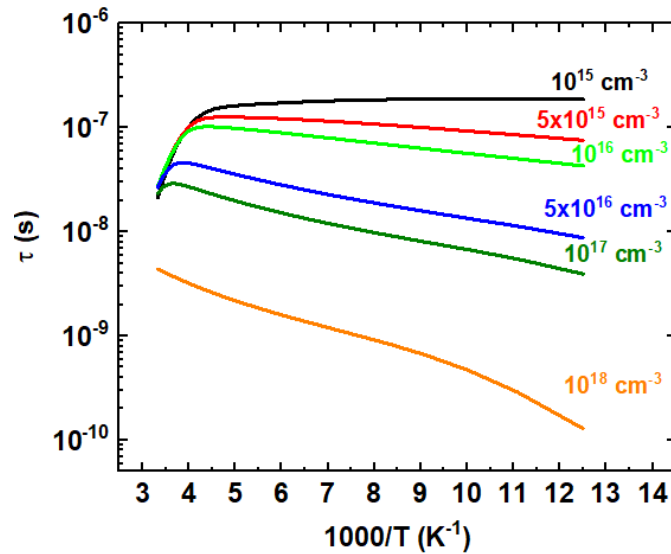
Figure 2.5 n-type $Ge_{0.89}Sn_{0.11}$ lifetime for various impurity concentrations
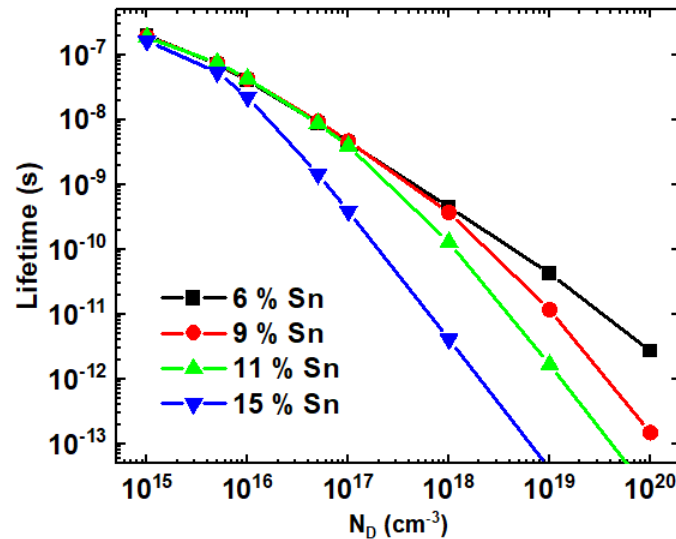
Figure 2.6 Hole lifetime at 300 K of the GeSn materials with various Sn percentages as a function of impurity concentrations

2.3. Estimation of carrier lifetime using GeSn photoconductors

2.3.1. Procedure for the study of lifetime and diffusion constant

The carrier bulk lifetime and the diffusion constant were studied in the following way. First, near the band edges, the density of states can be approximated by a parabolic band structure. Given that the material thickness is much thinner than the penetration depth of incident light (determined by the incident light wavelength and absorption coefficient of the material at such wavelength), the photocurrent ΔI can be expressed as:

$$\Delta I(h\nu) = \frac{P_{inc}}{h\nu}\eta_i(1-R)q\frac{\tau_{eff}}{\tau_t}Ad\frac{\sqrt{h\nu - E_g^\Gamma}}{h\nu} \tag{2.3.1}$$

The value or interpretation of each variable or constant in Eq. (2.3.1) is given in Table 2.1.

Table 2.1 Interpretation of each variable or constant in Eq. (2.3.1)

$P_{inc} / h\nu$	$h\nu$ is photon energy, P_{inc} is the incident light power. For Fourier transform infrared spectroscopy measurement, $P_{inc} / h\nu$ is a constant for whatever wavelength.
η_i	Internal quantum efficiency, assuming $\eta_i = 1$ in this study.
R	Reflectance at the surface. Since refractive index of GeSn is around 4.2, $R = 0.38$.
q	Unit charge.
τ_{eff}	Effective excess carrier lifetime.
τ_t	Transit time for the excess carriers to drift across the photoconductor.
A	Depend on effective masses of electron and hole, obtained from ellipsometry measurement.
d	GeSn film thickness, shown in Table 2.2.
E_g^Γ	Direct bandgap energy of GeSn alloy.

For the given material and device structure, the τ_{eff}, τ_t and A are temperature-dependent variables in Eq. (2.3.1), which therefore can be written as:

$$(\Delta I \times h\nu)^2 = (CAd)^2 \times \left(h\nu - E_g^\Gamma\right) \qquad (2.3.2)$$

where $C = \frac{P_{inc}}{h\nu}\eta_i(1-R)q\frac{\tau_{eff}}{\tau_t}$. By linear fitting the $(\Delta I \times h\nu)^2$ versus $h\nu$ curve that obtained from measured spectral response via Fourier transform infrared (FTIR) spectroscopy, the slope $(CAd)^2$ can be extracted.
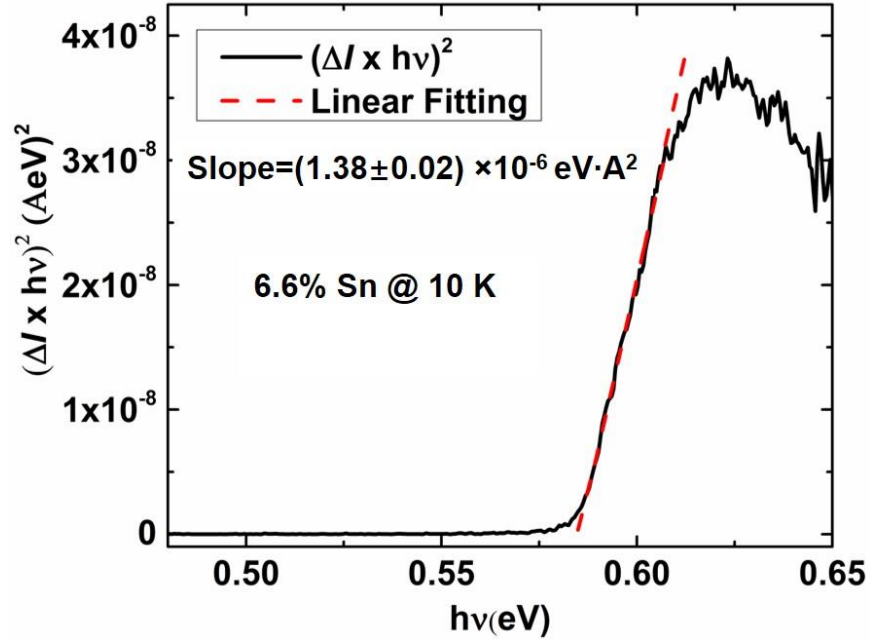
Figure 2.7 A representative spectral response of GeSn photoconductor with 6.6% Sn composition. The solid curve is measurement data, and the dashed line is the linear fitting.

Figure 2.7 shows a representative spectral response of GeSn photoconductor with 6.6% Sn composition. The solid curve is the plot of $(\Delta I \times h\nu)^2$ versus $h\nu$ and the dashed line is the linear fitting. The slope value of $(1.38 \pm 0.02) \times 10^{-6}$ eV·A^2 was extracted.

In order to obtain the value of τ_{eff}/τ_t, the A needs to be determined (the values of R and η_i are given in Table 2.1). The following method is used to determine the values of A at various temperatures. Since[86,87]:

$$A(T) \approx \frac{q^2}{nch^2 m_e^\Gamma(T)}\left(\frac{2m_e^\Gamma(T)m_h(T)}{m_e^\Gamma(T)+m_h(T)}\right)^{3/2} \qquad (2.3.3)$$

where T, n, c, and h are the temperature, refractive index, speed of light, and Planck constant, m_e^Γ and m_h are electron effective mass at Γ-valley and hole effective mass, respectively. The temperature variation of m_e^Γ follows [86,87]:

$$m_e^\Gamma(T) = 0.0505 m_0 \times E_g^\Gamma(T) \tag{2.3.4}$$

where the m_0 is free-electron rest mass (9.11×10^{-31} kg) and $E_g^\Gamma(T)$ was obtained from our photoluminescence study [88]. Therefore, using Eq. (2.3.4) the $m_e^\Gamma(T)$ can be determined. For the m_h (T), it follows a temperature-dependent relationship:

$$m_h(T) = m_{0,h} + m_{1,h} \times (300/T) \tag{2.3.5}$$

where $m_{0,h} = \left(m_{lh}^{3/2} + m_{hh}^{3/2}\right)^{2/3}$. The m_{lh} and m_{hh} are effective masses of the light hole and heavy hole in the valence band, respectively, whose values are calculated by [89]

$$m_{lh} = m_0 \times 1/(\gamma_1 + 2\gamma_2) \tag{2.3.6}$$

$$m_{hh} = m_0 \times 1/(\gamma_1 - 2\gamma_2) \tag{2.3.7}$$

where the γ_1 and γ_2 are given by γ_1 = 14.31-37.04x+560.24x^2 and γ_2 = 4.95-19.16x+280.14x^2, respectively, where the x is the Sn composition. Then the $m_{0,h}$ can be determined using Eqs. (2.3.6) and (2.3.7). Since the value of A at 300 K was obtained from ellipsometry spectroscopy [90], with the calculated m_e^Γ at 300 K giving by Eq. (2.3.4), the m_h at 300 K can be calculated using Eq. (2.3.3). Consequently, by using Eq. (2.3.5), i.e., m_h (300 K) = $m_{0,h} + m_{1,h}$, with known $m_{0,h}$, the $m_{1,h}$ can be determined. Since the parameters $m_{0,h}$, and $m_{1,h}$ are independent of temperature, the variable $A(T)$ is obtained via Eqs. (2.3.3)-(2.3.5).

Since the variable $A(T)$ is obtained, the ratio τ_t / τ_{eff} can be extracted from the slope that fitted in Eq. (2.3.2), which is denoted as $B = \tau_{eff} / \tau_t$. For the carrier transit time τ_t, as we know,

$$\tau_t = \frac{1}{\mu_p}(1+b)\frac{l^2}{V} \tag{2.3.8}$$

where V is the applied voltage, l is the spacing between the electrodes, μ_p is the hole mobility

and b is the ratio of hole mobility μ_p to electron mobility μ_n, respectively. Since $B = \tau_{eff} / \tau_t$, the

Eq. (2.3.8) can be written as

$$\frac{1+b}{\tau_{eff}} = B\mu_p V \frac{1}{l^2} \tag{2.3.9}$$

The temperature variation of hole mobility μ_p can be expressed with the power law:

$$\mu_p(T) = \mu_p(300K) \times \left(\frac{T}{300}\right)^{\gamma_p} \tag{2.3.10}$$

where μ_p (300 K) is the hole mobility at 300 K, γ_p is the index coefficient. As the μ_p (300 K) and

μ_p (77 K) were obtained from Hall measurement, the γ_p can be determined. Therefore, under the

fixed applied voltage, for a given l, the value of $(1+b)/\tau_{eff}$ in Eq. (2.3.9) can be calculated.

For our photoconductor devices, due to the non-passivated surface, the surface recombination

velocity reflecting carrier diffusion towards the surface is considerably high. As the result, the

effective lifetime τ_{eff} is determined by recombination in the bulk and the carrier diffusion towards

the surfaces, not depends on the recombination rate at the surface, as almost all carriers reaching

the surface immediately recombine. Therefore,

$$\frac{1}{\tau_{eff}} = \frac{1}{\tau_{bulk}} + D_n\left(\frac{\pi}{l}\right)^2 \tag{2.3.11}$$

where τ_{bulk} is the bulk effective lifetime, and D_n is the minority carrier diffusion constant. By

multiplying both sides of Eq. (2.3.11) with (1+b), the Eq. (2.3.11) becomes:

$$\frac{1+b}{\tau_{eff}} = \frac{1+b}{\tau_{bulk}} + (1+b)D_n\left(\frac{\pi}{l}\right)^2 \tag{2.3.12}$$

By linear fitting, the $(1+b)/\tau_{eff}$ versus $1/l^2$, the $(1+b)/\tau_{bulk}$ and $(1+b)D_n$ can be extracted from fitted

intercept and slope, respectively. In order to determine each parameter, the Einstein relation is

used,

$$D_n = \frac{\mu_n k_B T}{q} \tag{2.3.13}$$

where k_B is Boltzmann constant. Using Eq. (2.3.13) and extracted value of $(1+b)D_n$, the

temperature-dependent electron mobility μ_n can be determined. Consequently, the D_n, τ_t and τ_{bulk}

are determined.
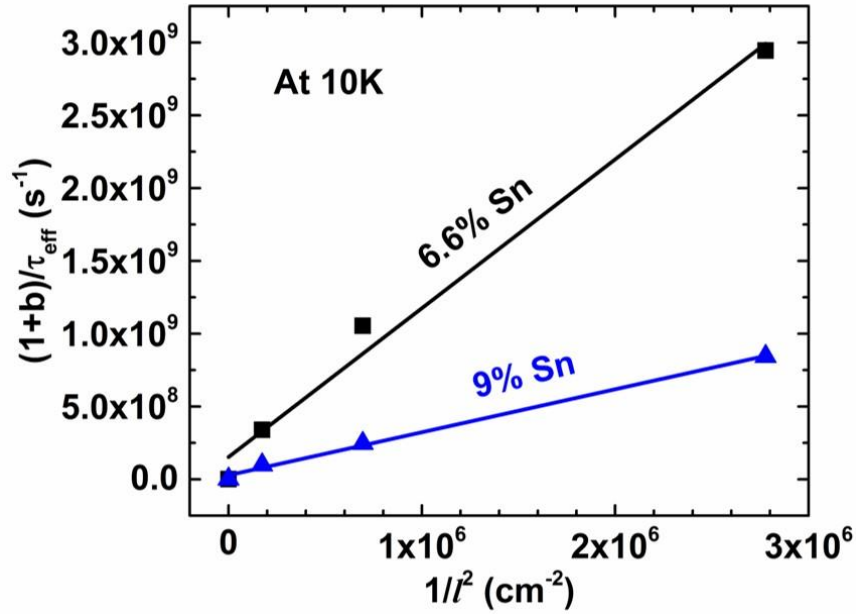
Figure 2.8 A representative linear fitting the $(1+b)/\tau_{bulk}$ versus $1/l^2$ at 10 K. The $(1+b)/\tau_{bulk}$ and $(1+b)D_n$ can be extracted from fitted intercept and slope, respectively.

The representative linear fittings for GeSn photoconductors with Sn compositions of 6.6%

and 9% using Eq. (2.3.12) at 10 K are shown in Fig. 2.8. The slopes and intercepts were

extracted as 1022 cm^2/s and 1.52×10^8 s^{-1}, and 295.2 cm^2/s and 2.76×10^7 s^{-1} for 6.6% and 9% Sn devices, respectively, based on which the bulk lifetimes and the electron diffusion constants were calculated as 7×10^{-9} s and 97.4 cm^2/s, and 3.9×10^{-8} s and 38.1 cm^2/s for 6.6% and 9% Sn devices, respectively.

2.3.2. Experimental methods

In this study, the Ge$_{1-x}$Sn$_x$ samples were grown using an ASM Epsilon® 2000 Plus reduced pressure chemical vapor deposition (RPCVD) system using SnCl$_4$ and GeH$_4$ as precursors. A strain relaxed Ge buffer layer was first grown on the Si (001) substrate, followed by the growth of the GeSn alloy. The growth temperature was kept below 450 °C to be compatible with the Si complementary metal-oxide-semiconductor (CMOS) process. After growth, the material quality, the layer thickness, and the strain of the as-grown wafer were systemically analyzed by using transmission electron microscopy (TEM) and high-resolution X-ray diffraction (XRD) techniques [88]. TEM results showed that the majority of defects were localized at the Ge/Si interface, indicating high material quality. The material characterizations are summarized in Table 2.2.

Table 2.2 Summary of material characterization

Sn composition	GeSn thickness (nm)	Unintentional doping (cm^{-3})	Compressive strain (%)
6.6%	500	p-type, ~10^{17}	0.08
9.0%	600	p-type, ~10^{18}	0.14

The samples were then fabricated into photoconductor devices with the mesa sizes of 0.5 × 0.5 mm^2. Four types of contact were patterned on the mesa, i.e., two electrodes without

interdigitated structures, the interdigitated electrodes with finger width/spacing of 3 µm/6 µm, 6 µm/12 µm, and 12 µm/24 µm (annotate as 3-6, 6-12 and 12-24 hereafter). The contacts consist of 10 nm Cr and 200 nm Au. Based on our current voltage study, these contacts showed a linear I-V behavior indicating the Ohmic contact, thus no annealing process was needed [36].

The spectral response testing setup consists of an FTIR spectrometer to measure the normalized spectral response and a lock-in amplifier with a 1.55 µm laser diode optically chopped at 380 Hz for responsivity measurements (determine the absolute value of spectral response). The temperature-dependent bandgap energies were measured with our off-axis PL measurement system [88]. The spectroscopic ellipsometry data were collected using a Variable-Angle Spectroscopic Ellipsometer (WVASE32) in the range of 0.496 to 4.768 eV (260 to 2500 nm) with a resolution of 10 nm. The electron mobility was tested by Hall measurement that was conducted at 300 and 77 K. The detailed experimental setup and procedure are well described in our previous studies [28].

2.3.3. Results and discussions

Figure 2.9 (a) and (b) show the spectral $(\Delta I \times h\upsilon)^2$ of $Ge_{0.934}Sn_{0.066}$ photoconductor and $Ge_{0.91}Sn_{0.09}$ photoconductor versus photon energy for different temperatures from 10K to 300K, respectively. The photocurrents are proportional to the absorption coefficient, and as a result, the band edges are clearly shown. The increase in the percentage of Sn also creates the shift in the spectrum to a narrow bandgap. The cut-off wavelength at 300K extends to 2.3µm for 6% Sn photoconductor and to 2.6µm for 9% Sn. For the 9% Sn photoconductor, the photocurrent shows enhancement at low temperatures. For the 6.6% Sn photoconductor, the enhancement is at 140K. In fact, as the temperature changes, bulk lifetime and surface lifetime take place on the photoconductive gain. Further discussion about carrier lifetime will be shown below. The

photocurrent strongly depends on the absorption coefficient. Hence, in order to study the dependence of the photocurrent on temperature, it is necessary to acquire absorption coefficients at different temperatures. At the band edge, the magnitude of the absorption coefficient relates to the electron and hole effective masses.
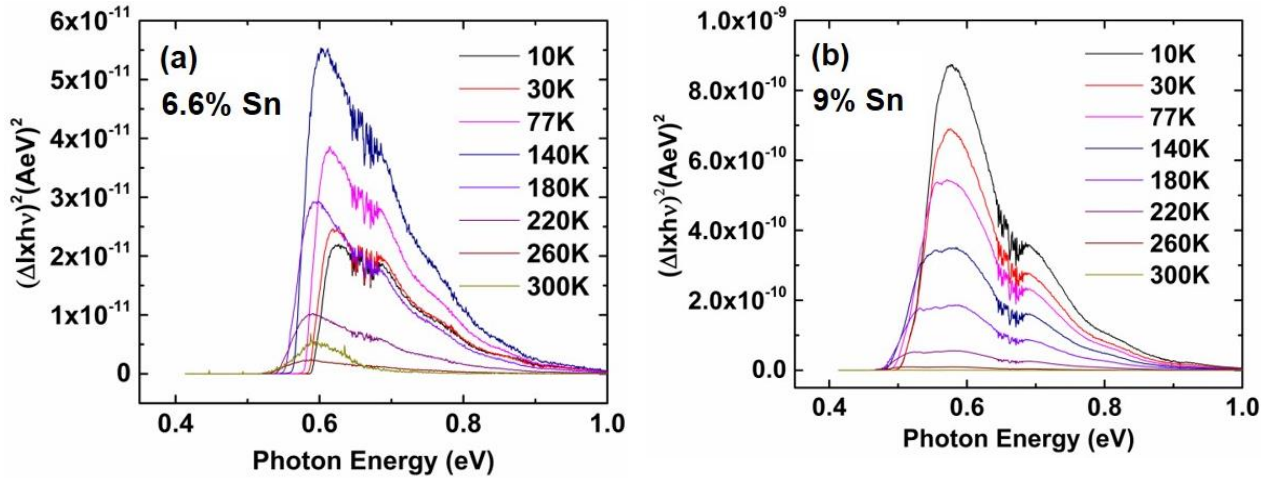
Figure 2.9 Spectral $(\Delta I \times h\upsilon)^2$ of GeSn photoconductors with Sn compositions of (a) 6.6% and (b) 9% at temperatures from 10 to 300 K.
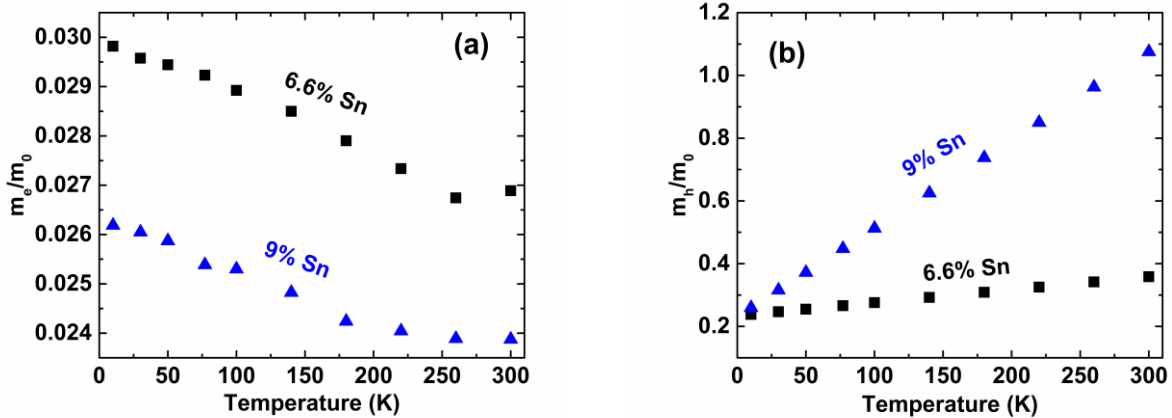
Figure 2.10 The calculated (a) electron effective mass and (b) hole effective mass at different temperatures from 10K to 300K.
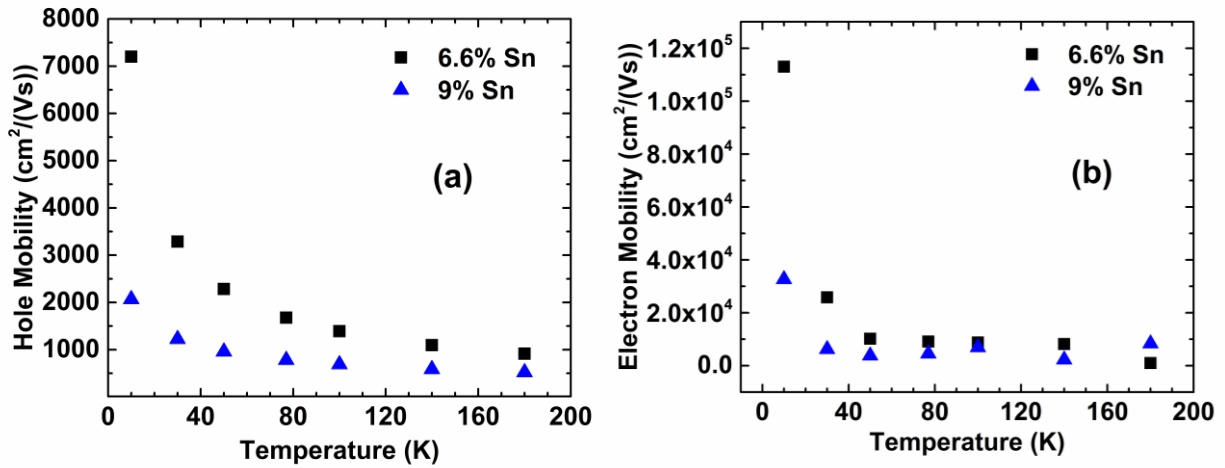
Figure 2.11 (a) Hole mobility and (b) electron mobility for different temperatures from 10 K to 180 K.

Figure 2.10 (a) and (b) shows the calculated electron effective mass and hole effective mass at different temperatures from 10K to 300K, respectively. From those data, the magnitudes of the absorption coefficient at different temperatures at the band edge are obtained. Figure 2.11 (a) and (b) show the hole mobility and electron mobility for different temperatures fromm 10K to 180K, respectively. The hole mobility is extrapolated from Hall measurement at 300 and 77K. However, as the photoconductor operating temperature increases, the thermal dark current mechanism becomes stronger and lead signal to noise (S/N) ratio to be small especially for device 3-6. After 180K, we do not have enough data points for the linear fitting from Eq. (2.3.7). Hence, studies of electron mobility, bulk lifetime, and diffusion constant are observed in the range from 10K to 180K. As the temperature increases, the carrier mobilities are reduced, which is true as atoms are thermally excited. At low temperatures, high carrier mobilities help to shorten transit time, but unfortunately, they enhance surface recombination. Hence, the 6.6% photoconductor can achieve a high gain at 140K instead of a very low temperature. However, for the 9% photoconductor, their carrier mobilities are lower than those of 6.6% Sn at low

temperatures. Its photocurrent is enhanced at 10K, and then it decreases as temperature increases. As a result, for these photoconductors, surface recombination takes an important role in their performances at uncooled operating temperatures.
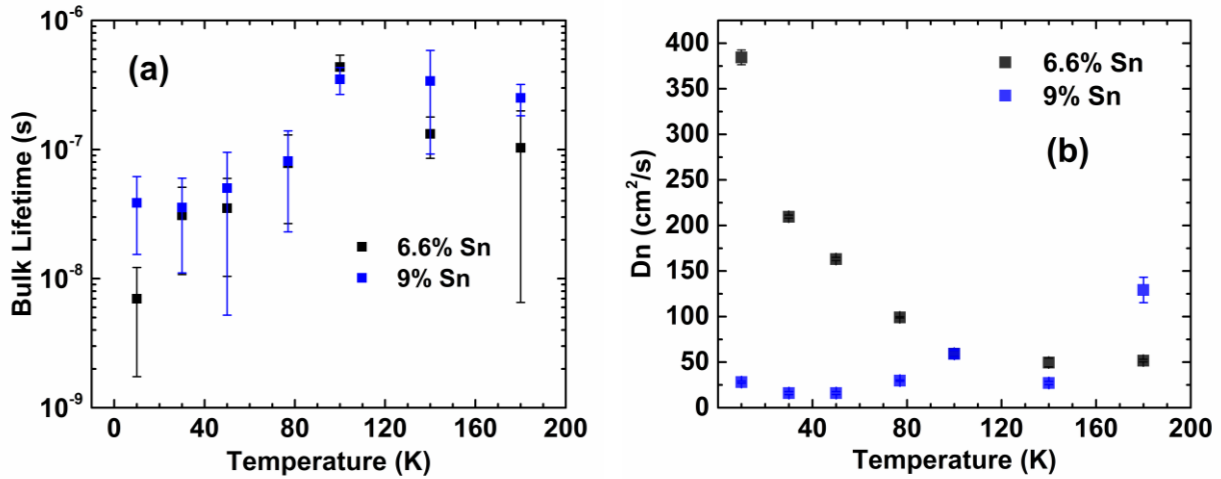
Figure 2.12 (a) Temperature-dependent bulk lifetimes of 6.6% and 9% Sn samples; (b) temperature-dependent minority diffusion constants at samples' surfaces.

Temperature-dependent bulk lifetimes of 6.6% and 9% Sn samples are shown in figure 2.12 (a). Both of the bulk lifetimes show the same trend following the increase in temperature. The bulk lifetime is on the increase as temperature increases in the range from 10 K to 100 K, and then, it decreases. In fact, at very low temperatures, radiative recombination is an impact of the whole process of recombination. However, as we know, Shockley-Read-Hall (SRH) lifetime decreases exponentially following the increase of temperature. After some temperature, the SRH lifetime will be shortened than the radiative lifetime. Then, it will be dominant in the process of recombination. In our cases, after 100K, the SRH lifetime will be a component that mostly affects the bulk lifetime.

Moreover, these 6.6% Sn and 9% photoconductors have the same range of bulk lifetime from several nanoseconds to several hundred nanoseconds. Hence, the photoconductive gain is

determined by those samples' surfaces and quality. In fact, figure 2.12 (b) shows temperature-dependent minority diffusion constants at the surfaces of 6.6% Sn and 9% Sn samples. Comparing between 6.6% Sn and 9% Sn photoconductors, the 6.6% Sn photoconductor has higher mobility reflecting lower doping concentration that leads to slower transit time, but it has a higher probability for carriers to recombine at its surfaces. The 9% Sn photoconductor has a thicker absorber layer, which enhances absorption inside the active layer, but it also increases the probability of recombination, which will reduce the performance of those devices. However, the bulk lifetimes of the 6.6% and 9% Sn photoconductors are in the same range of values even that those samples are 100nm different in thickness. In other words, an increase in thickness helps to enhance photocurrent, and not shorten bulk lifetime much. As we know, the thickness needs to be optimized to enhance the photoconductor, and we believe that the thicker the active layer is the stronger photocurrent will be.

In summary, the responsivity and spectral response of $Ge_{0.934}Sn_{0.066}$ and $Ge_{0.91}Sn_{0.09}$ devices are measured over the operating temperatures ranging from liquid helium and liquid nitrogen cooling up to room temperature. Moreover, to analyze the surface recombination and effective lifetime, the ellipsometry and Hall measurements have been used to obtain the absorption coefficient and majority mobility for those materials, respectively. Without surface passivation, the higher the mobility is the shorter the surface recombination lifetime even that there is an enhancement in transit time. In other words, excess carriers have recombined at the surface as the mobility is higher. We observe the slight dependence of bulk lifetime on the thickness of those thin films, which can help to increase the thickness of the film till the optimized thickness enhances absorption but does not shorten the bulk lifetime.

2.4. Silvaco simulation with a lifetime as a dominant factor in SRH mechanism

In order to simulate the lifetime effects on the performance of the detectors, Silvaco is used with the SRH model. The SRH recombination is modeled as follows:

$$R_{SRH} = \frac{pn - n_{ie}^2}{TAUP0\left[n + n_{ie}exp\left(\frac{ETRAP}{kT_L}\right)\right] + TAUN0\left[p + n_{ie}exp\left(\frac{-ETRAP}{kT_L}\right)\right]} \qquad (2.4.1)$$

where $ETRAP$ is the difference between the trap energy level and the intrinsic Fermi level, T_L is the lattice temperature in Kelvin degree and $TAUN0$ and $TAUP0$ are the electron and hole lifetimes. This model is activated by using the SRH parameter of $MODELS$ statement. The electron and hole lifetime parameters, $TAUN0$ and $TAUP0$, are user-definable in the $MATERIAL$ statement. As shown in Fig. 2.12, the Silvaco simulated dark current is a function of a lifetime at room temperature. It shows a significant decrease of dark current as lifetime increases. As above estimated, the lifetime is in the range of 0.1 µs to 0.1 ns, which yields to the dark current ranging from 10 µA to 1 mA. The simulated dark current shows a similar range to that of the practical devices.
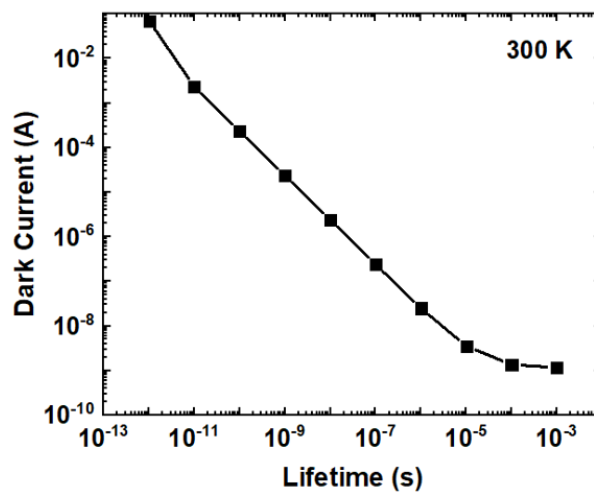
Figure 2.13 Dark current as a function of the lifetime at room temperature.

Chapter 3.   Systematic study of GeSn optical properties

The optical properties of the material create the changes that light experiences upon interacting with that material. These optical properties are influenced by the material's surface and its electronic structure. There are many optical properties including reflection, refraction, transmission, and absorption. Two important optical constants such as the refractive index and absorption coefficient associate with the optical properties. Ellipsometry is a sensitive measurement technique that uses polarized light to characterize thin films. Ellipsometry can determine optical constants, layer thicknesses, and many physical quantities which affect the optical constants [91, 92].
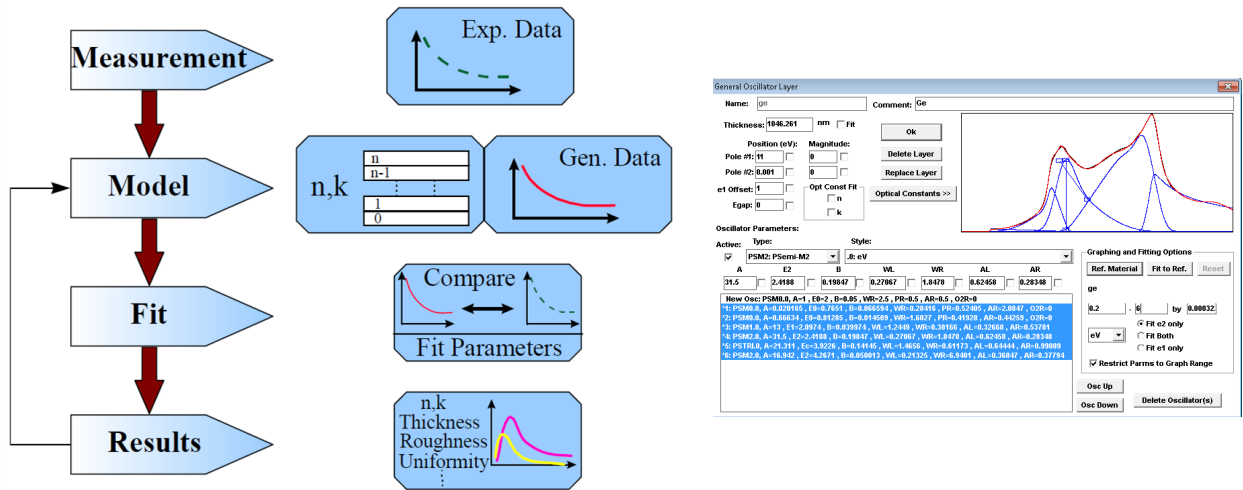
Figure 3.1 (a) The procedure used in ellipsometry measurements. (b) Dialog box to model the material properties [91].

Fig. 3.1 (a) shows the procedure to operate ellipsometry [91]. First, the sample is measured. The reflected or transmitted beam intensities or polarization states are measured rather than optical constants. Second, the dielectric function of each layer of our samples is modeled. Fig. 3.2 (b) shows the typical GeSn dielectric function including the Oscillator list. The Oscillators

42

contain some unknown parameters. Third, after developing a model, the unknown parameters are varied to generate data until a set of optimized parameters that yield calculated data closely match our measured optical data. It is worth noting that the best fit set of parameters needs to be unique, physically reasonable, and no strongly correlated.

The researchers have been using ellipsometry to measure GeSn dielectric functions. Several papers reported on optical transitions [93-95]. However, there is a lack of a database of GeSn absorption and refractive indices. They are significant inputs for GeSn detector and laser design. Hence, it is motivating us to study GeSn absorption and develop a physics-based empirical formula.

In this chapter, the systematic study of the absorption coefficient and refractive index of $Ge_{1-x}Sn_x$ thin films (x from 0% to 10%) was conducted via spectroscopic ellipsometry at room temperature. The physical models were used to fit the obtained data in the wavelength range from 1500 to 2500 nm. Then, two empirical formulae consisting of the Sn compositional- and strain-dependent absorption coefficient and refractive index were built. For the absorption coefficient formula since the absorption coefficient is associated with bandgap energy, which is mainly determined by the Sn composition and strain, the input can be only these two parameters. While for the refractive index formula, the spectral refractive index curve can be also obtained by inputting these two parameters. Therefore, for a given $Ge_{1-x}Sn_x$ with specific Sn composition (up to 10% Sn) and strain, the developed formulae could be used to predict the spectral absorption coefficient and spectral refractive index. The parameter-based expressions are valuable to input into any standard software to simulate devices. Therefore, they could provide key information for the design of GeSn-based optoelectronic devices.

3.1.GeSn absorption coefficient

3.1.1. Theory model for absorption coefficient

The absorption coefficient is a function of the photon energy in a typical semiconductor, demonstrating various possible absorption processes. The important features of the behavior of the absorption coefficient versus the photon energy can be summarized as (i) Free carrier absorption, including impurity absorption, Reststrahlen or lattice absorption, etc; (ii) Exciton absorption; (iii) Urbach tail; (iv) Fundamental interband absorption, including indirect (for indirect bandgap semiconductors) and direct bandgap absorptions [96]. The process (i) usually occurs at longer wavelengths which is beyond the cutoff of the Ellipsometer. The process (ii) is usually observed at low temperatures. Therefore in this chapter, the processes (iii) and (iv) were discussed, based on which the absorption behavior near the band edge was investigated, leading to the determined cutoff wavelength that could apply to the design of the photodetectors. In fact, the absorption coefficient can be written as

$$\alpha(hv) = \alpha_{ID}(hv) + \alpha_D(hv) + \alpha_U(hv) \tag{3.1.1}$$

Those three significant transitions such as direct absorption, Urbach tail, and indirect absorption are dominant at different energy. Fig. 3.2 shows the E-k diagram including absorption processes. At higher energy, the direct bandgap transition is dominant. After that, the Urbach tail is dominant. As shown in the E-k diagram, the absorption that happens at the impurity level is known as the Urbach tail. At lower energy, the indirect bandgap transition is dominant. For indirect transition, there are two mechanisms such as phonon emission and phonon absorption. As a photon has higher energy than an indirect bandgap, it excites an electron to an indirect valley and emits the phonon as well. As a photon has smaller energy than an indirect bandgap, it excites an electron, and the electron absorbs the energy of phonon to

44

reach the indirect valley. The GeSn absorption can be modeled at different energy regions. Therefore, Eq. (3.1.1) can be rewritten as follows:

$$\alpha(hv) = \begin{cases} \alpha_D(hv), \text{ when direct bandgap transition is dominant at higher energy;} \\ \\ \alpha_U(hv) + \alpha_{ID}(hv), \text{ when Urbach tail is dominant, while indirect bandgap} \\ \qquad\qquad \text{transition contributes at lower energy;} \\ \\ \alpha_{ID}(hv), \text{ when indirect bandgap transition is dominant at lower energy.} \end{cases} \qquad (3.1.2)$$
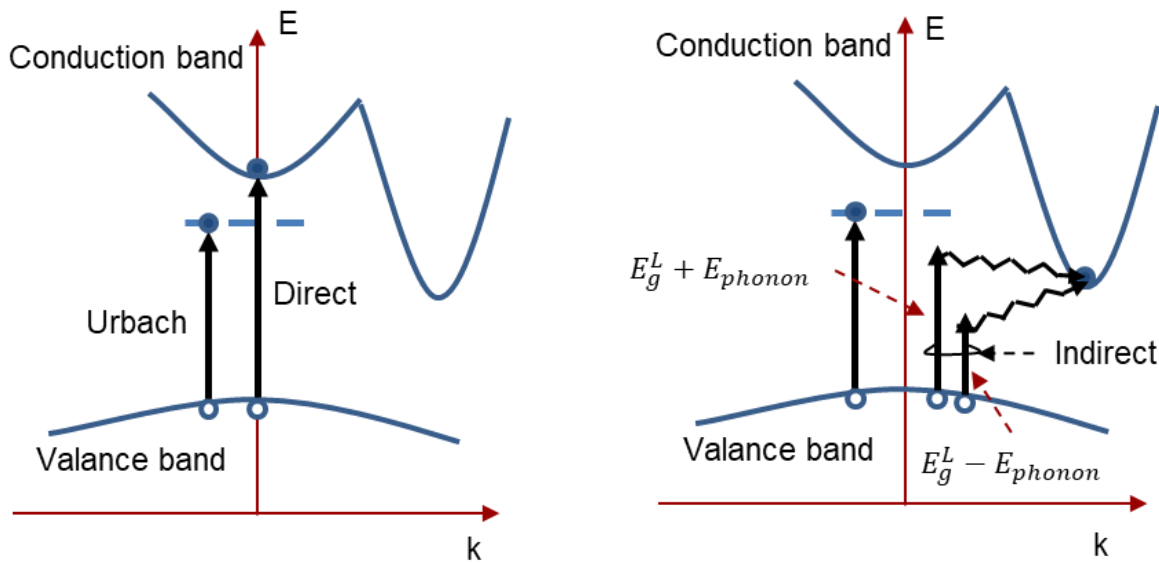
Figure 3.2 Band diagram involving optical transitions

3.1.1.1. Interband absorption

There are two types of interband absorption, i.e., direct and indirect transitions. When the incident photo energy $hv \geq$ direct bandgap energy E_g^D, the direct transition becomes a dominant process. Near the band edges, a parabolic dependence of direct bandgap absorption is widely used as following [96]

$$(\alpha_D hv)^2 = A^2(hv - E_g^\Gamma) \qquad (3.1.3)$$

where α_D is the absorption coefficient regarding the direct transition, A is a constant, $h\upsilon$ is the incident photon energy, E_g^Γ is the direct (Γ valley of GeSn) bandgap energy. A and E_g^Γ are the material-dependent parameters.

For the indirect bandgap material, when the incident photon energy lies in $E_g^{ID} \leq h\upsilon < E_g^D$, the indirect transition with phonon assistant dominates the photoexcitation process. Two types of indirect transition associated with phonon absorption and phonon emission processes contribute to the α, as described in the following [96]

$$\alpha_{ID}^{1/2} = \begin{cases} B^{1/2}[f_{BE}(h\theta)]^{1/2}[h\upsilon - (E_g^L - h\theta)] \ , & (E_g^L - h\theta) < h\upsilon < (E_g^L + h\theta); \\ C^{1/2}[1 - f_{BE}(h\theta)]^{1/2}[h\upsilon - (E_g^L + h\theta)] \ , & (E_g^L + h\theta) < h\upsilon. \end{cases} \tag{3.1.4}$$

where α_{ID} is the absorption coefficient regarding the indirect transition, B and C are constants, E_g^L is the indirect (L valley of GeSn) bandgap energy, $f_{BE}(h\theta)$ is the Bose-Einstein distribution with the phonon energy $h\theta$, given by [96]

$$f_{BE}(h\theta) = \frac{1}{exp(h\theta/k_B T) - 1} \tag{3.1.5}$$

where k_B is the Boltzmann constant and T is the temperature. When $(E_g^L - h\theta) < h\upsilon < (E_g^L + h\theta)$, the absorption is controlled by the phonon absorption process; while when $h\upsilon > (E_g^L + h\theta)$, both processes contributed to the absorption but the phonon emission process is dominant. In equations (3.1.4) and (3.1.5), the $B, C, h\theta$ and E_g^L are the material-dependent parameters.

3.1.1.2. Urbach tail

The bandtail states involve energy levels inside the bandgap, which are usually originated from doping and defects in the crystal [97, 98]. The Urbach tail is attributed to the transition between bandtail states. The photoexcitation in this region follows Urbach's rule, given by [97-99]

$$\alpha_U(h\nu) = \alpha_0 \exp\left(\frac{h\nu - E_g}{\Delta E}\right) \tag{3.1.6}$$

where α_0 and ΔE (called Urbach width) are material-dependent parameters. The detailed Urbach tail absorption has been discussed elsewhere [100]. A semiempirical approach can be used to describe the connection between the direct bandgap and Urbach absorption, which requires continuity at the connection point E_0 [101]

$$\alpha_U(E_0) = \alpha_D(E_0), \quad \alpha'_U(E_0) = \alpha'_D(E_0) \tag{3.1.7}$$

From equations (3.1.1), (3.1.4), and (3.1.5) we can obtain:

$$E_0 = E_g^\Gamma + \frac{\Delta E}{2}, \quad \alpha_0 = Ae^{-\frac{1}{2}}\left(\frac{\Delta E}{2}\right)^{\frac{1}{2}} \tag{3.1.8}$$

where A is a constant (the same as in equation (3.1.3)), and e is Euler's number. Then the equation (3.1.6) can be rewritten as:

$$\alpha_U(h\nu) = Ae^{-\frac{1}{2}}\left(\frac{\Delta E}{2}\right)^{\frac{1}{2}}\exp\left(\frac{h\nu - E_g}{\Delta E}\right) \tag{3.1.9}$$

Equation (3.1.9) indicates that the ΔE plays an important role in the Urbach absorption process.

3.1.2. Experimental and data processing methods

3.1.2.1. Experimental method

GeSn thin films were grown using a commercially available ASM Epsilon® reduced pressure chemical vapor deposition reactor (RP-CVD). A 700-nm thick strain relaxed Ge buffer layer was first grown on the Si (001) substrate, followed by the growth of GeSn layers. GeH$_4$ and SnCl$_4$ were used as precursors for Ge and Sn, respectively. The growth temperature was kept below 450 °C to be compatible with a Si CMOS process. A detailed growth method was

reported in the previous study [102]. All $Ge_{1-x}Sn_x$ layers were unintentionally doped with a p-type background doping concentration of 10^{17} cm^{-3}. The GeSn layer thickness, Sn composition, and strain level were confirmed by material characterization including TEM, XRD, etc. The measurement results are summarized in Table 3.1.

Table 3.1 Summary of material characterization [90].

No.	Sn (%)	$Ge_{1-x}Sn_x$ film thickness (nm)	Compressive strain (%)	E_g^Γ (eV)
A	0 (Ge reference)	300	0	0.805 ± 0.0366
B	1	327	0.02	0.792 ± 0.027
C	2	40	0.22	0.772 ± 0.022
D	3	128	0.24	0.761 ± 0.046
E	4	70	0.5	0.723 ± 0.020
F	5	88	0.67	0.721 ± 0.042
G	6	96	0.82	0.713 ± 0.024
H	7	240	0.45	0.682 ± 0.017
I	8	90	0.80	0.626 ± 0.015
J	9	117	1.01	0.617 ± 0.012
K	10	59	1.16	0.604 ± 0.012

The complex reflectance ratio was collected using a Variable-Angle Spectroscopic Ellipsometer (WVASE32) in the range of 0.496 to 4.768 eV (260 to 2500 nm) with a resolution of 0.04 eV at three angles of incidence (65°, 70°, and 75°). The amplitude component ψ and the phase difference Δ were fitted using the Johs-Herzinger model. Sample A was firstly measured and fitted as it consists of Si substrate and Ge buffer layers only since Ge dielectric function is in the WVASE32® software database. Sample A serves as a reference for other samples. For samples B to K, a four-layer model was built and used for the data processing, including Si substrate, Ge buffer, $Ge_{1-x}Sn_x$, and surface layer (50% air and 50% GeSn, given by the software). Figs. 3.3 (a) and 1(b) show the experimental ψ and Δ data and the model fit for sample K (10% Sn) as an example.
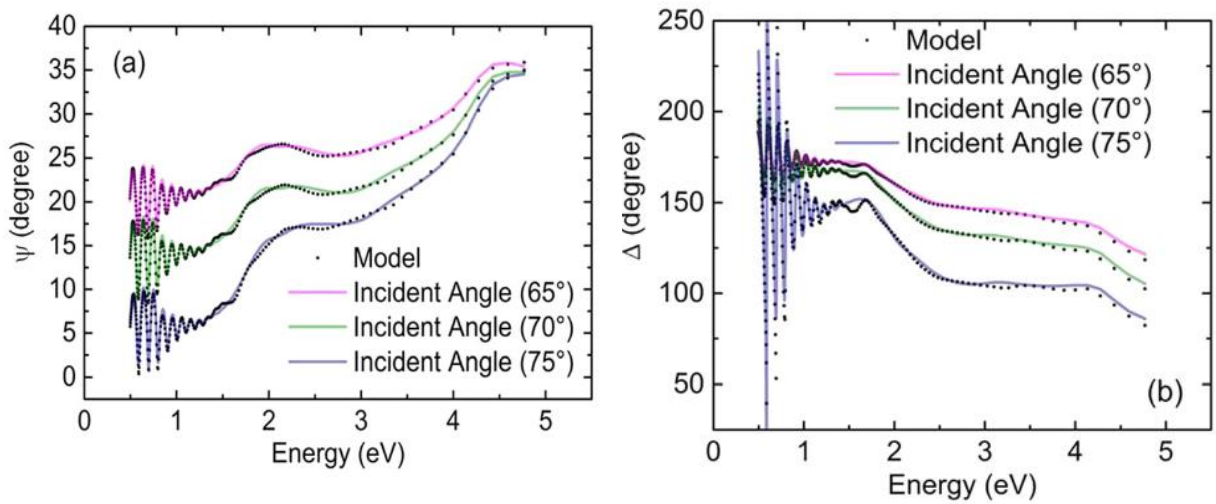
Figure 3.3 Experimental (a) ψ and (b) Δ data and the model fit for the 10% Sn sample [90]

Figure 3.4 (a) shows a representative spectral absorption coefficient of a sample with an Sn composition of 3 %. The solid symbols were obtained from the Johs-Herzinger model and the dashed and solid curves were fitted to identify each absorption process. The direct and indirect absorptions and Urbach tail are detected, as marked by arrows in Fig. 3.4 (a). The zoom-in of Fig. 3.4 (a) in each region with the respective fitting method is shown in Fig. 3.4 (b)-(d). A plot

49

of $(\alpha h\upsilon)^2$ against $h\upsilon$ is shown in Fig. 3.4 (b), corresponding to the direct bandgap absorption near the bandgap. According to equation (3.1.3), a linear fitting was used to describe the $(\alpha h\upsilon)^2$-$h\upsilon$ relationship. The extrapolation to photon energy axis gives the direct bandgap E_g^Γ (0.761 eV for $Ge_{0.97}Sn_{0.03}$), and the slope of the fitted curve gives the value of parameter A in equation (3.1.3).
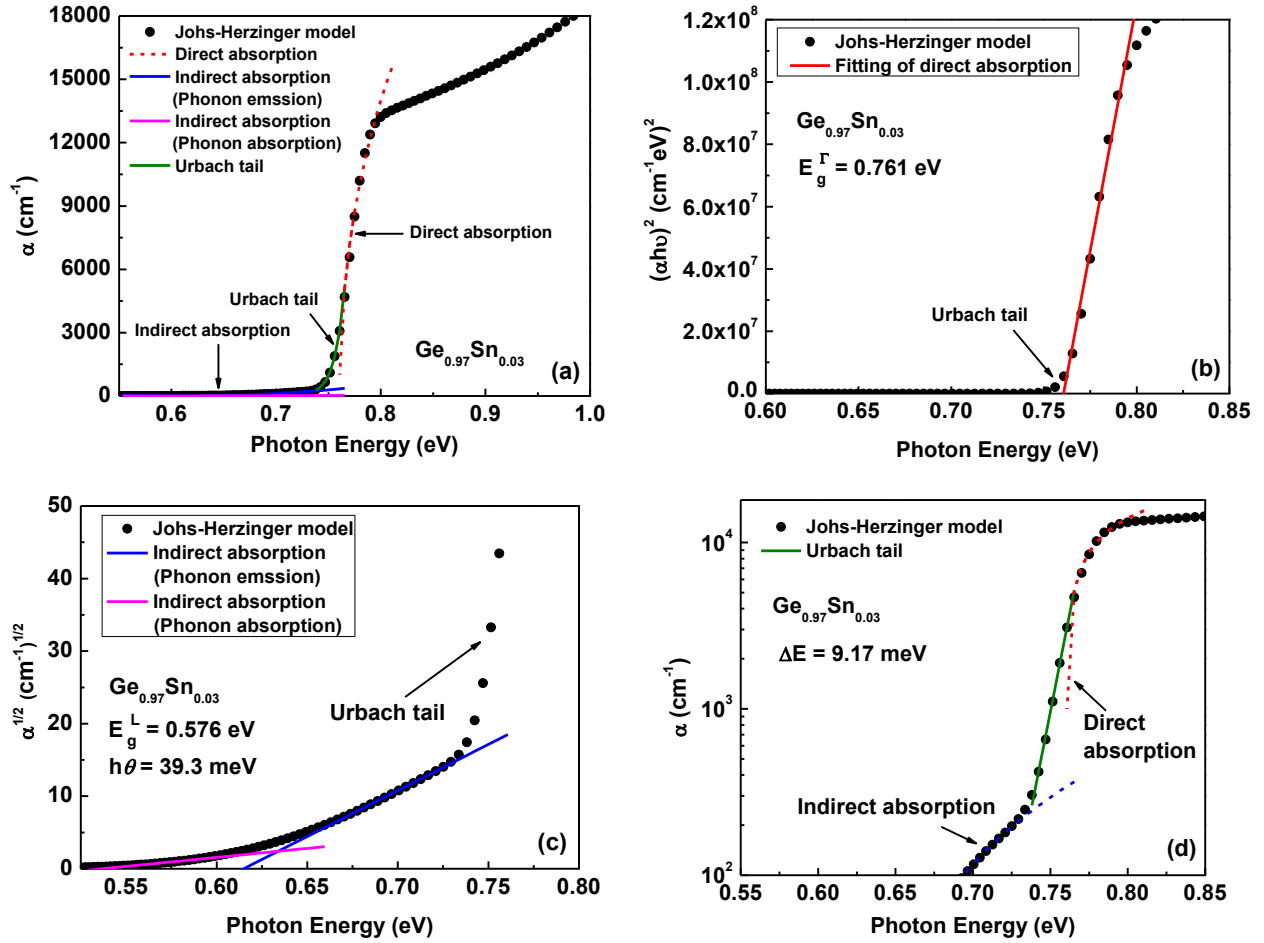
Figure 3.4 (a) Spectral absorption coefficient of $Ge_{0.97}Sn_{0.03}$ alloy. The interband transitions and Urbach tail are identified. (b) Close-up of (a) in the direct bandgap absorption region. The linear fitting of $(\alpha h\upsilon)^2$-$h\upsilon$ relationship allows for the extraction of the direct bandgap. (c) Close-up of (a) in the indirect bandgap absorption region. Two transitions, with respect to phonon absorption and phonon emission, are observed. The indirect bandgap energy and phonon energy are extracted by linear fittings of $\alpha^{1/2}$-$h\upsilon$ in phonon absorption and emission regions. (d) Close-up of (a) in Urbach tail region, where the exponential relationship between α and $h\upsilon$ follows Urbach's rule [90].

Figure 3.4 (c) illustrates the α in the indirect bandgap absorption region. Since the phonon assistant is involved, two types of absorptions with respect to the phonon absorption and

emission contribute to the α, as can be seen in Fig. 3.4 (c). The linear fittings of $\alpha^{1/2}$-$h\upsilon$ based on equation (3.1.4) were used to explicate the α behavior near the bandgap. The two fitted curves intersect the photo energy axis at E_g^L-$h\theta$ and E_g^L+$h\theta$, by which the E_g^L and $h\theta$ can be calculated (0.576 eV and 39.3 meV for Ge$_{0.97}$Sn$_{0.03}$). Moreover, the slopes of two fitted curves give the values of parameters B and C in equation (3.1.4), respectively.

Figure 3.4 (d) shows the Urbach tail between the direct and indirect bandgap absorption. Since the Urbach tail is attributed to the transitions between bandtail states below the band edge, the absorption coefficient in this region decreases exponentially as the photon energy away from the direct bandgap energy. There is an unambiguous turning point at about 0.74 eV, below which the indirect bandgap absorption becomes dominating the absorption coefficient, as shown in Fig. 3.4 (c) and (d). By linearly fitting the ln(α)-$h\upsilon$ in the Urbach tail region, the Urbach parameters α_0 and ΔE in equation (3.1.9) can be obtained.

Based on band structure study of Ge$_{1-x}$Sn$_x$ alloy, with x < 0.08, the alloy is an indirect bandgap material, the direct and indirect bandgap absorptions, and Urbach tail are identified because of the sufficient bandgap energy difference; while with the x ≥ 0.08, due to the very small separation between the direct and the indirect conduction band edge (minimum points of Γ- and L-valley), the band tail near the Γ-valley could be lower than the L-valley, resulting in the suppression of indirect bandgap absorption, and only direct bandgap absorption and Urbach tail can be observed. Therefore in this study, the absorption behavior associated with the indirect transition was discussed with the samples A-H (Sn compositions from 0 to 7 %); while the absorption behaviors related to direct bandgap transition and Urbach tail were investigated from each sample. The data analysis follows the methods describing Fig. 3.4 (b), (c), and (d), respectively.

3.1.3. Results and discussions

3.1.3.1. Interband absorption
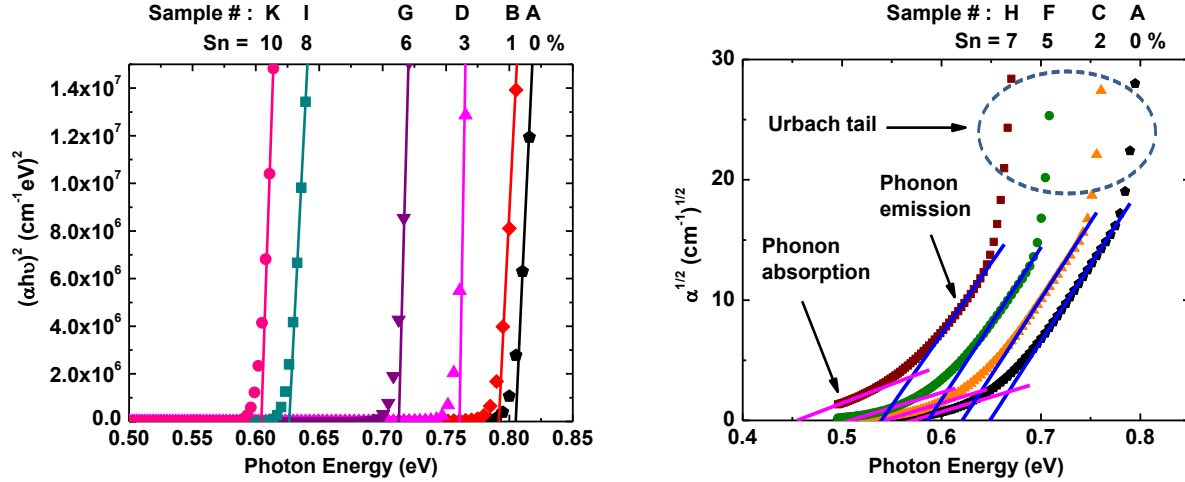
Figure 3.5 Sn compositional-dependent absorption coefficients attributed to the (a) direct bandgap transition and (b) indirect bandgap transition. The solid symbols were obtained from the Johs-Herzinger model and the solid curves were the linear fitting. Only representative samples are shown here for clarity [90].

The samples A-K were used to study the direct bandgap absorption behavior. Figure 3.5 (a) shows the Sn compositional-dependent absorption coefficient attributed to the direct transition. Some representative samples are shown here for clarity. The solid symbols were obtained from the Johs-Herzinger model and the solid curves were the linear fitting in order to extract the E_g^Γ, as summarized in Table 3.1. As Sn composition increases, the absorption edge shifts towards lower energy, reflecting the gradually reduced bandgap as expected. The slope of the fitting curve reflects the value of parameter A. It is worth pointing out that each sample in this study is with different Sn composition and strain status, however, the slopes of their absorption curves are mostly identical as can be seen in Fig. 3.5 (a), indicating that parameter A is independent of Sn composition and strain. The value of A was calculated as (3.68 ± 0.864)E4, with which the absorption coefficient relating to the direct transition near the bandgap can be calculated for any $Ge_{1-x}Sn_x$ alloy once the E_g^Γ was determined.

Figure 3.5 (b) shows the absorption coefficient attributed to the indirect transition for samples A-H (only the samples A, C, F, and H were shown for clarity). The solid symbols and curves were from the Johs-Herzinger model and linear data fitting, respectively. Two types of absorption can be identified as noted in the figure, corresponding to the phonon absorption and emission processes, respectively. The extrapolations to the phonon energy axis give the E_g^L-$h\theta$ and E_g^L+$h\theta$, with which the bandgap E_g^L and the phonon energy $h\theta$ were calculated. The E_g^L was listed in Table 3.1 and the $h\theta$ was calculated as 39.0±1.50 meV, which is consistent with the previous study. For each sample, the slopes of two fitted lines corresponding to phonon absorption and emission provide the parameters *B* and *C*, respectively. The values of *B* and *C* were found to be independent of the Sn composition and strain, given by calculated values as (2.25±0.0260)E3 and (2.17±0.105)E4, respectively.

Since parameters *A*, *B*, *C,* and phonon energy $h\vartheta$ were obtained, according to equation (3.1.3)-(3.1.5), the absorption coefficient in the direct and indirect bandgap absorption regions can be calculated once the E_g^Γ and E_g^L were determined. The quadratic polynomial is widely used to calculate the bandgap energy:

$$E_{g,\ GeSn}^{\Gamma,\ L}(x) = xE_{g,\ Sn}^{\Gamma,\ L} + (1-x)E_{g,\ Ge}^{\Gamma,\ L} + x(1-x)b_{GeSn}^{\Gamma,\ L} \qquad (3.1.10)$$

where b_{GeSn}^Γ and b_{GeSn}^L are bowing factors for direct and indirect bandgaps of GeSn, respectively. Note that equation (3.1.10) is applied only for relaxed GeSn material, therefore the obtained E_g^Γ and E_g^L, shown in Table 3.1 (also shown in Fig. 3.6 as open symbols) cannot be directly used to extract the bowing factors, but the strain-induced band edge offset should be considered.

The strain results in the conduction band (CB) and valence band (VB) edges shift. Therefore, the strain-induced changes of bandgap energies should be considered. The change of bandgap energy can be express as

$$\Delta E_g^{\Gamma,L} = \Delta E_{CB}^{\Gamma,L} + \Delta E_{VB} \tag{3.1.11}$$

where $\Delta E_g^{\Gamma,L}$ is the change of the bandgap energy at $\Gamma(L)$ valley, the $\Delta E_{CB}^{\Gamma,L}$ is the band offset of CB at $\Gamma(L)$ valley, and the ΔE_{VB} is the band offset of VB. The $\Delta E_{CB}^{\Gamma,L}$ and ΔE_{VB} can be evaluated by [103]

$$\Delta E_{CB}^{\Gamma,L} = d_C^{\Gamma,L}(2e_\parallel + e_\perp) \tag{3.1.12}$$

$$\Delta E_{VB} = d_{V1}(2e_\parallel + e_\perp) + d_{V2}(e_\perp - e_\parallel) \tag{3.1.13}$$

where $d_C^{\Gamma,L}$, d_{V1}, and d_{V2} are the deformation potentials of CB at $\Gamma(L)$ valley and VB, and the $e_\parallel$ and $e_\perp$ are inplane and out of plane strain. They are described as [103]

$$e_\parallel = (a^{Ge} - a^{GeSn})/a^{GeSn} \tag{3.1.14}$$

$$e_\perp = -2(C_{12}/C_{11})e_\parallel \tag{3.1.15}$$

where a^{Ge} and a^{GeSn} are the relaxed lattice constants of Ge and Ge$_{1-x}$Sn$_x$, and C_{12} and C_{11} are the elastic constants. Table 3.2 summarized parameters for the calculation of the change of bandgap energy.

Table 3.2 Summary of parameters for the calculation of the change of bandgap energy [90]

	d_C^{Γ} (eV)	d_{V1} (eV)	d_{V2} (eV)	C_{12}(GPa)	C_{11}(GPa)	Lattice constant $(\overset{\circ}{A})$
Ge	-8.24	1.24	-2.9	48.26	128.53	5.6573
Sn	-6	1.58	-2.7	29.3	69.0	6.4892

Following the method explained above, the band edge offset of the conduction band and the valence band for samples A-K was calculated, with which the E_g^Γ and E_g^L for relaxed GeSn were obtained, as shown in Fig. 3.6 (solid symbols). The bowing factors were then fitted as 2.917±0.1059 and 1.812±0.1523, for direct and indirect bandgap, respectively. The fitting curves are shown in Fig. 3.6 as solid lines, which are consistent with the experimental data.
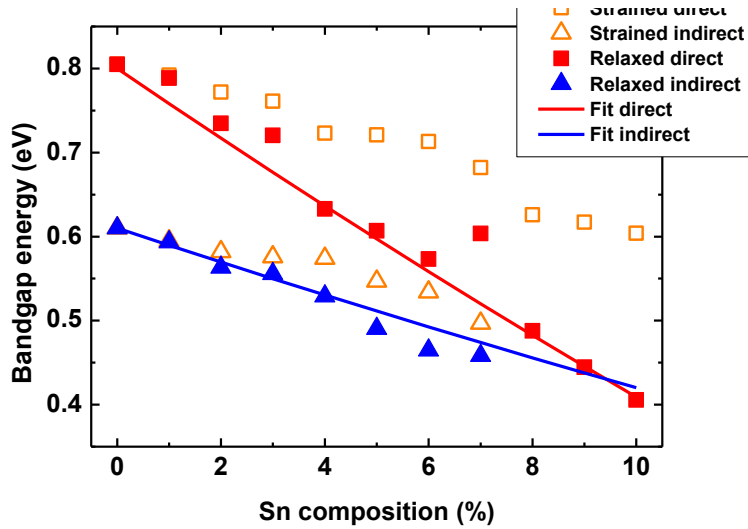
Figure 3.6 Bandgap energy as a function of Sn composition. The open symbols are strained values (experimental data) and the solid symbols are correspondingly relaxed values. The solid lines are fitting curves using quadratic polynomial, from which the bowing factors were extracted [90].

3.1.3.2. Urbach tail

The Urbach tail of each sample is shown in Fig. 3.7 (a). The samples A, B, D, F, H, I, and K were shown for clarity. The solid symbols were obtained from the Johs-Herzinger model and the solid curves were the fitting for the Urbach tail. The clear exponential decay of absorption coefficient as photon energy decreases was observed. The linear fitting between the ln (α) and photon energy was used to extract the Urbach parameter ΔE. For the samples A-H (Sn composition from 0 to 7%), the indirect absorption was distinctly observed at the low energy part, whose data points were excluded from the data fitting.

The Urbach parameter ΔE was extracted and shown in Fig. 3.7 (b). The ΔE varying from 9.000 (sample F, 5% Sn) to 12.05 eV (sample C, 2% Sn) exhibits independence of direct bandgap energy (sample H with 7% Sn showing large deviation is not included in the statistics) and was calculated as 10.58±1.060 meV. Therefore the Urbach width ΔE is constant or weakly dependent on Sn composition and strain. In Fig. 3.7 (b), the fluctuation of ΔE may be due to the non-uniform quality of the samples.
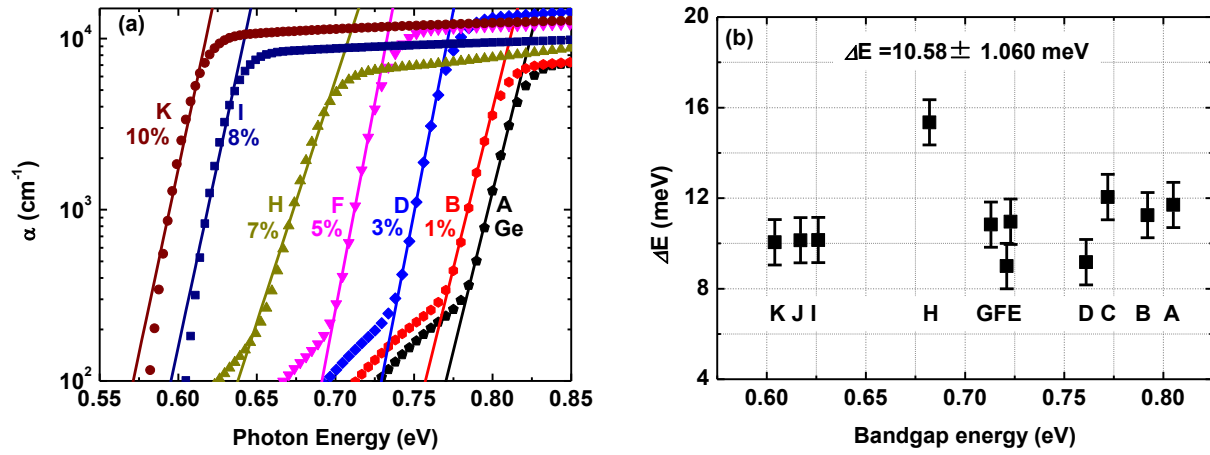
Figure 3.7 (a) Urbach tail for each sample (Only selected samples were shown for clarity). The clear exponential decay of absorption coefficient as photon energy decreases was observed. (b) The Urbach parameter ΔE extracted from (a) as 10.58±1.060 meV [90].

By combining the equations (3.1.3), (3.1.4), and (3.1.9), the absorption coefficient near the bandgap can be written as:

$$\alpha(h\upsilon) = \begin{cases} \dfrac{A(h\upsilon - E_g^\Gamma)^{1/2}}{h\upsilon}, & \left(E_g^\Gamma + \dfrac{\Delta E}{2} \le h\upsilon\right); \\[2em] Ae^{-\frac{1}{2}}\left(\dfrac{\Delta E}{2}\right)^{\frac{1}{2}} \exp\left(\dfrac{h\upsilon - E_g^\Gamma}{\Delta E}\right) + C\left[1 - \dfrac{1}{\exp\left(\dfrac{h\theta}{k_B T}\right) - 1}\right][h\upsilon - (E_g^L + h\theta)]^2, \\[1em] \hspace{5em} \left(E_g^L + h\theta \le h\upsilon \le E_g^\Gamma + \dfrac{\Delta E}{2}\right); \\[2em] B\left[\dfrac{1}{\exp\left(\dfrac{h\theta}{k_B T}\right) - 1}\right][h\upsilon - (E_g^L - h\theta)]^2, & \left(E_g^L - h\theta \le h\upsilon < E_g^L + h\theta\right). \end{cases}$$

$(3.1.16)$

The parameters in equation (3.1.16) are summarized in Table 3.3. With the bandgap energy calculated from equation (3.1.11), for a GeSn alloy with given Sn composition and strain, the absorption coefficient near the bandgap can be calculated, and therefore the absorption edge cutoff can be determined.

Table 3.3 Summary of parameters for calculation of absorption coefficient

$A \times 10^4$ (cm^{-1}(eV)$^{1/2}$)	$B \times 10^3$ (cm^{-1}(eV)$^{-2}$)	$C \times 10^4$ (cm^{-1}(eV)$^{-2}$)	$h\theta$ (meV)	b_{GeSn}^{Γ} (eV)	b_{GeSn}^{L} (eV)	ΔE (meV)
3.68±0.864	2.25±0.0260	2.17±0.105	39.0±1.50	2.917±0.1059	1.812±0.1523	10.58±1.060

3.2. GeSn refractive index

The Sellmeier dispersion equation is widely used recently [96]. The full Sellmeier equation is the summation of infinite terms in the form of $A_i\lambda^2/(\lambda^2-\lambda_i^2)$, where i =1, 2, …, A_i and λ_i are Sellmeier coefficients. However, since only the near- and shortwave-IR wavelength range is of interest in this study, the satisfactory approximation could be made by a summation of only a few terms while neglecting the rest. By fitting the Sellmeier coefficients based on measured data, the equation can be used as guidance for the design of the semiconductor devices such as waveguide and laser.

3.2.1. Experimental and data processing methods

A dispersion relationship for semiconductors can be written as [104]:

$$n^2 = D + \frac{E\lambda^2}{(\lambda^2 - F)} + \frac{G\lambda^2}{(\lambda^2 - H)} \qquad (3.2.1)$$

where n is the refractive index, the parameters D, E, F, G, and H are called Sellmeier coefficients, and λ is the wavelength of the incident light. The first and second terms in equation (3.2.1) are associated with the higher- and lower-energy bandgaps of electronic absorption, respectively,

while the third term accounts for the lattice absorption. For Ge material, the value of G and H are 0.213 and 3870.1, which makes the third term negligible small in the near- and shortwave-IR region. It is physically acceptable to assume that the GeSn alloy follows the same optical property as Ge. Therefore, the third term can be dropped and the equation (3.2.1) is simplified to:

$$n^2 = D + \frac{E\lambda^2}{(\lambda^2 - F)} \tag{3.2.2}$$

It is worth noting that equation (3.2.2) is only applied to the unstrained materials. Since the refractive index is altered by the induced strain, the change of refractive index Δn can be calculated based on the Lorentz-Lorenz equation and is given by:

$$\Delta n = \frac{(n^2 - 1)(n^2 + 2)}{6n} \varepsilon \tag{3.2.3}$$

where ε is the strain of the material (can be found in Table 3.1), with the positive and negative signs for tensile and compressive strain, respectively. In order to obtain the parameters D, E, and F, for each sample, the following procedure was implemented: Obtaining the refractive index $n_e(\lambda)$ from Johs-Herzinger model (strained value); Based on Table 3.1 and equation (3.2.3), solving the equation $n_e(\lambda) = n(\lambda) + \Delta n(\lambda)$ to obtain $n(\lambda)$ (relaxed value); Fitting the $n(\lambda)$ curve using equation (3.2.2) and extracting the parameters D, E and F.

The representative refractive index for $Ge_{0.95}Sn_{0.05}$ is shown in Fig. 3.8. The data below the E_0 critical point (CP) (bandgap at Γ-point) were used for the fitting since no absorption peak was observed in this region. A clear discrepancy between the strained and relaxed data for $Ge_{0.95}Sn_{0.05}$ can be seen in Fig. 3.8. With the compressive strain, the refractive index of $Ge_{0.95}Sn_{0.05}$ decreases. The parameters D, E, and F were extracted as 16.43 ± 0.04030, 0.7434 ± 0.02651, and 2.226 ± 0.01806, respectively.
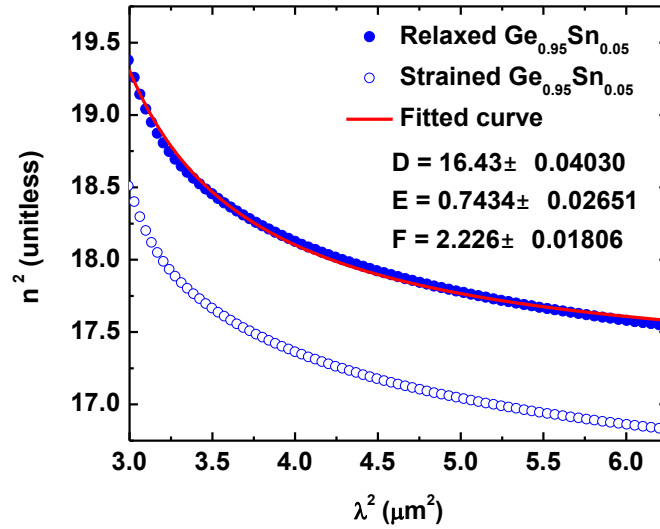
Figure 3.8 Refractive index of sample F (5 % Sn). The open and solid symbols are from the Johs-Herzinger model (strained) and calculated values (relaxed), respectively. The latter one was fitted (solid curve) and the parameters D, E, and F were extracted.

3.2.2. Results and discussions
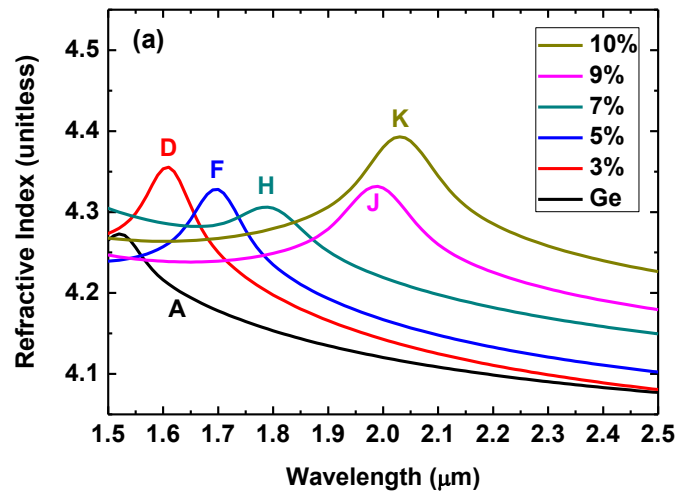
Figure 3.9 Refractive index as a function of wavelength for samples A-K (only selected samples were shown for clarity). The peak in each curve is due to the Γ-valley bandgap absorption.

Figure 3.9 shows the refractive index for samples A-K (only selected samples were shown for clarity). As Sn composition increases, the refractive index increases at the same wavelength.

The clear peak in each curve is related to the E_0 CP. A peak shift towards a longer wavelength in

E_0 CP was observed with the increase of the Sn composition, which agrees well with the bandgap narrowing characteristic of $Ge_{1-x}Sn_x$ as x increases. Moreover, the absorption feature of the *L*-valley (the indirect bandgap) was not observed. This may be due to the weaker indirect bandgap absorption compared to the direct one.

Using the fitting method introduced in section 3.2.1, the parameters *D*, *E* and *F* were extracted and plotted as functions of Sn composition, shown as solid symbols in Fig. 3.10. For the binary material, a quadratic polynomial with a bowing factor is commonly used to describe the material characterizations. However, for this novel GeSn material, little is known about the dispersion relationship, resulting in the difficulty of determining the bowing factor for parameters *D*, *E,* and *F*. A convenient and effective way to represent them is to assume the validity of Vegard's law by interpolating linearly between Ge and Sn. Therefore the linear fitting was used to explicate the variation of parameter *D* (*E*, *F*) as a function of Sn composition, as shown in Fig. 3.10 (solid lines). The consistency between the data points and the fitted curves indicates the applicability of the linear fitting. The expressions of parameters *D*, *E,* and *F* are given below:

$$
\left\{
\begin{array}{l}
D = (33.59 \pm 2.824)x + (14.67 \pm 0.1671) \\
E = -(9.621 \pm 1.088)x + (1.334 \pm 0.06439) \\
F = (21.98 \pm 2.365)x + (1.163 \pm 0.1399)
\end{array}
\right.
\tag{3.2.4}
$$

Combining the equations (3.2.2) and (3.2.3), the refractive index can be written as:

$$
n(\lambda) = [D + \frac{E\lambda^2}{(\lambda^2 - F)}]^{1/2} + \frac{\left[D + \frac{E\lambda^2}{(\lambda^2 - F)} - 1\right]\left[D + \frac{E\lambda^2}{(\lambda^2 - F)} + 2\right]}{6[D + \frac{E\lambda^2}{(\lambda^2 - F)}]^{1/2}}\varepsilon
\tag{3.2.5}
$$

Using the parameters in equation (3.2.4), for a $Ge_{1-x}Sn_x$ alloy with given x and strain ε, the refractive index can be calculated.
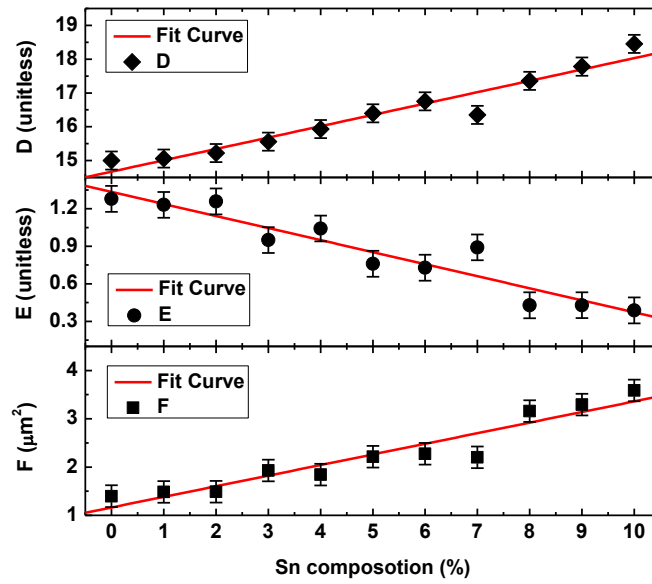
Figure 3.10 The parameters *D*, *E* and *F* plotted as functions of Sn composition. A linear fitting was used to describe the D (E, F)-x (Sn composition) relationship.

In conclusion, by spectroscopic ellipsometry data processing, the formulae of absorption coefficient and refractive index for $Ge_{1-x}Sn_x$ alloys were proposed, which offer clear guidance for the design of GeSn-based optoelectronic devices including photodetector, waveguide, laser, etc. These devices could make up a complete set of components for Si photonics.

Chapter 4.   Systematic study of GeSn photoconductors

4.1. Motivation

Infrared detection falls into two broad categories such as photon detectors and thermal detectors. For the photon detectors, photons are absorbed, and the carriers are generated, which are measured by a readout circuit. On the other hand, for thermal detectors, the photons are absorbed by a thermally isolated detector element, causing an increase in the temperature of the element, which is detected by monitoring a parameter such as resistivity or dielectric constant. There are two basic types of photon detectors: the majority carrier and the minority carrier. The photoconductors have a dominant carrier as the majority carrier, while for minority carrier devices, both photoconductive and photovoltaic modes of detection can be exploited [3, 111]. Two parameters are utilized to evaluate the performance of the different material systems and device architectures, explicitly responsivity and noise. Responsivity is characterized as the ratio of the voltage or the current created by the known photon flux over the input power of the illuminating light. Noise is related to the fluctuation in the voltage or the current of the detector measured on the same point as the responsivity. It is standard for responsivity to be large enough to elevate the detector noise floor above that of the signal processing system noise [111]. Moreover, the photoconductor is a much simple structure that has a semiconductor sandwiched between two Ohmic contacts, so it is preferred to study preliminary material quality as well as device quality. Over the past years, GeSn photoconductors with Sn compositions up to 10 %, showcasing gain using interdigitated electrodes was reported. These results provided a baseline for the performance at the SWIR wavelength range. This chapter focuses on studying the GeSn photoconductors. For the early study of GeSn photodetectors, the Sn percentages were low, which limits the cutoff wavelength. Recently, it has been discovered that Sn incorporation into

Ge is limited by high compressive strain, so relaxed GeSn epitaxy growth is persuaded. The new growth technique is the spontaneous-relaxation-enhanced (SRE) Sn incorporation mechanism. The mechanism can help to incorporate more Sn in the material systems, which extends the cutoff wavelength of the devices. As a result, the Sn can achieve 22.3 %, which extends the operating wavelength range to mid-infrared [58]. In fact, the set of GeSn photoconductors with Sn compositions from 10.5 % to 22.3 % and cutoff wavelength up to 3.65 µm. The peak D* of 1.1×10^{10} cm·Hz$^{1/2}$·W^{-1} is obtained at 77 K, which is comparable with that (~4×10^{10} cm·Hz$^{1/2}$·W^{-1}) of the commercial extended-InGaAs detectors [58].

4.2. Photoconductive Detectors

4.2.1. Theoretical study

4.2.1.1. Photoconductivity Theory

The photoconductive detector is a resistor whose value changes as it is illuminated. Figure 4.1 shows a readout circuit to measure the radiation-sensitive voltage through a series resistor. When a photon of energy $h\nu$ greater than the band-gap energy E_g is absorbed by the semiconductor, electron-hole pairs are generated, which makes the device's electrical conductivity change. For narrow gap semiconductors, the optical absorption is higher than that in extrinsic detectors.

Commonly, the change in conductivity is measured using a readout circuit shown in Fig. 4.1. The induced voltage is measured using a series resistor. For high conductive material, where the sample resistance is typically 10-100 Ω, the photoconductor is usually operated in a constant current circuit. The series load resistance is large compared to the sample resistance, and the signal is detected as a change in voltage developed across the load resistor. This case usually happens for the GeSn photoconductors due to high carrier concentration as a nature of narrow-

gap semiconductors. For low conducive materials, a constant voltage circuit is desired, and the change in current in the bias circuit is detected.
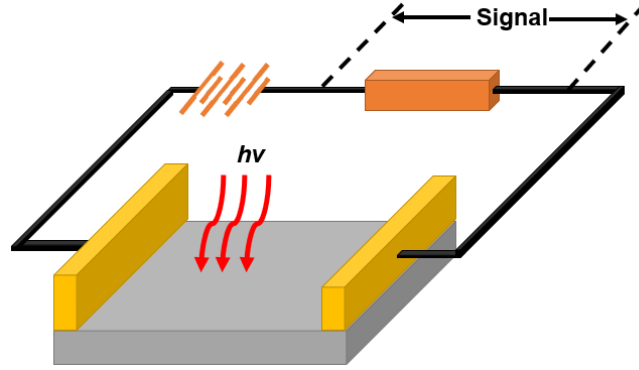
Figure 4.1 Geometry and readout circuit of a photoconductor.

The signal photon flux density $\Phi_s(\lambda)$ is incident on the detector area $A = \omega l$, and the detector is operated under constant current conditions. The excess carrier lifetime τ is assumed to be the same for the majority and minority carriers. The detector thickness t is further presumed to be small with respect to minority carrier diffusion length. The effect of recombination at the front and sidewall also is neglected. As a result, the photoconductivity effects are due to the influence of bulk material properties over other factors. Under equilibrium excitation, i.e., steady-state, the photocurrent is described following:

$$I_{ph} = q\eta A\Phi_s g \tag{4.2.1}$$

where I_{ph} is the short circuit photocurrent at zero frequency (DC); that is, the increase in the current above the dark current accompanying irradiation. The photoconductive gain, g, is determined by the properties of the detector.

For photoconductor, two carriers are contributing to the total photocurrent, so the photocurrent which is the combination of collected electrons and holes is given as:

$$I_{ph} = \frac{qwt(\Delta n \mu_e + \Delta p \mu_h)V_b}{l},$$ (4.2.2)

where μ_e is the electron mobility, μ_h is the hole mobility; V_b is the bias voltage and

$$n = n_o + \Delta n; \ p = p_o + \Delta p,$$ (4.2.3)

n_o and p_o are the average thermal equilibrium carrier, densities, and Δn and Δp are the excess carrier concentrations.

It is reasonable to only have the photocurrent be dominated by an electron since it has higher mobility. Then, the rate equation for the excess electron concentration in the sample is

$$\frac{d\Delta n}{dt} = \frac{\Phi_s \eta}{t} - \frac{\Delta n}{\tau},$$ (4.2.4)

where τ is the excess carrier lifetime. In the equilibrium condition, the excess carrier lifetime is estimated following:

$$\tau = \frac{\Delta n t}{\eta \Phi_s}$$ (4.2.5)

Making Eq. (4.2.1) equal to Eq. (4.2.2) gives

$$g = \frac{tV_b\mu_e\Delta n}{l^2\eta\Phi_s},$$ (4.2.6)

and applying Eq. (4.2.5), the photoconductor gain can be achieved as

$$g = \frac{\tau\mu_e V_b}{l^2} = \frac{\tau}{l^2/\mu_e V_b}.$$ (4.2.7)

So, the photoconductive gain can be defined as

$$g = \frac{\tau}{t_t},$$ (4.2.8)

where t_t is the transit time of electrons between Ohmic contacts. As a result, the photoconductive gain is assessed by the ratio of a free-carrier lifetime, τ, to transit time, t_t, between the electrodes. If the drift length, $L_d = v_d\tau$, is less than or greater than spacing, l, between electrodes, the gain can be less than or greater than unity. In fact, if the drift length is greater than the spacing, an equivalent free charge carrier at an opposite electrode is immediately injected to replace a free charge carrier flew out at one electrode. It is continuous for a free charge carrier to circulate until recombination takes place. In other words, after photogeneration of an electron-hole pair, the minority carrier may be trapped at impurity or defect sites. The majority carrier drifts out of one contact and in order to maintain charge neutrality, another majority carrier is injected at the other contact. This drift/injection process continues until the majority carrier recombines with the minority carrier. This increases the majority carrier lifetime and results in gain because more than one majority carrier flows in the external circuit for every photogenerated carrier. Even though this process does lead to very high values for the current responsivity, but the response time, which is equal to the majority carrier lifetime, is also increased [112]. The mechanism suggests that the extrinsic photodetectors having a high impurity level can have high gain.

When $R_L \gg R$, for an open circuit voltage, the voltage is described as

$$V_s = I_{ph}R_d = I_{ph}\frac{l}{qwtn\mu_e}, \tag{4.2.9}$$

where R_d is the detector resistance. If the photocurrent is small compared to the dark current, the voltage responsivity is expressed as

$$R_v = \frac{V_s}{P_\lambda} = \frac{\eta}{lwt}\frac{\lambda\tau}{hc}\frac{V_b}{n_o} \tag{4.2.10}$$

where the absorbed monochromatic power $P_\lambda = \Phi_s A h\nu$. Eq. (4.2.10) clearly shows the basic requirements for high photoconductive responsivity at a given wavelength λ. In fact, it is required to have high quantum efficiency η, long excess carrier lifetime τ, the smallest dimensions, low thermal equilibrium carrier concentrations n_o, and the highest possible bias voltage V_b.

The frequency-dependent responsivity can be determined by the equation

$$R_v = \frac{\eta}{lwt} \frac{\lambda \tau_{ef}}{hc} \frac{V_b}{n_o} \frac{1}{\left(1 + \omega^2 \tau_{ef}^2\right)^{1/2}} \qquad (4.2.11)$$

where τ_{ef} is the effective carrier lifetime. However, the performance of the photoconductors is limited to other effects such as sweep-out effects or surface recombination. These are presented in the below sections.

4.2.1.2. Sweep-Out Effects

As shown in Eq. (4.2.11), the voltage responsivity increases monotonically as the bias voltage increases. However, there are two limits on applied bias voltage such as Joule heating and sweep-out of minority carriers. The fabrication process determines the thermal conductance of the detector. If the bias is applied, the minority carriers can drift to the Ohmic contacts in a short time compared to the recombination time. The sweep-out effect is to remove carriers at an Ohmic contact in this way. Minority carrier sweep-out limits the maximum applied voltage of V_b. If the minority carrier diffusion length exceeds the detector length, the effective carrier lifetime can be substantially reduced. With small applied voltages, if the drift length is shorter than the detector length l, the minority carrier lifetime is determined by the bulk recombination. The carrier densities are uniform along the length of the detector. At high applied voltages, the drift length of the minority carriers is comparable to or longer than l. Some of the excess minority carriers are lost at an electrode, and to maintain space charge equilibrium, a

67

deterioration in excess majority carrier density is necessary, which reduces the majority carrier lifetime. It is worth mentioning that the loss of the majority carriers at one Ohmic contact is refilled by injection at the other, but minority carriers are not replaced.

Under the sweep-out condition, the excess carrier density is nonuniformly distributed along the length of the device. Hence, the excess carrier concentration $\Delta p(x,t) = p(x,t) - p_o$ within the semiconductor is governed by ambipolar transport. The ambipolar continuity equation for a one-dimensional case under steady-state and electrical neutrality conditions may be written as

$$\frac{\partial^2(\Delta p)}{\partial x^2} + \frac{L_d}{L_D^2}\frac{\partial(\Delta p)}{\partial x} + \frac{\Delta p}{L_D^2} + G_s = 0, \tag{4.2.12}$$

where

$$L_d = \tau\mu_e E \qquad\qquad \text{drift length,}$$

$$L_D = (D_d\tau)^{1/2} \qquad\qquad \text{diffusion length,}$$

$$\mu_a = \frac{(n_o - p_o)\mu_e\mu_h}{n_o\mu_e + p_o\mu_h} \qquad\qquad \text{ambipolar drift mobility,}$$

$$D_D = \frac{D_e p_o \mu_h + D_h n_o \mu_e}{n_o\mu_e + p_o\mu_h} \qquad\qquad \text{ambipolar diffusion coefficient.}$$

where $D_{e,h} = (kT/q)\mu_{e,h}$ are the respective carrier diffusion coefficients, G_s is the signal generation rate, $E = V_b/l$ is the bias electrical field, and k is the Boltzmann constant.

For the Ohmic contacts, the interface can be modeled as having infinite recombination velocity. The boundary conditions are described as:

$$\Delta p(0) = \Delta p(l) = 0. \tag{4.2.13}$$

The solution of Eq. (4.2.12) is

$$\Delta p = G_s\tau[1 - C_1 exp(\alpha_1 x) + C_2 exp(\alpha_2 x)], \tag{4.2.14}$$

where

$$\alpha_{1,2} = \frac{1}{2L_D^2}\left[-L_d \pm (L_d^2 + 4L_D^2)^{1/2}\right]. \tag{4.2.15}$$

Applying the boundary conditions (Eq. (4.2.13)), the coefficients can be obtained as:

$$C_{1,2} = \frac{1 - \exp(\alpha_{2,1}l)}{exp(\alpha_2 l) - exp(\alpha_1 l)}. \tag{4.2.16}$$

By integrating Eq. (4.2.14) over the length of the devices, the total number of carriers is obtained:

$$\Delta P = \eta \Phi_s \tau_{ef} \tag{4.2.17}$$

where

$$\tau_{ef} = \gamma \tau \tag{4.2.17}$$

$$\gamma = 1 + \frac{(\alpha_1 - \alpha_2)th(\alpha_1 l/2)th(\alpha_2 l/2)}{\alpha_1 \alpha_2 (l/2)[th(\alpha_2 l/2) - th(\alpha_1 l/2)]} \tag{4.2.18}$$

The voltage responsivity is

$$R_v = \frac{\eta}{lwt}\frac{\lambda \tau_{ef}}{hc}\frac{V_b(b+1)}{bn+p}\frac{1}{\left(1 + \omega^2 \tau_{ef}^2\right)^{1/2}} \tag{4.2.19}$$

where $b = \mu_e/\mu_h$. Practically, a recombination velocity can vary from infinity (ohmic contacts) to zero (perfectly blocking contacts). For blocking contacts, a more intensely doped region at the contact causes a built-in electric field that repels minority carriers, which leads to reduce recombination and increases the effective lifetime and the responsivity.

Under very high bias conditions, the voltage responsivity saturates to the value

$$R_v = \frac{\eta q \lambda}{2hc}(b+1)\frac{\mu_h}{\mu_a}R' \tag{4.2.19}$$

where R' is the device resistance; $\mu_a = \mu_h$ in the n-type material and $\mu_a = \mu_e$ in p-type material.

4.2.1.3. Noise Mechanisms in Photoconductors

The noise consists of the radiation noise and the internal noise. The radiation noise includes signal and background fluctuation noises. The background fluctuation noise affects the performance of the infrared detectors. The internal noise is created from the random processes happening in semiconductors even in the unavailability of illumination. There are two fundamental processes responsible for the noise: fluctuations in the velocities of free carriers due to their random thermal motion, and fluctuations in the densities of free carriers due to randomness in the rates of thermal generation and recombination. Many internal noise sources are usually operative in photoconductive detectors. The fundamental types are Johnson–Nyquist (sometimes called thermal) noise and generation– recombination (g–r) noise. The third form of noise, not amenable to exact analysis, is called 1/f noise because it exhibits a 1/f power-law spectrum to a close approximation.

The total noise voltage of a photoconductor is

$$V_n^2 = V_{gr}^2 + V_j^2 + V_{1/f}^2 \qquad\qquad (4.2.20)$$

Johnson–Nyquist noise is correlated with the finite resistance R of the device. This noise is due to the random thermal motion of charge carriers and not due to fluctuations in the total number of these charge carriers. It happens without the external bias as a fluctuating voltage or current depending upon the method of measurement. Small changes in the voltage or current are due to the random arrival of charge.

At finite bias currents, the carrier density fluctuations cause resistance variations, which are observed as noise exceeding Johnson–Nyquist noise. This noise in photoconductive detectors is referred to as g–r noise. The g–r noise is due to the random generation of free charge carriers by the crystal vibrations and their subsequent random recombination. Because of the randomness of the generation and recombination processes, it is unlikely that there will be the same number of

charge carriers in the free state at succeeding instances of time. This leads to conductivity changes that will be reflected as fluctuations in current flow through the crystal. Generation–recombination noise usually dominates the noise spectrum of photoconductors at intermediate frequencies. It should be noted that in the high bias regime, the expressions for g–r noise are different from those at low bias. The 1/f noise is characterized by a spectrum in which the noise power depends approximately inversely upon frequency. Infrared detectors usually exhibit 1/f noise at low frequency. At higher frequencies, the amplitude drops below that of one of the other types of noise: the generation-recombination noise and Johnson noise.

4.2.1.4. Quantum Efficiency

Generally, the internal quantum efficiency η_0 is nearly unity since almost all photons absorbed contribute to the photoconductive phenomenon. For a detector, as a piece of material, shown in Fig. 4.1, with surface reflection coefficients r_1 and r_2 (on the top and bottom surfaces, respectively) and absorption coefficient α, the internal photogenerated charge profile in the y-direction is:

$$S(y) = \frac{\eta_0(1-r_1)\alpha}{1 - r_1 r_2 exp(-2\alpha t)} [exp(-\alpha y) + r_2 exp(-2\alpha t)exp(-\alpha y)] \tag{4.2.21}$$

The external quantum efficiency is simply the integral of this function over the detector thickness:

$$\eta = \int_0^1 S(y)dy = \frac{\eta_0(1-r_1)[1 + r_2 exp(-\alpha t)][1 - exp(\alpha t)]}{1 - r_1 r_2 exp(-\alpha t)} \tag{4.2.22}$$

when $r_1, r_2 = r$, the quantum efficiency is reduced to

$$\eta = \frac{\eta_0(1-r)[1 - exp(\alpha t)]}{1 - rexp(-\alpha t)} \tag{4.2.23}$$

71

4.2.2. Silvaco Simulation

The commercial Silvaco with Atlas simulator was used to simulate the devices. The material parameters including bandgap energies, the effective density of states, and intrinsic carrier concentration for GeSn were applied in the simulation. The Shockley-Read-Hall (SRH) recombination model was used with reasonably estimated electron and hole lifetimes of 1 ns. Surface recombination on the devices' surfaces and sidewalls was considered with the recombination velocities of 10^5 cm/s for electrons and holes. Fig.4.2 shows the current flowing through the layers of the devices. Based on the current flowlines, the current flow path is not only through the top high-quality GeSn layer, but also includes the bottom defective GeSn layers.
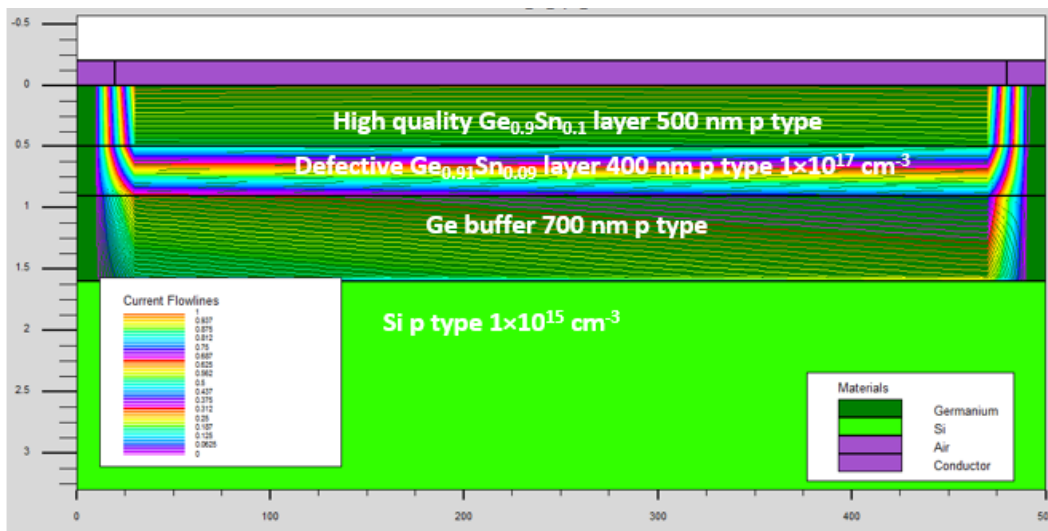
Figure 4.2 Cross-sectional device with current flowlines

4.3. Figures of Merit

This chapter focuses on the characterization and analysis of the GeSn photoconductors. The GeSn samples were grown using an industry-standard ASM Epsilon® 2000 Plus reduced pressure chemical vapor deposition system (RPCVD) with commercially available precursors. The material characterization results including layer thickness and Sn composition are

summarized in Table 4.1. The samples are annotated from A to F according to the Sn compositions.

Table 4.1 Summary of GeSn samples [58]

Sample	GeSn layer	Thickness (nm)	Spontaneous relaxed gradient Sn% (by SIMS)
A	1st layer	180	8.8% – 10.5%
	2nd layer	660	10.5% – 12.5%
B	1st layer	250	12.5% – 13.2%
	2nd layer	670	13.2% – 15.9%
C	1st layer	165	9.2% – 10.0%
	2nd layer	585	10.0% – 13.2%
	3rd layer	254	13.2% – 15.7%
D	1st layer	310	11.6% – 12.2%
	2nd layer	550	12.2% – 16.2%
	3rd layer	260	16.2% – 17.9%
E	1st layer	450	11.5% – 15.3%
	2nd layer	950	15.3% – 20.0%
F	1st layer	380	11.8% – 15.5%
	2nd layer	830	15.5% – 22.3%

The transmission electron microscopy (TEM) image for each sample shows a well-confined layer structure. For GeSn, the distinct multi-layer feature was observed. Figure 4.3 (a) shows a typical TEM image of sample E. Two distinctive layers include a 450-nm-thick bottom layer with relatively high defect density, and a 950-nm-thick top layer highlighting the high material quality. Both layers exhibit a spontaneously Sn-enhanced gradient, from 11.5% to 15.3%, and from 15.3% to 20% for the bottom and top layers, respectively. The increased Sn composition is mainly due to the ease of compressive strain, which facilitates the Sn incorporation. Although the bottom GeSn layer is defective, the formation of threading dislocation loops in the bottom

layer prevents the defects from propagating into the top GeSn layer, generating a high-quality top layer.
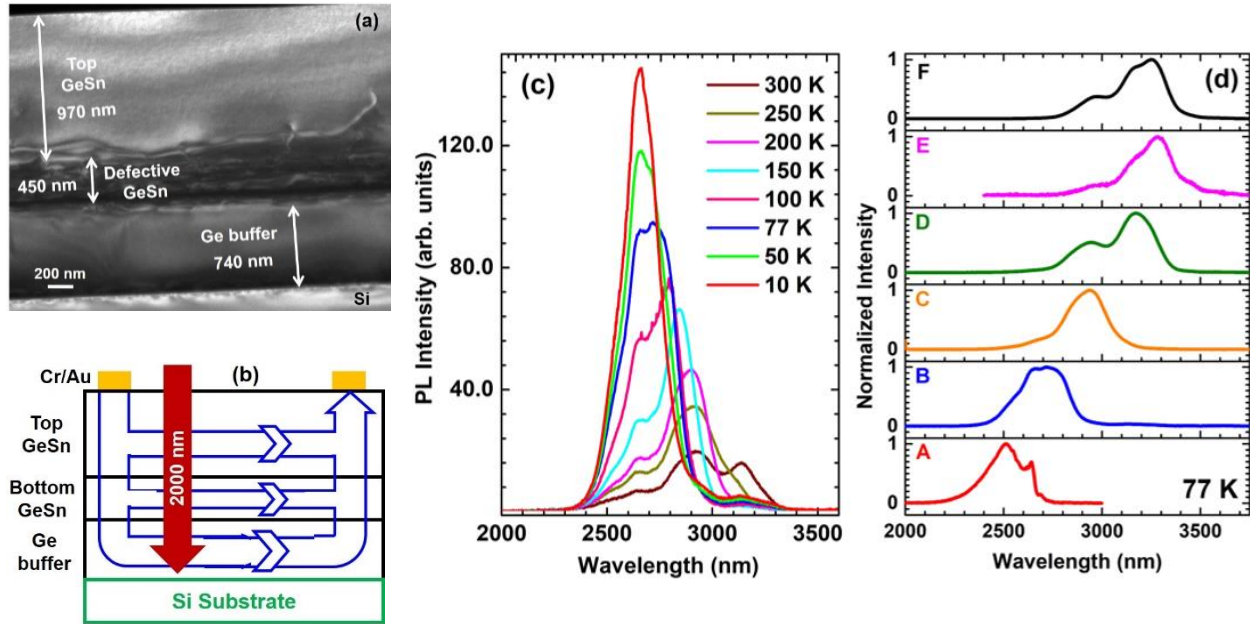
Figure 4.3 (a) A typical TEM image of sample E; (b) Schematic drawing of a typical photoconductor, showing the penetrating depth of 2 μm laser diode and the current flowing (not to scale); (c) Temperature-dependent PL spectra of sample B; (d) PL spectra at 77 K of all samples. Note that the "two peaks" featured in the PL spectra are due to the H_2O absorption at 3.0 μm, which results in the valley at this wavelength [58].

The GeSn samples were studied using photoluminescence (PL). For each sample, as the temperature decreases from room temperature, a significantly increased PL intensity was observed. The typical temperature-dependent PL spectra for sample B are exhibited in Fig. 4.3 (c). The observed PL peak blue-shift at lower temperatures is expected since the bandgap increases. From 300 to 10 K, the integrated PL intensity increases about 12 times. The PL emission is from band-to-band transitions. Note that due to ~ 100 nm penetration depth of the 532-nm excitation laser beam in the GeSn layer, only the region close to the surface involves in the light absorptions. Due to the tilted band edge as a result of compositionally graded Sn content, the photogenerated carriers tend to transport from the wider bandgap region (the deeper

74

region in GeSn) to the narrower bandgap region (surface region), i.e., the carrier funneling effect, resulting in light emission mainly occurs at the surface. The PL spectra of all samples measured at 77 K are shown in Fig. 4.3 (d). As the Sn composition increases, the emission peak shifts towards a longer wavelength due to the bandgap shrinkage of GeSn as more Sn incorporates. Note that although sample F has higher Sn composition (22.3%) than that of sample E (20%), the PL peak of sample F was obtained at a shorter wavelength, which is attributed to the higher compressive strain of sample F. The GeSn samples were fabricated into photoconductor devices. It is worth pointing out that based on the Silvaco, which is described in section 4.2.2, the current flow path is not only through the top high-quality GeSn layer, but also includes the bottom defective GeSn layer as well as the Ge buffer layer, as shown in Fig. 4.3 (b).

4.3.1. Responsivity

The responsivity was measured using a 2.0-µm laser. As shown in Fig. 4.3(b), the illuminated light can penetrate to the Ge buffer. However, the Ge buffer does not absorb the light with the energy smaller than the bandgap. Hence, it is achievable to eliminate the contribution from the Ge buffer. The incident laser beam has a spot size of ~1 mm in diameter and a power density of 8.9 mW/cm^2. The temperature-dependent responsivity of sample A is shown in Fig. 4.4 (a). As temperature decreases, the responsivity increases because of the increased carrier lifetime and mobility at lower temperatures. At 77 K, the peak responsivity of 16.1 A/W was obtained at -4 V, which is more than five times higher than our previously reported device (2.85 A/W), which was measured at 1.55 µm) and therefore the Ge absorption also contributes to such device. This can be explained by the fact that the thicker GeSn layer significantly enhances the total light absorptance, resulting in more photo-generated carriers. On the other hand, the responsivity increases as the reverse bias voltage increases due to the reduced

75

carrier transit time, which increases the photoconductive gain. However, at each temperature, the responsivity saturation was observed at a certain voltage. This is mainly due to Joule heating of the device element and the sweep-out of minority carriers, which limits the applied bias voltage.

Figures 4.4 (a) and (b) show the responsivity of all devices at 77 K. Generally, as the Sn composition increases from samples A to F, the responsivity decreases under the same bias voltage. This can be explained as follows: (1) the higher Sn composition results in a narrower bandgap; (2) the photon at 2 µm still generates just one e-h pair, and the extra energy is dissipated through phonon emission such as heat. Note that since the quality of samples shows a slight difference, the deviation from this trend can be observed, such as samples D and E.
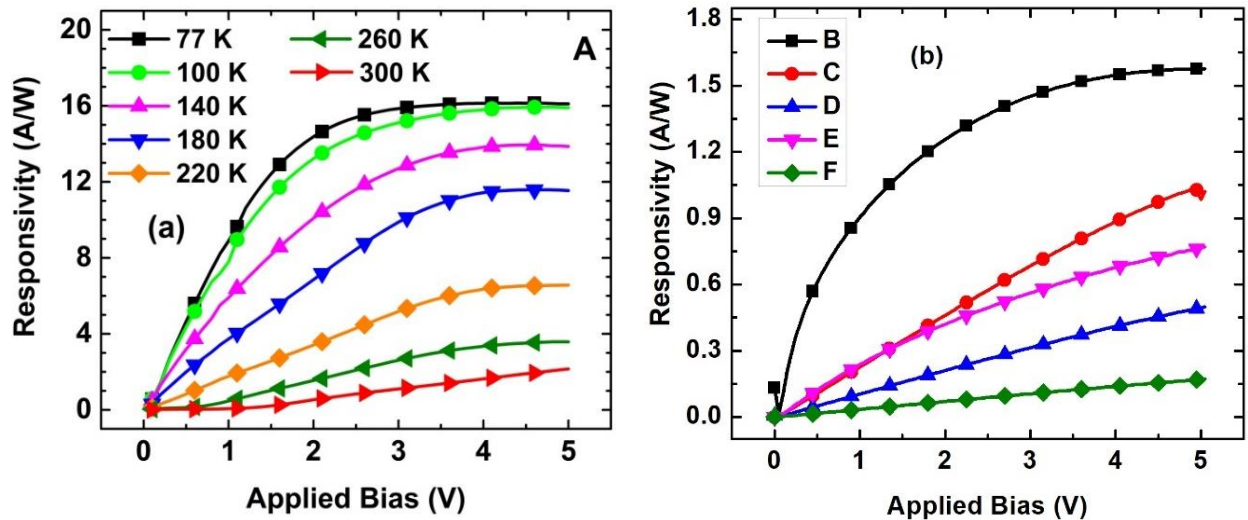
Figure 4.4 (a) Temperature-dependent responsivity of sample A; (b) Responsivity of samples B to F at 77 K [58].
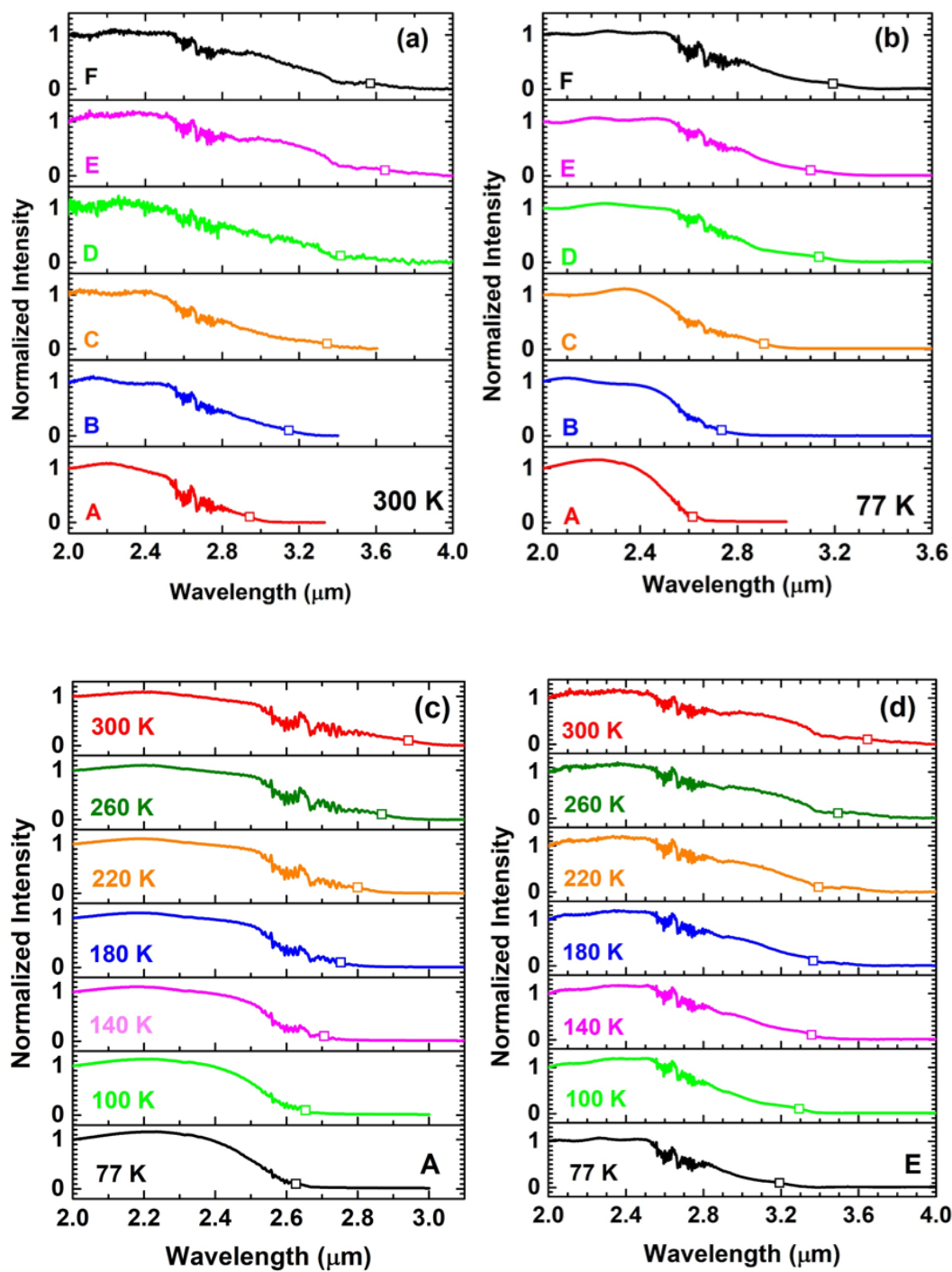
Figure 4.5 Spectral response of all devices measured at (a) 300 K and (b) 77 K; Temperature-dependent spectral response of samples (c) A and (d) E (squares represent cut-off wavelengths) [58].

Spectral responses of the photoconductors were characterized in the wavelength range from 2.0 µm to 4.0 µm with a Fourier transform infrared (FTIR) spectrometer at a bias of -2 V. Figure 4.5 (a) and (b) show the spectral responses of all photoconductors at 300 and 77 K, respectively. The cut-off wavelength is defined as where the 90% intensity decreases. As the Sn composition increases, the cut-off wavelength shifts towards a longer wavelength due to the bandgap shrinkage. At 300 K, the longest cut-off at 3.65 µm was obtained with sample E. Temperature-dependent spectral responses of samples A and E are plotted in Fig. 4.5 (c) and (d), respectively. As temperature increases, the absorption edge shifts to a longer wavelength as expected. From 77 to 300 K, the cut-off wavelengths range from 2.65 to 2.95 µm, and from 3.2 to 3.65 µm for samples A and E, respectively.

4.3.2. Detectivity

Specific detectivities (D*) were determined using noise equivalent power (NEP) at 1Hz frequency bandwidth and device area, where the NEP was calculated based on mean squared noise current and responsivity. The detailed calculated D* are reported in the supplementary. The spectral D* of all devices at 77 and 300 K are plotted in Fig. 4.6 to compare with commercial photodetectors. The D* dropped at higher temperatures, which is mainly attributed to the increased noise at higher temperatures. Among all devices, sample A exhibits the highest peak D* due to its relatively high responsivity. At 2.4 µm, the peak D* of 1.1×10^{10} cm·Hz$^{1/2}$W^{-1} was achieved. Note that at the wavelength range from 1.5 to 2.6 µm, the D* of sample A exceeds that of commercial PbSe detector, and only a few times smaller than extended-InGaAs and PbS detectors.
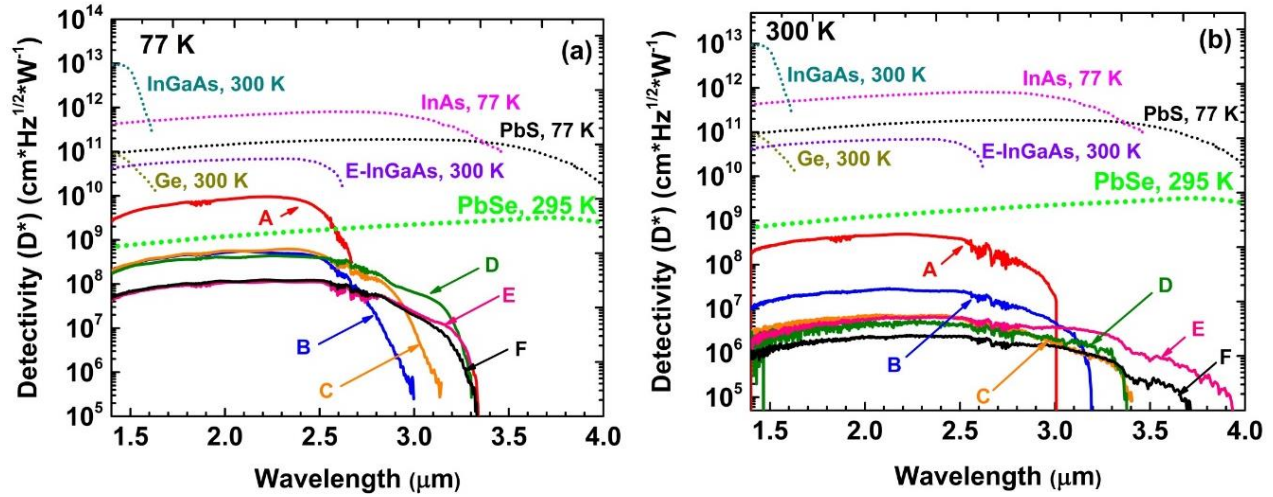
Figure 4.6 Spectral D* of all devices at (a) 77 K and (b) 300 K [58].

4.4. Discussions

4.4.1. Achievements

Due to the high carrier concentration, the GeSn photodetectors bear a high dark current. The simulation shows the reason for the high dark current comes from the current flowing through the defective layer. Further IV analysis such as activation energy is needed to explain the behavior to improve the next generation of the photodiode. Due to gain, the peak responsivity of 16.1 A/W is achieved at 77 K for the $Ge_{0.9}Sn_{0.1}$ photoconductor. From 77 to 300 K, the cut-off wavelengths range from 2.65 to 2.95 µm, and from 3.2 to 3.65 µm for samples A and E, respectively. At 2.4 µm, the peak D* of 1.1×10^{10} cm·Hz$^{1/2}$W^{-1} was achieved. Note that at the wavelength range from 1.5 to 2.6 µm, the D* of sample A exceeds that of commercial PbSe detector, and only a few times smaller than extended-InGaAs and PbS detectors. The device performance is summarized in Table 4.2, showing the peak responsivity, D*, and cut-off wavelength.

79

Table 4.2 Summary of photoconductor performance

Sample	Max. Sn %	Peak D* $(cm \cdot Hz^{1/2}W^{-1})$	Peak Responsivity (A/W)		Cut-off wavelength (μm)	
			77 K	300 K	77 K	300 K
A	12.5%	1.1×10^{10}	16.1	2.0	2.65	2.95
B	15.9%	5.5×10^{8}	1.6	4.4×10^{-2}	3.00	3.20
C	15.7%	6.2×10^{8}	1.0	7.2×10^{-3}	3.15	3.40
D	17.9%	4.4×10^{8}	0.5	3.8×10^{-3}	3.30	3.35
E	20.0%	1.1×10^{8}	0.8	6.7×10^{-3}	3.00	3.65
F	22.3%	1.1×10^{8}	0.2	3.2×10^{-3}	3.35	3.65

4.4.2. Challenges

4.4.2.1. Activation Energy of Photoconductors

The temperature dependence of the conductivity depends on the temperature dependence of carrier density and the temperature dependence of mobility. Figure 4.7 shows the temperature dependence of the conductivity of an extrinsic semiconductor. There are three distinct regions such as intrinsic, saturation, and freeze-out [113]. At low temperatures, essentially none of the impurities is ionized, and they are frozen out. When the temperature is raised, the impurities are ionized. In some intermediate temperature ranges, all impurities are ionized, and the carrier concentration corresponds to the concentration of the impurities. This temperature range is the saturation region. Since the carrier is a constant in the saturation region, the conductivity is dominated by mobility, which decreases with increasing temperature. At higher temperatures, the excitation of intrinsic carriers across the bandgap becomes significant, leading again to a strong increase of the carrier concentration. This happens in the intrinsic region.
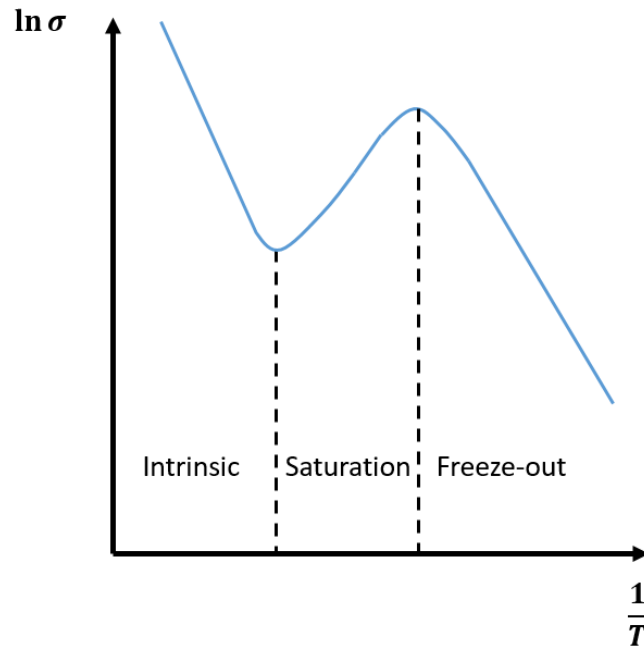
Figure 4.7 Temperature dependence of the conductivity of an extrinsic semiconductor.

Figure 4.8 shows the conductivities of all samples as the function of temperature. Even though all of the samples are intentionally un-doped, but background doping shows the level of 10^{17} cm^{-3}. Hence, the conductivities as the function of temperatures behave similarly to the extrinsic semiconductor. The conductivities of samples A and B show three distinct regions of intrinsic, saturation, and freeze-out, while other samples' conductivities show saturated behaviors in the temperature range from 77 K to 300 K. Higher Sn compositions, which leads to narrower bandgap and higher carrier concentrations, should reduce the temperature at which intrinsic behavior takes over, but it is not a case for those samples C to F. It is worth noting that below the high-quality GeSn layer, there is the defective layer, which can significantly affect the conductivity of samples. The defective layer can be treated as a heavily doped layer, which can retain the conductivity at low temperatures.
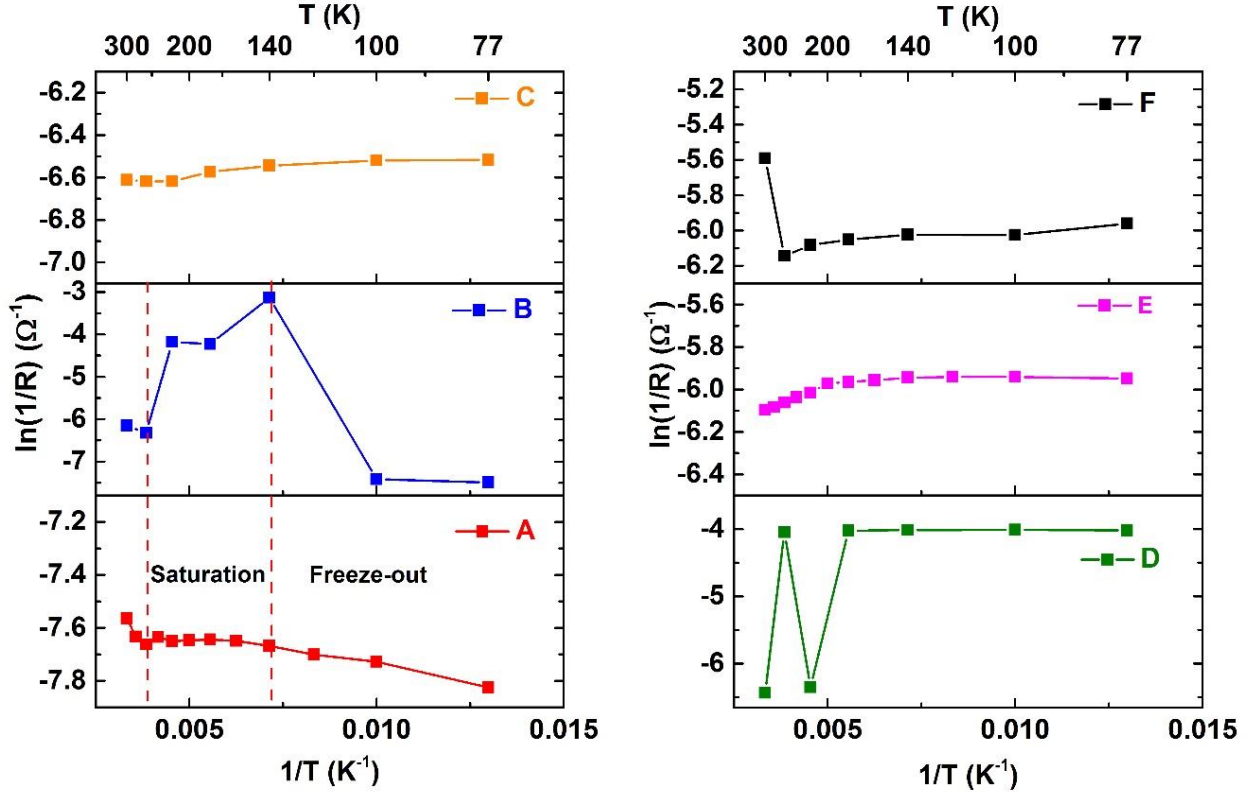
Figure 4.8 Temperature dependence of conductivities of all samples.

4.4.2.2. Lifetime analysis

To extract bulk lifetime and minority carrier mobility, the measured photocurrent was analyzed. The photocurrent ΔI can be expressed as

$$\Delta I = \underbrace{\frac{P_{inc}}{hv}\eta_i(1-R)q\frac{\tau_{eff}}{\tau_t}dA}_{\sqrt{slope}}\frac{\left(hv-E_g^{\Gamma}\right)^{1/2}}{hv} \tag{4.4.1}$$

where P_{inc}/hv is constant for FTIR measurement; η_i is internal quantum efficiency, assuming it equals to 1 in this study; R is reflectance at the surface, which is calculated using the refractive index; q is the unit charge; τ_{eff} is the effective lifetime of excess carriers; τ_t is transit time; d is thickness; A is obtained from absorption coefficient and depends on effective masses of hole and electron. The refractive index and absorption coefficient were characterized using spectroscopic

82

ellipsometry. From the slope of linear fitting of $(\Delta I \times h\nu)^2$, which is shown in Fig. 4.9 (a) at different temperature for device A, the ratio of τ_{eff}/τ_t is determined. The carrier transit time depends on the mobilities of excess holes and electrons as:

$$\tau_t = \frac{1}{\mu_p}(1+b)\frac{l^2}{V} \tag{4.4.2}$$

where V is the applied voltage; l is the spacing between the electrodes; μ_p is the hole mobility and b is the ratio of hole mobility μ_p to electron mobility μ_n. The hole mobility was characterized using Hall measurement and a two-layer Hall model. Hence, from the ratio of τ_{eff}/τ_t and Eq.(4.4.2), the ratio of $(1+b)/\tau_{eff}$ is determined. Moreover, there is a relationship between effective lifetime and bulk lifetime such as:

$$\frac{1+b}{\tau_{eff}} = \frac{1+b}{\tau_{bulk}} + (1+b)D_n\left(\frac{\pi}{l}\right)^2 \tag{4.4.3}$$

where τ_{bulk} is the bulk effective lifetime, and $D_n = \frac{\mu_n k_B T}{q}$ is the minority carrier diffusion constant; k_B is Boltzmann constant. By linear fitting the $(1+b)/\tau_{eff}$ versus $1/l^2$, the temperature-dependent electron mobility and a bulk lifetime can be determined.

Figure 4.9 (b) and (c) show the extracted bulk lifetime and minority carrier diffusion constant of the Ge$_{0.9}$Sn$_{0.1}$ material. The lifetime is decreasing as the temperature increases, which leads the devices' performance at high temperatures to be reduced. Moreover, due to the non-passivated surface, the carrier diffusion towards the surface will determine the surface recombination rate. At high temperatures, the surface recombination rate increases. It is worth mentioning that the effective carrier lifetime of the 10 % Sn photoconductor is much shorter than the ones presented in Chapter 2. One possible reason is that the material becomes directness because of more Sn incorporation in the material, which leads to a shorter lifetime. Still, it is

possible to achieve high gain due to high carrier mobility. Hence, in order to achieve high performance at high temperatures, it is necessary to optimize the surface recombination rate via fabrication, and the lifetime is needed to optimized using k-space separation.
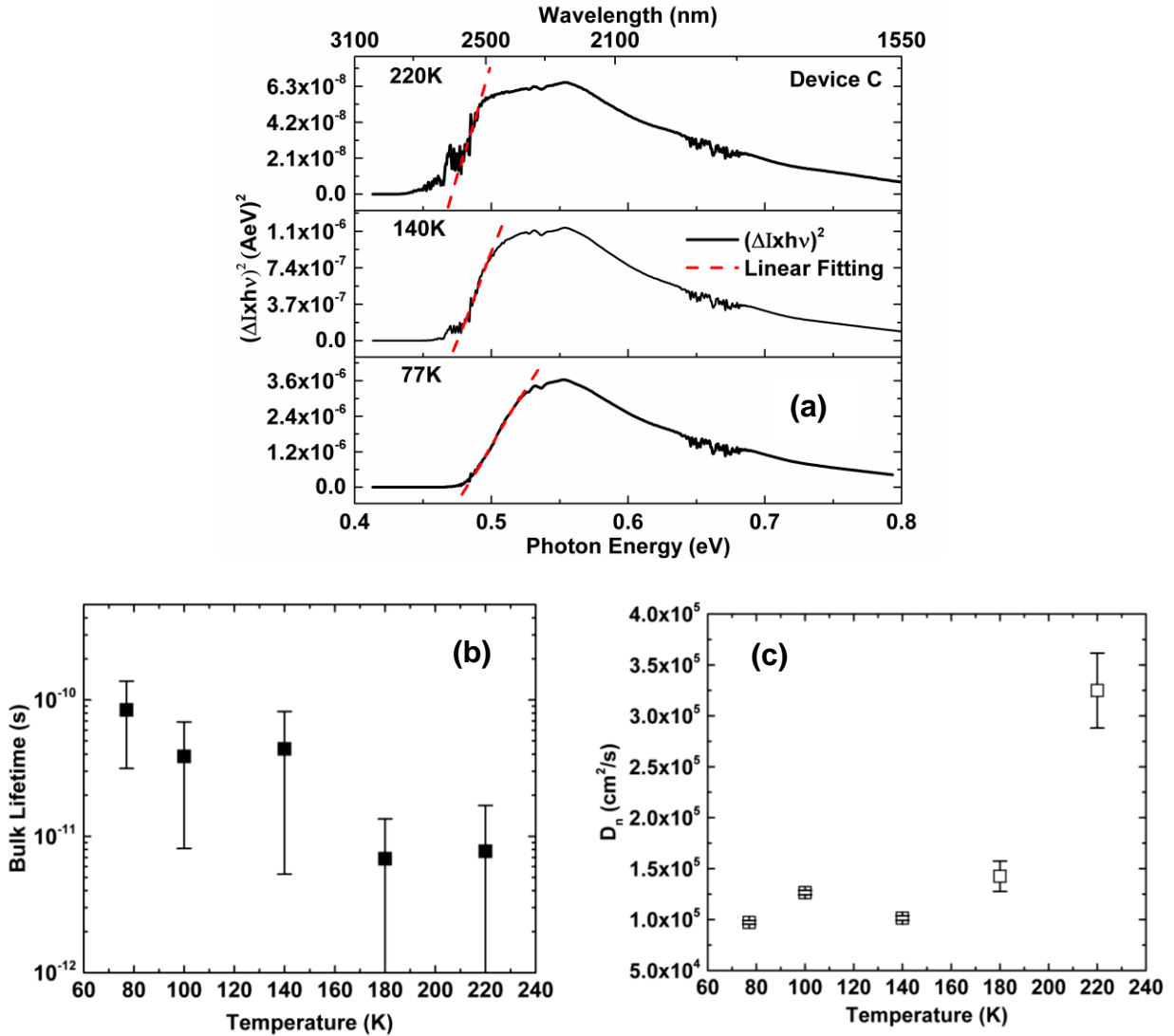
Figure 4.9 (a) The linear fitting of $(\Delta I \times h\nu)^2$ to extract the ratio of τ_{eff}/τ_t ; (b) Bulk lifetime and (c) Minority carrier diffusion constant of the $Ge_{0.9}Sn_{0.1}$ photoconductor.

4.4.3. Future study

• To increase the range of the detection, it is necessary to have more Sn incorporation in the GeSn photoconductor

84

- To block the defective layer, it is necessary to introduce doping to create the inversion layer.

- Design materials to achieve k-space charge separation

Chapter 5.   Systematic study of infrared GeSn photodiodes

5.1. Motivation

There are several factors such as detectivity, cost, and cooling requirements, that affect the choice of type of detector and detector material. There are numerous distinctions between a photoconductor and a photodiode. First, for device structure, it is required to form two types of doping for the photodiode compared to the photoconductor. Second, as one achieves high sensitivity detection in the infrared, it becomes difficult to create a photoconductor attaining both satisfactory gain and high resistance, while the photodiode has relatively high impedance owing to the existence of the junction and uniform collection efficiency. Third, diodes have lower power dissipation than conductors as diodes operate at low bias. Last, photodiodes have less generation-recombination noise by a factor of $\sqrt{2}$ because carriers do not recombine in the depletion region. Hence, the photodiode utilizes intrinsic absorption better than in the photoconductor.

In the last few years, several published GeSn photodiodes showed relatively high responsivity ranging from 0.2 to 0.35 A/W at 1.55 µm. In 2016, Chang *et al*. first successfully demonstrated a GeSn-based 320×256 focal-plane array imaging sensor [13]. However, the operating wavelength only covered till 1.9 µm. Our group previously reported a $Ge_{0.9}Sn_{0.1}$ photodiode with decent performance. It is feasible to provide a standard evaluation for the SWIR detectors. The device exhibited a peak responsivity of 0.19 A/W on 1.55 µm at 77 K and a longwave cutoff of 2.6 µm at room temperature [36]. However, that device performance is limited by several factors including the following: (i) because of the immature growth technique, the active GeSn layer (~250 nm) is thin, which results in low absorption; (ii) the compressive strain of the active GeSn layer, which limits cutoff wavelength; (iii) the poor carrier collection

and high dark current (25 mA/cm^2 at -0.1 V) due to defective layer at the Ge/GeSn interface. Moreover, since the responsivity was measured using a 1.55 µm laser diode, the absorption from the Ge buffer layer contributes to the responsivity which led to over-estimating the device performance for the longer wavelength range.

In this chapter, we report Ge$_{0.89}$Sn$_{0.11}$ photodiodes featuring dramatically improved performance, which is attributed to adopting solutions that systematically address the above-mentioned issues as follows: (i) the growth of a much thicker Ge$_{0.89}$Sn$_{0.11}$ layer ($\sim$700 nm) with high material quality, which enhances the light absorption and reduces defect-related nonradiative recombination loss; (ii) the thick GeSn layer is fully relaxed to extend the long-wavelength-side cutoff; and (iii) the optimized doping profile improves the carrier collection efficiency. The 500 µm device shows a dark current density of 7.9 mA/cm^2 at 0.1 V and a longwave cutoff at 2.65 µm. The room temperature responsivity was measured as 0.32 A/W at 2.0 µm, corresponding to an external quantum efficiency (EQE) of 20%. It is worth noting that since the responsivity was measured using a 2.0 µm laser, the contribution from the Ge buffer layer was mostly eliminated, leading to a more accurate characterization of the GeSn photodiodes. The passivation technique on GeSn photodiode was investigated. Based on the in-depth current-voltage analysis, the significantly reduced dark current was achieved with passivated device [58].

5.2. *np* Junction Photodiodes

5.2.1. Theoretical study

The most common photodiode is the abrupt *np* junction formed by a semiconductor, which is doped by p-type and n-type as shown in Fig. 5.1 (a). In Fig. 5.1 (b), the operation of the *np* junction photodiode is illustrated. The incident light with energy greater than the energy gap

illuminates on the top surface of the device. The light is absorbed and excites electron-hole pairs in the material on both sides of the junction. The electron-hole pairs are diffused to the space-charge region within a diffusion length from the junction. Then, the strong electric field separates electron-hole pairs and readily accelerates minority carriers to become majority carriers on the other side. Hence, a photocurrent is generated and increases the output current, as shown in Fig. 5.1 (c). Figure 5.2 presents the equivalent circuit of a photodiode. The circuit of the photodiode includes a resistance R_s in series with the device, a load resistor R_L, and a total capacitance C_d involving junction and packaging capacitances. The series resistance contains contact resistance as well as the bulk *p*- and *n*- regions. Generally, the series resistance is smaller than the load resistance. The total current density in the *np* junction under illumination is described as

$$J(V, \Phi) = J_d(V) - J_{ph}(\Phi) \tag{5.2.1}$$

where the dark current density, J_d, depends only on V and the photocurrent depends only on the photon flux density Φ with an assumption that the electrical collection efficiency is 100 %. Because the gain is equal to 1, the photocurrent is written as

$$I_{ph} = \eta q A \Phi. \tag{5.2.2}$$

However, there is a report of the current gain in photodiode structures [114]. It shows that for optical illumination close to an *n+p* junction, whose low-doped side is purely intrinsic, the effective gain can be very high, comparable to the photoconductive gains experienced in photoconductors. It is already known that the leakage current obeys a relationship of minority carrier diffusion constant, the minority carrier concentration, and its diffusion length, while for the infinitely long diode where the low-doped side is purely intrinsic, the diffusion length is substituted by the ambipolar diffusion length. The space charge fields stop one carrier from

88

diffusing away from a region faster than the other carrier, and also an electric field that is close

to the junction cancels the diffusion of majority carriers into the heavily doped contact. This

field causes a minority carrier to drift current flow into the contact, equal to the diffusion current

of the minority carriers, and is large if the mobility ratio of the electron over the hole is large.

The gain applies to excitation close to the junction. This effect can cause occasionally low

resistance for the junction. The theory of a conventional photodiode with a gain equal to 1 will

be considered below.
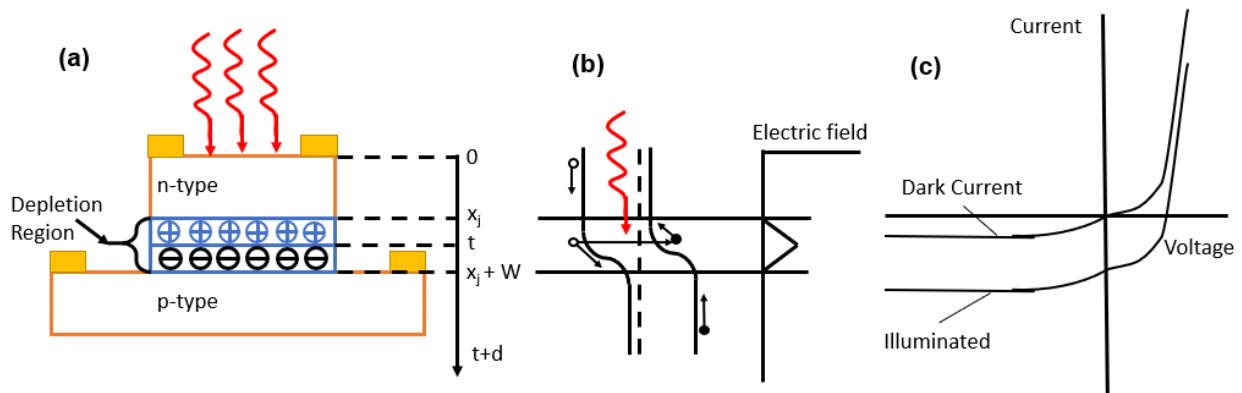
Figure 5.1 (a) *np* junction. (b) Band diagram. (c) *IV* characteristics of the photodiode under illumination and non-illumination
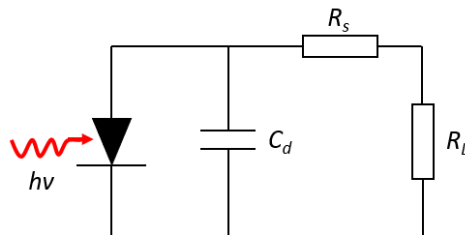
Figure 5.2 Equivalent circuit of photodiode under illumination (the series resistance includes the contact resistance and the bulk *p*- and *n*- regions.

Even when the dark current and photocurrent are significant, they are linearly independent,

and the quantum efficiency can be straightforwardly calculated. As presented in Fig. 5.1 (c), if

the *pn* junction is not connected to any load resistor, which is called open-circuit configuration,

the accumulation of electrons and holes on the two sides of the junction creates a voltage. If the load is connected to the diode, there is the current flowing through the circuit. To obtain the maximum current, the short-circuited configuration is employed.

To obtain the output voltage as known as the open-circuited voltage, the short-circuited current multiplies with the diode resistance, which is described as $R = (\partial I / \partial V)^{-1}$ at $V = V_b$

$$V_{ph} = \eta q A \Phi R, \tag{5.2.3}$$

where V_b is the bias voltage and $I = f(V)$ is the current-voltage characteristic of the diode. For solar cell application, the photodiode is operated at zero-bias voltage:

$$R_o = \left(\frac{\partial I}{\partial V}\right)^{-1}_{|V_b=0}. \tag{5.2.4}$$

A frequently corresponding figure of merit for a photodiode is the $R_o A$ product

$$R_o A = \left(\frac{\partial J}{\partial V}\right)^{-1}_{|V_b=0}, \tag{5.2.5}$$

where $J = I/A$ is the current density.

For photon detectors, the photodiode is operated at any point of the IV characteristics. For high-frequency applications, the photodiodes are operated under reverse bias to reduce the RC time constant of the devices.

5.2.1.1. Quantum Efficiency

Three regions contribute to photodiode quantum efficiency: two neutral regions of different types of conductivity and the spatial charge region as shown in Fig. 5.1. The total quantum efficiency is a superposition of those three regions, which is given by [115]:

$$\eta = \eta_p + \eta_{DR} + \eta_n. \tag{5.2.6}$$

When the incident light with the wavelength λ illuminates on the surface of the device, the generation rate of hole-electron pairs as a function of distance x from the surface is written as

$$G(\lambda) = \alpha(\lambda)F(\lambda)[1 - R(\lambda)]exp(-\alpha(\lambda)x), \tag{5.2.7}$$

where $F(\lambda)$ is the number of incident photons per cm^2 per second per unit bandwidth and R is the reflectivity from the surface. By using the minority carrier continuity equations, the photocurrent can be calculated with an assumption of low injection level conditions. For the holes and electrons in n-type and p-type materials, correspondingly, the continuity equations are described as

$$(1/q)(dJ_{p,n}/dx) \mp G_{p,n} \pm (p_n, n_p - p_{n0}, n_{p0})/\tau_{p,n} = 0. \tag{5.2.8}$$

The hole and electron currents are equal to:

$$J_{p,n} = q\mu_{p,n}p_n, n_pE \mp qD_{p,n}(d\,p_n, dn_p/dx), \tag{5.2.9}$$

where E is the electric field, p_n and n_p are the photogenerated minority carrier densities, and p_{n0} and n_{p0} are the minority carrier densities in equilibrium in the dark.

In the simplest model, it is assumed that the two sides of the junction are uniform in doping, mobility, and lifetime. If both sides are uniformly doped, there are no electric fields outside of the depletion region. For the case of an *np* junction, where the top side is n-type, the combination of 5.2.7-9 equations becomes

$$D_p \frac{d^2(p_n - p_{n0})}{dx^2} + \alpha F(1 - R)exp(-\alpha x) - \frac{(p_n - p_{n0})}{\tau_p} = 0 \tag{5.2.10}$$

The general solution is

$$(p_n - p_{n0}) = A\cosh\left(\frac{x}{L_p}\right) + B\sinh\left(\frac{x}{L_p}\right) - \frac{\alpha F(1 - R)\tau_p}{(\alpha^2 L_p^2 - 1)}exp(-\alpha x), \tag{5.2.11}$$

where $L_p = (D_p\tau_p)^{1/2}$. There are two boundary conditions. At the surface, the recombination occurs:

$$At\ x = 0, D_p \frac{d(p_n - p_{n0})}{dx} = S_p(p_n - p_{n0}) \tag{5.2.12}$$

Physically, the top n-type region includes a narrow section near the surface and a wider section near the junction edge (x_j) as marked in Fig. 5.1 (a). The narrow region is modeled as a uniform top region with a 1 ns lifetime and a surface recombination velocity of 10^6 cm/s or higher. At the junction edge, the excess carrier density approaches by the electric field in the depletion region:

$$At\ x = x_j, (p_n - p_{n0}) = 0. \tag{5.2.13}$$

From the boundary equations, the hole density is calculated as:

$$(p_n - p_{n0}) = \frac{\alpha F(1-R)\tau_p}{\alpha^2 L_p^2 - 1}$$

$$\times \left\{ \frac{\left(\frac{S_p L_p}{D_p} + \alpha L_p\right) sinh\frac{x_j - x}{L_p} + exp(-\alpha x_j)\left(\frac{S_p L_p}{D_p} sinh\frac{x}{L_p} + cosh\frac{x}{L_p}\right)}{\frac{S_p L_p}{D_p} sinh\frac{x_j}{L_p} + cosh\frac{x_j}{L_p}} - e^{-\alpha x} \right\}, \tag{5.2.14}$$

The photocurrent density per unit bandwidth at the junction edge would be collected as:

$$J_p = \frac{qF(1-R)\alpha L_p}{\alpha^2 L_p^2 - 1}$$

$$\times \left\{ \frac{\left(\frac{S_p L_p}{D_p} + \alpha L_p\right) - exp(-\alpha x_j)\left(\frac{S_p L_p}{D_p} cosh\frac{x_j}{L_p} + sinh\frac{x_j}{L_p}\right)}{\frac{S_p L_p}{D_p} sinh\frac{x_j}{L_p} + cosh\frac{x_j}{L_p}} - \alpha L_p e^{-\alpha x_j} \right\}, \tag{5.2.15}$$

The boundary conditions for the p-type layer are:

$$At\ x = x_j + W, (n_p - n_{p0}) = 0, \tag{5.2.16}$$

$$At\ x = H + W, S_n(n_p - n_{p0}) = -D_n[d(n_p - n_{p0})/dx] \tag{5.2.17}$$

where W is the width of the depletion region, and H is the width of the whole cell. Equation 5.2.16 shows that the excess minority carrier density decreases to zero at the edge of the depletion region. Equation 5.2.17 presents that surface recombination is at the back of the *np*

junction. If the contact is Ohmic, there is a perfect "sink" for the minority carriers and S_n is infinite.

The electron density is determined as:

$$(n_p - n_{p0}) = \frac{\alpha F(1-R)\tau_n}{\alpha^2 L_n^2 - 1} exp[-\alpha(x_j + W)]$$

$$\left[cosh\frac{x - x_j - W}{L_n} - exp[-\alpha(x_j + W)] - \right.$$

(5.2.18)

$$\left. \frac{\left(\frac{S_n L_n}{D_n}\right)\left[cosh\frac{H'}{L_n} - exp(-\alpha H')\right] + sinh\frac{H'}{L_n} + \alpha L_n exp(-\alpha H')}{\frac{S_n L_n}{D_n} sinh\frac{H'}{L_n} + cosh\frac{H'}{L_n}} sinh\frac{x - x_j - W}{L_n} \right]$$

The photocurrent per unit bandwidth due to electrons at junction edge is described as:

$$J_n = \frac{qF(1-R)\alpha L_n}{\alpha^2 L_n^2 - 1} exp[-\alpha(x_j + W)]$$

$$\left[\alpha L_n - \frac{\left(\frac{S_n L_n}{D_n}\right)\left[cosh\frac{H'}{L_n} - exp(-\alpha H')\right] + sinh\frac{H'}{L_n} + \alpha L_n exp(-\alpha H')}{\frac{S_n L_n}{D_n} sinh\frac{H'}{L_n} + cosh\frac{H'}{L_n}} \right]$$

(5.2.19)

where $H' = H - (x_j + W)$ is the whole-cell thickness minus the junction depth and depletion width.

The depletion region current is

$$J_{dr} = qF(1-R)exp(-\alpha x_j)[1 - exp(-\alpha W)]$$

(5.2.20)

The internal quantum efficiency

$$\eta = \frac{J_n}{qF(1-R)} + \frac{J_{dr}}{qF(1-R)} + \frac{J_p}{qF(1-R)}$$

(5.2.21)

Based on Eqs. 5.2.6, 5.2.15, 5.2.20, and 5.2.21, each internal quantum efficiency is defined as:

$$\eta_p = \frac{\alpha L_p}{\alpha^2 L_p^2 - 1}$$

$$\times \left\{ \frac{\left(\frac{S_p L_p}{D_p} + \alpha L_p\right) - exp(-\alpha x_j)\left(\frac{S_p L_p}{D_p}\cosh\frac{x_j}{L_p} + \sinh\frac{x_j}{L_p}\right)}{\frac{S_p L_p}{D_p}\sinh\frac{x_j}{L_p} + \cosh\frac{x_j}{L_p}} - \alpha L_p e^{-\alpha x_j} \right\}, \tag{5.2.22}$$

$$\eta_{dr} = exp(-\alpha x_j)[1 - exp(-\alpha W)] \tag{5.2.23}$$

$$\eta_n = \frac{\alpha L_n}{\alpha^2 L_n^2 - 1} exp[-\alpha(x_j + W)]$$

$$\left[\alpha L_n - \frac{\left(\frac{S_n L_n}{D_n}\right)\left[\cosh\frac{H'}{L_n} - exp(-\alpha H')\right] + \sinh\frac{H'}{L_n} + \alpha L_n exp(-\alpha H')}{\frac{S_n L_n}{D_n}\sinh\frac{H'}{L_n} + \cosh\frac{H'}{L_n}}\right] \tag{5.2.24}$$

It is observed that surface and bulk recombination losses can be reduced by decreasing the junction depth and surface recombination velocity, and by increasing the minority carrier diffusion length. Moreover, an analytical result for the photocurrent cannot be obtained if there are no assumptions of constant material parameters regarding the position in the whole device. The numerical solutions are also obtained by dividing the device into a first region near the junction where the field, lifetime, and mobility are all variables, and a second region extending to the Ohmic contact in which the lifetime and mobility are constant and the field is zero.

Figure 5.3 (a) shows the components of the $Ge_{0.91}Sn_{0.09}$ photodiode quantum efficiency as a function of the ratio of junction edge and diffusion length x_j/L_p with an assumption of the infinite thickness of the p-type region. The calculation is performed for the typical absorption of 5×10^3 cm^{-1} at a wavelength close to the intrinsic absorption edge and for $L_n = L_p = 3\,\mu m, W = 0.3\,\mu m$. The quantum efficiency of the depletion layer gradually decreases with increasing x_j, but it is small and plays no major role. The total quantum efficiency reaches its

maximum at $x_j \approx 0.5L_p$ for $S_p = 0$. As the surface recombination velocity S_p increase, this maximum is shifted toward smaller x_j values. Figure 5.3 (b) presents that the position of the peak IQE also depends on the absorption coefficient. When the absorption coefficient increases, the depth of the junction at which the IQE achieves maximum decreases. Based on this calculation, the highest IQE theoretically attains at $x_j \approx 0.05L_p$, which corresponds to $x_j \approx 160\ nm$.

For high absorption coefficients, the penetration depth of the radiation known as $1/\alpha$ is small, which leads to the surface recombination velocity significantly affects η. However, it was found that there is a certain value of the surface recombination velocity of $S_o = (D_p/L_p)cth(x_j/L_p)$, and when the surface recombination velocity is much smaller $S_p \ll S_o$, the absorption coefficient does not affect the quantum efficiency. Based on the analysis above, the photodiode is generally designed so that most of the radiation is absorbed in one side of the junction, p-type region for the case shown in Fig 5.1. It is enabled to make the n-type region very thin or to use a material whose bandgap is larger than the photon energy of the incident radiation so that most of the incident radiation can reach the junction without being absorbed. If the back contact is away from the junction by several minority-carrier-diffusion lengths, L_n, the IQE is given by

$$\eta(\lambda) = \frac{\alpha(\lambda)L_n}{1 + \alpha(\lambda)L_n}. \tag{5.2.25}$$

If the back contact is less than a diffusion length away from the junction, the IQE prefers to

$$\eta(\lambda) = \left[1 - e^{-\alpha(\lambda)d}\right], \tag{5.2.26}$$

where d is the thickness of the p-type region, with assumptions that the back contact has zero surface recombination velocity and that no radiation is reflected from the back surface. Hence, based on the above conditions, a high quantum efficiency can be achieved using an antireflection

95

coating to minimize the reflectance of the front surface ensuring that the device is thicker than

the absorption length.
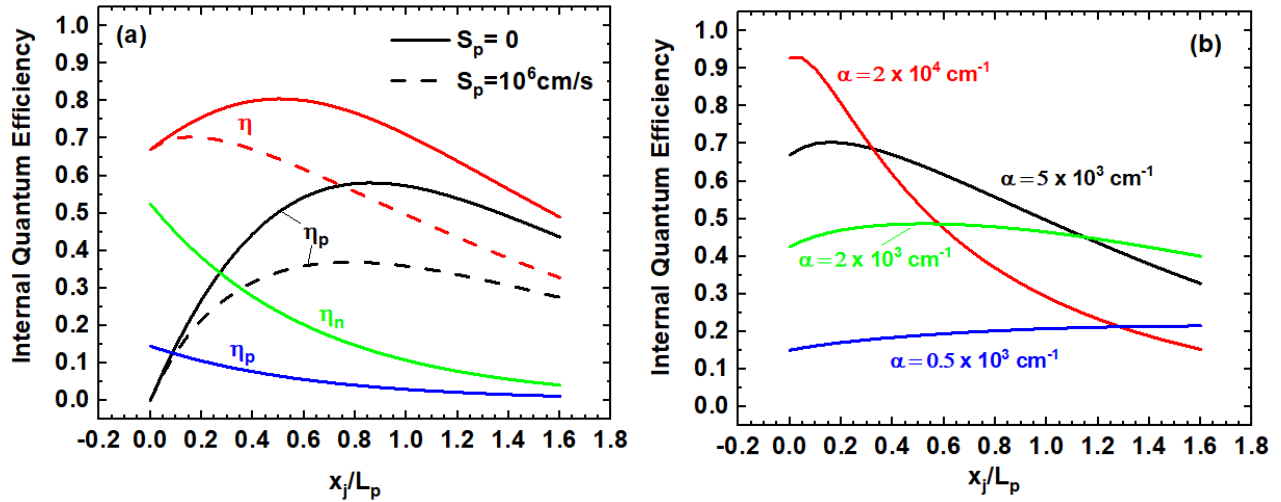
Figure 5.3 (a) Internal quantum efficiency (IQE) versus the ratio of junction edge over diffusion length at $S_p = 0$ and $S_p = 10^6 \ cm/s$ with the assumption of p-type region thickness $d = \infty$. (b) IQE versus x_j/L_P with different absorption coefficients.

5.2.1.2. Noise

For the thermal noise mechanisms, the two fundamental processes that are fluctuations in the

velocities of free carriers due to their random movements, and due to randomness in the rates of

thermal generation and recombination (g-r), are distinguishable in photoconductors, while in

photodiodes, they are less readily distinctive, giving rise jointly to shot noise on the minority

carrier components, which make up the net junction current. In fact, in the neutral regions of

photodiodes, the random thermal motion is responsible for fluctuations, while g–r fluctuations

happen both in the neutral regions and in the depletion region. As the voltage is applied, the

intrinsic noise mechanism of a photodiode is shot noise. For an ideal diode, assumed that

diffusion current is the fundamental current mechanism, it is generally accepted that the noise is

described as [3]

$$I_n^2 = \left[2q(I_D + 2I_s) + 4kT\left(G_J - G_o\right) \right]\Delta f, \tag{5.2.27}$$

where $I_D = I_s \left[exp \left(\frac{qV}{kT} \right) - 1 \right]$; G_J is the conductance of the junction and G_o is the low-frequency value of G_J. In the low-frequency region, the second term on the right-hand side is zero. On the other hand, without applied bias voltage and external photon flux, a diode is in thermal equilibrium, so the noise current is just the Johnson–Nyquist noise of the photodiode zero-bias resistance ($R_o^{-1} = qI_s/kT$):

$$ I_n^2 = \frac{4kT}{R_o} \Delta f, \tag{5.2.28} $$

and

$$ V_n = 4kTR_o\Delta f. \tag{5.2.29} $$

Note that the mean-square shot noise in reverse bias is half the mean-square Johnson–Nyquist noise at zero bias.

For a diode exposed to background flux density Φ_b, an additional current $I_{ph} = qnA\Phi_b$ contributes to the mean square noise current. Then, the noise is calculated as:

$$ I_n^2 = 2q \left[qnA\Phi_b + \frac{kT}{qR_o} exp \left(\frac{qV}{\beta kT} \right) + \frac{kT}{qR_o} \right] \Delta f, \tag{5.2.30} $$

where

$$ R_o = \left(\frac{dI}{dV} \right)_{|V=0}^{-1} = \frac{\beta kT}{qI_s}, \tag{5.2.31} $$

is the dark resistance of the diode at zero bias voltage. As the bias voltage is equal to zero, the eq. 5.2.28 becomes

$$ I_n^2 = \frac{4kT\Delta f}{R} + 2q^2nA\Phi_b\Delta f, \tag{5.2.32} $$

and then

$$ V_n = (4kT + 2q^2nA\Phi_bR_o)R_o\Delta f. \tag{5.2.33} $$

It is assumed that as the applied voltage is set to zero, these forms of the noise equation are independent of the other sources of current. Moreover, 1/f noise is ignored in those equations. Equation 5.2.30 expects that the shot noise is decreased by operating the diode under a reverse bias. Without a background-generated current, the current noise is equal to the Johnson noise $(4kT\Delta f / R_o)$ at zero bias, and it becomes $(2qI_D\Delta f)$ for voltages greater than a few kT in either direction. In real devices, the current noise often increases under a reverse bias, due to presumably 1/f noise in the leakage current.

5.2.1.3. Real *pn* junctions

In practice, several additional excess mechanisms are involved in determining the dark current-voltage characteristics of the photodiode on top of the fundamental mechanism known as diffusion current. The dark current is the superposition of current contributions from three diode regions: bulk, depletion region, and surface. Between them we can distinguish:

i)   Thermally generated current in the bulk and depletion region

        • Diffusion current in the bulk p and n regions

        • Generation–recombination current in the depletion region

        • Band-to-band tunneling

        • Intertrap and trap-to-band tunneling

        • Anomalous avalanche current

        • The ohmic leakage across the depletion region

ii)   Surface leakage current

        • Surface generation current from surface states

        • Generation current in a field-induced surface depletion region

        • Tunneling induced near the surface

        • The ohmic or nonohmic shunt leakage

• Avalanche multiplication in a field-induced surface region

iii)   Space-charge-limited current

Figure 5.4 illustrates schematically some fundamental mechanisms of the dark current that happened under reverse bias. Each of the components has its relationship to voltage and temperature. The method to the analysis of the *IV* characteristics of the diode that is performed based on an assumption that only one mechanism dominates in a specific region of the diode bias voltage is not always valid. A better solution is to numerically fit the sum of the current components to experimental data over a range of both applied voltage and temperature. In the section below, the mechanisms of the dark current of the GeSn photodiodes are analyzed in detail, and the method of analysis of the diode's *IV* curves is also presented.
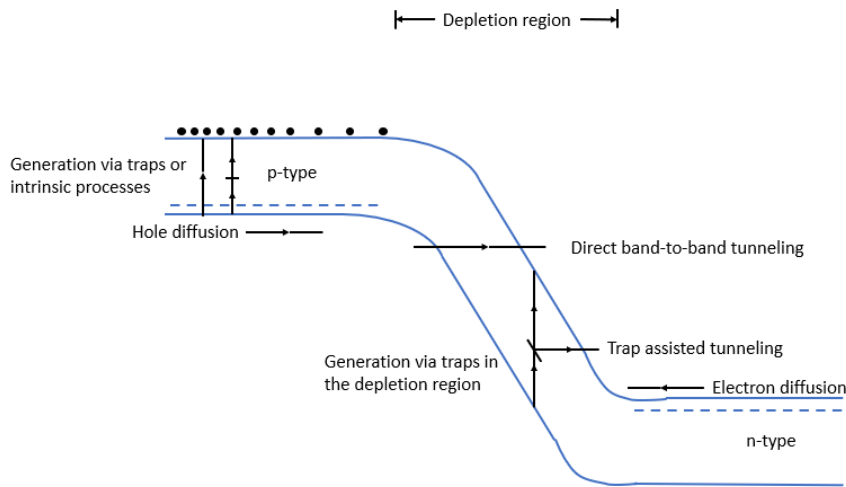
Figure 5.4 Band diagram of the photodiode under reverse bias involving some fundamental mechanisms [3]

5.2.1.4. Mechanisms of dark current

The dark current of GeSn photodiode includes diffusion, generation-recombination (G-R), trap-assisted tunneling (TAT), band-to-band tunneling (BBT), and Ohmic leakage currents. While the diffusion and G-R currents partially dominate forward bias, the TAT, BBT, and G-R currents dominate reverse bias. The Ohmic leakage current contributes near-zero voltages. The

dark current from bulk, depletion region, and surface all contributed to the overall dark current. Figure 5.5 shows (a) the structure and (b) band diagram of the photodiode with bulk and surface states that contribute to R-G and TAT mechanisms. Note that considering the surface trap energy levels and G-R centers (different from bulk), the G-R and TAT currents include the contributions from both bulk and surface [3, 116].
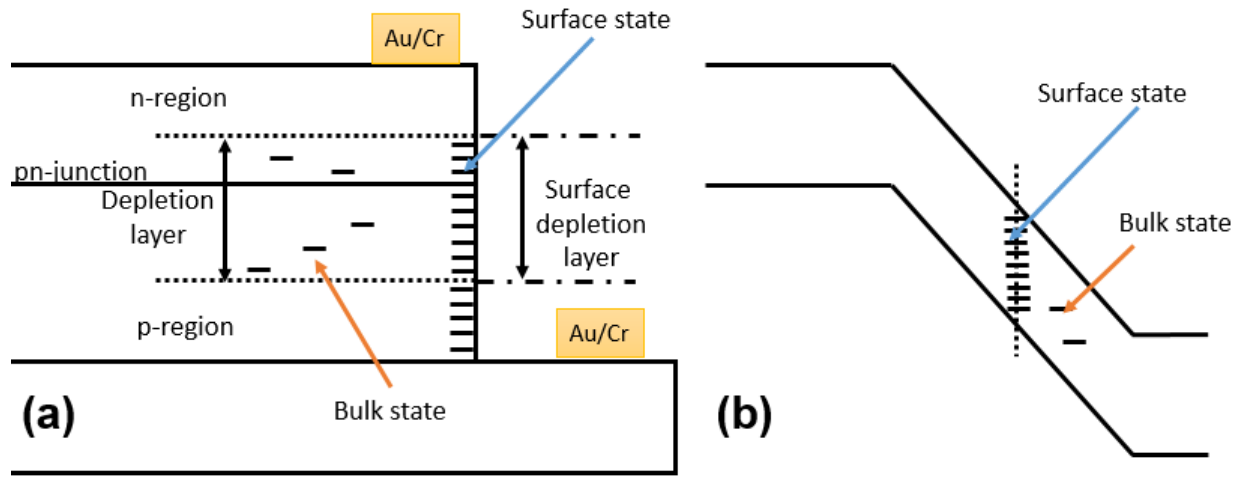
Figure 5.5 (a) Device structure and (b) band diagram of the GeSn photodiode.

A. Diffusion current

The net flow of minority carriers from higher to lower concentration is known as diffusion current, which is given by:

$$I_{diff} = A_{diff} \left[exp\left(\frac{qV}{nkT}\right) - 1 \right] \tag{5.2.34}$$

where A_{diff} is a temperature-dependent coefficient, and V is the bias voltage. The minority-carrier concentrations satisfy the boundary conditions at the edges of the space-charge region. For diffusion current, $n = 1$.

B. Generation-recombination current

Impurities or defects in the space-charge region can act as G-R centers, which produce G-R current. With an assumption that the potential varies linearly with distance over the depletion region, the G-R current is given by [3, 117-119]:

$$I_{g-r} = A_{g-r} \frac{\sinh\left(\frac{qV}{2kT}\right)}{\left(1 - \frac{V}{V_0}\right)^{1/2}} f(b)$$

(5.2.35)

where A_{g-r} is a temperature-dependent coefficient; V_0 is the built-in potential of the diode, and $f(b)$ is given approximately by:

$$f(b) = \int_0^\infty \frac{du}{u^2 + 2bu + 1}$$

(5.2.36)

where

$$b = exp\left(\frac{-qV}{2kT}\right) cosh\left[\frac{E_{g-r} - E_i}{kT} + \frac{1}{2} ln\left(\frac{\tau_{p0}}{\tau_{n0}}\right)\right]$$

(5.2.37)

where E_i is the position of the intrinsic energy; E_{g-r} is the energy level of the G-R center. Since there is no report on carrier lifetime in GeSn, our initial study indicated that the lifetime for electron and hole are the same order of magnitude. Therefore, we assume that $\tau_{p0} = \tau_{n0}$ to simplify the model.

C. Trap-assisted tunneling

There are two components regarding the TAT mechanism which contribute to dark current: 1) from bulk by thermal excitation from the valence band to a Shockley-Read (S-R) recombination center, and then via tunneling from the S-R recombination center to the conduction band, and 2) from surface by thermal excitation from the valence band to a surface state, and then via tunneling from the surface state to the conduction band. Figure 5.6 shows the band diagram of the device involving TAT mechanisms of bulk and surface of the device.

Based on the tunneling rate out of the trap centers, the TAT current is given by [118, 120, 121]

$$I_{TAT} = A_{TAT}(V_0 - V)exp\left[-\frac{B_{TAT}}{(V_0 - V)^{1/2}}\right] \qquad (5.2.38)$$

where

$$A_{TAT} = \frac{2q^3 A\pi^2 m_e M^2}{h^3\left(E_g - E_t\right)} N_t, \qquad (5.2.39)$$

$$B_{TAT} = \frac{4(2m_e)^{1/2}\left(E_g - E_t\right)^{3/2}}{\{3qh[(2qN_A)/(\varepsilon_0\varepsilon_s)]^{1/2}\}} \qquad (5.2.40)$$

where ε_0 is the static dielectric constant; ε_s is the dielectric constant of GeSn; m_e is the electron effective mass; E_g is the bandgap; M is the matrix element associated with the trap potential; h is Planck's constant; E_t is the position of the trap in the band; and N_t is the density of the trap. Note that M represents the matrix element of the trap potential energy between the un-normalized trap-state wave function and the band-edge Bloch wave function, being normalized in unit volume. The experimentally determined value of $M^2(m_e/m_0)$ for silicon is found to be 10^{-23} Vcm^3. We can assume a similar value for GeSn.
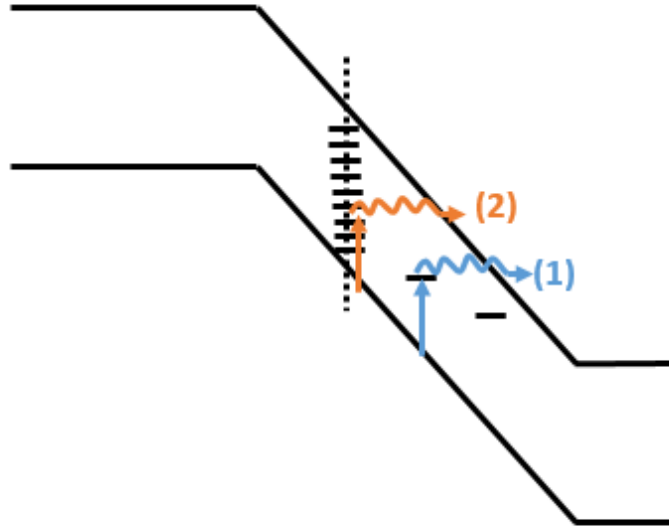
Figure 5.6 Band diagram showing TAT mechanisms of (1) bulk and (2) surface of the device.

D. Band-to-band tunneling

At relatively higher bias voltages, the electrons directly tunneling from the valance band to the conduction band are responsible for the BBT current. The direct BBT current is given by [120, 121]

$$I_{BBT} = -A_{BBT}(V_0 - V)^{3/2} exp\left[-\frac{B_{BBT}}{(V_0 - V)^{1/2}}\right]$$ (5.2.41)

E. The Ohmic leakage

The *I-V* characteristics of the GeSn photodiodes indicate the existence of an excess current as Ohmic leakage current, which can be expressed as

$$I_{shunt} = \frac{V}{R_{shunt}}$$ (5.2.42)

5.2.2. Simulation

5.2.2.1. One-dimension discretization simulator to model *pn* junction

A. Objectives

The device simulation became an important tool for investigating the potential distribution and the carrier transport in semiconductor structures. Even though this section is only to develop a simulator to solve Poisson's equation and two carrier continuity equations in steady-state and on a one-dimensional spatial grid, it can assist to gain experience in the modeling of semiconductor devices before using the commercial software Silvaco.

B. Device modeling

The semiconductor device modeling deal with the transport of charge carriers in semiconductor structures, under the impact of the potential distribution, the properties of the material, the geometry and doping distribution, and the contacts or terminals are boundaries.

The basic equations to describe the transport are the classical semiconductor equations, including Poisson's equation:

$$\nabla \cdot \varepsilon \nabla \Psi = -q[p - n + N_D^+ - N_A^-],$$

(5.2.43)

and the current continuity equations

$$\frac{\partial n}{\partial t} = G - R - \nabla \cdot \overrightarrow{J_n},$$

(5.2.44)

$$\frac{\partial p}{\partial t} = G - R - \nabla \cdot \overrightarrow{J_p},$$

(5.2.45)

for the electron and hole currents $\overrightarrow{J_n}$ and $\overrightarrow{J_p}$, respectively, as:

$$J_p = q\mu_p pE - kT\mu_p \frac{\partial p}{\partial x}$$

(5.2.46)

$$J_n = q\mu_n pE + kT\mu_n \frac{\partial n}{\partial x}.$$

(5.2.47)

The potential and carrier densities are solutions of those partial differential equations. Poisson's equation is solved in the whole simulation region such as in the semiconductor and all insulating materials, while the continuity equations are solved in the semiconductor only. To obtain a unique solution for this system of differential equations, a set of boundary conditions is necessary, imposed on the variables. There are four device boundaries:

- contacts, which allow a current flow into and out of the devices;

- contacts, where only voltages can be applied;

- interfaces, where current flow disappears;

- artificial boundaries, where neither electric nor current flow exists

Figure 5.7 shows the spatial discretization of the *pn* junction. The choice of the mesh and the distribution of the grids have a remarkable effect not only on the convergence but also on the accuracy of the numerical solutions. The discretization of Eq. 5.2.43 becomes [122-124]:

$$\nabla^2 V = \frac{V_{k-1} - 2V_k + V_{k+1}}{\Delta x^2} = -\frac{\rho_k}{\varepsilon},$$

(5.2.48)

Figure 5.7 also presents the characteristic matrix A that was formed from Eq. 5.2.48 with N discretized points. Eq. 5.2.48 can be represented by:

$$[A] \cdot [V] = [B].$$

(5.2.49)

x = 1 µm

Dirichlet
$V_1 = V_a$
V_2
V_k
$\Delta x = 1$ nm
Neumann
V_{N-1} $V_{N-1} = V_N$

Finite Difference Equation: $\nabla^2 V = \dfrac{V_{k-1} - 2V_k + V_{k+1}}{\Delta x^2} = -\dfrac{\rho_k}{\epsilon}$

A	1st	2nd	...	(k-2)th	(k-1)th	kth	...	(N-1)th
1st	-2	1						
2nd	1	-2	1					
...								
(k-2)th				-2	1			
(k-1)th				1	-2	1		
kth					1	-2	1	
...								
(N-1)th								-1

V	1st
1st	V_2
2nd	V_3
...	
(k-2)th	
(k-1)th	V_k
kth	
...	
(N-1)th	V_{N-1}

B	1st
1st	$-\rho_2/\varepsilon - V_a$
2nd	$-\rho_3/\varepsilon$
...	
(k-2)th	
(k-1)th	$-\rho_k/\varepsilon$
Kth	
...	
(N-1)th	$-\rho_{N-1}/\varepsilon$
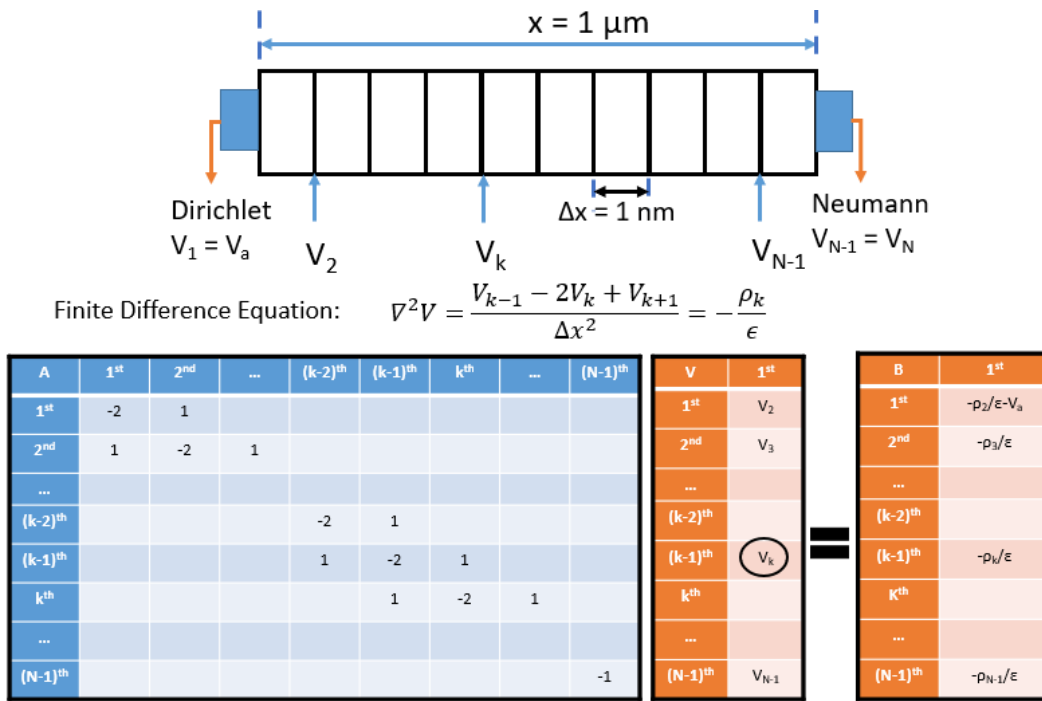
Figure 5.7 Discretization Poisson's equation with the characteristic matrices

Mathematically, there are two different types of boundary conditions, Dirichlet and Neumann conditions. The Dirichlet condition fixes the value of a solution variable, while the Neumann condition uses the derivative of the variable at the boundary. Table 5.1 shows the correspondence between the contact type and the mathematical boundary condition for the semiconductor equations. Because the contact is Ohmic, the Dirichlet boundary is applied,

which leads to that the voltage at the first node is equal to the applied voltage V_a. Moreover, as the last node is treated as the floating contact (interface), then the voltage at the last node is equal to zero. The diagonal of matrix A includes -2s except for the endpoint, and the first element of matrix B is substrated by V_a.

Table 5.1 (D)irichlet and (N)eumann boundary conditions [122].

	Poisson equation	Continuity equations
Ohmic contact	D	D
Schottky contact	D	N
Interface	N	N
Artificial	N	N

The discretization that is applied to the continuity equation requires the determination of the currents on the midpoints of the mesh lines connecting neighboring grids. However, the solutions are only existing on the grids, so interpolation schemes are necessary to determine the currents. Based on Poisson's equation, it is assumed that the potential varies linearly between two neighboring grids, which is corresponding to a constant field along the mesh lines, and the field at the midpoint is obtained by centered finite differences of the potential values. To value the current, it is also needed to evaluate the carrier density at the midpoints. They are averaged between two neighboring grids with a condition that a very small potential variation between the points and the field between those is zero. The continuity equations for each increment are written as:

$$\frac{dp}{dt}(k) = (G - R)(k) - \Big(J_p(i) - J_p(i-1)\Big)/\Delta x \qquad (5.2.50)$$

$$\frac{dn}{dt}(k) = (G - R)(k) - \Big(J_n(i) - J_n(i-1)\Big)/\Delta x \qquad (5.2.51)$$

where the ith mesh point is located midway between the major mesh points $k+1$ and k.

While spatial discretization leads to a boundary value problem, time discretization results in an initial value problem. The Poisson's and two continuity equations under transient conditions are obtained:

$$\nabla \cdot \varepsilon \nabla \Psi(t_{i+1}) = -q[p(t_{i+1}) - n(t_{i+1}) + N_D^+ - N_A^-] \tag{5.2.52}$$

$$\frac{n(t_{i+1}) - n(t_i)}{t_{i+1} - t_i} = (G - R)(t_{i+1}) - \nabla \cdot \overrightarrow{J_n}(t_{i+1}) \tag{5.2.53}$$

$$\frac{p(t_{i+1}) - p(t_i)}{t_{i+1} - t_i} = (G - R)(t_{i+1}) - \nabla \cdot \overrightarrow{J_p}(t_{i+1}) \tag{5.2.54}$$

The simplest time discretization scheme is the fully explicit forward Euler method. The method requires a severe restriction on the time step. From the explicit method, one can obtain:

$$n_i^{t_{i+1}} = n_i^t + \frac{t_{i+1} - t_i}{\Delta x}\left(J_{n,i+1}^t - J_{n,i}^t\right) \tag{5.2.55}$$

$$p_i^{t_{i+1}} = p_i^t + \frac{t_{i+1} - t_i}{\Delta x}\left(J_{p,i+1}^t - J_{p,i}^t\right) \tag{5.2.56}$$

C. Device simulation process

As shown in Fig. 5.8, the flow chart explains the methodology to solve the coupled set of semiconductor equations together with Poisson's equation via a decoupled procedure as known as Gummel's method. The following steps are presented to simulate the non-equilibrium condition of a 1D *pn* diode.

i)   Initialization including mesh size, material parameters, and mobility models

ii) Poisson solver

iii) Calculation of the current densities based on mobility models and carrier distributions

iv) Update of carrier distributions by solving the continuity equation

v)   Checking if the steady-state is reached

vi)   Repeating step ii) to step v) until the steady-state is reached

For the initialization step, the analytic calculation is performed to obtain the minority carrier concentrations and depletion region. Then, the values of minority carrier concentrations are feed to the Poisson matrix to solve the voltage distribution across the device. Also, the electric field is obtained from the derivative of voltage over the discretization mesh. The Poisson solver is validated as the built-in voltage is close to the analytic solution at the same doping levels. The mesh is optimized in this step. To check for convergence, one can calculate the residuals obtained by positioning all the terms to the left-hand side of the equations and substituting the variables with the iteration values. For the exact solution, the residuals should be zero. Convergence is assumed when the residuals are smaller than a set tolerance.
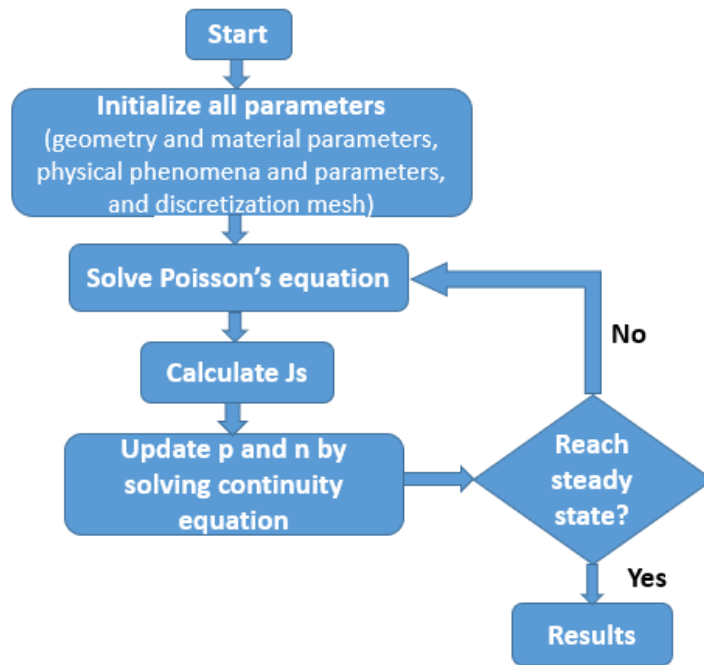
Figure 5.8 Gummel's iteration scheme [124].

The current densities are calculated based on the carrier distributions and field-dependent mobilities. The field-dependent equations and their parameters are specified as below:

$$\mu_{n,p} = \frac{1}{E}\left(\frac{\mu_{n0,p0}E + v_{sat}(E/E_0)^j}{1 + (E/E_0)^j}\right) \tag{5.2.57}$$

$$D_{n,p} = \mu_{n,p}\frac{k_B T}{q} \tag{5.2.58}$$

where $\mu_{n,p} = 3900, 1900 \frac{cm^2}{V \cdot s}$, $v_{sat} = 1 \times 10^7 \frac{cm}{s}$, $E_0 = 8 \times 10^3 \frac{V}{s}$, and $j = 4.5$.

The optimization of $\Delta x/\Delta t$ is a key process of the continuity solver. For this problem setup with the mesh size of 1 nm, the Δt of 1 attosecond is used to obtain the numerical velocity of 1×10^{11} cm/s. This value is much larger than the physical velocity of 1×10^7 cm/s, which is necessary to stabilize the numerical process for the explicit method. The condition to stop when max Δn is greater than 1×10^{15} cm^{-3}.

D. Results and Discussions

The total charge density at the applied voltage of -1 V across the *pn* junction is plotted in Fig. 5.9 (a), which is asymmetric due to the difference between the doping levels of *p* and *n* such as 1×10^{17} cm^{-3} and 2×10^{18} cm^{-3}, respectively. The convergence depends on the initial guess of minority carrier densities. It is slightly fast to achieve the solutions as the relaxation velocity is as high as 10^{11} cm/s. The electric field across the *pn* junction is shown in Fig. 5.9 (b). Due to the uniform spatial Δx and the Dirichlet boundary is forced at the first node as well, the electric field is not constant on the quasi-neutral *p* region. Moreover, it is challenging for this method to be converged, and it is required to have proper timesteps Δt to achieve convergence. The IV characteristics of the device are presented in Fig. 5.9 (c). The voltage is ranging from -5 to 0.2 V, and this model does not support to estimate of the forward bias that is higher than the built-in voltage. For the reverse bias range, the dark current is quite high, which is in the range of mA due to high doping levels of both *p*- and *n*- regions. One issue of drift-diffusion simulators is the calculation of the current. In near-equilibrium conditions for small applied voltages, the net

current is very small compared with the individual components of the current including the drift and diffusion currents. Hence, it is necessary to employ a very small mesh to ensure current conservation in the depletion regions, and more accuracy is essential for the currents in the quasi-neutral regions.
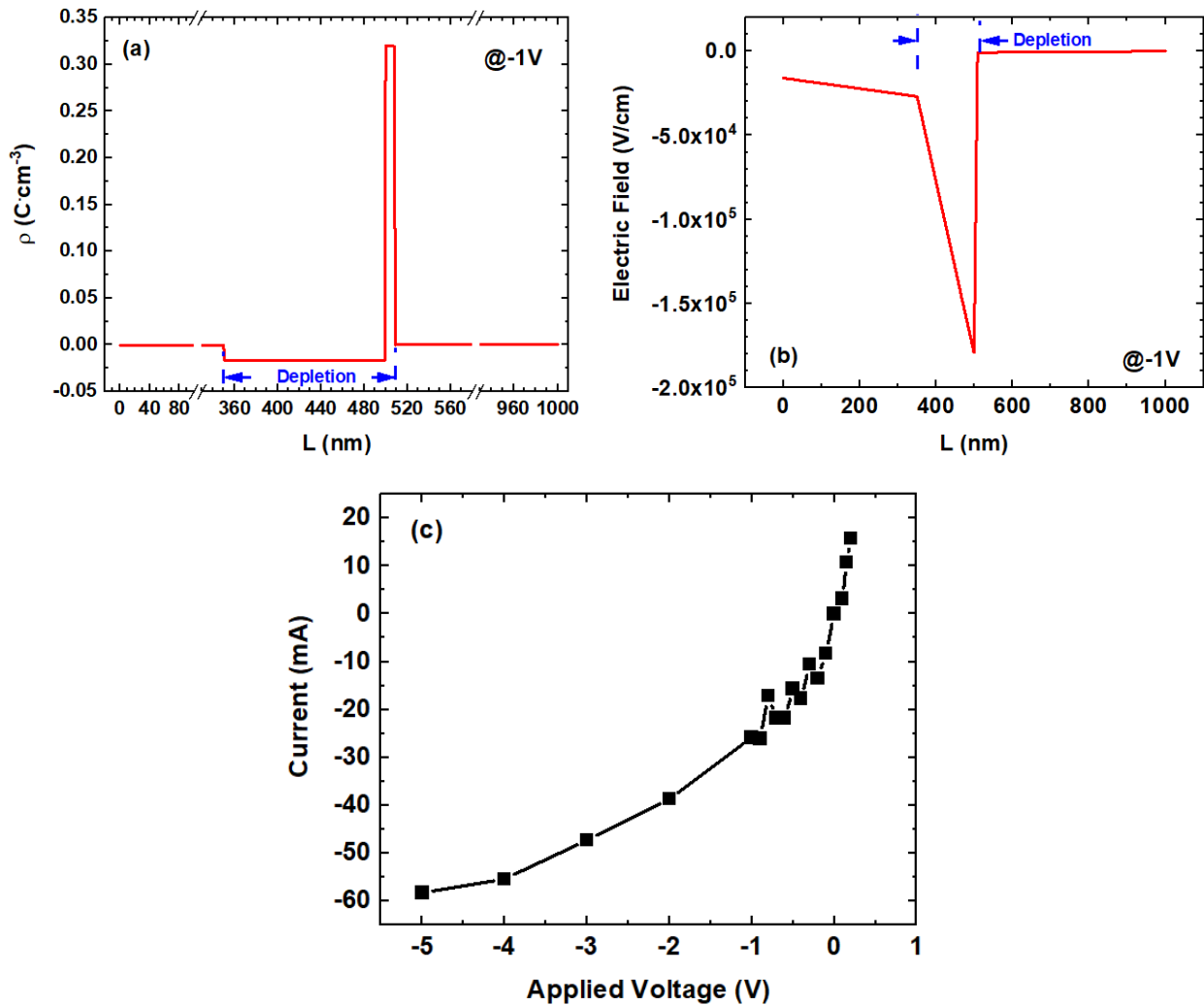
Figure 5.9 (a) Charge density across the *pn* junction. (b) Electric field. (c) *IV* characteristics.

As a result, the *pn* junction simulator is performed using the drift-diffusion model under equilibrium conditions. Both Poisson and electron and hole continuity equations are solved to obtain the spatial characteristics and time discretization as well. By understanding the process of

the simulator, it is helpful to further study the pn junction characteristics using commercial software such as Silvaco.

5.2.2.2. Silvaco simulation

The device was simulated using the commercial Silvaco with Atlas simulator. Because the mesa has a cylindrical shape, a pseudo-3D method employing cylindrical mesh was used to form the meshes of the detectors. The structure The GeSn materials were modeled using the default Ge material whose bandgap, the effective density of states, and intrinsic carrier concentrations were modified. The GeSn materials' refractive index and extinction coefficient that was measured using ellipsometry, overwrote the Ge ones to simulate the devices under illumination. The light intensity that is assumed to be uniform across the width of the beam has a density of 0.01 W/cm^2. The drift-diffusion transport model was used with field-dependent mobility. The Shockley-Read-Hall (SRH) recombination model was used with electron and hole lifetimes of 1 µs for the high-quality GeSn layer, while the defective layer has a lifetime of 0.1 ns. Surface recombination on the devices' surfaces and sidewalls was considered with the recombination velocities of 10^5 cm/s for electrons and holes. Figure 5.10 (a) shows the simulation of the Ge$_{0.89}$Sn$_{0.11}$ photodiode including that the current flows across the junction. Even though the model includes surface recombination, the current density at the sidewall does not significantly contribute to the dark current as shown in the inset of Fig. 5.10 (a). Figure 5.10 (b) shows the *IV* characteristics of such diode. For forward bias, the turn-on voltage is ~0.3V, and the current density is in the range from 1 A/cm^2 to 10 A/cm^2, while for the reverse bias, the current density is in the range of 1 mA/cm^2. Because the major models for such photodiode are Shockley-Read-Hall (SRH) and surface recombination, the dark current is still small and not accurate. The

111

model of the GeSn photodiodes should include several mechanisms as abovementioned. Hence, further IV analysis of the practical IV characteristics can help to complete the device modeling.
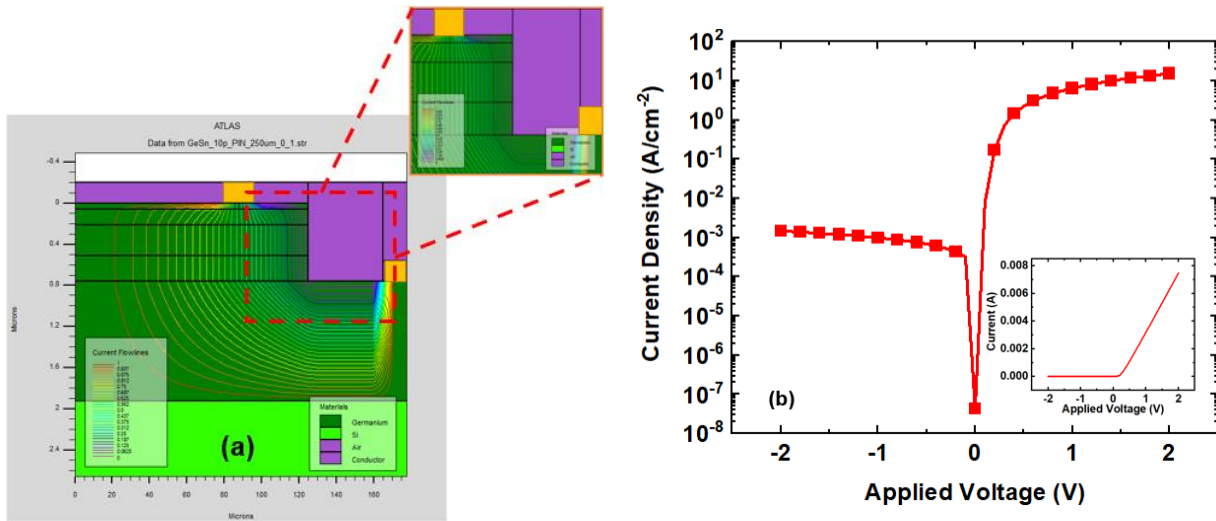
Figure 5.10 (a) Cross-sectional of the $Ge_{0.89}Sn_{0.11}$ photodiode simulated by Silvaco, showing the current flowlines. (b) *IV* characteristics of the same device.

5.3. Figures of Merit

As mentioned above, this chapter focuses on the characterization and analysis of the homojunction GeSn. Due to the growth technique, the 9 % Sn growth recipe repeatedly shows a high quality of material, so the recipe is employed to grow the material for the homojunction GeSn. The materials were grown using an industry-standard ASM Epsilon® 2000 RPCVD with SnCl4 and GeH4 as Sn and Ge precursors, respectively. First, the Ge buffer was grown on a Si wafer with a thickness of 1160 nm and p-doped by Boron. Then a 550-nm-thick p-type (unintentionally doped) $Ge_{0.89}Sn_{0.11}$ layer was grown followed by a 150-nm thick n-type $Ge_{0.89}Sn_{0.11}$ layer (Arsenic as a dopant). The growth was completed by capping with a 60-nm-thick heavily doped n-type Ge layer. Figure 5.11 (a) shows cross-sectional TEM and SIMS, which identifies the thickness and doping profile, and the Sn composition is also defined by SIMS. The TEM image clearly shows a 250 nm defective layer and a 450 nm high-quality layer.

Due to the relaxation of the film, the Sn composition achieves 11 % Sn at the high-quality layer, while the defective layer consists of 9 % Sn, which is similar to the target Sn composition of the recipe. The *n-* and *p-* doping levels of the GeSn layer are measured as 2×10^{18} cm^{-3} (from SIMS) and 1×10^{17} cm^{-3} (unintentional doping, measured separately from a different reference sample), respectively. As above designed, the junction edge should be ~160 nm to achieve the peak IQE, which is accomplished in this growth as the n-type GeSn layer is 150 nm. Our previous work on the photodiode detector indicated that the device performance can be dramatically improved by passivation of the surface and sidewall to reduce leakage currents [36]. Hence, the $Ge_{0.89}Sn_{0.11}$ photodiode was also passivated by GeON with a thickness of 3 nm, which covers the top and sidewall as shown in Fig. 5.11 (b). Note that although photoconductors show higher responsivity and D*, passivation could not further improve their performance since surface leakage current is not dominant in photoconductor, but the current leakage in the Ge buffer. Therefore, the photodiode was selected for the passivation study.
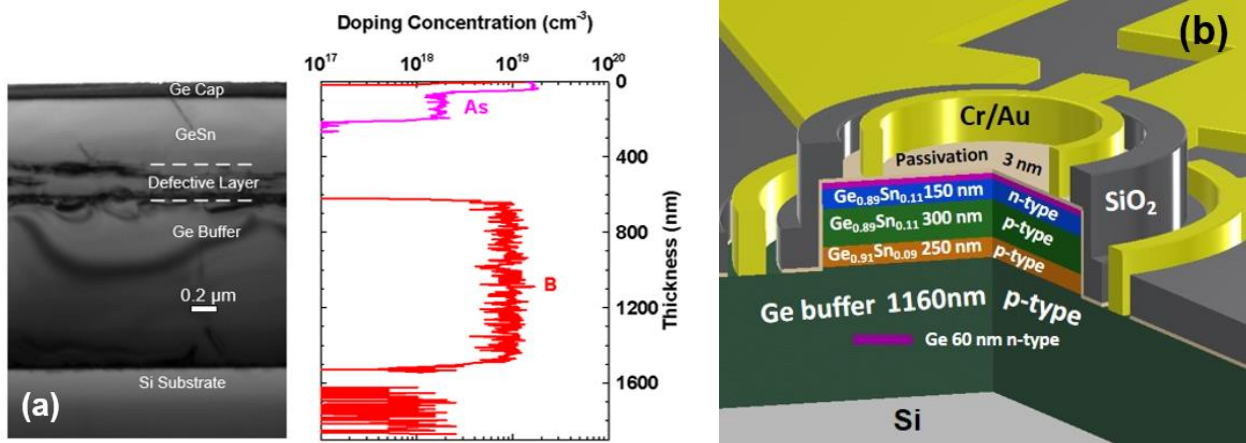
Figure 5.11 (a) Cross-sectional TEM image and doping profile by SIMS. (b) Device structure schematic diagram [41, 58].

5.3.1. Dark current

Dark current-voltage *IV* characteristics were measured with a direct current (DC) source. Figure 5.12 (a) and (b) show the *IV* characteristics for the devices (250 µm of mesa diameter) without and with passivation from 300 to 77 K, respectively. It is worth mentioning that all the fabricated devices are tolerated by lateral etching due to the wet etch technique, and the effect of sidewalls makes the devices endure high dark current. The smaller the device is, the more effective the sidewalls are. The rectifying behavior was observed at each temperature. Compared with the non-passivated device, the passivated device exhibits ~50% lower reverse dark current under lower bias at all temperatures. To better understand the effect of passivation, an in-depth study on the mechanism of each dark current component and its comparison between non-passivated and passivated devices was conducted via data fitting in the section below, which explains the reduced dark current as following: passivation reduces the surface defect density of states, trap density, and thus generation-recombination centers. Therefore, the shunt resistance, trap-assisted tunneling resistance, and generation-recombination resistance increase, resulting in reduced corresponding current components.
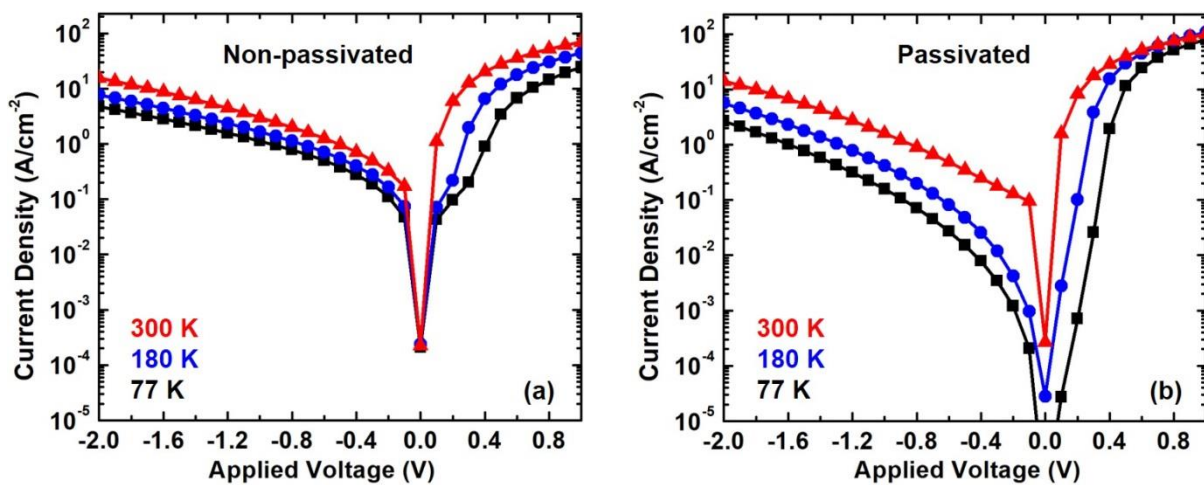
Figure 5.12 Dark current-voltage characteristics of (a) non-passivated and (b) passivated device [58].

5.3.2. Responsivity

A 2.0 µm laser diode optically chopped at 380 Hz illuminates the device which is placed inside the cryostat cooled by liquid nitrogen, and then the photocurrents are collected using a lock-in amplifier through 50 Ω. The incident laser beam has a spot size of ~1 mm in diameter and a power density of 8.9 mW/cm^2. Figure 5.13 (a) and (b) shows the comparison of temperature-dependent responsivity between non-passivated and passivated devices. For each device, as the temperature decreases from 300 K, the measured responsivity decreases. There are two major factors, which cause the decrease of responsivity such as i) as temperature decreases, the bandgap increases, resulting in reduced light absorption coefficient; and ii) activation of deep or shallow level traps in the top GeSn layer, which affects the non-radiative recombination of the photo-generated carriers: At lower temperature, the photo-excited carriers partially recombine at the deep level trap, so that they cannot be collected due to insufficient thermal energy; while at a higher temperature, the carriers could recombine through the shallow trap level, where they can be excited by sufficient thermal energy, leading to that the photo-generated carriers were effectively transported to the contacts. In other words, at high temperatures, the carriers are trapped and then de-trapped at shallow levels, so they can transit and be collected at the contacts. For the non-passivated device, the peak responsivity of 0.32 A/W was obtained at 300 K. For the passivated device, due to reduced dark current, the peak responsivity of 0.38 A/W was achieved at 300 K, showing ~20% improvement.

Spectral responses of the photodiodes were characterized from 1.7 µm to 3.0 µm with a Fourier transform infrared (FTIR) spectrometer at a bias of -0.1 V. The temperature-dependent spectral response for the passivated device is shown in Fig. 5.13 (c). As temperature increases

from 77 to 300 K, the cut-off wavelength shifts towards a long wavelength, from 2.3 to 2.7 µm, which is similar to the non-passivated device as expected.
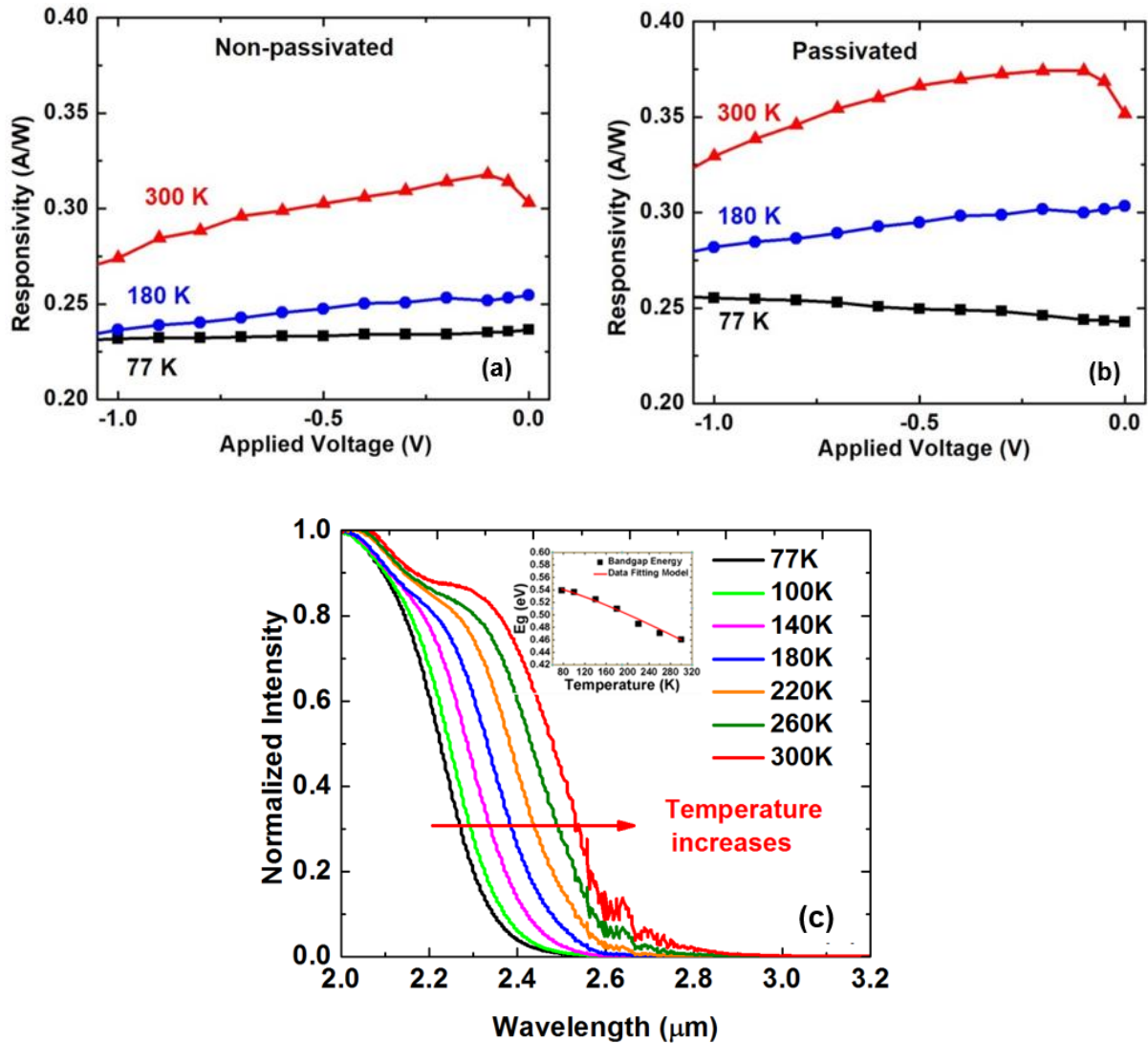
Figure 5.13 Temperature-dependent responsivity for (a) non-passivated and (b) passivated devices. (c) Temperature-dependent spectral response. (Inset) The fitting of the temperature dependence of energy gap with Varshni equation [58].

Also, near the absorption edge, the product of the absorption coefficient and the layer thickness, in this case, is much smaller than unity. Therefore, the spectral response signal is

approximately proportional to the absorption coefficient, which is related to the energy bandgap of direct semiconductors through the following equation:

$$\alpha = C\frac{\left(h\nu - E_g\right)^{1/2}}{h\nu} \tag{5.3.1}$$

where α is the absorption coefficient, C is a constant, $h\nu$ is the photon energy, and E_g is the bandgap. The bandgap of the GeSn absorbing layer at different temperatures was extracted by plotting $(S \cdot h\nu)^2$ against $h\nu$, where S is the spectral response signal. The extracted bandgap at 300 K was 0.46 eV. The temperature dependence of the bandgap can be well described by Varshni's equation [130]:

$$E_g(T) = E_g(0) - \frac{\alpha T^2}{(T + \beta)} \tag{5.3.2}$$

with fitting parameters $E_g(0) = 0.55\ eV$, $\alpha = 5.1 \times 10^{-4}\ eV/K$, and $\beta = 194\ K$ (inset of Fig. 5.13 (c)). This result suggests that the Varshni effect was responsible for the change of the bandgap.

5.3.3. Detectivity

The spectral D* with the operating voltage of 0.3 V at 77 and 300 K are plotted in Fig. 5.14 (a) and (b), respectively. At 77 K, the peak D* of 1.1×10^{10} cm·Hz$^{1/2}$·W^{-1} was obtained for the passivated device, which is about four times higher than that of the non-passivated device (2.0×10^9 cm·Hz$^{1/2}$·W^{-1}). It is worth noting that this D* value is superior to the PbSe detector at the given wavelength range and is comparable to that of the commercial extended-InGaAs detector ($\sim 4 \times 10^{10}$ cm·Hz$^{1/2}$·W^{-1}) at the same wavelength range. Even at 300 K, the passivated device shows a little better D* compared to the PbSe detector from 1.5 to 2.2 μm.
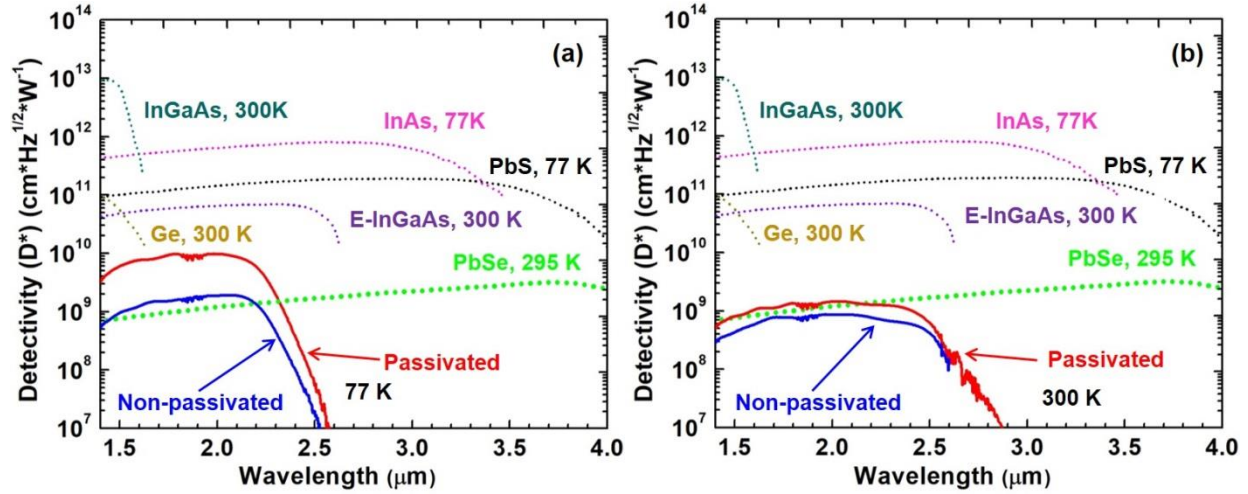
Figure 5.14 D* of non-passivated and passivated devices at (a) 77 K and (b) 300 K [58].

5.4. Discussions

5.4.1. Achievements

For dark current at 0.1 V and 77 K, the non-passivated device shows a dark current density of 5.0 mA/cm^2, while the passivated device shows the density of 0.2 mA/cm^2. The passivation technique aids to decrease the dark current at low temperature and low bias, which is also the operating bias for the device, so it is enabled to claim that the passivation technique enhances the performance with the aid of a cooling system. Further IV analysis is needed to explore dominant mechanisms of *IV* characteristics to improve the next generation of the photodiode.

Another figure of merit of the photodetector is responsivity. While the non-passivated device demonstrates peak responsivity of 0.32 A/W corresponding to an EQE of 20 % at 300 K and 2 µm, the passivated device, due to reduced dark current, achieves the peak responsivity of 0.38 A/W, equivalent to the EQE of 23.8 %, showing ~20% improvement. The spectral response can cover from 2.3 µm to 2.65 µm as the temperature increases from 77 K to 300 K.

At 77 K, the peak D* of 1.1×10^{10} cm·Hz$^{1/2}$·W^{-1} for the passivated device is about four times higher than that of the non-passivated device (2.0×10^9 cm·Hz$^{1/2}$·W^{-1}). It is obvious to observe

118

that this D* value is higher than that of the PbSe detector at the given wavelength range and is comparable to that of the commercial extended-InGaAs detector (~4×10^{10} cm·Hz$^{1/2}$·W^{-1}) at the same wavelength range. All the figure of merits proves that the GeSn photodetector can be a candidate for infrared applications.

5.4.2. Challenges

The GeSn detectors with such figures of merits have shown their potentials to become a key component in IR detection technology. This material system is quite new, and still in the developing phase. Stability, energy bands, carrier lifetime, defects are not known for nearly all possible compositions, so it is challenging to design a photodetector without knowing those characteristics. Let us first look at a simple detector: dark current and EQE are two key parameters most frequently used to evaluate detector performance. As presented in section 5.2.2.2, when SRH recombination and surface recombination effects are considered in the calculation, the dark current is still smaller than in the real GeSn detector. Therefore, there must be other physical effects, which contribute to the dark current of the device. Hence, this section focuses on the analysis of the dark current to explain the measured dark current to some extent, and then those parameters can be reused to simulate the device to assist on design a new batch of the device to improve the performance.

5.4.2.1. Data Fitting Process

It is worth noting that due to the background illumination, the total "dark" current also includes the background photocurrent. To eliminate the influence from the background photocurrent, the dynamic resistance-voltage (R-V) curves were used to quantify the dark current performance of the detector. Since the background photocurrent is independent of applied voltage, the *R-V* characteristics, which can be calculated by mathematical differentiations from

measured *I-V* characteristics, could reflect the GeSn photodiode performance more accurately. According to each component of the dark current, the corresponding resistance component can be expressed by the following equation [120, 121]

$$R_{total} = R_{dynamic} + R_{series} \tag{5.4.1}$$

where $R_{dynamic} = \left(\dfrac{1}{R_{diff}} + \dfrac{1}{R_{g-r}} + \dfrac{1}{R_{TAT}} + \dfrac{1}{R_{BBT}} + \dfrac{1}{R_{shunt}} \right)^{-1}$, and $1/R_{diff} = \partial I_{diff}/\partial V$,

$1/R_{g-r} = \partial I_{g-r}/\partial V$, $1/R_{TAT} = \partial I_{TAT}/\partial V$, $1/R_{BBT} = \partial I_{BBT}/\partial V$ and $1/R_{shunt} = \partial I_{shunt}/\partial V$.

A. Series resistance

The series resistance can be obtained from the diode conductance in the forward bias range, $g_d = \dfrac{\partial I}{\partial V}$. Under the forward bias, where R_{series} is dominant, Eq. (5.4.1) can be rewritten as [131]

$$I_{diff} \approx A_{diff} \left[exp\left(\frac{q(V - I_{diff}R_{series})}{nkT} \right) \right] \tag{5.4.2}$$

Therefore,

$$g_d = \frac{qI_{diff}(1 - R_{series}g_d)}{nkT} \tag{5.4.3}$$

We can rewrite Eq. (5.4.3) as

$$\frac{g_d}{I_{diff}} = \frac{q}{nkT} - \frac{qR_{series}}{nkT}g_d \tag{5.4.4}$$

Figure 5.15 plots the g_d/I_{diff} versus g_d, and the R_{series} can be calculated by $\dfrac{g_d}{I_{diff}} = 0$ intercept. After obtaining the R_{series}, the dynamic resistance and the corresponding bias voltage can be written as $R_{dynamic} = R_{total} - R_{series}$ and $V = V_{bias} - I \times R_{series}$, respectively.
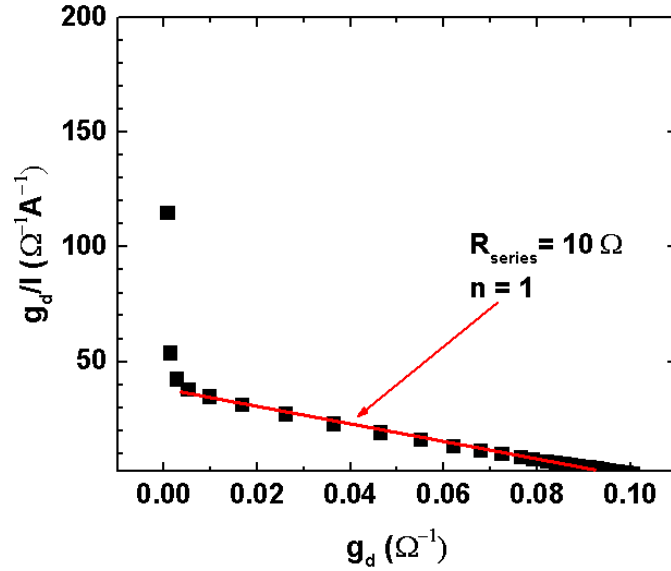
Figure 5.15 g_d/I versus g_d of the diode to extract the series resistance [58].

It is necessary to mention that Eq. (5.4.2) uses the diffusion behavior to describe the part of the forward bias, so the ideality factor n should be unity. However, the ideality factor may be in the range of 1 to 2 due to recombination saturation effects. For the case of ideality factors larger than 2, especially happened at low temperatures, two major explanations can be applied in the GeSn homojunction devices:

i)   Sarusi *et. al.* reported the tunneling-recombination process is the dominant mechanism that determines dark current at the forward bias [136]. For the multistep tunneling-recombination mechanism with uniformly distributed traps in the energy and space as shown in Fig 5.5 where the uniformly distributed traps happen at the sidewall, the forward current is given by:

$$I = const. N_t e^{[-CQ^{1/2}(V_{bi}-V)]} \qquad (5.4.5)$$

where

$$C = \frac{8}{3h}\sqrt{\frac{m_e^* \varepsilon_0 \varepsilon_s}{N_D}} \qquad (5.4.6)$$

121

N_t is the density of trap states, V_{bi} is the built-in voltage, m_e^* is the electron effective mass, ε_0 and ε_s are the dielectric constant of the vacuum and the GeSn, respectively, h is Plank's constant, and $1/Q$ is the number of the tunneling recombination steps required to transverse the diode depletion region.

ii)   Gopal *et.al.* mentioned the excess current component is the best described by an exponential function of the type [121]

$$I_{excess} = I_{r0} + K_1 exp(K_2 V), \qquad (5.4.7)$$

where I_{r0}, K_1 and K_2 are fitting parameters and V is the applied voltage. The existence of the excess current may be due to high dislocation densities that are influencing the electrical properties of the diodes.

It is obvious to observe from Eq. (5.4.2) the effect from R_{series} shifts the turn-on voltage close to the zero bias. The sources of the series resistance involve the metal contacts and the finite resistivity in the quasi-neutral regions. At low temperatures, the series resistance effect can increase due to the low-temperature behavior of the quasi-neutral regions.

B. Simultaneous fitting

The typical fitting process for *R-V* curves is sequentially performed at different bias ranges with an assumption that only one dark current mechanism has a dominant effect on a fitted curve in the particular bias range [120]. However, the GeSn detector has more than one mechanism with comparable effects in most biased regions. Hence, the *R-V* curves were fitted with the simultaneous fitting process in all bias regions. In our fitting procedure, we use Matlab *fminsearch* built-in function to minimize the function value of $F = \sum_{i=1}^{N} \left[log\left(R_{fit}(V_{di}) \right) - log\left(R_d(V_{di}) \right) \right]^2$, where R_d is the experimental data of the dynamic resistance, which eliminated series resistance, and N is the number of data. The initial values were found using the

sequentially fitting process with the assumption as only one mechanism dominates fitted data at the particular bias range. Eight parameters were used in the fitting process such as: A_{diff}, A_{g-r}, E_{g-r}, E_t, N_t, A_{BBT}, B_{BBT}, and R_{shunt}. Figure 5.16 shows the flowchart of the fitting procedure. The first step is to input the initial values of parameters and the experimental data. Secondly, the *fminsearch* function was used to minimize the objective function. After the first conditions were satisfied, to check if the obtained parameters are converged, the third step was performed such as:

    i)   Randomly fixing parameters of one mechanism

    ii)   Refitting for other parameters

    iii)   Checking if the parameters approach the previously obtained parameters as the fitting conditions were satisfied.
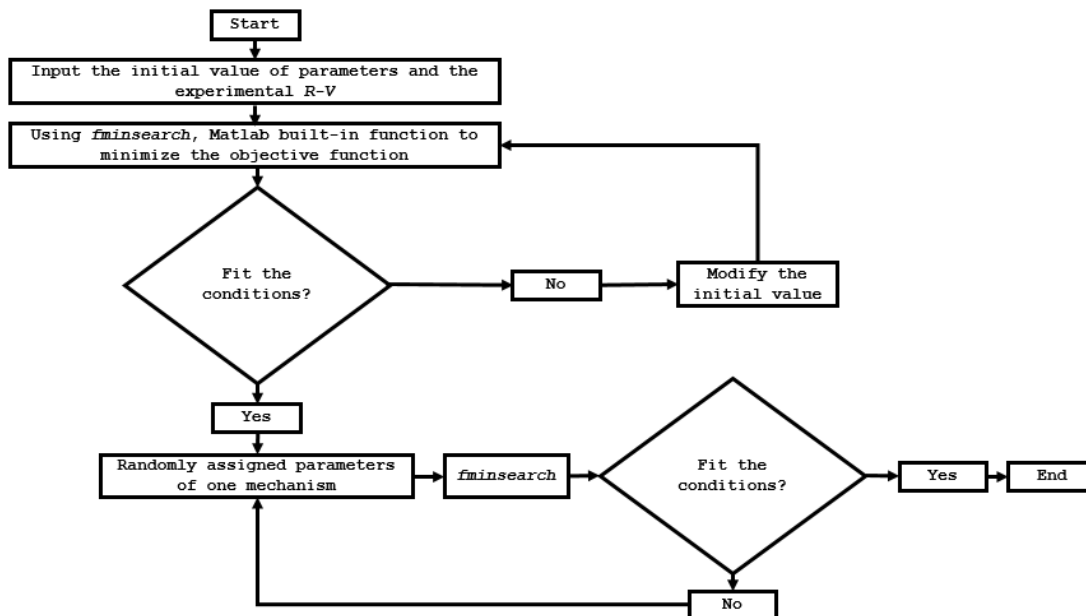
Figure 5.16 The flowchart of data fitting procedure.

5.4.2.2. Results and discussion

Figure 5.17 shows the fitted resistance components of the devices with and without passivation at temperatures from 300 to 40 K. Followings are the analysis of each resistance.

123

A. Shunt resistance R_{shunt}

At each temperature, the passivated device shows higher R_{shunt} comparted to the non-passivated device since the passivation reduces defect density of states (DOS) at the surface. As temperature decreases, both devices exhibit increased R_{shunt} due to partially deactivated surface defect DOS at lower temperatures. This phenomenon is more pronounced with the passivated device, as R_{shunt} increases more than four orders of magnitude.

B. Trap-assisted tunneling R_{TAT}

At relative higher temperature (above 200 K), the non-passivated and passivated devices show similar R_{TAT}. As temperature further decreases, the non-passivated device shows almost unchanged R_{TAT}, while the passivated device shows increased R_{TAT} about one order of magnitude. This can be interpreted as following: at relatively high temperatures, the TAT current from bulk is dominant, leading to the similar R_{TAT} of non-passivated and passivated devices. At lower temperatures, particular below 100 K, the TAT current from the surface is dominant. Since the passivation reduces surface trap DOS, the passivated device shows increased R_{TAT}.

The effective trap energy E_t was also extracted. Figure 5.18 plots the temperature-dependent ratio of E_t/E_g (since E_g increases as temperature decreases). For non-passivated device, E_t/E_g shows monotonous increases as temperature decreases. For passivated device, E_t/E_g shows two clear levels at lower temperatures: 0.3 below 100 K, and 0.25 at 200~250 K (annotated as regions I and II in Fig. 5.18). Since DOS at surfaces is significantly reduced by passivation and deactivation at lower temperatures, the two clear energy levels of $0.25E_g$ and $0.3E_g$ may indicate two possible bulk trap energy levels.

C. Generation-recombination R_{g-r}

At each temperature, the passivated device shows two orders of magnitude higher R_{g-r} than that of the non-passivated device, which is due to that passivation reduces the number of G-R centers at the surface. As temperature decreases, both devices exhibit dramatically increased R_{g-r} since some G-R centers are deactivated at lower temperatures.

D. Band-to-band tunneling R_{BBT}

Since the band-to-band tunneling mainly occurs in bulk, there is no significant difference between non-passivated and passivated devices. As reverse bias increases, the R_{BBT} decreases due to the enhanced BBT process.

E. Diffusion R_{diff}

The diffusion current dominates at the forward bias. There is no significant difference between non-passivated and passivated devices.
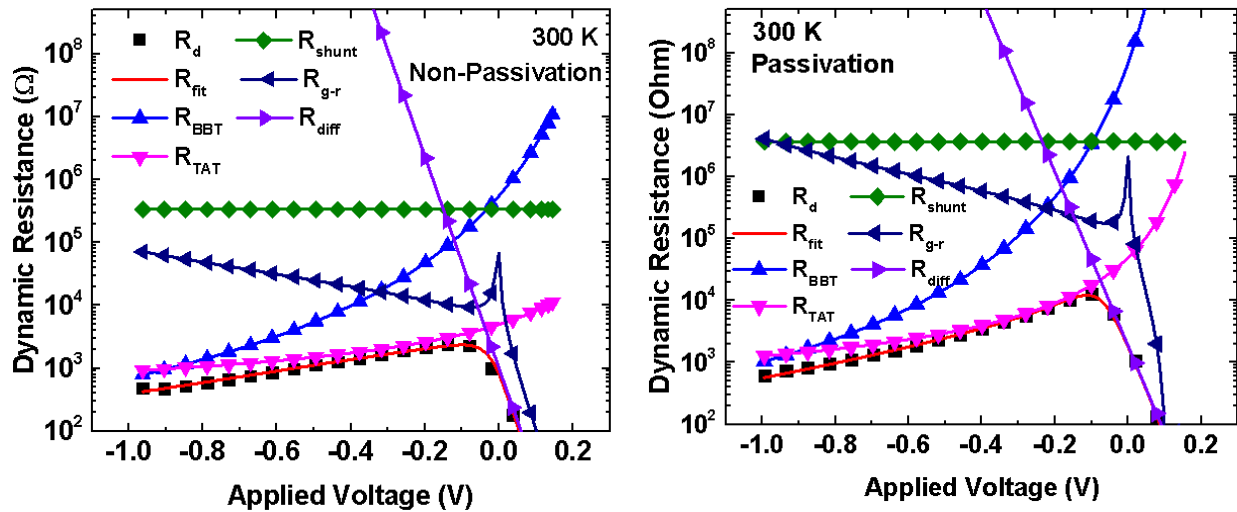
Figure 5.17 Fitted dynamic resistance of non-passivated and passivated devices at temperatures from 300 to 40 K [58].
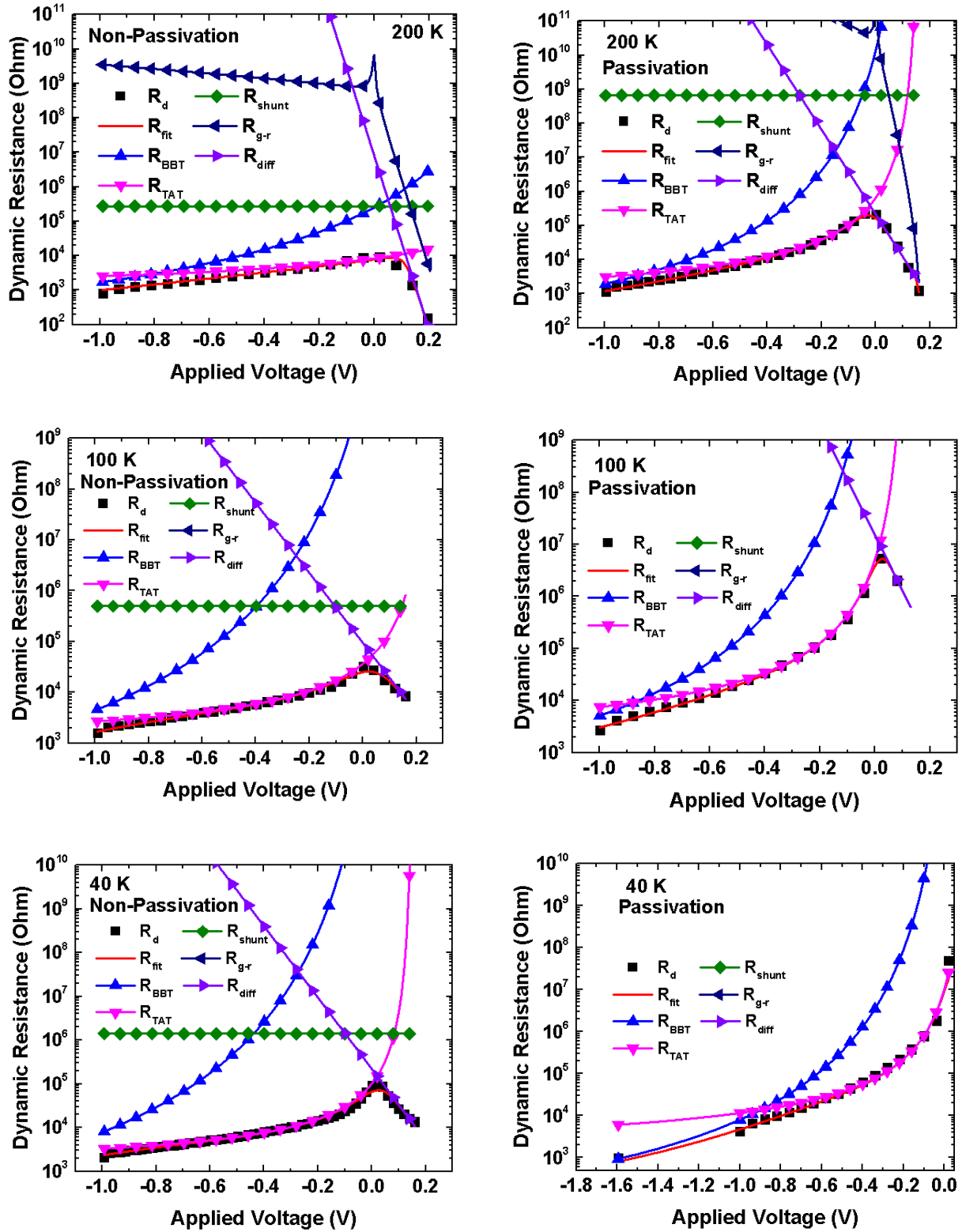
Figure 5.17 (Cont.)

The characteristic parameters such as E_t, N_t, and E_{g-r} as a function of the temperature for the devices with and without passivation, as shown in Fig. 5.18, 5.19, and 5.20, respectively, are extracted from the fitting of dynamic resistances. Figure 5.18 (a) shows temperature-dependent effective trap energy, and then the ratio of E_t/E_g is replotted versus temperature, as shown in Fig. 5.18 (b). For device with passivation, there are two distinct regions: 0.3 E_g from 40 K to 180 K and 0.25 E_g from 200 K to 260 K. Moreover, Fig. 5.19 (a) shows temperature-dependent effective trap density, and Fig. 5.19 (b) plots the effective trap density versus the E_t/E_g ratio. For device with passivation and in each region, the trap densities also show small variance such as: in region I, the trap density ranges from 1×10^{18} to 2×10^{18} cm^{-3}, and in region II, the trap density is around 5×10^{17}. Therefore, it is possible to consider that GeSn bulk has two characteristic trap levels. However, the device without passivation behaves differently compared with the passivated one. There are no distinct regions for trap energy and trap density as temperature changes. As temperature increases, the trapped energy reduces, and the trap density is not monotonously increased. The trap density is continuously distributed in the energy gap of GeSn. Figure 5.20 shows the TAT mechanism (a) inside bulk and (b) on the surface. Note that the trap density on the surface is likely to be continuously distributed in the energy gap. It is possible to consider that the TAT mechanism of the device with passivation happens inside bulk, while the un-passivated device's TAT current likely happens on the surface. Figure 5.21 shows the effective R-G energy levels versus temperature. As temperature increases, the effective R-G energy levels move from shallow levels to deep levels. In fact, at high temperatures, with the assistance of thermal energy, the trapping rate of the carrier likely equals the de-trapping rate at the shallow levels, so the shallow levels are not effective as R-G centers. Also, there is a difference between the R-G centers of the passivated and un-passivated devices in the range of

260 K to 300 K. At high temperature, the effective R-G centers are likely on the surface rather than bulk.
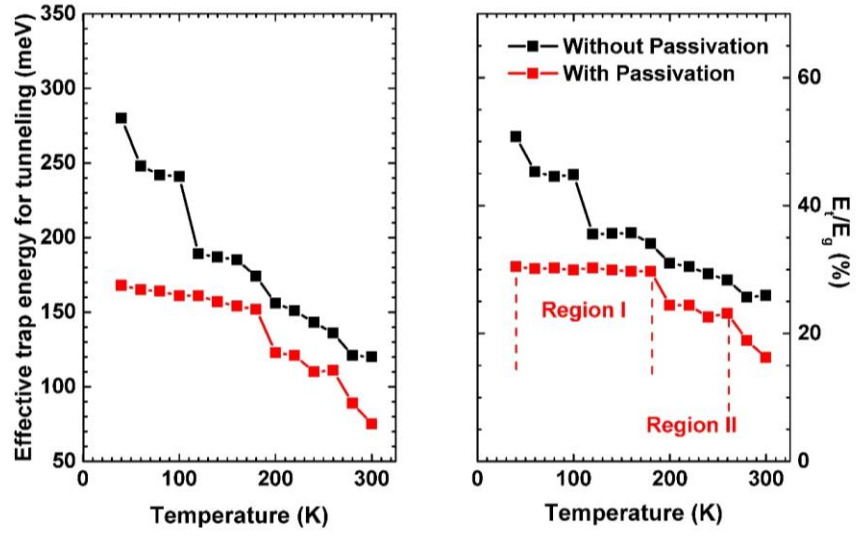
Figure 5.18 (a) Temperature-dependent effective trap energy for TAT current and (b) temperature-dependent E_t/E_g ratio. For the device with passivation, two distinct regions of temperatures were observed. In each region, the ratio is slightly dependent on temperatures.
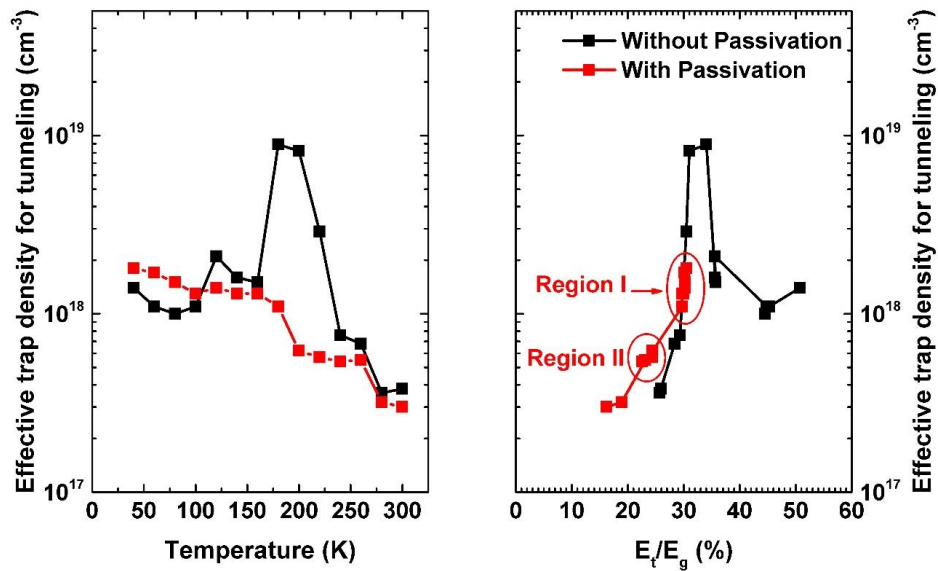
Figure 5.19 (a) Temperature-dependent effective trap density for TAT current and (b) effective trap density for TAT current versus the E_t/E_g ratio. For each region that has the stable E_t/E_g ratio, the effective trap densities show a small variance.

128
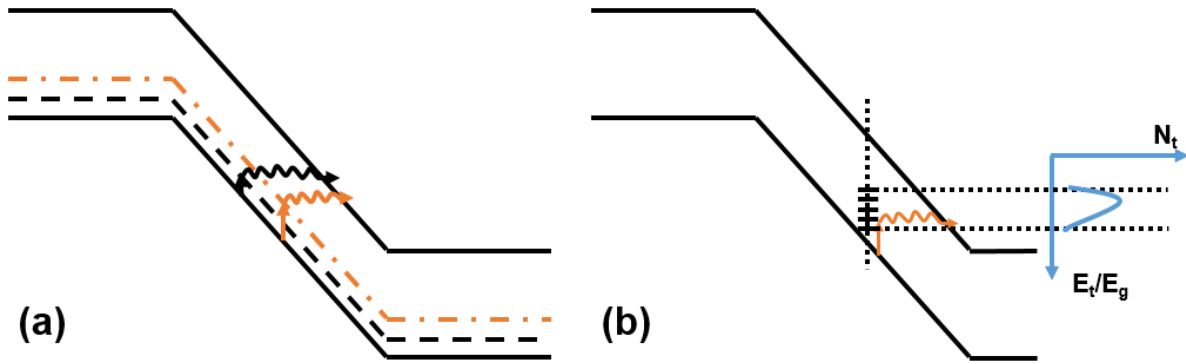
Figure 5.20 Band diagram with TAT mechanism (a) in bulk and (b) on the surface.
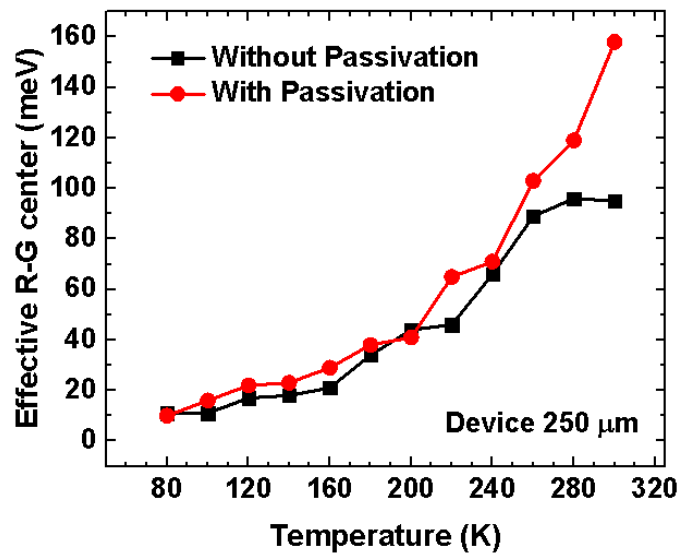
Figure 5.21 Temperature-dependent effective R-G center.

5.4.2.3. Silvaco simulation with TAT and series resistance effects

As above mentioned, when the Silvaco simulation is presented with SRH recombination and surface recombination effects, the dark current is still smaller than that in the real GeSn detector. Hence, the TAT and series resistance effects are added to the models of the device. In Silvaco, there are several models of the TAT effect, but based on the data fitting that is obtained from real dark current, the TAT model below is used:

$$G - R = \frac{Q^3 m_0 m^* F M^2 N_t G_t}{8 \pi \hbar^3 (E_g - E_t)} exp \left(-\frac{4 \sqrt{2 m_0 m^* (E_g - E_t)^3}}{3 Q \hbar F} \right)$$ (5.4.8)

where F is the magnitude of the local electric field; m^* is the effective mass; E_g is the bandgap; N_t is the trap density, and G_t is the trap degeneracy. The factor M^2 is the square of the matrix element associated with the trap potential. The Eq. (5.4.8) is similar to the equation that is used above as the TAT mechanism in the dark current fitting process. Hence, it is direct to input the values from the fitting process to the Silvaco model. There are 3 parameters for the TAT model in Silvaco such as JTAT.LEVEL, which is the trap level relative to the midgap energy, JTAT.M2, which is the square of the matrix element, and JTAT.DENSITY, which is the trap density. Those parameters are obtained from the fitting process. For the series resistance effect, there are two syntaxes such as CON.RESIST ($\Omega \cdot cm^2$), which specifies a distributed contact resistance and RESISTANCE ($\Omega \cdot \mu m$), which specifies a lumped resistance value. Keep in my that they may not be used together. Figure 5.23 shows the current density of three distinct models such as Model I, which only considers SRH and surface recombination, Model II, which adds series resistance effect on top of those two mechanisms, and Model III, which adds TAT effect. The series resistance effect shifts the turn-on voltage closer to zero, and it also decreases the forward current, but it does not affect the magnitude of the reverse current. The TAT effect brings the current close to the level of the current of the real GeSn diode.
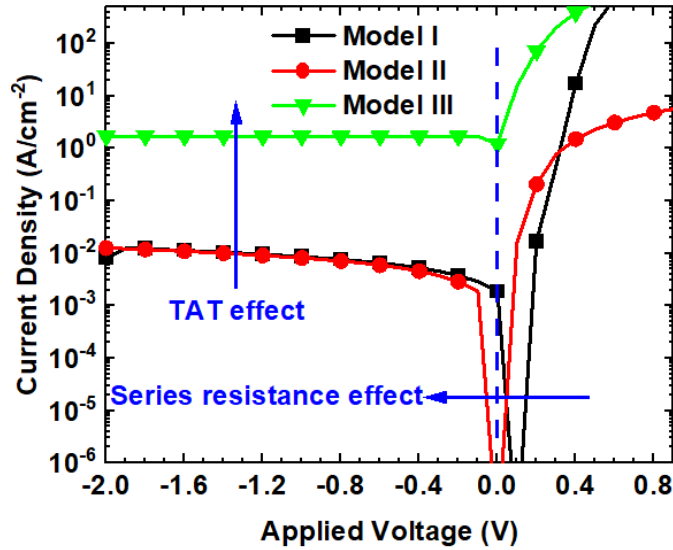
Figure 5.22 *IV* characteristics of three different models showing TAT and series resistance effects.

5.4.3. Future study

- To increase the range of the detection, it is necessary to have more Sn incorporation in the active layer of the GeSn photodiode.

- The heterojunction can be used with GeSn layer sandwiching between SiGeSn layer to reduce dislocations of material growth by engineering SiGeSn materials to achieve lattice-match growth.

- For modeling, it is necessary to define the sidewall portion of the device with uniformly distributed traps to succeed in modeling the forward bias.

- Design materials to achieve k-space charge separation.

Chapter 6.   Imaging system

6.1. Optical path and circuit design

The imaging system was established and further improved to obtain the infrared images from a single-pixel along with a 1D array. The current imaging system is shown in Fig. 6.1 (a), which includes a white light source, focus lenses, 3D stage for scanning, filters to block all visible light only allowing infrared light to pass. The white light spectrum spans from 300 nm to 2400 nm. The focus lenses have the focal length F = 7.5 cm, and the object plate was located between F and 2F in order to obtain the real image and larger for image dimensions. In order to prevent image distortion, the Brewster angle between the incident ray and the reflected light was kept being small. The device under tests (DUT) such as a single detector or a detector array was mounted inside the cryostat held on the 3D stage. The x- and y- stages were in-plane scanned to obtain the object's image, and the z stage was used to find the focus point. Figure 6.1 (b) and (c) show scanned steps of 3D stages for the single photodetector and the arrays, respectively. For the single photodetector, the scanned step of the x-direction is 500 µm, and the step of the y-direction is 500 µm. For the arrays, the scanned step of the x-direction is 100 µm, while the step of the y-direction is 2 mm. In fact, the scanned steps were determined by the dimensions of the devices. The photocurrent of the single detector was collected with/without the lock-in amplifier while the photocurrent of the detector array was collected by the readout circuit consisting of 16-channel data acquisition (DAQ).
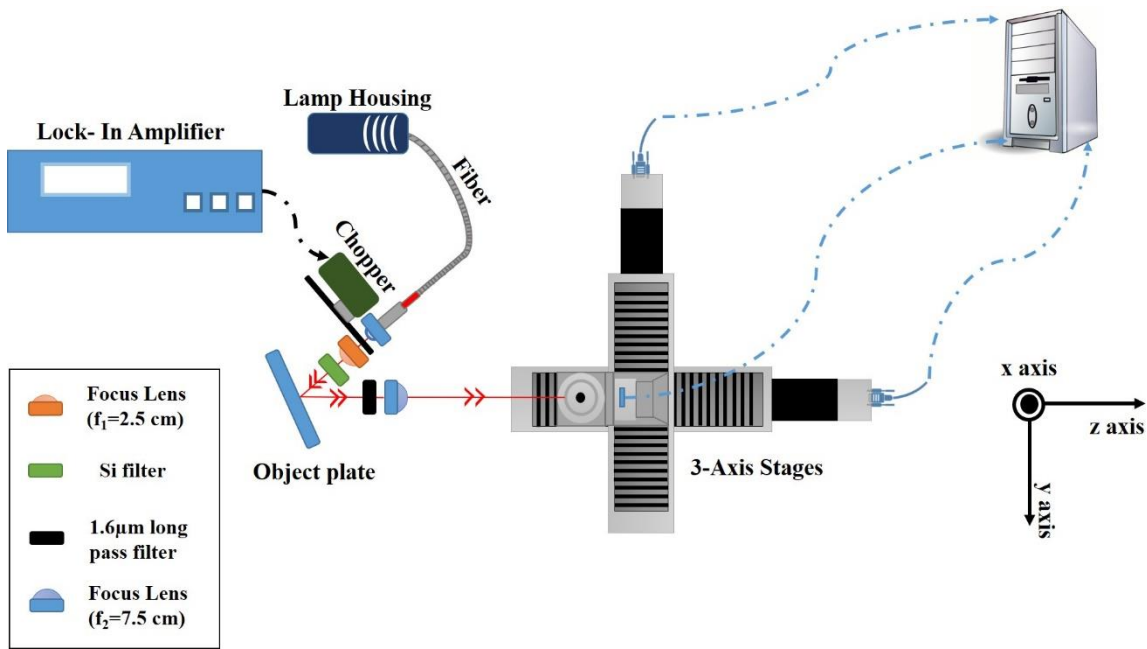
(a)
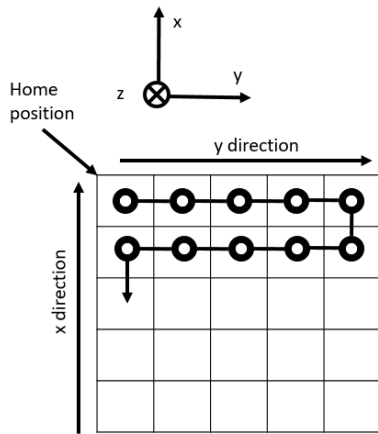
(b)
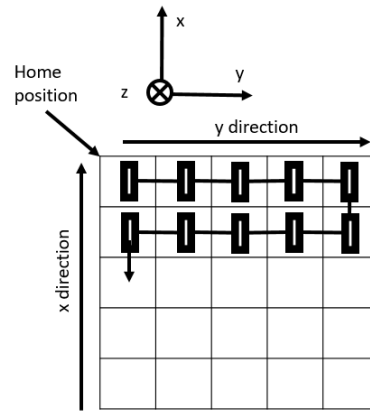
(c)

Figure 6.1 (a) The top view of the imaging system using single detectors and detector arrays. In-plane scanning using x- and y- stages (b) for the single photodetector and (c) for the arrays

Unlike the single photoconductor, the change of current in each pixel of a photodetector array as it was illuminated is collected by an external readout circuit as a substitute for the lock-in amplifier technique. The 16-channel National Instrument data acquisition (DAQ) was

employed in our imaging system. It is necessary to have a basic differential op-amp with a gain

of 10 for each channel because the DAQ has a minimum detection voltage of 300 µV and a total

applied voltage of +/- 10 V. Figure 6.2 shows the schematic diagram of the readout circuit for

the ith channel. The covered device has a similar mesa size as DUT, and its top contact caps the

device to avoid incident light absorption, so it only collects dark current. Then, the collected

dark voltage V_{i2} is subtracted from the illuminated i^{th} device's voltage V_{i1} to obtain the V_{out},

which is fed to the ith channel of the DAQ.
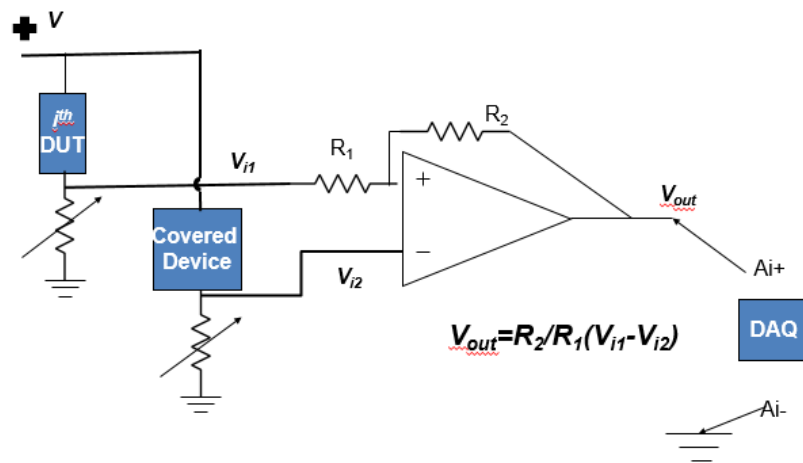
Figure 6.2 The schematic diagram of the readout circuit for the ith channel.

6.2. Device Fabrication

First, the photoconductor array was designed as shown in Fig. 6.3. Figure 6.3 (a) and (b)

correspondingly illustrate the layout of the 1D photoconductor array and the zoom-in layout of

the array. Green patterns represent metal pads, and red shapes are mesas of the pixels. Blue

patterns are opened-oxide regions. The layout includes two arrays at the center and 6 covered

devices at the corners. As abovementioned, the covered device was used to collect dark current.

The photocurrent from each pixel will be collected by subtracting the dark current of the covered

device from the current of the illuminated pixel as mentioned above. Only one of the two arrays

and only one of the covered devices were used, and the others are reserved. Each pixel has an area of 100×100 µm^2 with two contacts on top of its mesa. Each pixel has one contact connecting to the common pin as shown in Fig. 6.3 (b). It is necessary to design the common pin for the 16-pixel array as a purpose to adapt the standard chip carrier, which has 24 pins. Moreover, the distance between two adjacent pixels is either 20 or 10 µm.

(a)   **(b)**
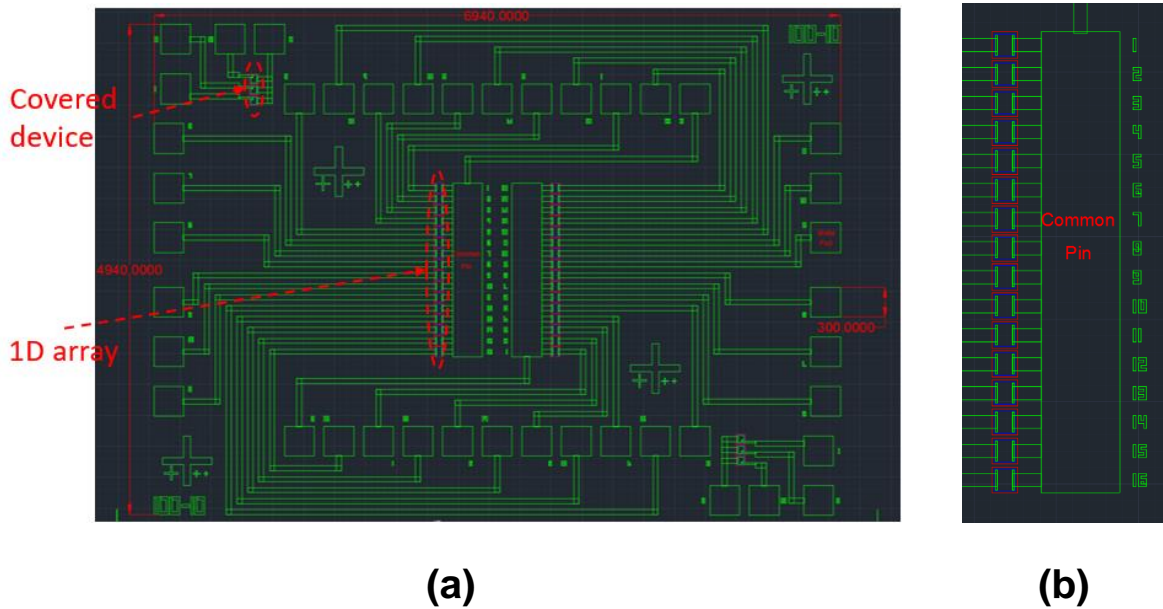
Figure 6.3 (a) The layout of the 1D photoconductor array. Green patterns represent metal pads. (b) The zoom-in layout of the array. Red shapes represent the mesas of the pixels. Blue patterns determine the opened-oxide regions.

Second, two GeSn bulk samples (0108-ASM and 0129-ASM) were fabricated into an array by photolithography and wet chemical etch processes. As demonstrated in Chapter 4, the 0108-ASM (11 % Sn) has the highest responsivity, while 0129-ASM (20 % Sn) has the longest cutoff wavelength. Hence, they are chosen as candidates for arrays to obtain infrared images. The mesa structures with an area of 100×100 µm^2 were etched by using the solution of HCl: H_2O_2: H_2O = 1:1:10 at 0^0C. A stable etching rate of 20 nm/min at low temperature regardless of Sn composition was observed. The etching depth was controlled to be around

135

1700 nm to reach the Si substrate for the elimination of connection between pixels, which helps to reduce crosstalk between the pixels. The etching depth was then evaluated. Because of the limitation of the wet etching process, the array with a 10 µm distance between two neighboring pixels shows that the etching process could not reach to Si substrate, while the array with a 20 µm distance between two neighboring pixels could isolate each pixel. A 300-nm-thick SiO_2 passivation layer was then deposited by an electron beam (e-beam) evaporator. There is a challenge for SiO_2 deposition using an e-beam evaporator. It would be necessary to heat substrates with optimized temperature to achieve high-quality SiO_2 deposition. However, SiO_2 deposition on our sample has to be performed without heating substrates. Therefore, to achieve reasonably good quality deposition, the e-beam current needs to be monitored very precisely to maintain a constant deposition rate. Otherwise, the deposition would fail. Moreover, the SiO_2 source, which was formed by SiO_2 crystals, the e-beam needs to be moved around several spots to avoid penetrating the crucible. The deposition rate will change during the movement of the e-beam, which also affects the film quality. After the SiO_2 deposition, the sample's temperature was higher than room temperature because of evaporation and therefore it was cooled down to room temperature before any further process. The SiO_2 was patterned and opened at some regions for the metal contacts. Electrode pads were patterned and metalized with 10/300 nm of Cr/Au.

Next, the fabricated devices were on-wafer tested at room temperature. The dark current of the pixel of the sample 0108-ASM is about 3.1 mA at 5V, and the dark current of the sample 0129-ASM is about 9.1 mA. Each pixel was tested, and the blocks with high performance were selected. The samples were diced. The diced pieces were then mounted on

the chip carriers using nonconductive silver paste and were wire-bonded for low-temperature imaging.
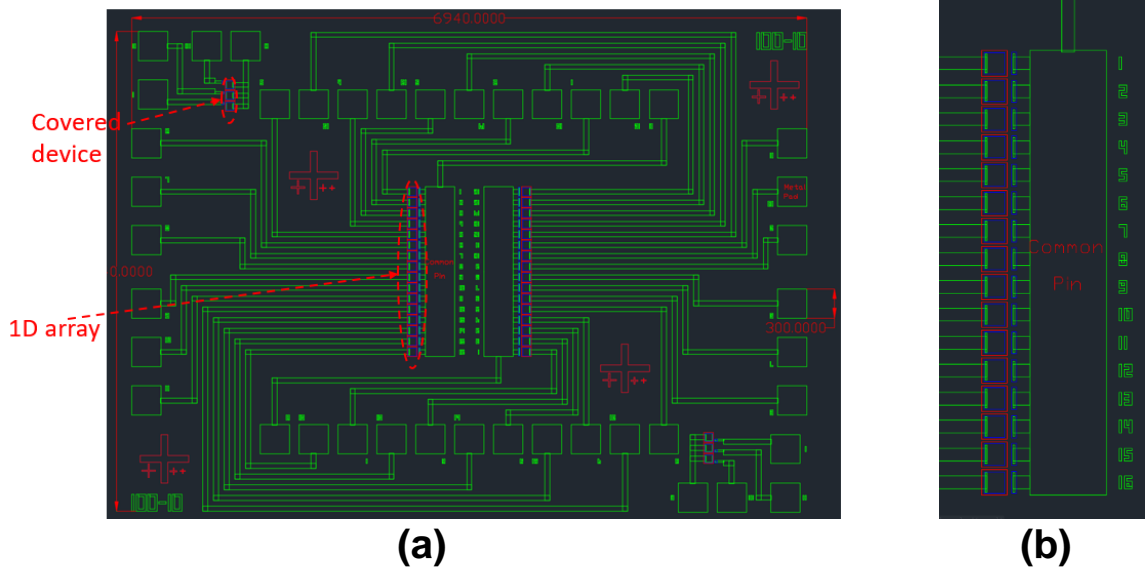
Figure 6.4 (a) The layout of the 1D photodiode array. Green patterns represent metal pads. (b) The zoom-in layout of the array. Red shapes represent the mesas of the pixels. Blue patterns determine the opened-oxide regions.

The photodiode array design is shown in Fig. 6.4. Figure 6.4 (a) and (b) show the layout of the 1D photodiode array and the zoom-in layout, respectively. Green patterns represent metal pads, and red shapes are mesas of the pixels. Blue patterns are opened-oxide regions. The layout includes two arrays at the center and 6 covered devices at the corners. Only one of the two arrays and only one of the covered devices were used, and the others are reserved. Each pixel has an area of 100×100 μm^2 with two contacts, and only one contact is on the mesa. The other contact, which does not lie on top of the mesa, connects to the common pin (as shown in Fig. 6.4 (b)). Moreover, the distance between two adjacent pixels is either 20 or 10 μm. The fabrication process is similar to that of the photoconductor arrays. However, the etch depth is around 700 nm to expose the p-type Ge layer for metal contact. The fabricated devices were on-wafer tested at room temperature. The dark current of the pixel of the sample 0123-ASM is about 0.13 mA at 0.1V. Each pixel was tested, and the blocks with high performance were

137

selected. The samples were diced. The diced pieces were then mounted on the chip carriers using nonconductive silver paste and were wire-bonded for low-temperature imaging.

6.3. Demonstration of mid-infrared imaging

Table 6.1 Summary of imaging work and results.

| Sample ID | Single detector imaging | | | | Array imaging | |
| | 77 K | | 300 K | | 77 K | 300 K |
	With lock-in amplifier	Without lock-in amplifier	With lock-in amplifier	Without lock-in amplifier	DAQ	DAQ
0108-ASM	√	√	No Image	No Image	√	No Image
0129-ASM	√	√	No Image	No Image	√	No Image
0123-ASM	√	No Image	√	No Image	No Image	No Image
0123-ASM (passivation)	√	No Image	√	No Image	Device not available	Device not available

The imaging measurement work of four samples (photoconductors of the samples 0108-ASM and 0129-ASM and the photodiodes of sample 0123-ASM with and without passivation) has been conducted extensively. The object used for our experiment is a golden star as shown in Fig. 6.5 (a). The imaging results are summarized in Table 6.1. With the lock-in amplifier, the images were obtained from all four single detectors at 77 K, but without a lock-in amplifier, only two photoconductors can give the images. At 300 K, only two photodiodes with and without passivation can give the images using a lock-in amplifier while in other cases, there was no

image output.   For the detector arrays, only two photoconductor arrays can give the images at 77 K while in other cases, there was no image output. Such initial image results are consistent with the detector performance summarized above. In addition, a 32 by 32 PbSe commercial camera was used to capture the image at room temperature for comparison and guidelines to our imaging work development.

All images obtained using the single detector and the detector array are shown in Fig. 6.5. In Fig. 6.5 (b) and (f), the images captured at 300 K by the PbSe commercial camera and the single passivated photodiode are shown, respectively.   The image from the passivated photodiode looks better just because the lock-in technique was used, which eliminated noise. Theoretically, the quality of the images from this photodiode and the PbSe camera would be similar or comparable. At 77 K, the image from the photoconductor of the sample 0108-ASM as shown in Fig. 6.5 (g) is brighter than that from the photodiode with and without passivation shown in Fig. 6.5 (e) and (c), respectively, because the responsivity of the photoconductor is much higher than that of the photodiode. The image from the detector arrays shows the stitching problem which probably came from the ununiformed pixels. One way to solve the stitching problem could be using advanced post-imaging processing, which would be explored in the future.

Figure 6.6 shows infrared images of some other objects including a coin and a barcode, which were taken by the passivated photodiode and the PbSe detector at 300 K. The images taken from the GeSn photodiode exhibit clearer features comparing with the PbSe detector. In fact, the power of the reflected light depends on the materials of the testing objects. The golden star was made by a material that reflects the infrared light well, while the bar code was not. The image becomes blurry even with the PbSe detector. Moreover, the coin can represent the 3D

object as the head has z-dimension. Another 3D object made by plastic was also captured by a single photoconductor (0108-ASM) at 77 K without a lock-in amplifier, and the result was shown in Fig. 6.7.
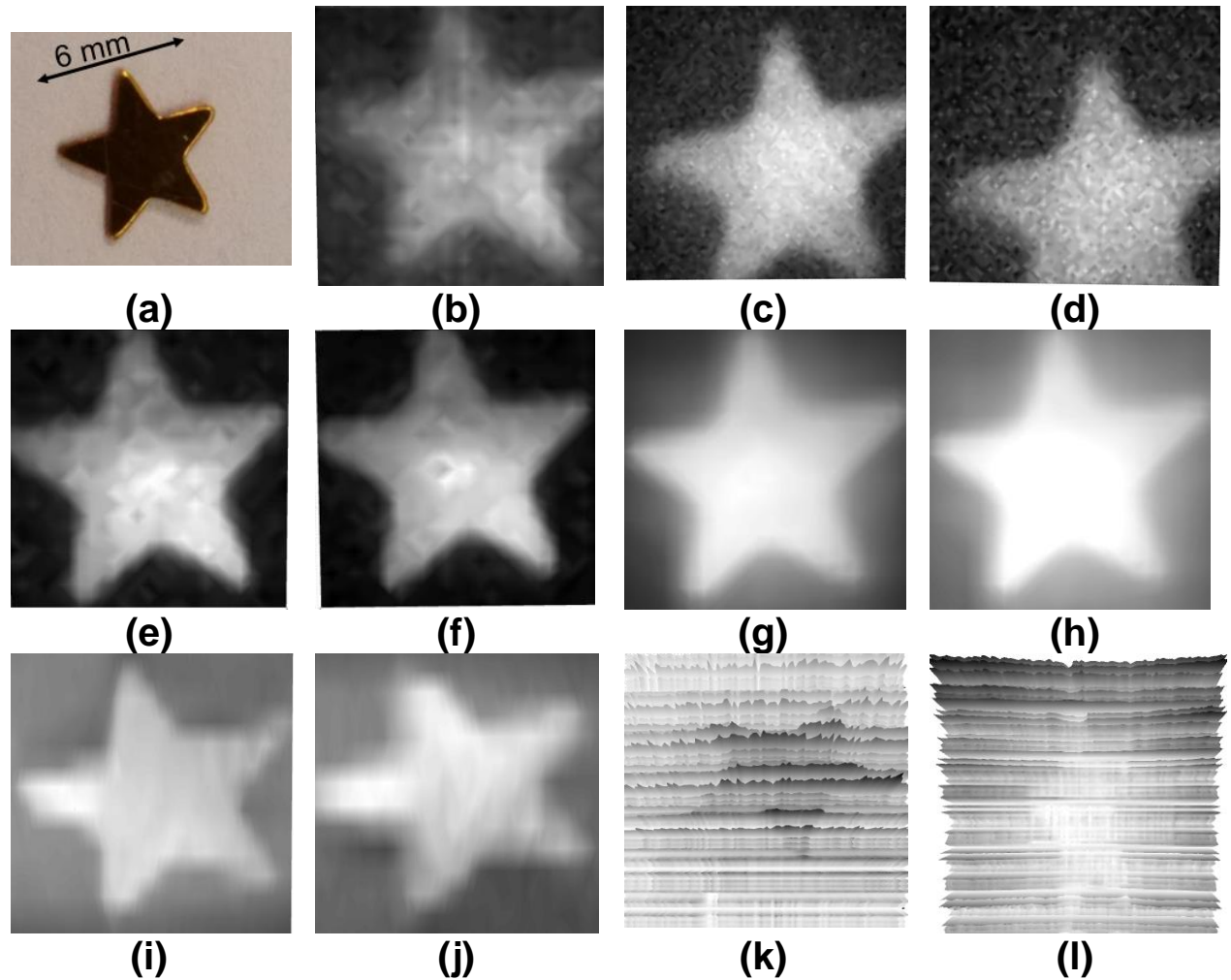
Figure 6.5 Images of the golden star object taken by (a) a camera under room light; (b) PbSe commercial camera at 300 K; single photodiode (0123-ASM) (c) at 77 K and (d) at 300 K with lock-in amplifier; single photodiode with GeON passivation (0123-ASM) (e) at 77K and (f) at 300 K with the lock-in amplifier; single photoconductor (0108-ASM) at 77 K (g) with lock-in amplifier and (h) without the lock-in amplifier; single photoconductor (0129-ASM) at 77 K (i) with lock-in amplifier and (j) without the lock-in amplifier; (k) photoconductor array (0108-ASM) at 77 K; (l) photoconductor array (0129-ASM) at 77 K

Objects

Passivated Photodiode

PbSe Single Detector
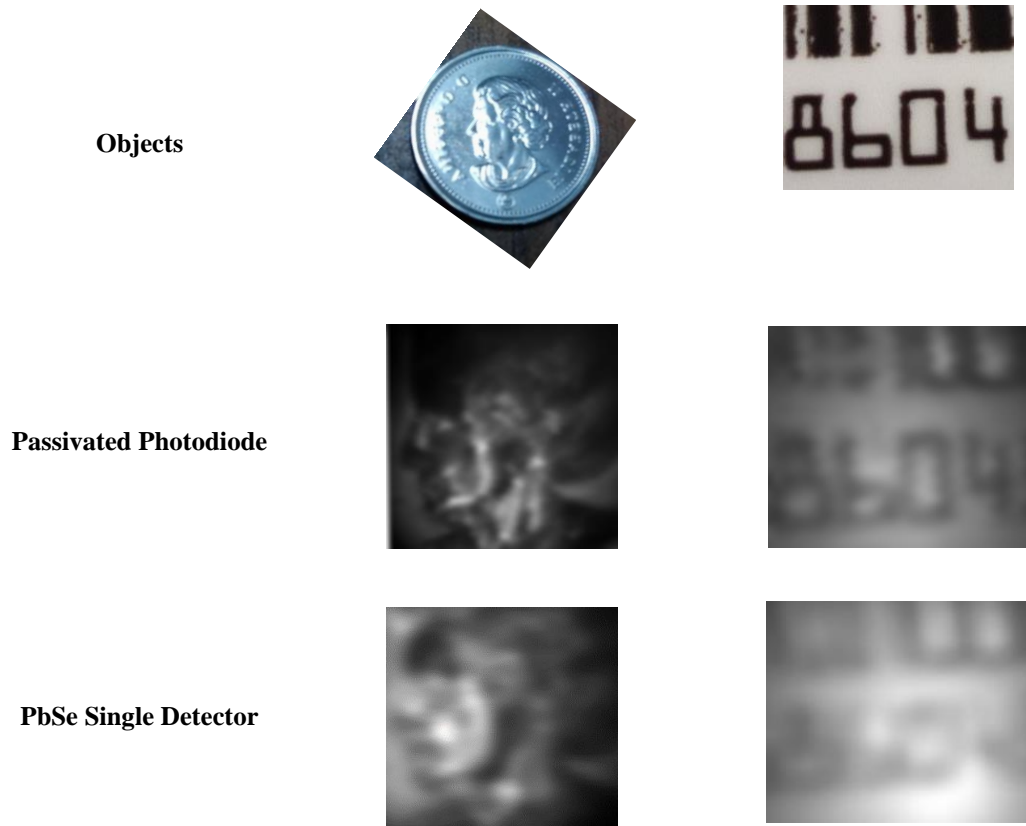
Figure 6.6 Infrared results from the passivated photodiode and the commercial PbSe single detector at 300 K.
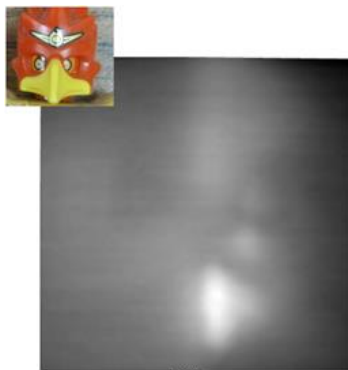
Figure 6.7 The image for the 3D object using 0108-ASM photoconductor at 77 K without lock-in amplifier

As a result, this chapter demonstrates the setup of the imaging system including the electrical

readout circuit and optical path. Several objects from 2D to 3D were captured by the GeSn

photodetectors and arrays. The infrared images taken by the GeSn photodetectors and arrays show comparable quality with those depicted by the commercial PbSe single detector and PbSe camera. The demonstration of the imaging system illustrates that the GeSn detectors can be nominees for commercialization along with the direction of low-cost IR cameras.

Chapter 7.   Systematic study of high-speed GeSn photodiodes

7.1. Motivation

Before 1985, the only photonic chip that could interface to fiber in fiber-optic communications was the III-V semiconductor chip. In 1986, Soref invented a silicon-on-insulator waveguide, which has become the mainstream approach for the silicon photonics industry. Over the past several decades, Si-based photonics has been developing through large-scale manufacture based on optoelectronic components directly integrated on Si substrates. Many materials have been researched for large-scale photonic integration such as group III-V semiconductors as well as group IV materials. Silicon-germanium-tin materials offer strong potential in standard telecommunications and the mid-infrared bands. Photodetectors (PDs) are the key element in the system receiver chain. Many GeSn-based photodetectors have been developed over the decade to extend cut-off wavelength to mid-infrared and to enhance the performances. However, the high-speed GeSn photodetectors are mentioned in only a few reports. It is needed to understand the prospect of GeSn detectors as high-speed components in the mid-infrared ranges. In addition, the GeSn-based PDs with the peak responsivity and detectivity which were in the same order as the market-dominating Ge and InGaAs PDs show a promising future. That success was based on the newly developed growth technique to produce a fully relaxed high-quality thick GeSn layer on top of thick Ge buffer that provides a structure with reduced defect-related nonradiative recombination loss. In this chapter, the high-speed characteristics of the GeSn detectors will be analyzed from simulation to fabricated devices. The comparison between the simulation and the measured results will also be presented to show an agreement. Furthermore, smaller dimension devices and waveguide devices will be studied to

143

show achievements of bandwidth to beyond 10 GHz and of detections up to 2 to 3 µm wavelength range.

7.2.High-speed detectors

7.2.1. Theoretical study

Because of low-pass or delay mechanisms, which come from the device capacitance and the effect of the transit time that photocarriers experience before being collected, the output current does not follow its instantaneous value when the input power varies too rapidly. Hence, the photodetectors' bandwidths define their performances, and the frequency domain responsivity is typically low-pass. Table 7.1 was established to compare and then define which structures of photodetectors are suitable for high-speed applications.

Table 7.1 A comparison between different structures of photodetectors
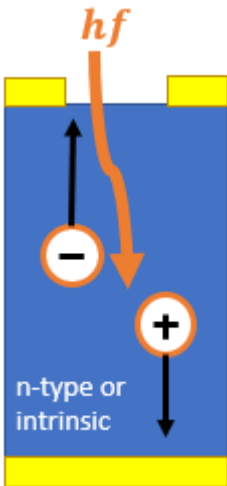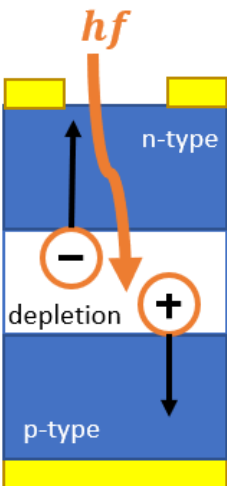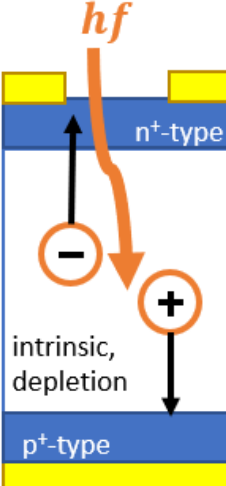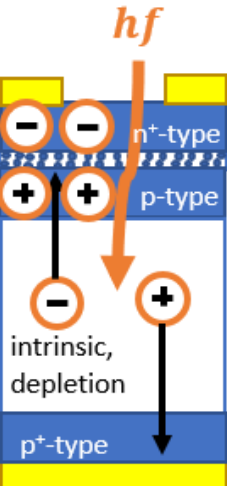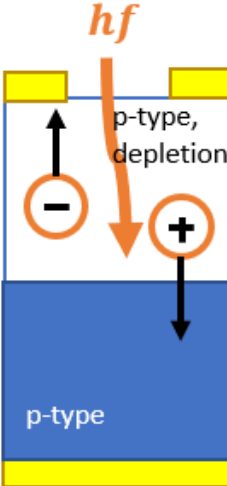
	Photoconductors	*pn* photodiodes	*pin* photodiodes	APD	Schottky
Structure					
Photocarrier generation mechanism	• Resistive region	• The small width of the depletion region	• A large intrinsic region sandwiched between high-doped layers • The width of the intrinsic layer: large enough regarding the absorption length to have the related photocurrent contribution dominant over the photocurrent from the diffusion regions	• the structure is a *pin* diode to which an additional *pn* junction has been added with a highly doped *n* side • Photogenerated electrons in the intrinsic layer are removed to the high-field region associated with the $n+$ p junction depletion layer and,	• the operation is similar to that of *pn* or *pin* diodes • photogeneration mechanism is introduced by carriers photoexcited from the metal into the semiconductor

Table 7.1 (Cont.)

	Photoconductors	*pn* photodiodes	*pin* photodiodes	APD	Schottky
Photocarrier generation mechanism (Cont.)				undergo avalanche multiplication	
Advantages	• Simple • High gain	• Dark current: small	• Dark current: small • PiN heterostructure devices: the doped layers are widegap and do not absorb light altogether at the operating wavelength	• The increase in responsivity	• Simple
Disadvantages	• Bandwidth is limited by photocarrier lifetime • Dark current: high but can be capacitively decoupled • Thermal noise: large • Low speed	• Photon is absorbed in the adjacent diffusion regions, leading to poor frequency response, limited by transit time and lifetime • RC capacitive effects • Shot noise	• Frequency response is limited by transit time and RC effects • Shot noise • Unit gain • Sensitivity is not outstanding	• increased noise (multiplied shot noise and excess noise) and a reduction of bandwidth (due to the additional delay introduced by the avalanche buildup)	• the frequency response is often affected by slow tails, which make the device less appealing for high-speed applications

146

From the above comparison, the *pin* photodiode is a high-performance device, with achievable bandwidths in tenths of the GHz range. Hence, we will use the *PiN* heterostructure devices, whose doped layers are widegap Ge and do not absorb light altogether at the operating wavelength to study the high-speed applications in mid-infrared ranges. In order to define which materials such as direct or indirect-bandgap materials to be used to enhance absorption and also to optimize bandwidth, the below arguments are presented as a preliminary study.

To generate e-h pairs, the material absorption threshold must overlap the incident wavelengths. Both direct-bandgap (III-V or II-VI groups) and indirect-bandgap (Si, Ge) semiconductors can be exploited in PDs. Typically, the direct-bandgap semiconductors have higher absorption, which outcomes in a smaller absorption region and higher speed. In order to absorb the incident light completely, the detector's absorption region must have thickness d suitably larger than or equal to L_α (absorption length = $1/\alpha$). Because of higher absorption coefficients for direct-bandgap comparing with indirect-bandgap detectors, it is straightforward to observe that in a direct-bandgap material the thickness of the absorption region should be $d \approx 1\,\mu m$, while in indirect-bandgap materials $d \approx 100\,\mu m$. As the thickness increases, it is corresponding to a high transit time, which leads to the delay from the collection of the excited carriers. Hence, the indirect-bandgap detectors' speeds typically are limited. Moreover, the depletion region (also absorption regions for most of the devices) acts as a capacitor in RC cutoff. The capacitance is inversely proportional to the thickness of the depletion region ($C \propto d^{-1}$). Increasing the thickness d, the transit time-limited speed decreases, while the RC limited speed increases, which leads to the need for optimization. In direct-bandgap detectors, the optimization happens between transit time and RC cutoff, while indirect-bandgap detectors are typically limited by transit time.
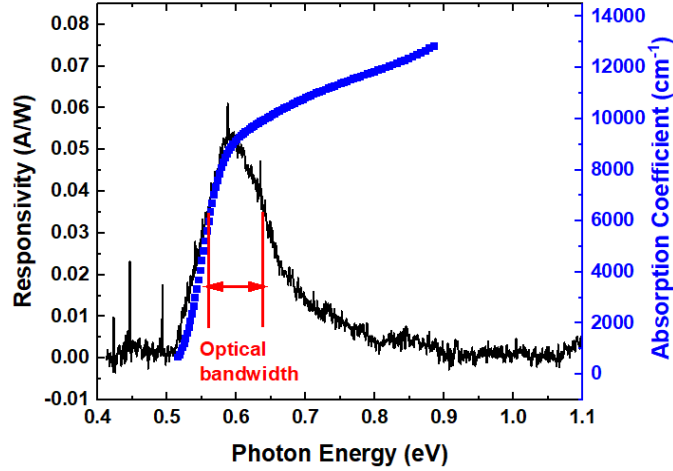
Figure 7.1 Absorption coefficient and responsivity versus the photon energy.

For photon energies below the absorption threshold, the responsivity is zero. For the photon energies above the bandgap, the responsivity ideally decreases with increasing photon energy as following:

$$\mathcal{R}(E_{ph}) \approx \mathcal{R}_{max} \frac{E_g}{E_{ph}} \qquad (7.2.1)$$

In fact, one physical standpoint to explain the decrease of responsivity as the photon energy increases is that the energy still generates just one e-h pair, and the extra energy is dissipated through phonon emission such as heat. Figure 7.1 shows the behavior of absorption coefficient and responsivity for the typical GeSn material. For energies close to the bandgap, the responsivity follows the absorption coefficient, and for higher energies, it decreases as explained. In practice, the number of excited carriers collected in the external circuit can be considerably lower than the number of incident photons, which leads to a responsivity smaller than the ideal value. In fact, the incident light has to endure many steps before efficiently converted into a photocurrent. First, the incident light is partially reflected at the PD surface due to dielectric mismatch. Second, part of the incident power is absorbed in regions where it does not contribute

to useful output. Third, part of the power is transmitted through the PD without being absorbed. As a result, the photocurrent is generated by the remained power.

To enhance the frequency response and efficiency, the depletion region width should be made much larger than the width of the diffusion region to make the diffusion photocurrent negligible. Moreover, it is necessary to balance between speed and responsivity because the device speed is dominated by transit time and the parasitic capacitance. In fact, four key mechanisms limit the speed of pin photodiodes under dynamic excitation:

- the total diode capacitance from the depleted region diode capacitance and any other external parasitic capacitance

- the transit time of the carriers drifting across the depletion layer

- for homojunction devices, the diffusion time of carriers generated outside the undepleted regions

- for heterojunction device, the charge trapping at heterojunctions

It is insignificant from transit time effects in *pn* junction photodiodes due to the small deletion width, but in *pin* devices, they become dominant. Transit time and RC cutoff are thus the main limitations in practical *pin* photodiodes. Moreover, the photoexcited carrier diffusion slower the device response. The diffusion current can be minimized in homojunction devices by heavily doped layers. For heterojunction detectors, the excited carriers can be trapped at heterojunctions, related to the valence and/or conduction band discontinuities there. Charge trapping can be optimized by creating a *Ppi* junction instead of *Pi* junction. In addition, for our thin diodes, the transit time-limited bandwidth can be quantitatively evaluated as:

$$f_{3dB,tr} = \frac{3.5\bar{v}}{2\pi W} \qquad (7.2.2)$$

149

where $\frac{1}{\bar{v}^4} = \frac{1}{2}\left(\frac{1}{v_{n,sat}^4} + \frac{1}{v_{p,sat}^4}\right)$. Furthermore, the 3dB RC-limited bandwidth is given by:

$$f_{3dB,RC} \approx \frac{1}{2\pi RC},$$ (7.2.3)

where $R \approx R_S + R_L, C \approx C_j + C_p, C_j = \frac{\varepsilon_s A}{W}$. The total cutoff frequency can be evaluated as:

$$f_{3dB} \approx \frac{1}{\sqrt{f_{3dB,RC}^{-2} + f_{3dB,tr}^{-2}}}$$ (7.2.4)

In a vertically illuminated photodiode, optimization of the external quantum efficiency suggests $W \gg L_\alpha = 1/\alpha$. However, as the active region thickness increase, the junction capacitance decreases, which increases the RC-limited bandwidth. Also, it decreases the transit time-limited bandwidth. Moreover, in order to enhance the coupling with the external source, the detection area A should be large. There is no influence on the transit time-limited bandwidth as the area increases, but it makes the capacitance larger and then decreases the RC-limited bandwidth. If the device area is kept constant, the RC-limited bandwidth is proportional to the thickness $(f_{3dB,RC} \propto W)$ but the transit time-limited bandwidth is inversely proportional to the thickness $(f_{3dB,tr} \propto 1/W)$. Since $f_{3dB} < min(f_{3dB,RC}, f_{3dB,tr})$, the total bandwidth is dominated by RC-limited bandwidth with low W, or by transit time-limited bandwidth with large W. The total bandwidth then first increases as a function of W, then decreases. As the device area decreases, the total bandwidth has a maximum, which shifts toward smaller values of W. At the same time, the efficiency always increases with W. As a result, the high-frequency operation requires small-area diodes, with small W and increasingly poor efficiency. Figure 7.2 shows the trade-off between speed and efficiency with an assumption of zero surface reflectivity and no parasitic capacitance. As shown in Fig. 7.2, the 40 GHz operation requires diodes with a

diameter as low as 10 μm, and with an absorption thickness layer of 1 μm, the efficiency is around 50 %.
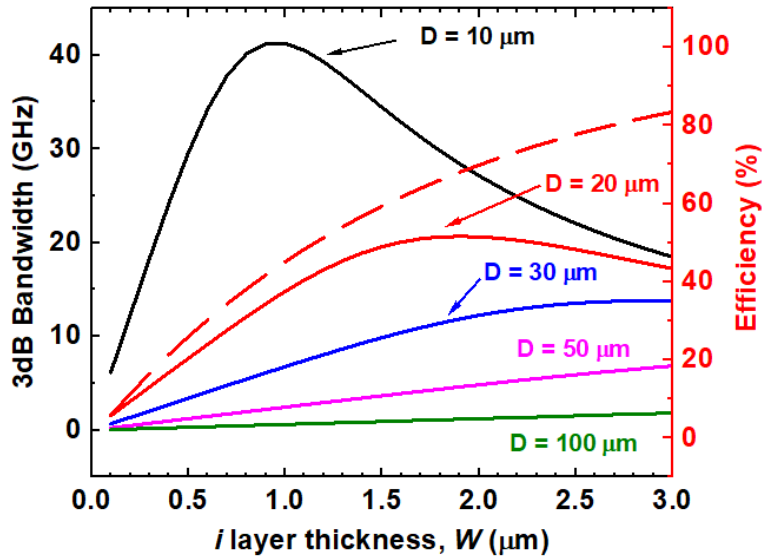
Figure 7.2 Trade-off between speed and efficiency for high-speed pin diode.

7.2.1. Simulation

All of the devices in this chapter were simulated using the commercial Silvaco with modular ATLAS. All structures were constructed using the ATLAS command language. Table 7.1 shows ATLAS command groups of statements that must occur in the correct order. Each composed file must contain these five groups in order. An error message and termination of the program or an incorrect operation of the program will happen if the order is not correct. Moreover, the order of statements is also important. The statement keyword must happen first, and then the order of parameters is not important. There are several numerical methods to calculate the solutions to the device problems. There are up to six equations to solve different combinations of models. For each model type, there are three solution techniques: (a) GUMMEL, (b) NEWTON, and (c) BLOCK. In the GUMMEL method, which is decoupled technique, each unknown is solved in turn keeping the other variables constant until a stable

solution is achieved. The NEWTON method, which is a fully coupled technique will solve the total system of unknowns together. The BLOCK method will solve some equations coupled and others decoupled. Because the Gummel method effectively solves the system of equations decoupled, it can be used to start a solution to generate a better guess and then switch to Newton, which requires a more accurate initial guess to obtain convergence. The syntax is executed as follows:

METHOD GUMMEL BLOCK NEWTON

Table 7.2 ATLAS command groups with the correct order.

Group	Statements
1. Structure specification	MESH REGION ELECTRODE DOPING
2. Material models specification	MATERIAL MODELS CONTACT INTERFACE
3. Numerical method selection	METHOD
4. Solution specification	LOG SOLVE LOAD SAVE
5. Results analysis	EXTRACT TONYPLOT

As a result, the specifications of structures, materials, and models will be presented in the sections below for device study.

7.3. Study of bandwidth of GeSn photodiodes

7.3.1. Surface illumination photodiodes with large mesas

7.3.1.1. Experimental Method

A. Growth and Fabrication

The GeSn double heterostructure (DHS) samples were grown using an industry-standard ASM Epsilon® 2000 Plus RPCVD with $SnCl_4$ and GeH_4 as Sn and Ge precursors, respectively. On Si substrate, a 750-nm-thick p-type (Boron as dopant) Ge was grown as a buffer. Then, a 200-nm-thick GeSn layer was grown with unintentionally dope. Lastly, a 50-nm-thick n-type (Arsenic as the dopant) Ge cap layer was grown. Because the GeSn layer has a background doping level of $1 \times 10^{17}\,cm^{-3}$, the doping concentrations at the Ge buffer and Ge cap layer were 5×10^{18} and $1 \times 10^{19}\,cm^{-3}$, respectively as attempting to create a junction. The X-ray diffraction (XRD) shows Sn compositions of 6.44% and 9.24%, corresponding to nominal 7 % and 10 % Sn, respectively.

The GeSn photodiodes were fabricated into circular mesa structures with diameters of 500, 250, and 100 μm by standard photolithography and then etched using a wet chemical etching process. The solution of HCl: H_2O_2: H_2O = 1:1:20 was used in the process at room temperature. A stable etching rate of 100 nm/min at room temperature regardless of Sn composition was observed. The mesas were etched until the p-type Ge buffer was reached. Because of the high doping levels of Ge cap and buffer, the Ohmic contacts were achieved. A 100-nm-thick SiO_2 passivation layer was then deposited by plasma-enhanced chemical vapor deposition to form an isolation layer and passivation as well. The oxide was opened to form the metal contacts. Electrode pads were patterned and metalized with 10/200 nm of Cr/Au. Figure 7.3 (a) shows the top-view scanning electron microscope (SEM) image. In Fig. 7.3 (a) inset, the schematic of the device cross-sectional view was plotted. The cross-sectional SEM image (as shown in Fig. 7.3 (b)) shows resolved Ge and GeSn layers, and it is obvious to observe the interface layers that trapped defects near GeSn/Ge and Ge/Si interfaces.
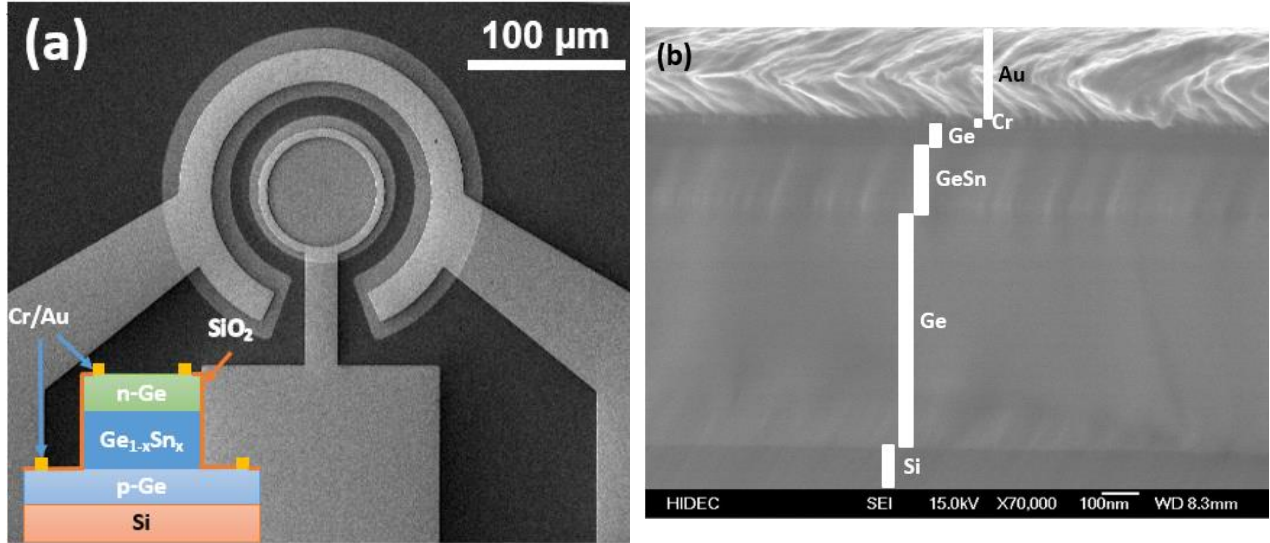
Figure 7.3 (a) The top-view SEM image of the typical device. (Inset) its cross-sectional view. (b) Cross-section SEM image [55].

B. Measurement

This chapter is to study the high-speed features of GeSn materials at room temperature, so the devices were characterized and simulated using material properties at room temperature. The *IV* characteristics were measured with Keithley 236 Source Measurement Unit. The spectral response of the devices was scanned using a Nicolet 8700 Fourier-transform infrared (FTIR) spectrometer at a bias of -2 V from 1.6 µm to 2.6 µm wavelength ranges. The devices' responsivity was illuminated under a 1.55 µm laser diode (Thorlabs ML925B45F), and the photocurrents were collected through a 50 Ω resistor using a lock-in amplifier (Stanford Research SR830) with a chopper at 380 Hz. The power of the light sources from the FTIR and the laser diode were calibrated using the pre-calibrated InGaAs and extended-InGaAs detectors under the same ambiance conditions.

For the high-frequency measurements, the detectors' electrical bandwidth and eye diagrams were performed. A 2 µm laser diode was fed to a fiber-coupled lithium niobate modulator (model MX-2000-LN-10) rated for 10 GHz, and the optical output illuminated the surface of the

154

detector via a lensed fiber. The modulator was connected to a network analyzer (N5225A-200) through port one using an RF probe. The electrical pads of the detector were contacted with an RF probe to collect photocurrent through a bias tee to port 2 of the network analyzer. The bias tee was used to allow a DC bias to be applied to the detector.

Figure 7.4 shows a 2 µm high-speed experiment to gather the eye diagrams. A fiber-coupled laser diode at a wavelength of 1.963 µm was used as a light source. A home-built thulium-doped optical fiber amplifier (TDFA) was used to boost input power before the LiNbO3 modulator. A polarization controller and PM2000 lensed fiber connected to the output of the modulator was used to vertically couple light into the device under test (DUT) mounted on a piezoelectric XYZ stage. The modulator was driven by a 1 Gbps bit pattern generator with an RF amplifier rated for up to 40 Gbps operation. The photodetector was interfaced with a 40 GHz RF probe with a ground-signal contact configuration. A picoseconds pulse labs model 5543 bias tee rated at 50 GHz was used to apply bias using a source meter. The AC signal was sent to a digital communications analyzer with electrical input rated for 80 GHz.
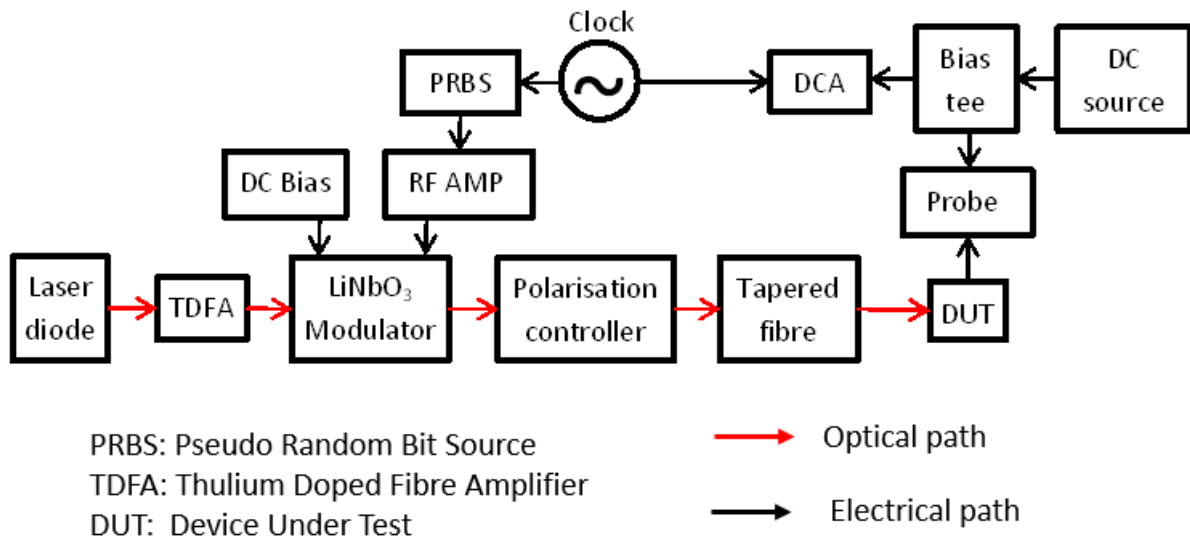
Figure 7.4 A schematic of the experimental setup to obtain eye diagrams at 2 µm [55].

7.3.1.2. Simulation

The three basic semiconductor equations such as Poisson, carrier continuity, and transport equations were solved using the commercial Silvaco software with Atlas simulator. In order to save time and memory consumptions, a pseudo-3D method which assumes that the devices have cylindrical geometry and symmetry by defining cylindrical mesh was used to form the meshes of the detectors. For GeSn materials, the bandgap, effective density of states, and intrinsic carrier concentration were modified from the default Ge materials. The drift-diffusion transport model was used with field-dependent mobility. The Shockley-Read-Hall (SRH) recombination model was used with electron and hole lifetimes of 1 ns. Surface recombination on the devices' surfaces and sidewalls was considered with the recombination velocities of 10^5 cm/s for electrons and holes. The GeSn materials' refractive index and extinction coefficient that was measured using ellipsometry, overwrote the Ge ones to simulate the devices under illumination. The light intensity that is assumed to be uniform across the width of the beam has a density of 0.01 W/cm^2. Interestingly, the Franz-Keldysh effect involves in the performances of the devices, but Silvaco doesn't have a built-in function for the Franz-Keldysh mechanism. Hence, the effect was integrated into Silvaco following the steps:

i) Silvaco was run to collect the electric field throughout the devices

ii) The absorption coefficient of the materials under the influence of the electric field was recalculated using:

$$\alpha = \alpha_p exp\left(-\frac{4}{3}\sqrt{\frac{2m}{\hbar^2}}\frac{i(\hbar\omega - E_g)^{3/2}}{q\varepsilon}\right) \tag{7.3.1}$$

where $\hbar\omega > E_g$. This Eq. introduces the oscillators at different applied voltages.

iii) Fed the new absorption coefficient into Silvaco to obtain the photocurrent.

7.3.1.3. Results and discussion

In Fig 7.5, the simulated (solid points) and measured (curves) current density-voltage *(J-V)* characteristics are demonstrated for the $Ge_{0.9356}Sn_{0.0644}$ and $Ge_{0.9076}Sn_{0.0924}$ photodiodes. The series resistance is a dominant factor under the forward bias. In fact, the parameter for series resistance was set in Silvaco, and a good agreement between the experimental and simulated data was observed. At the zero-bias voltage, the shunt resistance originally from surface leakage current becomes a dominant factor. At higher reverse bias, the SRH recombination becomes more effective than the others. As we observed before in Fig 7.3 (b), there is the lattice mismatch between Ge buffer and GeSn materials, which leads to the fact that the GeSn/Ge interface is defective, so it might be the main reason for the relative high dark current. Short carrier lifetimes are set in the SRH model to represent the defective layers. Because the bandgap of the 9.24 % Sn device is narrower than that of the 6.44 % Sn device, which leads to the 9.24 % Sn device having a higher intrinsic carrier concentration. Hence, at a certain reverse voltage, the current density of the 9.24 % Sn device is higher than that of the 6.44 % Sn device. Moreover, there is a deviation between the measurement and simulation for 6.44 % Sn device at small reverse bias from -0.4 V to -0.1 V, shown in Fig. 7.5 (a). The measured dark current may be limited by diffusion current, which leads to lower values comparing with the simulated current, in which SRH is assumed as a dominant mechanism.

The simulated and measured spectral response of 6.44 % and 9.24 % Sn photodiode detectors were shown in Fig. 7.6 (a) and (b), respectively. The 6.44 % Sn device exhibits a cutoff wavelength of 2.2 μm, while the 9.24 % Sn device, the spectral response is extended to 2.5 μm. The cutoff wavelength is much longer than the Ge band-to-band absorption edge (1.55 μm), indicating major photo response contribution is from the GeSn layer. This longer wavelength

coverage is due to the reduced bandgap for the increased Sn composition as expected. The simulated results match the measured ones, which indicates that the GeSn material models are valid. It is worth noting that the devices' spectral response not only covers the traditional L- and C-band, but also the 2 μm telecommunication band.
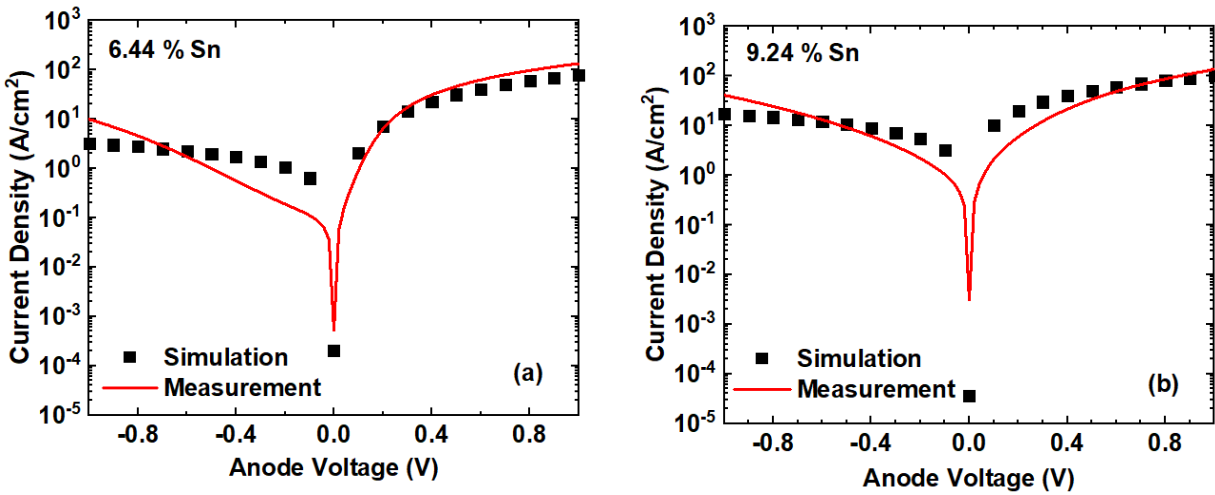
Figure 7.5 Simulated and measured J-V characteristics of (a) the $Ge_{0.9356}Sn_{0.0644}$ device and (b) the $Ge_{0.9076}Sn_{0.0924}$ device [55].
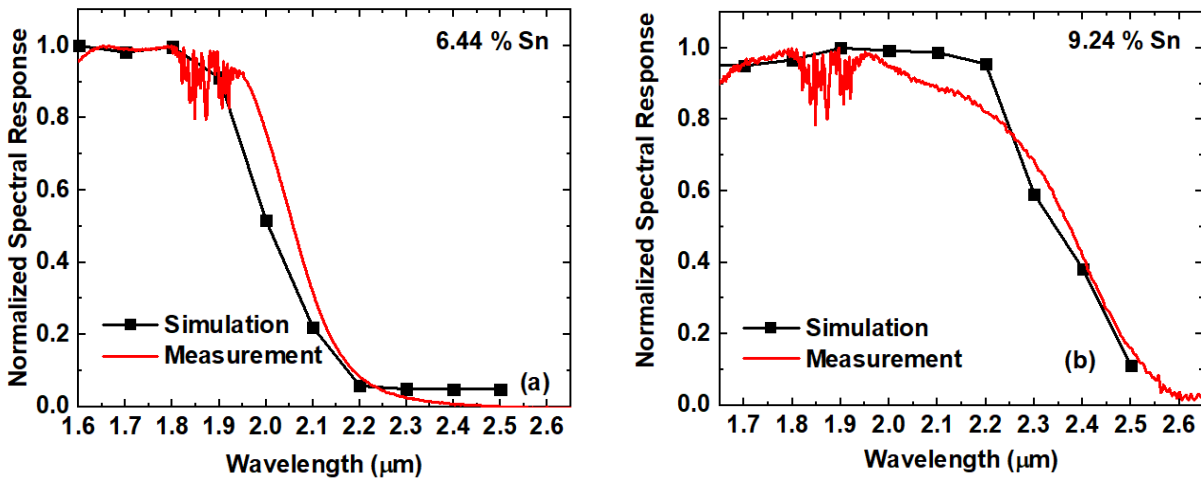
Figure 7.6 Spectral response of (a) the $Ge_{0.9356}Sn_{0.0644}$ device and (b) the $Ge_{0.9076}Sn_{0.0924}$ device [55].

Figure 7.7 presents the responsivity simulated and measured at 1.55 µm of the (a) 6.44 and (b) 9.24 % Sn photodiode devices. At 0.1 V reverse bias, the peak responsivities of 0.12 and 0.19 A/W were obtained for the 6.44 and 9.24 % Sn samples, respectively. The responsivities are corresponding to EQE of 9.6 % and 15.2 %, respectively. As the reverse bias voltage increases, the responsivity decreases. This responsivity reduction is possibly associated with the Franz-Keldysh effect. At a 1 V reverse bias voltage, the responsivities reduce to 0.08 and 0.07 A/W for the 6.44 and 9.24 % Sn devices, respectively. Moreover, the responsivity of both devices shows similar values, suggesting that the material qualities are comparable. The simulated data shows oscillators over the applied voltage ranges as key behavior under the Franz-Keldysh effect, and they fluctuate around the measured values. In fact, the measured data were obtained by several rounds of averaging to smooth noisy curve, which eliminates fluctuations. The simulated data were acquired based on the maximum electric field, which leads to lower values comparing with that of the measured data.
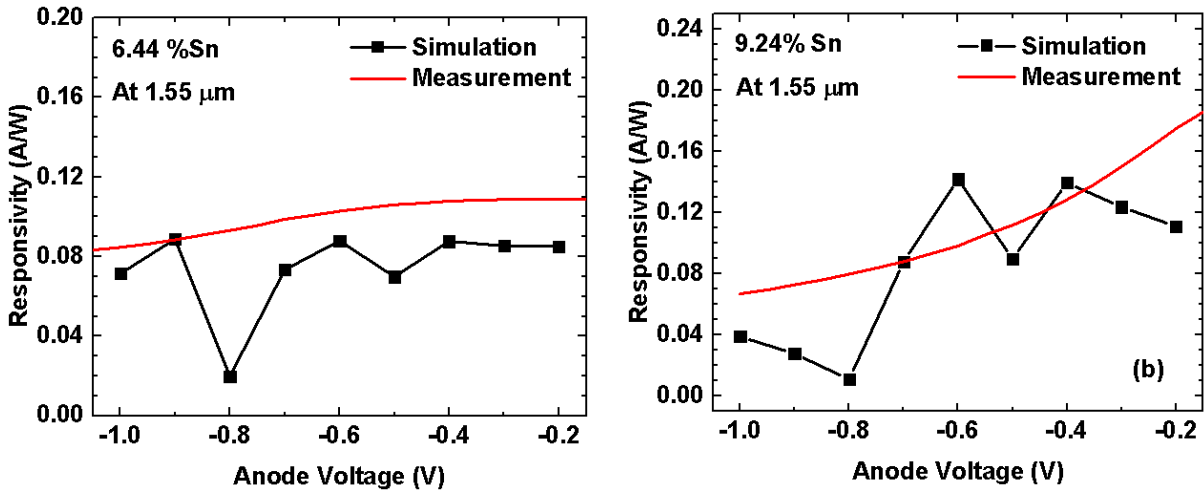
Figure 7.7 Responsivity measured at 1.55 µm of the (a) 6.44 % Sn and (b) 9.24 % Sn devices.

In Table 7.3, the GeSn devices with different mesa sizes of 500, 250, and 100 µm at different applied voltages were summarized to demonstrate high-frequency capabilities. The operation

bandwidth increases as the mesa size decreases, which is due to the reduction of junction resistance capacitance. As the reverse bias voltage increases, the depletion width increases, which also increases the bandwidth of the devices.

Table 7.3 Bandwidth of the GeSn devices with different mesa sizes and at different bias voltages [55].

	3dB Optical Bandwidth (GHz)					
Bias (V)	6.44 % Sn			9.24 % Sn		
	100	250	500	100	250	500
0	0.0849	0.035	0.035	0.0849	0.035	0.035
-1	0.21	0.0599	0.035	0.16	0.16	0.0849
-3	0.709	0.309	0.185	0.908	0.684	0.21
-5	1.78	0.534	0.309	1.53	0.933	0.759
-7	1.78	0.783	0.584	1.03	0.659	0.534

The RF response of the GeSn devices with mesa's diameter of 100 μm is shown in Fig. 7.8, while the simulated results are shown in the inset. The frequency response at -6 dB bandwidth is 1.78 GHz at -7V bias, while the simulations of optical bandwidth at -3 dB show 2 GHz measured at 2 μm and -7 V bias. As abovementioned, the bandwidths of the devices depend on two significant factors: i) the carrier lifetime, and ii) the junction resistance capacitance. The devices' dimensions were not optimized in this work. In order to achieve much higher bandwidth for the devices, the devices' size needs to be reduced. In the further simulation, which will be described in detail in the section below, the simulated -3dB bandwidth of the 10 μm diameter device was 10 GHz which was almost one order of magnitude higher than that of

the 100 μm mesa device. The frequency response achieved at 2 GHz indicates the great potential

of GeSn photodiodes for high-speed applications in microwave photonics.
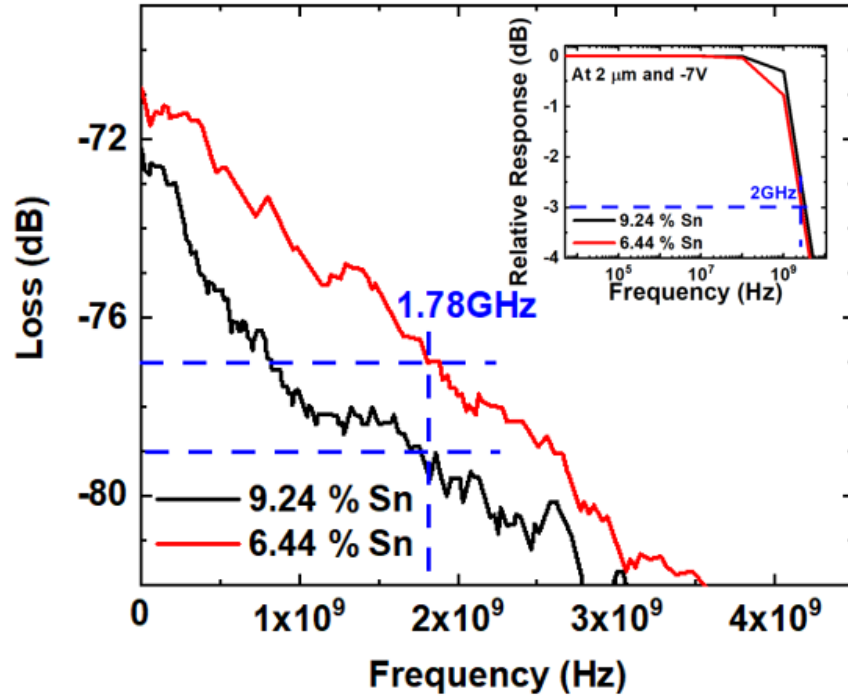
Figure 7.8 Electrical bandwidth of 1.78 GHz for both devices with mesa's diameter of 100 μm; (inset) simulated results for optical bandwidth of 2 GHz for both devices [55].
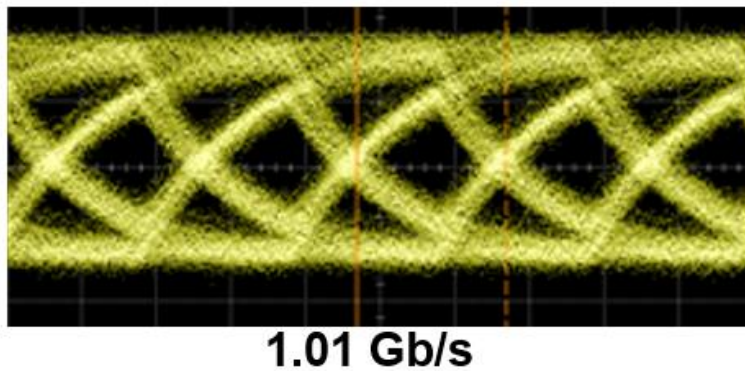
Figure 7.9 Eye diagram of the 6.44 % Sn device [55].

Figure 7.9 shows a 1 Gbit/s eye diagram obtained from the 6.44 % Sn device. The bit rate is lower than the bandwidth at 6 dB but close to the 3 dB bandwidth. It is worth noting that there may be a pitfall of relying on the bandwidth value for evaluating the time-domain performance. In fact, the behavior of the system in the frequency domain (i.e., the slope in the frequency domain) is also important. However, the determination of the bandwidth at -3dB is still valid in the case of the steeper slope of the frequency response.

7.3.1.4. Conclusions

In summary, systematic studies of $Ge_{0.9356}Sn_{0.0644}$ and $Ge_{0.9076}Sn_{0.0924}$ photodiodes were conducted. Detection of the reported 6.44 % Sn and 9.24 % Sn devices are up to 2.2 μm and 2.5 μm wavelengths, respectively. The measured bandwidths of the devices achieve 1.78 GHz, while the bitrate is 1 Gbit/s. The detection wavelengths can be extended to the mid- and far-infrared as more Sn is incorporated into the materials. The current GeSn photodetectors, together with the recently reported GeSn lasers and other GeSn microwave photonic components (i.e. high-speed modulator and waveguide) will be a potential candidate for integrated microwave photonic applications. Moreover, in the further simulation, the reduction of the mesa diameter could increase the bandwidth.

7.3.2. Surface illumination photodiodes with small mesas

7.3.2.1. Design using Silvaco simulation

As mentioned above, the new design was obtained to increase the bandwidth of the GeSn photodiodes. The thickness of the active layer in *NIP* structure was intended to be small to reduce the capacitance and increase the transit time for high-speed design. The spontaneous relaxation-enhanced (SRE) Sn incorporation process can aid growing high Sn, so the *NIP* structure was designed to grow SRE GeSn buffer as the sacrificial $Ge_{0.93}Sn_{0.07}$ layer with a large defect density,

162

and then the high-quality $Ge_{0.92}Sn_{0.08}$ *NIP* layers were grown. The input of Silvaco was set to have the carrier lifetime τ in the SRH model for the defective layer to be in the order of picoseconds, while the high-quality $Ge_{0.92}Sn_{0.08}$ *NIP* layers with small defect density ($\tau = 10$ ns). Furthermore, an incident light at 2 μm wavelength with a normal angle and the power of 10 mW/cm^2 was utilized in the simulation work as a light source, and the beam is Gaussian distribution.

After running the Silvaco simulation, the $Ge_{0.92}Sn_{0.08}$ PD's DC characteristics were investigated. The current flows inside the PD structure with the bias voltage of -0.1 V were shown in Fig. 7.10, and the current-voltage characteristic of the diode was also shown in Fig. 7.10's inset. As shown in the figure, the current flowlines mainly occurred within the *NIP* structure, and only a small amount leaks to the defective layer, which leads to a small dark current. In fact, the simulation shows that the dark current was as low as 1 nA. There is no denying that the low dark current is one of the significant merits in the PD with ultra-low noise. However, in the simulation, the sidewall's contribution was not considered, so it is not precise to claim the PD will have a very low dark current. It was worth noting that increasing the Sn composition resulted in a high dark current due to the lower bandgap energy and higher tunneling current, so the proposed design is capable of providing a low dark current with the 8% Sn composition in the structure.

Through the Silvaco simulation, the spectral response of the $Ge_{0.92}Sn_{0.08}$ *NIP* structure was scanned between 1.55 to 2.3 μm. As shown in Fig. 7.11, the responsivity was ~ 0.02 A/W at ~ 2 μm. The cutoff wavelength was extended to ~ 2.2 μm (E_g=0.56 eV). The band edge of the $Ge_{0.92}Sn_{0.08}$ material was shown clearly as spectral response decreases by the wavelength increase due to the less absorption near the band edge. It is worthy to note that the proposed structure is

not only capable of covering the traditional L- and C-band, but also the 2 μm telecommunication band.
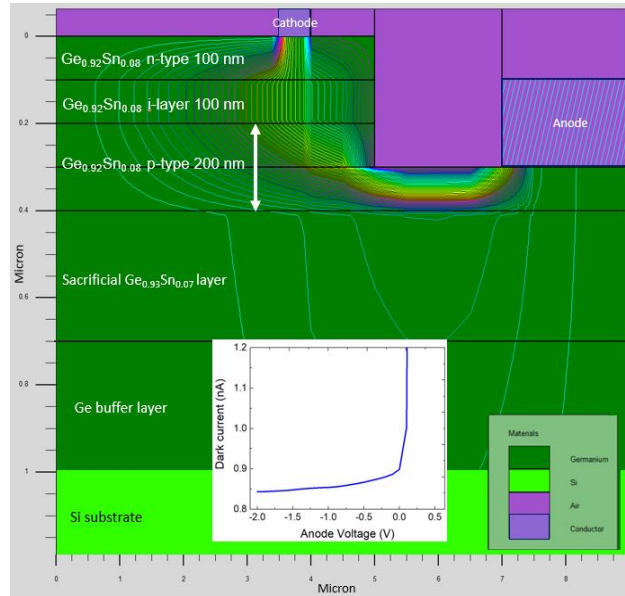
Figure 7.10 The simulated current flowlines inside the GeSn PD structure. Most of the current flows within the NIP region. (Inset): Dark current vs anode voltage indicating the very low dark current (~ 1nA) obtained from the simulation.
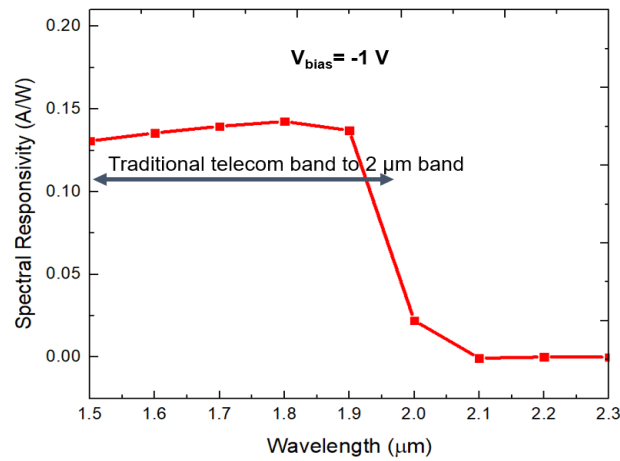
Figure 7.11 Spectral response of the GeSn PD at the bias voltage of -1 V covering the L- and C-bands up to the 2 μm band.

The Silvaco simulation was performed to obtain the RF response of the proposed GeSn NIP PD for the 2 μm wavelength and the reverse bias voltage of -1 V. As mentioned above, the mesa diameter was assumed to be 10 μm in order to enhance the bandwidth of the device. In order to

examine the change in the frequency response versus different mesa diameters, the results were compared with the same GeSn PD structure but were fabricated with 100 μm diameter. As shown in Fig. 7.12, the simulated -3dB bandwidth of the 10 μm diameter design was 10 GHz which was almost two orders of magnitude higher than the 100 μm mesa design. It is worthwhile to note that the -3dB bandwidth is 0.2 GHz for the 100 μm device, which is lower than the abovementioned devices. In fact, the structure's active thickness is 100 nm, which is lower than that of the previous devices. The active region's thickness also needs to be optimized as shown in Fig. 7.2. However, this design is used to demonstrate the influence of sizes of the mesas on high-speed characteristics. As a result, it was shown that reducing the mesa diameter increases the bandwidth. The frequency response achieved in the simulation indicates the ability of the GeSn *PIN* PD for the high-speed applications in microwave photonics
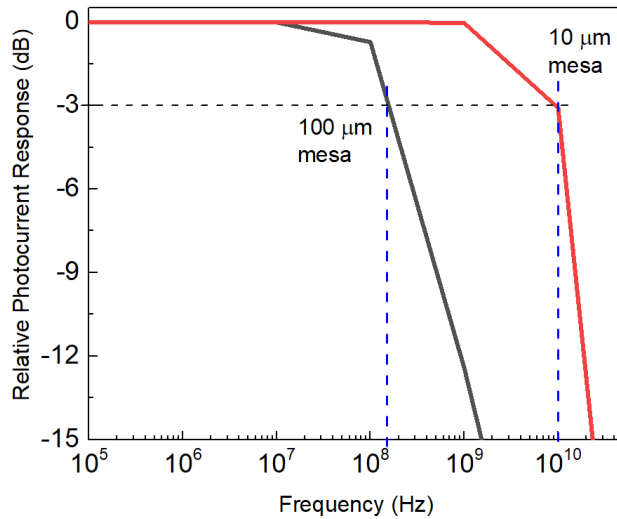
Figure 7.12 The simulation results of the relative photocurrent response vs frequency to examine the -3 dB bandwidth of the proposed GeSn PD. The bandwidth of the PD with 10 μm mesa is compared to the one with 100 μm mesa diameter.

7.3.2.2. Growth and material characterization

The design was grown by an industry-standard chemical vapor deposition reactor using commercially accessible precursors of GeH_4 and $SnCl_4$ on Si (100) substrate. Five epitaxial layers were grown to form two samples (IDs: 0053-FDY and 0054-FDY) as following:

i)   A 700-nm-thick Ge layer was grown as the buffer layer

ii)   An SRE GeSn was grown as a sacrificial layer with a large defect density because large lattice mismatch between GeSn and Ge

iii) A heavily p-type doped GeSn buffer with a nominal 7 % Sn was grown with the expectation of higher quality based on the SRE mechanism. The thicknesses are 100 nm and 300 nm for 0053-FDY and 0054-FDY, respectively. The purpose of the heavily doping level is to form the Ohmic contact.

iv)   A GeSn active layer with a nominal 8 % Sn was grown with an unintentional doping level around 10^{17} cm^{-3}, and the thicknesses are 100 nm and 300 nm corresponding to 0053-FDY and 0054-FDY.

v)   A GeSn cap layer was grown with a heavily n-type doping level around 10^{19} cm^{-3}, and the thicknesses are 100 nm and 300 nm respective to 0053-FDY and 0054-FDY.

Figure 7.13 (a) shows the cross-section schematic of the device structure. To verify that the growth samples received from the foundry agreed with our designs, material characterizations such as Raman Spectroscopy, XRD, Ellipsometry, and Hall measurements were conducted. Figure 7.13 (b) shows the 2θ-ω scan from symmetric (004) planes of samples 0053-FDY. The Si peak is at 69^0, and the peak from Ge buffer is at 66^0. The Ge peak is slightly shifted towards higher angles than 66^0 due to strain relaxation of the material. The peaks at angles below 66^0 are assigned to the GeSn for samples 0053-FDY. Figure 7.13 (c) shows the reciprocal space map (RSM) contour plots of samples 0053-FDY. The in-plane (a||) and out-of-plane (a$^\perp$) lattice

166

constants for each sample were extracted from RSM contour plots, and then the Sn percentages and strain information for each sample were evaluated, as summarized in Table 7.4. Hall measurement for each sample shows a carrier concentration greater than 1×10^{20} cm^{-3} and resistivity in $\mu\Omega \cdot$m range for the top-most n+ layer. The measured carrier concentration was one order of magnitude greater than what was proposed. Spectroscopic ellipsometry was employed to characterize the thickness and absorption coefficient of the samples. The absorption edge extends to ~2.4 µm, which means the Sn composition is higher than the design one of 8 %. Hence, it is expected to have a higher dark current for this set of samples compared to the previously mentioned samples. The Sn percentages of the active layer from growths are higher than the Sn percentages from designs. However, it is aimed to have the operating wavelength beyond 2 µm at 300 K as an establishing goal, so the samples can still feature to develop high-speed detectors. In fact, the thickness of each sample is close to the designed thickness, which will help to achieve the optimized bandwidth. Hence, the samples were fabricated as different generations of devices such as small mesas of 50, 70, and 100 µm, and waveguide with length and width dimensions of 50 µm × 5 µm, 70 µm × 5 µm, 100 µm × 5 µm.
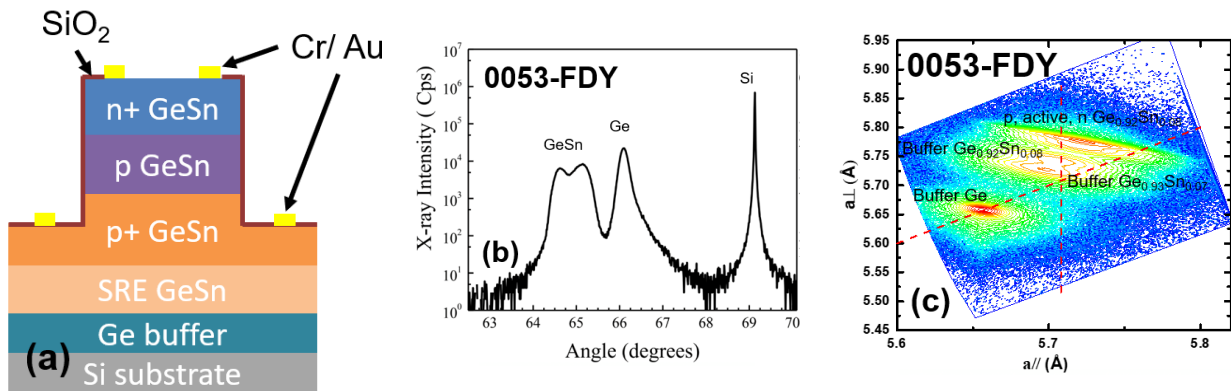
Figure 7.13 (a) The schematic cross-sectional view of the device structures. (b) 2θ-ω scan from symmetric (004) plane for 0053-FDY. (c) RSM of 0053-FDY

Table 7.4 Composition, thickness, and strain information

ID	Nominal Sn (%)	Measured Sn (%)	n+ GeSn thickness (nm)	Active GeSn thickness (nm)	p+ GeSn thickness	GeSn in-plane strain (%)
0053-FDY	8	11.1 %	127	131	166	0.41
0054-FDY	8	11.6 %	204	317	469	0.49

7.3.2.3. Fabrication

As analyzed above, the smaller mesa for surface illuminated photodetector will help to increase the bandwidth. The new mask was designed using AutoCAD software. Because of the current fabrication capability, the mesa diameter of the circular devices was limited. To achieve high yield in the existing fabrication, these were designed to have mesa diameters of 50, 70, and 100 μm. E-beam lithography eliminates these limitations, so the smaller mesa diameters (less than 50 μm) can be explored. For the design of the metal contacts, Ansys Q3D software was used to extract parasitic capacitance and resistance. Based on those values, it was feasible to design the metal contact pads that enhance the bandwidth to reach 60 GHz. The designed contact pads of these devices were circular with diameters of 100 μm and 300 μm. Figure 7.14 (a) shows the typical portion of the AutoCAD mask to show the shapes of the small mesa devices.

The GeSn photodiodes were fabricated into circular mesa structures by standard photolithography and then etched using a wet chemical etching process. The solution of HCl: H_2O_2: H_2O = 1:1:20 was used in the process at 0 ^{0}C. A stable etching rate of 20 nm/min at low temperature regardless of Sn composition was achieved. The mesas were etched until the p+ GeSn was reached. A 300-nm-thick SiO2 passivation layer was then deposited by the sputtering

system to form an isolation layer and passivation as well. The oxide was opened to form the metal contacts. Electrode pads were patterned and metalized with 10/350 nm of Cr/Au.
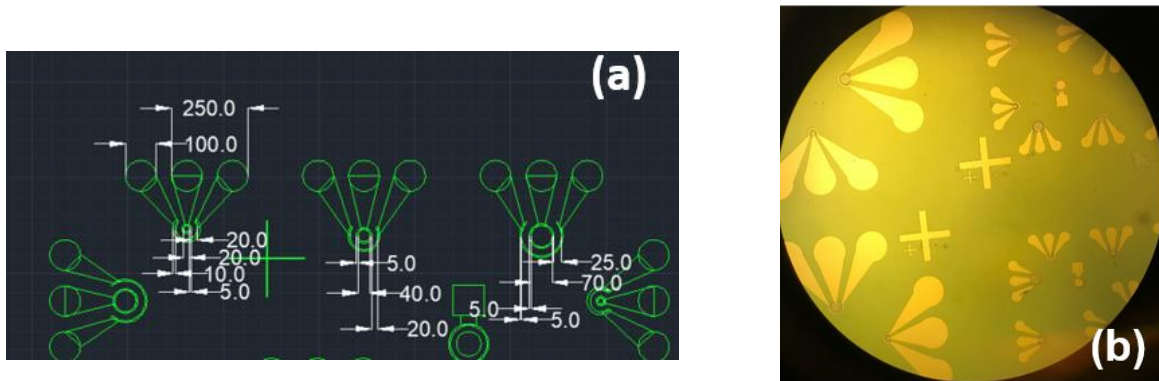
Figure 7.14 (a) AutoCAD design for the small mesa devices. (b) Optical images of the fabricated small mesa photodetectors of 0053-FDY

It is worth mentioning that due to facility matter, the SiO_2 was deposited using the sputtering system instead of PECVD. In the beginning, the system used Si as the target, and the bubbling surfaces that were created during the SiO_2 deposition lead to have high leakage current, and severely, it can short-circuit the devices. The SiO_2 deposition used Si target, which requires roughly high temperature on the substrate. The formation of bubbles is stress-induced at high temperatures. Differences in thermal expansion coefficients among the layered films lead to thermal stress. There is one available method that is to reduce the substrate temperature by using SiO_2 target, which requires lower deposition temperature. In addition, during SiO_2 deposition that used Si target in Oxide environment, it is possible to form layers of a-Si or poly-Si, or SiO, which can be conductive instead of isolative. Hence, it is planned to change to SiO_2 target as a replacement for Si target, and the RF power, pressure, and time are optimized to form a superior SiO_2 isolation layer. In fact, in the process of the fabrication for the small mesa photodetectors, the target was SiO_2. The sputtering parameters are the base pressure of 1.7E-7 mTorr, a chamber pressure of 5 mTorr, an RF power of 100 W, a chamber temperature of 150 ^{0}C which

corresponds to a substrate temperature of 75 ^{0}C. Oxygen was not used in this sputtering process since we had a SiO$_2$ target. Figure 7.14 (b) shows a typical optical image of the small mesa photodetectors of the 0053-FDY. Smooth surfaces indicate that we have decent SiO$_2$ isolation layers, which leads to having a high yield fabrication of the high-speed devices.

7.3.2.4. Characterization
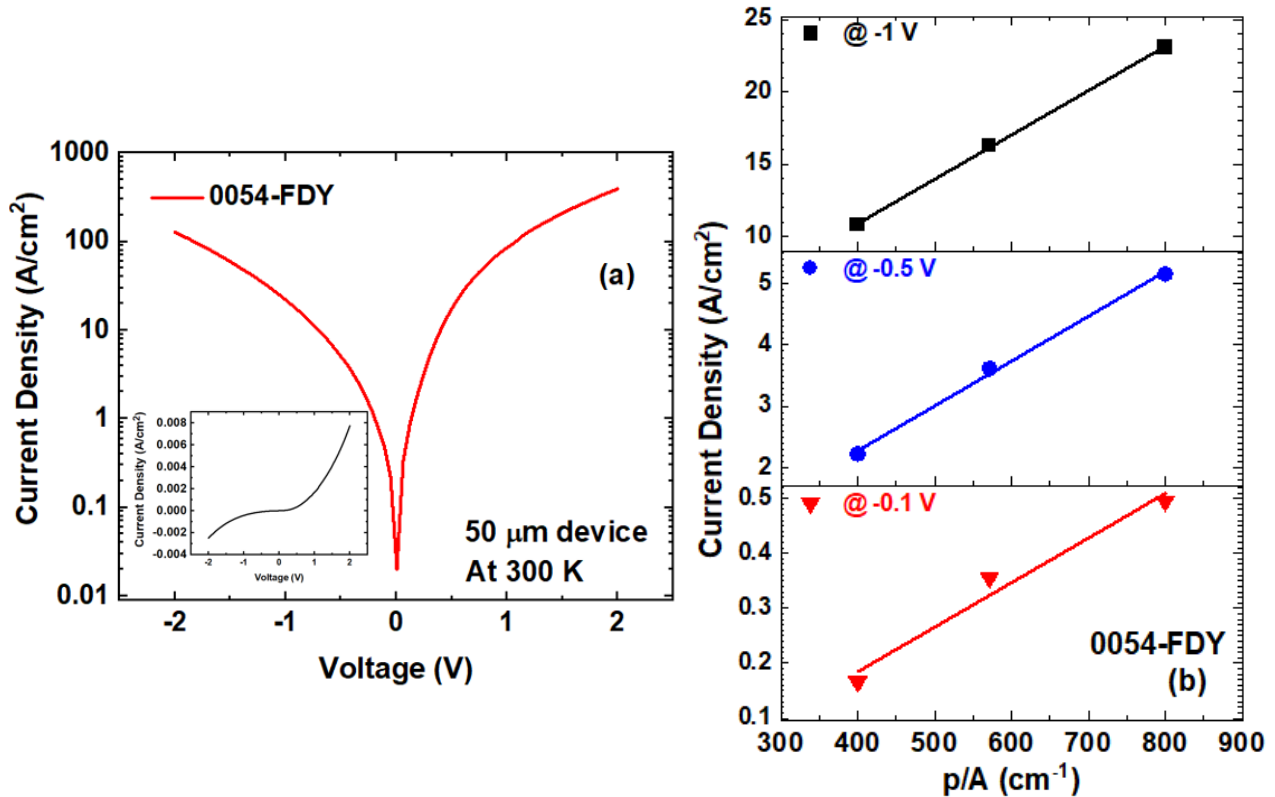
Figure 7.15 (a) The current density versus bias voltage for the 50 m device of the 0054-FDY at 300 K. (b) Total dark current density as a function of the ratio of p/A at the bias voltages of -0.1 V, -0.5 V, and -1 V, where p is perimeter and A is area.

The fabricated devices were characterized to obtain the *IV* characteristics at 300 K. Figure 7.15 (a) shows the current density of the typical 50 μm device for the 0054-FDY. The *IV* characteristic shows the rectifying diode-like behavior. The dark current can be related to bulk dark current density (J_{bulk}) and the peripheral surface leakage current density (J_{surf}) through

170

$$J_{Total} = J_{bulk} + J_{surf}\frac{p}{A} \tag{7.3.2}$$

where p is the perimeter and A is the area of the device. Figure 7.15 (b) shows total dark current density versus the ratio p/A. For the device operating at -1 V, J_{bulk} and J_{surf} can be evaluated by fitting as Eq. (7.3.2). J_{bulk} and J_{surf} are calculated as 1.32 A/cm^2 and 31 mA/cm, respectively. The surface leakage current is dominating the dark current. In fact, for the wet etching process, the mesa is also laterally etched, which increases the side-wall area. Then, the dangling bonds are exposed, which leads to a high leakage current. This effect is worse for the waveguide photodetector. It is necessary to further analyze the dark current of the waveguide photodetector in detail below to quantitative the trap on the sidewall of the devices.

7.3.3. Waveguide photodiodes

7.3.3.1. Design and Silvaco simulation

This design is mainly proposed to compare the bandwidth and saturation power between the waveguide photodiodes and top-illuminated GeSn photodetectors presented above. Figure 7.16 (a) shows the structure of the GeSn waveguide detector. The Silvaco simulation was performed regardless of the contribution of the sidewall, which leads to current flowlines flowing inside the bulk. The inset shows the *IV* characteristic of the device, indicating the rectified behavior. The effective lifetime was set as 0.1 µs for the active layer, while it was set as 1 ps for the defective layer. With the effects of tunneling and contact resistance, the turn-on voltage is reduced. As shown in Fig. 7.16 (b), the Silvaco simulation was performed using the refractive index and absorption coefficient measured by ellipsometry, which reveals that the fundamental mode propagates inside the waveguide. The optical confinement of the 2 µm beam is within the waveguide and does not reach the defective layer.

Figure 7.17 shows the 3dB bandwidth of the GeSn waveguide device, and the bandwidth is ~ 4 GHz. The junction capacitance is quite large as the area of the device is 500 μm^2, which limits the bandwidth. Moreover, the active region thickness is around 300 nm, which is not the optimized value to have maximum bandwidth as shown in Fig. 7.2.
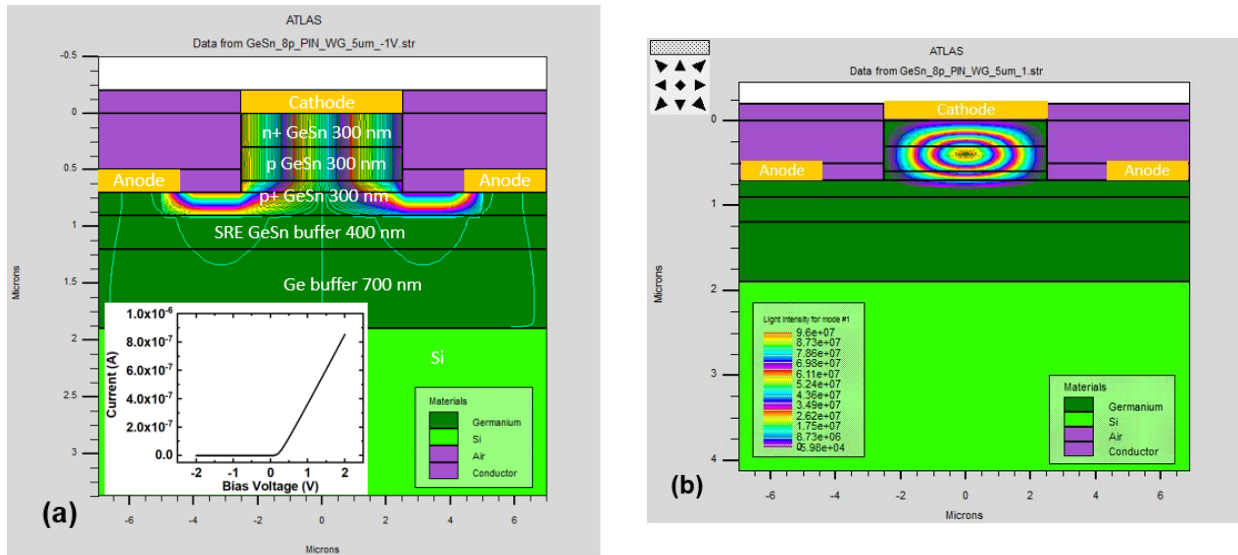
Figure 7.16 (a) The proposed layer structure of the GeSn homojunction n-i-p structure for waveguide photodetectors. (Inset) *IV* characteristics. (b) The fundamental mode propagation within the waveguide
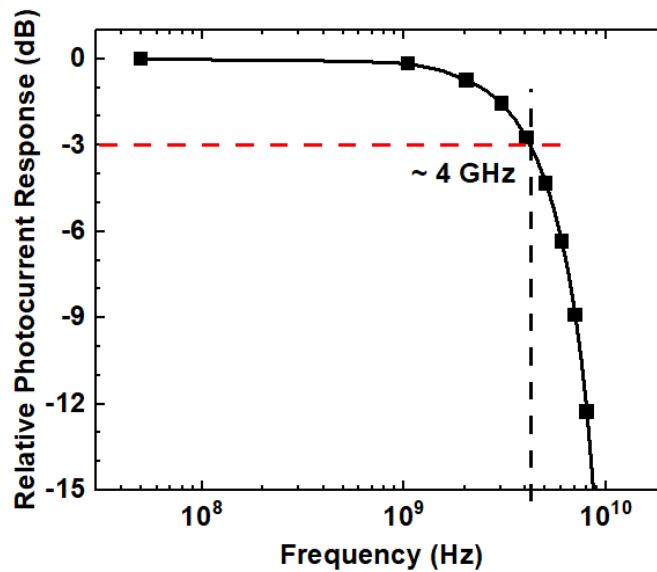
Figure 7.17 The simulation results of the relative photocurrent response vs frequency to examine the -3 dB bandwidth.

172

7.3.3.2. Fabrication, characterization, and discussion

The high-speed waveguide photodetector was designed to have length and width dimensions of 50 µm × 5 µm, 70 µm ×5 µm, 100 µm × 5 µm. The devices were designed to have square contacts of dimension 100 µm × 100 µm. After receiving the new mask, the devices were fabricated, and the wet etching method was used. Figure 7.18 (a) shows the optical images of the waveguide devices. As abovementioned in section 7.3.2.4, the side-wall leakage current will dominate the dark current, which affects the performance of our devices. The detailed analysis will be discussed below.

The fabricated devices were characterized to obtain the *IV* characteristics at 300 K. Figure 7.18 (b) shows the current density of the typical waveguide photodetector for the 0053-FDY. The *IV* characteristic shows the rectifying diode-like behavior. In order to quantitatively evaluate the trap of the sidewall of the device, an in-depth study on the mechanism of each dark current component was conducted. The method to analyze homojunction *IV* in Chapter 5 was re-applied here. Figure 7.18 (c) shows the result of the data fitting process of dynamic resistance of the 0053-FDY. In fact, let remind us about the dynamic resistance, which can be constructed as a combination of mechanisms such as diffusion (R_{diff}), generation-recombination (R_{g-r}), trap-assisted tunneling (R_{TAT}), band-to-band tunneling (R_{BBT}), and Ohmic leakage (R_{shunt}). Hence, the resistance component can be expressed by the following equation:

$$R_{total} = R_{dynamic} + R_{series} \tag{7.3.3}$$

where $R_{dynamic} = \left(\frac{1}{R_{diff}} + \frac{1}{R_{g-r}} + \frac{1}{R_{TAT}} + \frac{1}{R_{BBT}} + \frac{1}{R_{shunt}} \right)^{-1}$, and $1/R_{diff} = \partial I_{diff}/\partial V$, $1/R_{g-r} = \partial I_{g-r}/\partial V$, $1/R_{TAT} = \partial I_{TAT}/\partial V$, $1/R_{BBT} = \partial I_{BBT}/\partial V$ and $1/R_{shunt} = \partial I_{shunt}/\partial V$. The analysis yields:

- Trap-assisted tunneling is the dominant mechanism of dark current. Please keep in mind that this tunneling current happens through the trap density in the sidewall of the device.

- The sidewall's trap density is quantitatively estimated as 1.7×10^{18} cm^{-3}, and the trapping energy is close to mid-gap.

The analysis gives sufficient information to improve the device's performance. In fact, it is planned to use dry etching to reduce the lateral etching, and then wet etching for a few seconds to smooth the surfaces. Moreover, in order to produce smaller devices, it is necessary to use E-beam lithography as a substitute for our standard photolithography.
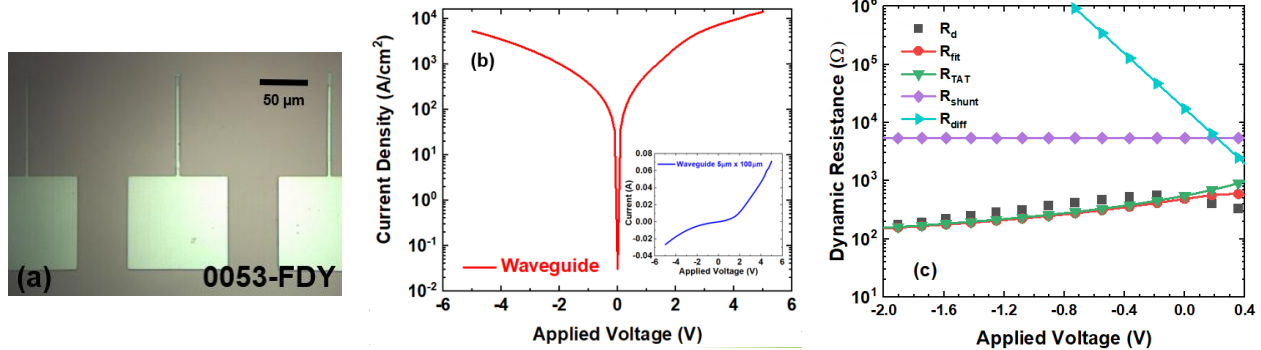
Figure 7.18 (a) Optical image of the 0053-FDY detector. (b) The *IV* characteristics at 300 K. (c) Fitted dynamic resistance of the 0053-FDY waveguide device at 300 K.

Again, the Silvaco was used to demonstrate the effect of the sidewall on the performance of the devices. Figure 7.19 (a) shows current flowlines at -1 V, which flow predominantly on the sidewalls instead of inside bulk as displayed in Fig. 7.16 (a). As the surface recombination velocity increases, the dark current at reverse bias becomes larger as shown in Fig. 7.19 (b), while the current at the forward bias has a smaller turn-on voltage and also becomes larger. As a result, the sidewall effect deteriorates the devices' performances, especially for dark current, which confirms the above analysis, which shows very high trap density. It is important to reduce the lateral etching by dry etching.

174
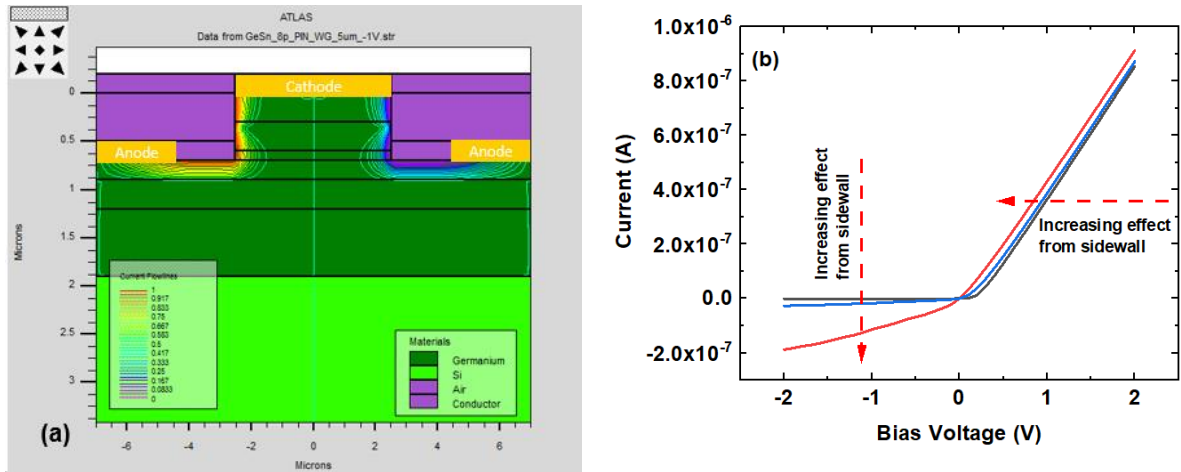
Figure 7.19 (a) Current flowlines flow on the sidewall instead of the bulk. (b) The *IV* characteristics at different surface velocities.
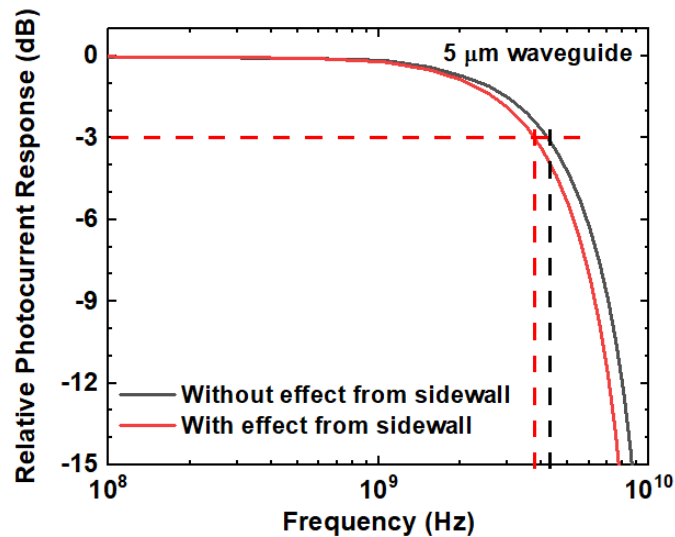
Figure 7.20 The 3dB bandwidth with or without effect from the sidewall.

Figure 7.20 plots the 3dB bandwidth results from simulation, which shows the effect of the sidewall. The 3dB bandwidth slightly increases as the device is not affected by the sidewall. It is reasonable to reveal that the sidewall does not affect much on the 3dB bandwidth of the devices. In fact, the junction capacitance is still the key character to influence on 3dB bandwidth. However, the noise from the devices still affects the performance of the devices in practice. Hence, it is considered to develop improved processing methods to reduce lateral etching as well as applying passivation techniques.

As a result, this chapter shows the high-speed capability of GeSn photodetectors. The GeSn photodetectors were designed, simulated, characterized, and analyzed to expose the GeSn material properties as the candidate for the high-speed applications in microwave photonics. Hence, the cost-effective silicon "Superchips" that merge silicon photonics with advanced silicon electronics on a silicon substrate can be made from significant electrooptical devices from Column IV materials (Si, Ge, C, and Sn).

Chapter 8.   Summary and Future work

8.1. Summary

Detecting and sensing infrared (IR) radiation is enormously critical in various applications. For decades, several alloys such as III-V, IV-VI, and II-VI compounds have enabled an exceptional degree of freedom in IR detector design due to high absorption coefficient, high electron mobility, and low thermal generation rate together with bandgap engineering capability. However, the mature IR photodetector technology is costly, hard to fabricate, and operates at low temperatures.   Recently, GeSn techniques have succeeded to demonstrate GeSn-based optoelectronic devices, which results in the launch of a new generation of infrared detectors. This research studied Si-based $Ge_{1-x}Sn_x$ photodetectors for infrared imaging and high-speed detections.

At first, the lifetime is estimated from theoretical and practical methods. From the theoretical perspective, the lifetime is ranging from 0.1 µs to 0.01 ns for the GeSn with 11 % Sn. For a high impurity concentration of 10^{18} cm^{-3}, the lifetime does not reduce as temperature increases. The limiting factor of the GeSn lifetime is radiative at low temperature and SRH at high temperature. For high impurity concentrations, which are higher than 10^{18} cm^{-3}, the lifetime does not depend on the Sn composition. For low impurity concentrations, the more Sn composition incorporates in the materials, the shorter the lifetime is. From the practical perspective, the carrier bulk lifetime and diffusion constant were studied using the GeSn photoconductors. The bulk lifetime is ranging from 0.5 µs to 5 ns for the GeSn materials with 6.6 % and 9 % Sn. In a later chapter, the 11 % Sn photoconductor was used to evaluate the bulk lifetime. The bulk lifetime is ranging from 0.5 ns to 0.05 ns, which agrees with that of theoretical calculations.

Secondly, the absorption coefficients and refractive indices were characterized to form the formulae as a function of Sn compositions. The formulae can be later used to design the GeSn optoelectronic devices.

Thirdly, high-performance GeSn photodetectors were studied in this work. A set of photoconductors with Sn compositions up to 22.3% was demonstrated. The longest wavelength cut-off was measured up to 3.65 µm. The peak D* is comparable with the commercial extended InGaAs detector. The passivation technique was developed and applied on a $Ge_{0.89}Sn_{0.11}$ photodiode. The significantly enhanced responsivity spectral D* was achieved. Furthermore, the mechanisms of the dark current of the photodiodes were discussed to identify which factor governs the detectors' performances. Moreover, the mid-IR imaging was demonstrated with GeSn photoconductors and photodiode. The images taken from GeSn photodetectors showed better quality compared with commercial PbSe detector.

Lastly, this work comprehensively discusses the performance of GeSn photodiodes with 6.44 and 9.24% Sn for high-frequency applications including high-speed measurements and simulations. With high Sn incorporation, the cutoff wavelength is extended up to 2.2 and 2.5 µm wavelengths for 6.44 and 9.24% Sn devices, respectively. The photodiodes' bandwidth is 1.78 GHz, and the simulation shows excellent agreement with measurement results. The reported GeSn photodetectors together with recently reported GeSn lasers and other GeSn microwave photonic components will be a potential candidate for integrated microwave photonics.

8.2. Future work
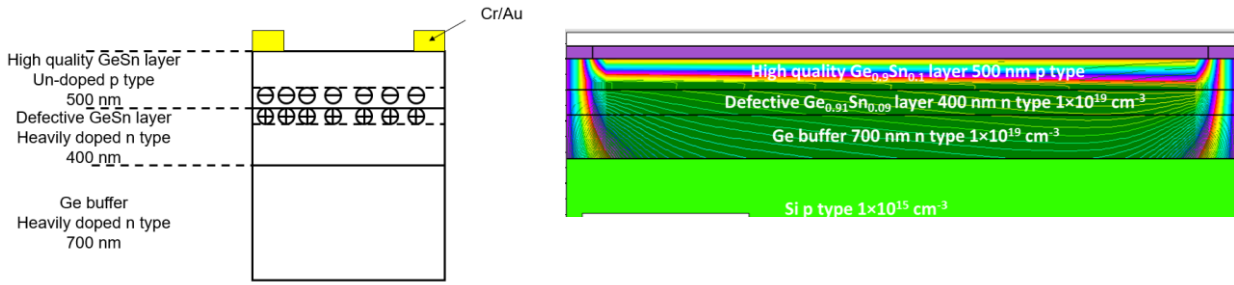
Figure 8.1 (a) Typical inversion layer to block the defective layer contribution, and (b) Silvaco simulation of the inversion layer

The GeSn bulk with inversion layer helps to block the defective layer contribution. Figure 8.1 (a) shows the structure of the inversion layer, and figure 8.1 (b) shows the Silvaco simulation result. In fact, the depletion region acts as the insulating layer because there is no charge population in the depletion region. The characteristics of GeSn bulk such as mobility and lifetime will be measured with higher accuracy.
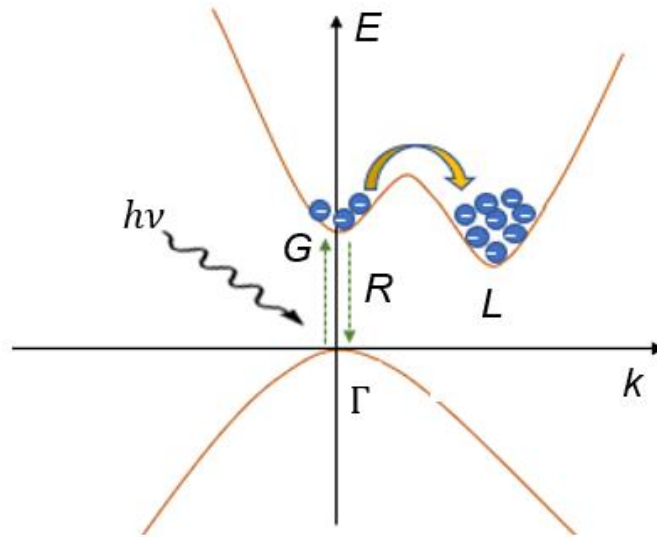
Figure 8.2 The k-space charge separation approach

Generally, while most direct band semiconductors with narrow bandgap have large absorption coefficients, but small effective mass (large tunneling), short lifetime (large SRH and Auger rates), indirect bandgap one have small absorption coefficients, but large effective mass, but long lifetime (small SRH and Auger rates). In order to reduce dark current and to enhance absorption coefficients, we need a large absorption coefficient, large effective mass, and long lifetime. Figure 8.2 shows one approach to achieve those desirable properties. The absorption edge (Γ - valley) is slightly below the X (or L) point (conduction band edge) to enhance the absorption, while the conduction band edge is at X point (as shown in Fig. 8.2).

References

1. Rogalski, A. Infrared detectors: status and trends. *Prog. Quantum. Electron* **2003**, 27 (2-3), 59-210.

2. Soref, R.; Buca, D.; and Yu, S. –Q. Group IV photonics: Driving integrated optoelectronics. *Opt. Photonics News* **2016,** 27 (1), 32-39.

3. Rogalski, A. *Infrared detectors* (CRC, 2010).

4. Homewood, K. P. and Lourenco, M. A. The rise of the GeSn laser. *Nat. Photonics* **2015,** 9, 78-79.

5. Dong, P.; Hu, T. -C.; Liow, T. -Y.; Chen, Y. -K.; Xie, C.; Luo, X.; Lo, G. -Q.; Kopf, R. and Tate, A. Novel integration technique for silicon/III-V hybrid laser. *Opt. Express* **2014,** 22 (22), 26854-26861.

6. Wirths, S.; Geiger, R.; Driesch, N. von den; Mussler, G.; Stoica, T.; Mantl, S.; Ikonic, Z.; Luysberg, M.; Chiussi, S.; Hartmann, J. M.; Sigg, H.; Faist, J.; Buca, D. and Grützmacher, D. Lasing in direct-bandgap GeSn alloy grown on Si. *Nat. Photonics* **2015,** 9, 88-92.

7. Al-Kabi, S.; Ghetmiri, S. A.; Margetis, J.; Pham, T.; Zhou, Y.; Dou, W.; Collier, B.; Quinde, R.; Du, W.; Mosleh, A.; Liu, J.; Sun, G.; Soref, R. A.; Tolle, J.; Li, B.; Mortazavi, M.; Naseem, H. A.; Yu, S. -Q. An optically pumped 2.5 μm GeSn laser on Si operating at 110 K. *Appl. Phys. Lett.* **2016,** 109 (17), 171105-1-171105-4.

8. Soref, R. Mid-infrared photonics in silicon and germanium. *Nat. Photonics* **2010,** 4, 495-497.

9. Wallace, P. M.; Senaratne, C. L.; Xu, C.; Sims, P. E.; Kouvetakis J. and Menéndez, J. Molecular epitaxy of pseudomorphic $Ge_{1-y}Sn_y$ (y = 0.06–0.17) structures and devices on Si/Ge at ultra-low temperatures via reactions of Ge_4H_{10} and SnD_4. *Semicond. Sci. Technol.* **2017,** 32, 025003-1-025003-10.

10. Margetis, J.; Mosleh, A.; Al-Kabi, S.; Ghetmiri, S. A.; Du, W.; Dou, W.; Benamara, M.; Li, B.; Mortazavi, M.; Naseem, H. A.; Yu, S. -Q.; Tolle, J. Study of low-defect and strain-relaxed GeSn growth via reduced pressure CVD in H_2 and N_2 carrier gas. *J. Cryst. Growth* **2017**, 463, 128-133.

11. Margetis, J.; Al-Kabi, S.; Du, W.; Dou, W.; Zhou, Y.; Pham, T.; Grant, P.; Ghetmiri, S.; Mosleh, A.; Li, B.; Liu, J.; Sun, G.; Soref, R.; Tolle, J.; Mortazavi, M.; Yu, S. -Q. Si-Based GeSn Lasers with Wavelength Coverage of 2–3 μm and Operating Temperatures up to 180 K. *ACS Photonics* **2018,** 5 (3), 827-833.

12. Reboud, V.; Gassenq, A.; Pauc, N.; Aubin, J.; Milord, L.; Thai, Q. M.; Bertrand, M.; Guilloy, K.; Rouchon, D.; Rothman, J.; Zabel, T.; Armand Pilon, F.; Sigg, H.; Chelnokov, A.; Hartmann, J. M. and Calvo, V. Optically pumped GeSn micro-disks with 16% Sn lasing at 3.1 μm up to 180 K. *Appl. Phys. Lett.* **2017**, 111 (9), 092101-1-092101-4.

13. Chang, C.; Li, H.; Ku, C. –T.; Yang, S. –G.; Cheng, H. H.; Hendrickson, J.; Soref, R. A. and Sun, G. Ge$_{0.975}$Sn$_{0.025}$ 320 × 256 imager chip for 1.6–1.9 μm infrared vision. *Appl. Opt.* **2016**, 55 (36), 10170-10173.

14. Mathews, J.; Roucka, R.; Xie, J.; Yu, S.-Q.; Menéndez, J.; and Kouvetakis, J. Extended performance GeSn/Si(100) *p-i-n* photodetectors for full spectral range telecommunication applications. *Appl. Phys. Lett.* **2019**, 95 (13), 133506-1-133506-3.

15. Werner, J.; Oehme, M.; Schmid, M.; Kaschel, M.; Schirmer, A.; Kasper, E. and Schulze, J. Germanium-tin p-i-n photodetectors integrated on silicon grown by molecular beam epitaxy. *Appl. Phys. Lett.* **2011**, 98 (6), 061108-1-061108-3.

16. Roucka, R.; Mathews, J.; Weng, C.; Beeler, R.; Tolle, J.; Menéndez, J. and Kouvetakis, J. High-Performance Near-IR Photodiodes: A Novel Chemistry-Based Approach to Ge and Ge–Sn Devices Integrated on Silicon. *IEEE J. Quantum Electron.* **2011,** 47 (2), 213-222.

17. Su, S.; Cheng, B.; Xue, C.; Wang, W.; Cao, Q.; Xue, H.; Hu, W.; Zhang, G.; Zuo, Y. and Wang, Q. GeSn p-i-n photodetector for all telecommunication bands detection. *Opt. Express* **2011,** 19 (7), 6400-6405.

18. Tseng, H. H.; Li, H.; Mashanov, V.; Yang, Y. J.; Cheng, H. H.; Chang, G. E.; Soref, R. A. and Sun, G. GeSn-based p-i-n photodiodes with strained active layer on a Si wafer. *Appl. Phys. Lett.* **2013**, 103 (23), 231907-1-231907-5.

19. Oehme, M.; Schmid, M.; Kaschel, M.; Gollhofer, M.; Widmann, D.; Kasper, E. and Schulze, J. GeSn p-i-n detectors integrated on Si with up to 4% Sn. *Appl. Phys. Lett.* **2012**, 101 (14), 141110-1-141110-4.

20. Gassenq, A.; Gencarelli, F.; Van Campenhout, J.; Shimura, Y.; Loo, R.; Narcy, G.; Vincent, B. and Roelkens, G. GeSn/Ge heterostructure short-wave infrared photodetectors on silicon. *Opt. Express* **2012**, 20 (25), 27297-27303.

21. Zhang, D.; Xue, C.; Cheng, B.; Su, S.; Liu, Z.; Zhang, X.; Zhang, G.; Li, C. and Wang, Q. High-responsivity GeSn short-wave infrared p-i-n photodetectors. *Appl. Phys. Lett.* **2013**, 102 (14), 141111-1-141111-4.

22. Lin, J.-Y. J.; Gupta, S.; Huang, Y.-C.; Kim, Y.; Jin, M.; Sanchez, E.; Chen, R.; Balram, K.; Miller, D.; Harris, J.; Saraswat, K. Fabrication of GeSn-On-Insulator (GSOI) to enable monolithic 3D co-integration of logic and photonics. *IEEE Symp. on VLSI Tech.*, **2013**, T32-T33.

23. Coppinger, M.; Hart, J.; Bhargava, N.; Kim, S. and Kolodzey, J. Photoconductivity of germanium tin alloys grown by molecular beam epitaxy. *Appl. Phys. Lett.* **2013**, 102 (14), 141101-1-141101-3.

24. Kim, S.; Gupta, J.; Bhargava, N.; Coppinger, M. and Kolodzey, J. Current-voltage characteristics of GeSn/Ge heterojunction diodes grown by molecular beam epitaxy. *IEEE Electron Device Lett.* **2013**, 34 (10), 1217-1219.

25. Peng, Y.-H.; Cheng, H. H.; Mashanov, V. I. and Chang, G.-E. GeSn *p-i-n* waveguide photodetectors on silicon substrates. *Appl. Phys. Lett.* **2014**, 105 (23), 231109-1-231109-4.

26. Oehme, M.; Kostecki, K.; Ye, K.; Bechler, S.; Ulbricht, K.; Schmid, M.; Kaschel, M.; Gollhofer, M.; Körner, R.; Zhang, W.; Kasper, E. and Schulze, J. GeSn-on-Si normal incidence photodetectors with bandwidths more than 40 GHz. *Opt. Express* **2014**, 22(1), 839-846.

27. Oehme, M.; Widmann, D.; Kostecki, K.; Zaumseil, P.; Schwartz, B.; Gollhofer, M.; Koerner, R.; Bechler, S.; Kittler, M.; Kasper, E. and Schulze, J. GeSn/Ge multiquantum well photodetectors on Si substrates. *Opt. Lett.* **2014**, 39 (16), 4711-4714.

28. Conley, B. R.; Mosleh, A.; Ghetmiri, S. A.; Du, W.; Soref, R. A.; Sun, G.; Margetis, J.; Tolle, J.; Naseem, H. A. and Yu, S.-Q. Temperature-dependent spectral response and detectivity of GeSn photoconductors on silicon for short wave infrared detection. *Opt. Express* **2014**, 22 (13), 15639-15652.

29. Conley, B. R.; Margetis, J.; Du, W.; Tran, H.; Mosleh, A.; Ghetmiri, S. A.; Tolle, J.; Sun, G.; Soref, R.; Li, B.; Naseem, H. A. and Yu, S.-Q. Si-based GeSn photoconductors with a 1.63 A/W peak responsivity and a 2.4 μm long-wavelength cutoff. *Appl. Phys. Lett.* **2014**, 105 (22), 221117-1-221117-5.

30. Kim, S.; Bhargava, N.; Gupta, J.; Coppinger, M. and Kolodzey, J. Infrared photoresponse of GeSn/n-Ge heterojunctions grown by molecular beam epitaxy. *Opt. Express* **2014**, 22 (9), 11029-11034.

31. Dong, Y.; Wang, W.; Lei, D.; Gong, X.; Zhou, Q.; Lee, S. Y.; Loke, W. K.; Yoon, S.-F.; Tok, E. S.; Liang, G. and Yeo, Y.-C. Suppression of dark current in germanium-tin on silicon p-i-n photodiode by a silicon surface passivation technique. *Opt. Express* **2015**, 23 (14), 18611-18619.

32. Pham, T. N.; Du, W.; Conley, B. R.; Margetis, J.; Sun, G.; Soref, R.A.; Tolle, J.; Li, B. and Yu, S.-Q. Si-based $Ge_{0.9}Sn_{0.1}$ photodetector with peak responsivity of 2.85 A/W and longwave cutoff at 2.4 μm. *Electron. Lett.* **2015**, 51 (11), 854-856.

33. Chang, C.; Li, H.; Huang, S. H.; Cheng, H. H.; Sun, G. and Soref, R. A. Sn-based Ge/$Ge_{0.975}Sn_{0.025}$/Ge p-i-n photodetector operated with back-side illumination. *Appl. Phys. Lett.* **2016**, 108 (15), 151101-1-151101-4.

34. Cong, H.; Xue, C.; Zheng, J.; Yang, F.; Yu, K.; Liu, Z.; Zhang, X.; Cheng, B. and Wang, Q. Silicon Based GeSn p-i-n Photodetector for SWIR Detection. *IEEE Photon. J.* **2016**, 8 (5), 1-7.

35. Zheng, J.; Wang, S.; Liu, Z.; Cong, H.; Xue, C.; Li, C.; Zuo, Y.; Cheng, B. and Wang, Q. GeSn p-i-n photodetectors with GeSn layer grown by magnetron sputtering epitaxy. *Appl. Phys. Lett.* **2016**, 108 (3), 033503-1-033503-4.

36. Pham, T.; Du, W.; Tran, H.; Margetis, J.; Tolle, J.; Sun, G.; Soref, R. A.; Naseem, H. A.; Li, B. and Yu, S.-Q. Systematic study of Si-based GeSn photodiodes with 2.6 µm detector cutoff for short-wave infrared detection. *Opt. Express* **2016**, 24 (5), 4519-4531.

37. Huang, Y.-H.; Chang, G.-E.; Li, H. and Cheng, H. H. Sn-based waveguide p-i-n photodetector with strained GeSn/Ge multiple-quantum-well active layer. *Opt. Lett.* **2017**, 42 (9), 1652-1655.

38. Morea, M.; Brendel, C. E.; Zang, K.; Suh, J.; Fenrich, C. S.; Huang, Y.-C.; Chung, H.; Huo, Y.; Kamins, T. I.; Saraswat, K. C. and Harris, J. S. Passivation of multiple-quantum-well $Ge_{0.97}Sn_{0.03}$/Ge p-i-n photodetectors. *Appl. Phys. Lett.* **2017**,110 (9), 091109-1-091109-5.

39. Dong, Y.; Wang, W.; Xu, S.; Lei, D.; Gong, X.; Guo, X.; Wang, H.; Lee, S.-Y.; Loke, W.-K.; Yoon, S.-F.; and Yeo, Y.-C. Two-micron-wavelength germanium-tin photodiodes with low dark current and gigahertz bandwidth. *Opt. Express* **2017**, 25 (14), 15818-15827.

40. Wang, W.; Dong, Y.; Lee, S.-Y.; Loke, W.-K.; Lei, D.; Yoon, S.-F.; Liang, G.; Gong, X. and Yeo, Y.-C. Floating-base germanium-tin heterojunction phototransistor for high-efficiency photodetection in short-wave infrared range. *Opt. Express* **2017**, 25 (16), 18502-18507.

41. Tran, H.; Pham, T.; Du, W.; Zhang, Y.; Grant, P. C.; Grant, J. M.; Sun, G.; Soref, R. A.; Margetis, J.; Tolle, J.; Li, B.; Mortazavi, M.; and Yu, S.-Q. High-performance $Ge_{0.89}Sn_{0.11}$ photodiodes for low-cost shortwave infrared imaging. *J. Appl. Phys.* **2018**, 124 (1), 013101-1-013101-5.

42. Yasar, F.; Fan, W.; and Ma, Z. Flexible Amorphous GeSn MSM Photodetectors. *IEEE Photo. J.* **2018**, 10 (2), 2800109-1-2800109-10

43. Xu, S.; Huang, Y.-C.; Lee, K. H.; Wang, W.; Dong, Y.; Lei, D.; Masudy-Panah, S.; Tan, C. S.; Gong, X.; and Yeo, Y.-C. GeSn lateral p-i-n photodetector on insulating substrate. *Opt. Express* **2018**, 26 (13), 17312-17321.

44. Huang, B.-J; Lin, J.-H.; Cheng, H. H.; and Chang, G. -E. GeSn resonant-cavity-enhanced photodetectors on silicon-on-insulator platforms. *Opt. Lett.* **2018**, 43 (6), 1215-1218.

45. Wang, W.; Lei, D.; Huang, Y.-C.; Lee, K. H.; Loke, W.-K.; Dong, Y.; Xu, S.; Tan, C. S.; Wang, H.; Yoon, S. -F.; Gong, X.; and Yeo, Y. -C. High-performance GeSn photodetector and fin field-effect transistor (FinFET) on an advanced GeSn-on-insulator platform. *Opt. Express* **2018**, 8 (16), 10305-10314.

46. Soref, R. A.; Leonardis, F. D.; and Passaro, V. M. N. Simulations of Nanoscale Room Temperature Waveguide-Coupled Single-Photon Avalanche Detectors for Silicon Photonic Sensing and Quantum Applications. *ACS Appl. Nano Mater.* **2019**, 2, 7503-7512.

47. Kumar, H.; and Basu, R. Effect of Active Layer Scaling on the Performance of $Ge_{1-x}Sn_x$ Phototransistors. *IEEE Trans. Elec. Dev.* **2019**, 66 (9), 3667-3873.

48. Kumar, H.; and Basu, R. Design and Analysis of Ge/Ge$_{1-x}$Sn$_x$/Ge Heterojunction Phototransistor for MIR Wavelength Biological Applications. *IEEE Sens. J.* **2019**, 20 (7), 3504-3511.

49. Abdel-Rahman, M.; Alduraibi, M.; Hezam, M.; Ilahi, B. Sputter deposited GeSn alloy: A candidate material for temperature sensing layers in uncooled microbolometers. *Infrared Phys. Technol.* **2019**, 97, 376-380.

50. Jiayin Yang, J.; Hu, H.; Miao, Y.; Dong, L.; Wang, B.; Wang, W.; Su, H.; Xuan, R.; and Zhang, H. High-quality GeSn Layer with Sn Composition up to 7% Grown by Low-Temperature Magnetron Sputtering for Optoelectronic Application. *Mater.* **2019**, 12 (17), 2662-1-2662-11.

51. Xu, S.; Han, K.; Huang, Y. -C.; Lee, K. H.; Kang, Y.; Masudy-Panah, S.; Wu, Y.; Lei, D.; Zhao, Y.; Wang, H.; Tan, C. S.; Gong, X.; and Yeo, Y. -C. Integrating GeSn photodiode on a 200 mm Ge-on-insulator photonics platform with Ge CMOS devices for advanced OEIC operating at 2 µm band. *Opt. Express* **2019**, 27 (19). 26924-26939.

52. Xu, S.; Wang, W.; Huang, Y. -C.; Dong, Y.; Masudy-Panah, S.; Gong, X.; and Yeo, Y. -C. High-speed photo detection at two-micron-wavelength: technology enablement by GeSn/Ge multiple-quantum-well photodiode on 300 mm Si substrate. *Opt. Express* **2019**, 27 (4), 5798-5813.

53. Wang, X.; Covian, A. C.; Je, L.; Fu, S.; Li, H.; Piao, J.; Liu, J. GeSn on Insulators (GeSnOI) Toward Mid-infrared Integrated Photonics. *Font. Phys.* **2019**, 7 (134), 1-15.

54. Qian, L.; Tong, J.; Sou, F.; Liu, L.; Fan, W.; Luo, Y.; Zhang, D. H. GeSn/GaAs Hetero-Structure by Magnetron Sputtering. *IEEE J. Quantum. Electron.* **2019**, 56 (2), 4000305-1-4000305-5.

55. Tran, H.; Littlejohns, C. G.; Thomson, D. J.; Pham, T.; Ghetmiri, A.; Mosleh, A.; Margetis, J., Tolle, J.; Mashanovich, G. Z.; Du, W.; Li, B.; Mortazavi, M.; and Yu, S.-Q. Study of GeSn Mid-infrared Photodetectors for High Frequency Applications. *Front. Mater.* **2019**, 6 (278), 1-7.

56. Yang, F.; Yu, K.; Cong, H.; Xue, C.; Cheng, B.; Wang, N.; Zhou, L.; Liu, Z.; and Wang, Q. Highly Enhanced SWIR Image Sensors Based on Ge$_{1-x}$Sn$_x$–Graphene Heterostructure Photodetector. *ACS Photonics* **2019**, 6 (5), 1199-1206.

57. Zhao, Y.; Wang, N.; Yu, K.; Zhang, X.; Li, X.; Zheng, J.; Xue, C.; Cheng, B.; and Li, C. High performance silicon-based GeSn p–i–n photodetectors for short-wave infrared application. *Chin. Phys. B* **2019**, 28 (12), 128501-1-128501-5.

58. Tran, H.; Pham, T.; Margetis, J.; Zhou, Y.; Dou, W.; Grant, P. C.; Grant, J. M.; Al-Kabi, S.; Sun, G.; Soref, R. A.; Tolle, J.; Zhang, Y. -H.; Du, W.; Li, B.; Mortazavi, M.; and Yu, S. -Q. Si-Based GeSn Photodetectors toward Mid-Infrared Imaging Applications. *ACS Photonics* **2019**, 6 (11), 2807-2815.

59. Dev, S.; Khiangte, K. R.; and Lodha, S. Wafer-scale mono-crystalline GeSn alloy on Ge by sputtering and solid phase epitaxy. *J. Appl. Phys. D* **2020**, 53 (21), 1-6.

60. Xu, H.; Wu, Y.; Yeo, Y. -C.; and Gong, X. A Ladder Transmission Line Model for the Extraction of Ultralow Specific Contact Resistivity - Part II: Experimental Verification. *IEEE Trans. Elec. Dev.* **2020**, 67 (7), 2690-2696.

61. Hogsed, M.; Choe, K.; Miguel, N.; Wang, B.; and Kouvetakis, J. Radiation-induced electron and hole traps in $Ge_{1-x}Sn_x$ (x = 0 - 0.094). *J. Appl. Phys.* **2020**, 065708-1-065708-10.

62. Dascalescu, I.; Zoita, N. C.; Slav, A.; Matei, E.; Iftimie, S.; Comanescu, F.; Lepadatu, A. -M.; Palade, C.; Lazanu, S.; Buca, D.; Teodorescu, V. S.; Ciurea, M. L.; Braic, M.; and Stoica, T. Epitaxial GeSn Obtained by High Power Impulse Magnetron Sputtering and the Heterojunction with Embedded GeSn Nanocrystals for Shortwave Infrared Detection. *ACS Appl. Mater. Interfaces* **2020**, 12 (30), 33879-33886

63. Schlykow, V.; Manganelli, C. L.; Römer, F.; Clausen, C.; Augel, L.; Schulze, J.; Katzer, J.; Schubert, M. A.; Witzigmann, B.; Schroeder, T. Ge(Sn) nano-island/Si heterostructure photodetectors with plasmonic antennas. *Nanotechnology* **2020**, 31, 345203-1-345203-11.

64. Lv, Y.; Li, H.; Lee, K. -C.; Chang, G. -E.; Shieh, T. -H.; Wu, X. -S.; Chang, C. -R.; Wu, H. -C.; Hung, K. -M.; and Cheng, H. -H. Amplifying photocurrent of graphene on GeSn film by sandwiching a thin oxide between them. *Appl. Phys. Lett.* **2020**, 117, 152106-1-152106-5.

65. Hung, W. -T.; Barshilia, D.; Basu, R.; Cheng, H. H.; and Chang, G. -E. Silicon-based high-responsivity GeSn short-wave infrared heterojunction phototransistors with a floating base. *Opt. Lett.* **2020**, 45 (5), 1088-1091.

66. Wu, J.; Huang, D.; Ye, Y.; Wang, J.; Huang, W.; Li, C.; Chen, S. and Ke, S. Theoretical study of a group IV p–i–n photodetector with a flat and broad response for visible and infrared detection. *J. Semicond.* **2020**, 41, 1-7.

67. Ghosh, S.; Mukhopadhyay, B.; Sen, G.; Basu, P. K. Performance analysis of GeSn/SiGeSn quantum-well infrared photodetector in terahertz wavelength region. *Physica. E Low Dimens. Syst. Nanostruct.* **2020**, 115, 113692-1-113692-9.

68. Li, X. Y.; Wang, J. Y.; Liu, Y. F.; Chen, J. J.; Du, Y.; Wang, W.; Cai, Y.; Ma, J. P.; and Yu, M. B. Design of $Ge_{1-x}Sn_x$-on-Si waveguide photodetectors featuring high-speed high-sensitivity photodetection in the C- to U-bands. *Appl. Opt.* **2020**, 59 (25), 7646-7651.

69. Ghosh, S.; Mukhopadhyay, B.; Chang, G. -E. Design and Analysis of GeSn-Based Resonant-Cavity-Enhanced Photodetectors for Optical Communication Applications. *IEEE Sens. J.* **2020**, 20 (14), 7801-7809.

70. Zhou, H.; Xu, S.; Lin, Y.; Huang, Y. -C.; Son, B.; Chen, Q.; Guo, X.; Lee, K. H.; Goh, S. C.-K.; Gong, X. and Tan, C. S. High-efficiency GeSn/Ge multiple-quantum-well photodetectors with photon-trapping microstructures operating at 2 µm. *Opt. Express* **2020**, 28 (7), 10280-10293.

71. Wang, L.; Zhang, Y.; Wu, Y.; Liu, T.; Miao, Y.; Meng, L.; Jiang, Z.; Hu, H. Effects of Annealing on the Behavior of Sn in GeSn Alloy and GeSn-Based Photodetectors. *IEEE Trans. Elec. Dev.* **2020**, 67 (8), 3229-3234.

72. Lv, Y.; Lib, H.; Coileáin, C. Ó; Zhang, D.; Henga, C.; Chang, C. -R.; Hunge, K.-M.; Cheng, H. H. and Wu, H. -C. Photoelectrical properties of graphene/doped GeSn vertical heterostructures. *RSC Adv.* **2020**, 10, 20921-20917.

73. Tsai, C. -H.; Huang, B. -J.; A. Soref, R. A.; Sun, G.; Cheng, H. H. and Chang, G. -E. GeSn resonant-cavity-enhanced photodetectors for efficient photodetection at the 2 μm wavelength band. *Opt. Lett.* **2020**, 45 (6), 1463-1466.

74. Ghosh, S.; Lin, K. -C.; Tsai, C. -H; Kumar, H.; Chen, Q.; Zhang, L.; Son, B.; Tan, C. S.; Kim, M.; Mukhopadhayay, B.; Chang, G. -E. Metal-Semiconductor-Metal GeSn Photodetectors on Silicon for Short-Wave Infrared Applications. *Micromachines* **2020**, 11 (9), 795-1-795-12.

75. An, S.; Wu, S.; Tan, C. S.; Chang, G. -E; Gong, X. and Kim, M. Modulation of light absorption in flexible GeSn metal–semiconductor–metal photodetectors by mechanical bending. *J. Mater. Chem. C*, **2020**, 8, 13557-13562.

76. Atalla, M. R. M.; Assali, S.; Attiaoui, A.; Lemieux-Leduc, C.; Kumar, A.; Abdi, S.; Moutanabbir, O. All-group IV transferable membrane mid-infrared photodetectors. *Adv. Funct. Mater.* **2020**, 2006329-1-2006329-9.

77. Yang, Y.; Wang, X.; Wang, C.; Song, Y.; Zhang, M.; Xue, Z.; Wang, S.; Zhu, Z.; Liu, G.; Panlin Li, Dong, L.; Mei, Y.; Chu, P. K.; Hu, W.; Wang, J.; and Di, Z. Ferroelectric Enhanced Performance of a GeSn/Ge Dual-Nanowire Photodetector. *Nano Lett.* **2020**, 20, 5, 3872-3879.

78. Lee, K. -C.; Lin, M. -X.; Li, H.; Cheng, H. -H.; Sun, G.; Soref, R.; Hendrickson, J. R.; Hung, K.-M.; Scajev, P.; and Medvids, A. Planar GeSn photodiode for high-detectivity photodetection at 1550 nm. *Appl. Phys. Lett.* **2020**, 117, 012102-1-012102-5.

79. Landsberg, P. *Recombination in Semiconductors* (Cambridge: Cambridge University Press, 1991).

80. Van Roosbroeck, W. V.; and Shockley, W. Photon-Radiative Recombination of Electrons and Holes in Germanium. *Phys. Rev.* **1954**, 94, 1558-1560.

81. Gupta, S.; Simoen, E.; Loo, R.; Madia, O.; Lin, D.; Merckling, C.; Shimura, Y.; Conard, T.; Lauwaert, J.; Vrielinck,H.; and Heyns, M. Density and Capture Cross-Section of Interface Traps in GeSnO$_2$ and GeO$_2$ Grown on Heteroepitaxial GeSn. *ACS Appl. Mater. Interfaces* **2016**, 8, 21, 13181–13186.

82. Beattic, A. and Landsberg, P. T. Auger Effect in Semiconductors. *Proc. Roy. Soc.* **1959**, A249, 16-29.

83. Soref, R.; Hendrickson, J.; and Cleary, J. W. Mid- to long-wavelength infrared plasmonic photonics using heavily doped n-Ge/Ge and n-GeSn/GeSn heterostructures. *Opt. Express* **2012**, 20 (4), 3814-3824.

84. Kinch, M. A.; Brau, M. J.; and Simmon, S. Recombination mechanisms in 8-14 µm HgCdTe. *J. Appl. Phys.* **1973**, 44, 1649.

85. Dominici, S.; Wen, H.; Bertazzi, F.; Goano, M.; and Bellotti, E. Numerical study on the optical and carrier recombination processes in GeSn alloy for E-SWIR and MWIR optoelectronic applications. *Opt. Express* **2016**, 24 (23), 26363-80.

86. Adachi, S. *Properties of Aluminium Gallium Arsenide* (Inspec, London, UK, 1993).

87. Adachi, S. *Properties of Group-IV, III-V and II-VI semiconductors* (John Wiley & Sons Ltd, 2005).

88. Al-Kabi, S.; Ghetmiri, S. A.; Margetis, J.; Du, W.; Mosleh, A.; Alher, M.; Dou, W.; Grant, J. M.; Sun, G.; Soref, R. A.; Tolle, J.; Li, B.; Mortazavi, M.; Naseem, H. A.; and Yu, S.-Q. Optical characterization of Si-based $Ge_{1-x}Sn_x$ alloys with Sn compositions up to 12%. *J. Electron. Mater.* **2016**, 45, 4, 2133 – 2141.

89. Low, K. L.; Yang, Y.; Han, G.; Fan, W.; and Yeo, Y.-C. Electric band structure and effective mass parameters of $Ge_{1-x}Sn_x$ alloys. *J. Appl. Phys.* **2012**, 112, 103715-1-9.

90. Tran, H.; Du, W.; Ghetmiri, S. A.; Mosleh, A.; Sun, G.; Soref, R. A.; Margetis, J.; Tolle, J.; Li, B.; Naseem, H. A.; and Yu, S.-Q. Systematic study of $Ge_{1-x}Sn_x$ absorption coefficient and refractive index for the device applications of Si-based optoelectronics. *J. Appl. Phys.* **2016**, 119, 103106-1 – 103106-10.

91. J. A. Woollam Co., Inc., Guide to Using WVASE32®.

92. Fujiwara, H. *Spectroscopic Ellipsometry: Principles and Applications* (John Wiley & Sons, Ltd, West Sussex, UK, 2007).

93. Kasper, E.; M. Kittler, M.; Oehme, M.; and Arguirov, T. Germanium tin: silicon photonics toward the mid-infrare. *Photon. Res.* **2013**, 1, 69–76.

94. V. R. D'Costa, V. R.; W. Wang, W.; Q. Zhou, W.; T. K. Chan, T. K.; T. Osipowicz, T.; E. S. Tok, E. S.; and Yeo, Y.-C. Compositional dependence of optical critical point parameters in pseudomorphic GeSn alloys. *J. Appl. Phys.* **2014**, 116, 053520.

95. Medikonda, M.; Muthinti, G. R.; Vasić, R.; Adam, T. N.; Reznicek, A.; Wormington, M.; Malladi, G.; Kim, Y.; Huang, Y. -C.; and Diebold, A. C. Optical properties of pseudomorphic $Ge_{1-x}Sn_x$ (x = 0 to 0.11) alloys on Ge(001). *J. Vac. Sci. Technol. B* **2014**, 32, 061805.

96. Kasap, S.; and Capper, P. *Springer Handbook of Electronic and Photonic Materials* (Springer, New York, 2006) p. 47-77.

97. Urbach, F. The long-wavelength edge of photographic sensitivity and of the electronic absorption of solids. *Phys. Rev.* **1953**, 92, 1324.

98. Grundmann, M. *The Physics of Semiconductors: An Introduction Including Devices and Nanophysics* (Springer-Verlag, Berlin, 2006) p. 223-225.

99. Grein, C. H.; and John, S. Temperature dependence of the Urbach optical absorption edge: A theory of multiple phonon absorption and emission sidebands. *Phys. Rev. B* **1989**, 39, 1140.

100. Chang, Y.; Badano, G.; Zhao, J.; Zhou, Y. D.; Ashokan, R.; Grein, C. H.; and Nathan, V. Near-bandgap infrared absorption properties of HgCdTe. *J. Electron. Mater.* **2004**, 33, 709.

101. Chang, Y.; Grein, C. H.; and Sivananthan, S. Narrow gap HgCdTe absorption behavior near the band edge including nonparabolicity and the Urbach tail. *Appl. Phys. Lett.* **2006**, 89, 062109.

102. Tolle, J. *U. S. Patent No. 20140087544* (27 March 2014).

103. Du, W.; Zhou, Y.; Ghetmiri, S. A.; Mosleh, A.; Conley, B. R.; Nazzal, A.; Soref, R.A.; Sun, G.; Tolle, J.; Margetis, J.; Naseem, H. A.; and Yu, S.-Q. Room-temperature electroluminescence from Ge/Ge$_{1-x}$Sn$_x$/Ge diodes on Si substrates. *Appl. Phys. Lett.* **2014**, 104, 241110.

104. Ghosh, G. *Handbook of Thermo-Optic Coefficients of Optical Materials with Applications* (Academic Press, San Diego, 1998) p. 9-15.

105. Yu, S. -Q.; Ghetmiri, S. A.; Du, W.; Margetis, J.; Zhou, Y.; Mosleh, A.; Al-Kabi, S.; Nazzal, A.; Sun, G.; Soref, R. A.; Tolle, J.; Li, B.; and Naseem, H. A. Si-based GeSn light emitter: mid-infrared devices in Si photonics. *Proc. SPIE 9367, Silicon Photonics X*, **2015**, 93670R.

106. Johs, B.; Herzinger, C. M.; Dinan, J. H.; Cornfeld, A.; Benson, J. D. Development of a parametric optical constant model for Hg$_{1-x}$Cd$_x$Te for control of composition by spectroscopic ellipsometry during MBE growth. *Thin Solid Films* **1998**, 313–314, 137–142.

107. Barnes, N. P.; and Piltch, M. S. Temperature-dependent Sellmeier coefficients and nonlinear optics average power limit for germanium. *J. Opt. Soc. Am.* **1979**, 69, 178–180.

108. Kao, K. C. *Dielectric Phenomena in Solids* (Elsevier Academic Press, San Diego, 2004) p. 143-144.

109. Haynes, J. R.; Lax, M.; and Flood, W. F. Exciton and phonon effects in the absorption spectra of germanium and silicon. *J. Phys. Chem. Solids* **1959**, 8, 392.

110. Gallagher, J. D.; Xu, C.; Jiang, L.; Kouvetakis, J.; and Menéndez, J. Fundamental bandgap and direct-indirect crossover in Ge$_{1-x-y}$Si$_x$Sn$_y$ alloys. *Appl. Phys. Lett.* **2013**, 103, 202104.

111. Kinch, M. A. *Fundamentals of infrared detector materials* (Washington: SPIE, 2007).

112. Diffey, B. L. *Radiation Measurement in Photobiology* (San Diego: Academic Press, 1989).

113. Mitchell, B. S. *An Introduction to Materials Engineering and Science for Chemical and Materials Engineers* (New Jersey: John Wiley & Sons, 2004).

114. Davis, A. P.; Elliott, C. T.; and White, A. M. Current gain in photodiode structures. *Infrared Phys.* **1991**, 31, 575-577.

115. Hovel, H. J. *Semiconductors and Semimetals*, Vol. 11, eds R. K. Willardson and A. C. Beer (Academic Press, New York, 1975).

116. Fukuda, M. "Photodiodes" in *Optical Semiconductor Devices.* Edited by K. Chang (New York: John Wiley & Sons, 1999) Chapter 4, pp. 211-217.

117. Rogalski, A. "Theory of Photon Detectors" in *Infrared Detectors* (Boca Raton: CRC Press, 2010) Chapter 9, pp. 197-213.

118. Kinch, M. A. "Metal-Insulator-Semiconductor Infrared Detectors," in *Semiconductors and Semimetals,* Vol. 18. Edited by R.K Willardson and A.C. Beer (New York: Academic Press, 1981) Chapter 7, pp. 313-377.

119. Sah, C.-T. "P/N and other Junction Diodes" in *Fundamentals of Solid-state Electronics* (Singapore: World Scientific Publishing, 1991) Chapter 5, pp. 382-517.

120. He, L.; Yang, D.; and Ni, G. "Design Methods for HgCdTe Infrared Detectors" in *Technology for Advanced Focal Plane Arrays of HgCdTe and AlGaN* (Berlin Heidelberg: Springer, 2016) Chapter 2, pp. 17-115.

121. Gopal, V.; Qiu, W.; and W. Hu. Modeling of illuminated current-voltage characteristics to evaluate leakage currents in long-wavelength infrared mercury cadmium telluride photovoltaic detectors. *J. Appl. Phys.* **2014**, 116, 184503-1-10.

122. Snowden, C. M.; and Miles, R. E. *Compound Semiconductor Device Modelling* (London: Springer-Verlag, 1993).

123. Kircher, R. and Bergner, W. *Three-Dimensional Simulation of Semiconductor Devices* (Munich: Springer Basel AG, 1991).

124. Vasileska, D.; Goodnick, S. M.; and Klimeck, G. *Computational Electronics: Semiclassical and Quantum Device Modeling and Simulation* (New York: CRC Press, 2010).

125. Dou, W.; Benamara, M.; Mosleh, A.; Margetis, J.; Grant, P.; Zhou, Y.; Al-Kabi, S.; Du, W.; Tolle, J.; Li, B.; Mortazavi, M.; Yu, S.-Q. Investigation of GeSn strain relaxation and spontaneous composition gradient for low-defect and high-Sn alloy growth. *Sci. Rep.* **2018**, 8 (5640), 1-11.

126. Basu, P.K. *Theory of optical processes in semiconductors: bulk and microstructures* (Oxford: University Press, 1997).

127. Dou, W.; Zhou, Y.; Margetis, J.; Ghetmiri, S. A.; Al-Kabi, S.; Du, W.; Liu, J.; Sun, G.; Soref, R. A.; Tolle, J.; Li, B.; Mortazavi, M.; and Yu, S.-Q. Optically pumped lasing at 3 µm from compositionally graded GeSn with tin up to 22.3%. *Opt. Lett.* **2018,** 43 (19), 4558-4561.

128. Long, D. "Photovoltaic and Photoconductive Infrared Detectors," in *Optical and Infrared Detectors*, ed. R. J. Keyes (Springer-Verlag, Berlin, 1977) 101–47.

129. Bratt, P. R. "Impurity Germanium and Silicon Infrared Detectors," in *Semiconductors and Semimetals*, Vol. 12, eds. R. K. Willardson and A. C. Beer (Academic Press, New York, 1977) 39–142.

130. Varshni, Y. P. Temperature dependence of the energy gap in semiconductors. *Physica* **1967**, 34 (1), 149-154.

131. Schroder, D. K. "Series Resistance, Channel Length and Width, and Threshold Voltage" in *Semiconductor Material and Device Characterization* (New Jersey: John Wiley & Sons, 2006) Chapter 4, pp. 185-188.

132. Sze, S. M.; and Ng, K. K. *Physics of Semiconductor Devices* (New Jersey: John Wiley and Sons, 2007).

133. Willeke, G. P.; and Weber, E. R. *Semiconductors and Semimetals, Volume 89* (San Diego: Academic Press, 2013).

134. Matlab (The Mathworks Inc.), 3 Apple Hill Drive, Natick, MA 01760.

135. SILVACO® (2016) ATLAS™ User's Manual.

136. Sarusi, G.; Zemel, A.; Sher, A.; and Eger, D. Forward tunneling current in HgCdTe photodiodes. *J. Appl. Phys.* **1994**, 76, 4420-4425.

137. Riben, A. R.; and Feucht, D. L. Electrical Transport in nGe-pGaAs Heterojunction. *Int. J. Electron.* **1966**, 20 (6), 583-599.

138. Henini, M.; and Razeghi, M. *Handbook of Infrared Detection Technologies* (New York: Elsevier Science, 2002).

139. Nalwa, H. S. *Photodetectors and Fiber Optics* (San Diego: Academic Press, 2001).

140. Ghione, G. *Semiconductor Devices for High-Speed Optoelectronics* (New York: Cambridge University Press, 2009).

141. Cao, W.; Hagan, D.; Thomson, D. J.; Nedeljkovic, M.; Littlejohns, C. G.; Knights, A.; Alam, S.-U.; Wang, J.; Gardes, F.; Zhang, W.; Liu, S.; Li, K.; Rouifed, M. S.; Xin, G.; Wang, W.; Wang, H.; Reed, G. T.; and Mashanovich, G. Z. High-speed silicon modulators for the 2 µm wavelength band. *Optica* **2018**, 5, 1055–1062.

142. Capmany, J.; Li, G.; Lim, C.; and Yao, J. Microwave photonics: current challenges towards widespread application. *Opt. Express* **2013**, 21, 22862–22867.

143. Capmany, J.; and Novak, D. Microwave photonics combines two worlds. *Nat. Photon.* **2007**, 1, 319–330.

144. Hagan, D. E.; Nedeljkovic, M.; Cao, W.; Thomson, D. J.; Mashanovich, G. Z.; and Knights, A. P. Experimental quantification of the free-carrier effect in silicon waveguides at extended wavelengths. *Opt. Express* **2019**, 27, 166–174.

145. Jenkins, D. W.; and Dow, J. D. Electronic properties of metastable Ge_xSn_{1-x} alloys. *Phys. Rev. B* **1987**, 36, 7994.

146. Kim, S.; Gupta, J.; Bhargava, N.; Coppinger, M.; and Kolodzey, J. Current-voltage characteristics of GeSn/Ge heterojunction diodes grown by molecular beam epitaxy. *IEEE Electron Device Lett*. **2013**, 34, 1217–1219.

147. Li, Z.; Hedit, A. M.; Simakov, N.; Jung, Y.J.; Daniel, M. O.; Alam, S. U.; and Richardson, D. J. Diode-pumped wideband thulium-doped fiber amplifiers for optical communications in the 1800-2050 nm window. *Opt. Express* **2013**, 21, 26450–26455.

148. Lin, J.-H.; and Chang, G.-E. "Mid-infrared electro-absorption optical modulation in GeSn photodiodes on Silicon," in *IEEE Photonics Society Summer Topical Meeting* **2018** (Waikoloa Village, HI).

149. Liu, W.; Li, M.; Guzzon, R. S.; Norberg, E. J.; Parker, J. S.; Lu, M.; Coldren, L. A.; and Yao, J. A fully reconfigurable photonic integrated signal processor. *Nat. Photon.* **2016**, 10, 190–195.

150. McEvoy, A.; Markvart, T.; and Castaner, L. *Practical Handbook of Photovoltaics, 2nd Edn* (Waltham, MA: Elsevier, 2012).

151. Oehme, M.; Kostecki, K.; Ye, K.; Bechler, S.; Ulbricht, K.; Schmid, M.; Kaschel, M.; Gollhofer, M.; Körner, R.; Zhang, W.; Kasper, E.; and Schulze, J. GeSn-on-Si normal incidence photodetectors with bandwidths more than 40 GHz. *Opt. Express* **2014**, 22, 839–846.

152. Roelkens, G.; Dave, U.; Gassenq, A.; Hattasan, N.; Hu, C.; Kuyken, B.; Leo, F.; Malik, A.; Muneeb, M.; Ryckeboer, E.; Uvin, S.; Hens, Z.; Baets, R.; Shimura, Y.; Gencarelli, F.; Vincent, B.; Loo, R.; Campenhout, J. V.; Cerutti, L.; Rodriguez, J.-B.; Tournié, E.; Chen, X.; Nedeljkovic, M.; Mashanovich, G.; Shen, L.; Healy, N.; Peacock, A. C.; Liu, X.; Osgood, R.; and Green, W. Silicon-based heterogeneous photonic integrated circuits for the mid-infrared. *Opt. Mater. Express* **2013**, 3, 1523–1536.

153. Soref, R. "Towards silicon-based longwave integrated optoelectronics (LIO)," in *SPIE Photonic West, Invited Paper Silicon Photonics III* **2008** (San Jose, CA), 6898–6895.

154. Thomson, D.; Zilkie, A.; Bowers, J. E.; Komljenovic, T.T; Reed, G.; Vivien, L.; Marris-Morini, D.; Cassan, E.; Virot, L.; Fédéli, J.-M.; Hartmann, J.-M.; Schmid, J. H.; Xu, D.-X.; Boeuf, F.; O'Brien, P.; Mashanovich, G. Z.; and Nedeljkovic, M. Roadmap on silicon photonics. *J. Opt*. **2016,** 18, 073003.

155. Zhang, W.; and Yao, J. Silicon-based integrated microwave photonics. *IEEE J. Quantum Electron.* **2016,** 52, 0600412.

156. Bulman, P. J.; Hobson, G. S.; and Taylor, B. C. *Transferred Electron Devices* (New York: Academic Press, 1972).

Appendix

Appendix A

Table A.1 The relevant parameters of GeSn for the calculation in this dissertation.

Parameters	Ge	Sn
Lattice constant a (nm)	0.56573	0.64892
Bowing parameter b (nm)	-0.0066	
Effective mass m_c (m0)	0.038	0.058
Effective mass $m_{t,L}$ (m0)	0.0807	0.075
Effective mass $m_{l,L}$ (m0)	1.57	1.478
Luttinger's parameters γ_1	13.38	-14.97
Luttinger's parameters γ_2	4.24	-10.61
Luttinger's parameters γ_3	5.69	-8.52
Bandgap E_g^Γ (eV)	0.7985	-0.413
Bandgap E_g^L (eV)	0.664	0.092
Deformation potentials a_c (eV)	-8.24	-6
Deformation potentials a_L (eV)	-1.54	-2.14
Deformation potentials a_v (eV)	1.24	1.58
Deformation potentials b_v (eV)	-2.9	-2.7
Elastic constants C_{11} (GPa)	128.53	69.00
Elastic constants C_{12} (GPa)	48.26	29.30
Elastic constants C_{44} (GPa)	68.30	36.20
Calculated Poisson ratio $$v = \frac{C_{12}}{C_{11} + C_{12}}$$	0.27	0.30
Shear modulus μ (GPa)[132] $$\mu = C_{44} - \frac{(2C_{44} + C_{12} - C_{11})}{3}$$	49.52	25.30
Interaction parameter α (eV)	0.27	

Appendix B

B1. Matlab Code for dark current analysis:

```matlab
options =
optimset('Display','iter','PlotFcns',{@optimplotx,@optimplotfval},'TolFun',1E
-1,'TolX',1E-1,'MaxIter',30);
%x0=[Adiff0,Agr0,Egrt0,ATAT0,BTAT0,ABBT0,BBBT0,inv_Rshunt0];
x0=[2.55048212715261e-
05,0.0102115510652944,0.0498683395632894,0.00836188741782544,5.3,0.4480142335
57376,8.71303095656367,0.000145731857760482];
fun=@objectivefcn2;
[x,fval,exitflag,output] = fminsearch(fun,x0,options);
%[x,fval,exitflag,output] = fzero(fun,x0,options);
Adiff=abs(x(1));
Agr=abs(x(2));
Egrt=abs(x(3));
ATAT=abs(x(4));
BTAT=abs(x(5));
ABBT=abs(x(6));
BBBT=abs(x(7));
inv_Rshunt=(x(8));
k=8.617E-5; %eV/K
q=1.6E-19;
h_bar=6.582E-16; %eVs
h= h_bar*2*pi; %eVs
ni_Ge=2.4E13;%Ge intrinsic Sze cm^-3
T=300; %K
%GeSn
x_Sn= 0.11;% percentage of Sn
delta_Ev= x_Sn*0.69;
Eg_GeSn=(1-x_Sn)*0.892+((-0.413)*x_Sn)-(1-x_Sn)*x_Sn*2.92;
delta_Eg=abs(Eg_GeSn-0.892);
delta_Ec=abs(delta_Eg-delta_Ev);
delta=((delta_Ec-delta_Ev)/2);
gamma1=14.31-37.04*(x_Sn)+560.24*(x_Sn)^2;
gamma2=4.95-19.16*(x_Sn)+280.14*(x_Sn)^2;
gamma3=6.32-18.69*(x_Sn)+280.59*(x_Sn)^2;
m_HH=1/(gamma1-2*gamma2);
m_LH=1/(gamma1+2*gamma2);
m_h_avg_GeSn=(m_HH^1.5+m_LH^1.5)^(2/3);
m_e_avg_GeSn=0.0505*Eg_GeSn;
m0=9.109E-31; %kg
h=6.626E-34;%J.s
Nc_GeSn=2*(2*pi*m_e_avg_GeSn*m0*k*T*1.6E-19/(h^2*10000))^(3/2);
Nv_GeSn=2*(2*pi*m_h_avg_GeSn*m0*k*T*1.6E-19/(h^2*10000))^(3/2);
ni_GeSn=sqrt(Nc_GeSn*Nv_GeSn)*exp(-Eg_GeSn/(2*k*T));
n_GeSn=sqrt(33.59*x_Sn+14.67+(-9.62)*x_Sn+1.33);
ni=ni_GeSn;
n_Ge=4;
epsi_s_Ge=n_Ge^2;
epsi_s_GeSn=n_GeSn^2;
epsi0=8.854E-12;%F/m
epsi_Ge=epsi_s_Ge*epsi0;
epsi_GeSn=epsi_s_GeSn*epsi0;
ND = 1E17; %cm^-3
```

```matlab
NA = 2E18; %cm^-3
A=pi*((125E-6)^2);%m^2
V0=(k*T)*log((NA.*ND)/(ni^2)); %V
RVread=xlsread('RV300K.xlsx');
V=RVread(:,1);
Rexp=RVread(:,2);
f=0;
% Diffusion
inv_Rdiff = Adiff*(1/(k*T)).*exp(V/(k*T));
% Generation Recombination
Ei = Eg_GeSn/2; %eV
b = exp(-V/(2*k*T))*cosh((Egrt-Ei)/(k*T));
der_b = -1/(2*k*T)*b;
for i = 1:length(V)
    if b(i) > 1
        f_b(i) = log(b(i)+sqrt(b(i)^2-1))/sqrt(b(i)^2-1);
        der_f_b(i) = 1/(b(i)^2-1)-(b(i)*log(b(i)+sqrt(b(i)^2-1))/(b(i)^2-
1)^3/2)*der_b(i);
    elseif b(i) == 1
        f_b(i) = 1/b(i);
        der_f_b(i) = -1/(b(i)^2)*der_b(i);
    else b(i) < 1
        f_b(i) = 1/sqrt(1-b(i)^2)*(pi()/2-atan(b(i)/sqrt(1-b(i)^2)));
        der_f_b(i) = (b(i)*(pi()/2-atan(b(i)/sqrt(1-b(i)^2)))/(1-b(i)^2)^3/2-
...
            (b(i)^2/(1-b(i)^2)^3/2+1/sqrt(1-b(i)^2))/((b(i)^2/(1-
b(i)^2))*sqrt(1-b(i)^2)))*der_b(i);
    end
end
for i = 1:length(V)
    inv_Rgr(i) = abs(Agr*sinh(V(i)/(2*k*T))/((1-V(i)/V0)^1/2)*der_f_b(i)...
            +Agr*f_b(i)*(sinh(V(i)/(2*k*T))/(2*V0*((1-
V(i)/V0)^3/2))+(2*k*T)*cosh(V(i)/(2*k*T))/((1-V(i)/V0)^1/2)));
end
% TAT
inv_RTAT =abs(ATAT*(-exp(-BTAT./sqrt(V0-V)))-(ATAT*BTAT*exp(-BTAT./sqrt(V0-
V))./(2*sqrt(V0-V))));
% BBT
inv_RBBT =abs(-1/2*ABBT*BBBT*exp(-BBBT./sqrt(V0-V))-3/2*(ABBT*sqrt(V0-
V).*exp(-BBBT./sqrt(V0-V))));

for i=1:length(V)
    inv_R_fit(i) = inv_Rdiff(i)+inv_Rgr(i)+inv_RTAT(i)+inv_RBBT(i)+inv_Rshunt;
end
Rdiff=1./inv_Rdiff;
Rgr=1./inv_Rgr';
RTAT=1./inv_RTAT;
RBBT=1./inv_RBBT;
Rshunt =1/inv_Rshunt*ones(length(V),1);
Rfit=1./inv_R_fit';
figure (2)
plot (V,Rexp,'*',V,Rfit)
figure (3)
semilogy (V,Rexp,'*',V,Rfit,'-or',V,Rgr,'-+k',V,Rshunt,'-db',V,RTAT,'-
sg',V,Rdiff,'-py',V,RBBT,'-xy','linewidth',2)
legend('Rexp','Rfit','Rgr','Rshunt','RTAT','Rdiff','RBBT')
```

B2. Trap Density

```
%N type Ge, undoped GeSn, P type Ge
k=8.617E-5; %eV/K
T=300; %K
q=1.6E-19;
h_bar=6.582E-16; %eVs
h= h_bar*2*pi; %eVs
ni_Ge=2.4E13;%Ge intrinsic Sze
%GeSn
x_Sn= 0.11;% percentage of Sn
delta_Ev= x_Sn*0.69;
Eg_GeSn=(1-x_Sn)*0.892+((-0.413)*x_Sn)-(1-x_Sn)*x_Sn*2.92;
delta_Eg=abs(Eg_GeSn-0.892);
delta_Ec=abs(delta_Eg-delta_Ev);
delta=((delta_Ec-delta_Ev)/2);
gamma1=14.31-37.04*(x_Sn)+560.24*(x_Sn)^2;
gamma2=4.95-19.16*(x_Sn)+280.14*(x_Sn)^2;
gamma3=6.32-18.69*(x_Sn)+280.59*(x_Sn)^2;
m_HH=1/(gamma1-2*gamma2);
m_LH=1/(gamma1+2*gamma2);
m_h_avg_GeSn=(m_HH^1.5+m_LH^1.5)^(2/3);
m_e_avg_GeSn=0.0505*Eg_GeSn;
m0=9.109E-31; %kg
h=6.626E-34;%J.s
Nc_GeSn=2*(2*pi*m_e_avg_GeSn*m0*k*T*1.6E-19/(h^2*10000))^(3/2);
Nv_GeSn=2*(2*pi*m_h_avg_GeSn*m0*k*T*1.6E-19/(h^2*10000))^(3/2);
ni_GeSn=sqrt(Nc_GeSn*Nv_GeSn)*exp(-Eg_GeSn/(2*k*T));
n_GeSn=sqrt(33.59*x_Sn+14.67+(-9.62)*x_Sn+1.33);
ni=ni_GeSn;
n_Ge=4;
epsi_s_Ge=n_Ge^2;
epsi_s_GeSn=n_GeSn^2;
epsi0=8.854E-12;%F/m
epsi_Ge=epsi_s_Ge*epsi0;
epsi_GeSn=epsi_s_GeSn*epsi0;
A1= 1/[0.00323272764291854];
B=[4.32568943912398];
A=pi*((125E-6)^2);
NA=2E18;
ND=1E17
Eg_GeSn_T=0.46+5.07E-4*((300^2/(300+194))-(T^2/(T+194)))
%
deltaE=(B*q*sqrt(1E6)*(3*h_bar*((2*NA/epsi_GeSn)^(1/2)))/(4*((2*m_e_avg_GeSn*
m0)^(1/2))))^(2/3)
deltaE=(B*(3*q*h_bar*sqrt(1E6)*((2*NA/epsi_GeSn)^(1/2)))/(4*((2*m_e_avg_GeSn*
m0)^(1/2))))^(2/3)
Et=Eg_GeSn_T-deltaE
Nt=A1*h^3*deltaE/(2*q^3*A*pi^2*1E-23*m0)
V0=(k*T)*log((NA.*ND)/(ni^2)); %V
```

Appendix C: All Publications Published, Submitted, and Planned

Chapter 3 was largely reproduced from publications in the Journal of Applied Physics. Chapters 4 and 5 were partly reproduced from the paper which was published in ACS Photonics. Chapter 6 was partly reproduced from the publication in Frontiers in Materials.

C.1 List of peer-reviewed published works

[16] Y. Zhou, Y. Miao, S. Ojo, **H. Tran**, G. Abernathy, J. M. Grant, S. Amoah, G. Salamo, W. Du, J. Liu, J. Margetis, J. Tolle, Y.-H. Zhang, G. Sun, R. A. Soref, B. Li, and S.-Q. Yu, *Electrically injected GeSn lasers on Si operating up to 100 K*, Submitted to Optica, Accepted.

[15] S. Madhusoodhanan, A. Sabbar, **H. Tran**, B. Dong, J. Wang, A. Mantooth, S.-Q. Yu, and Z. Chen, *High-Temperature Analysis of GaN-based MQW Photodetector for Optical Galvanic Isolations in High-Density Integrated Power Modules*, IEEE Journal of Emerging and Selected Topics in Power Electronics.

[14] **H. Tran**, C. G. Littlejohns, D. J. Thomson, T. Pham, S. A. Ghetmiri, A. Mosleh, J. Margetis, J. Tolle, G. Z. Mashanovich, W. Du, B. Li, M. Mortazavi, and S.-Q. Yu, *Study of GeSn Mid-infrared Photodetectors for High-Frequency Applications*, Frontiers in Materials, Vol. 6, Article 278 (2019).

[13] **H. Tran**, T. Pham, J. Margetis, Y. Zhou, W. Dou, P. C. Grant, J. M. Grant, S. Al-Kabi, G. Sun, R. A. Soref, J. Tolle, Y.-H. Zhang, W. Du, B. Li, M. Mortazavi, and S.-Q. Yu, *Si-based GeSn photodetectors towards mid-infrared imaging applications*, ACS Photonics 2019, 6, 11, 2807–2815

[12] P. C. Grant, W. Dou, B. Alharthi, J. M. Grant, **H. Tran**, G. Abernathy, A. Mosleh, W. Du, B. Li, M. Mortazavi, H. A. Naseem, S.-Q. Yu, *UHV-CVD Growth of High-Quality GeSn Using SnCl4: From Growth Optimization to Prototype Devices,* Optical Materials Express, Vol. 9, No. 8 pp 3277-3291(2019). Editors' suggestion.

[11] Y. Zhou, W. Dou, W. Du, S. Ojo, **H. Tran**, S. A. Ghetmiri, J. Liu, G. Sun, R. Soref, J. Margetis, J. Tolle, B. Li, Z. Chen, M. Mortazavi, S.-Q. Yu, *Optically Pumped GeSn Lasers Operating at 270 K with Broad Waveguide Structures on Si*, *ACS Photonics* 2019, 6, 6, 1434–1441.

[10] S. V. Kondratenko, Y. V. Hyrka, Y. I. Mazur, A.V. Kuchuk, W. Dou, H. Tran, J. Margetis, J. Tolle, W. Du, S.-Q. Yu, and G. J. Salamo, *Photovoltage spectroscopy of direct and indirect bandgaps of strained $Ge_{1-x}Sn_x$ thin films on Ge/Si(001) substrate*, Acta Materialia, Volume 171, 1 June 2019, 40-47.

[9] J. Margetis, Y. Zhou, W. Dou, P. C. Grant, W. Du, B. Alharthi, H. Tran, S. Ojo, G. Abernathy, S. A. Ghetmiri, J. Liu, G. Sun, R. Soref, J. Tolle, B. Li, M. Mortazavi, S.-Q. Yu, *All group-IV SiGeSn/GeSn/SiGeSn QW laser on Si operating up to 90 K*, Appl. Phys. Lett. 113, 221104 (2018).

[8] W. Dou, B. Alharthi, P. C. Grant, J. M. Grant, A. Mosleh, **H. Tran**, W. Du, M. Mortazavi, B. Li, H. Naseem, and S.-Q. Yu, *Crystalline GeSn growth by plasma-enhanced chemical vapor deposition*, Opt. Mater. Express 8, 3220-3229 (2018), Editors' suggestion.

[7] **H. Tran**, T. Pham, W. Du, Y. Zhang, P. C. Grant, J. M. Grant, G. Sun, R. A. Soref, J. Margetis, J. Tolle, B. Li, M. Mortazavi, and S.-Q. Yu, *High-performance $Ge_{0.89}Sn_{0.11}$ photodiode for low-cost shortwave infrared imaging*, Journal of Applied Physics 124, 013101 (2018).

[6] B. Alharthi, J. Margetis, **H. Tran**, S. Al-Kabi, W. Dou, S. A. Ghetmiri, A. Mosleh, J. Tolle, W. Du, M. Mortazavi, B. Li, H. Naseem, and S.-Q. Yu, *Study of material and optical properties of $Si_xGe_{1-x-y}Sn_y$ alloys for Si-based optoelectronic device applications*, Optical Materials Express, Vol. 7, Issue 10, pp. 3517-3528 (2017).

[5] W. Du, S. Al-Kabi, S. Ghetmiri, **H. Tran**, T. Pham, B. Alharthi, A. Mosleh, J. Margetis, J. Tolle, H. Naseem, M. Mortazavi, G. Sun, R. Soref, B. Li, and S. -Q. Yu, *Development of SiGeSn Technique towards Mid-Infrared Devices in Silicon Photonics*, ECS Transactions, 75 (8) 231-239 (2016)

[4] T. Pham, W. Du, **H. Tran**, J. Margetis, J. Tolle, G. Sun, R. A. Soref, H. A. Naseem, B. Li, and S.-Q. Yu, *Systematic study of Si-based GeSn photodiodes with 2.6 μm detector cutoff for short-wave infrared detection*, Opt. Express, Vol. 24, Issue 5, pp. 4519-4531 (2016).

[3] **H. Tran**, W. Du, S. A. Ghetmiri, A. Mosleh, G. Sun, R. A. Soref, J. Margetis, J. Tolle, B. Li, H. A. Naseem, and S.-Q. Yu, *Systematic Study of $Ge_{1-x}Sn_x$ absorption coefficient and refractive index for the device applications of Si-based optoelectronics*, Journal of Applied Physics 119, 103106 (2016).

[2] A. Mosleh, M. Alher, L. Cousar, H. Abu-safe, W. Dou, P. C. Grant, S. Al- Kabi, S. A. Ghetmiri, B. Alharthi, **H. Tran**, W. Du, M. Benamara, B. Li, M. Mortazavi, S.-Q. Yu, and H. Naseem, *Enhancement of Material Quality of (Si)GeSn Films Grown By SnCl4 Precursor*, ECS Transactions, 69 (5) 279-286 (2015).

[1] B. R. Conley, Joe Margetis, W. Du, **H. Tran**, A. Mosleh, S. A. Ghetmiri, J. Tolle, G. Sun, R. Soref, B. Li, H. A. Naseem, and S.-Q. Yu, *Si-based GeSn photoconductors with a 1.63A/W peak responsivity and a 2.4μm long-wavelength cutoff*, Applied Physics Letters, 105, 221117 (2014).

C.2 List of conference proceedings and publications

[21] S. A. Ghetmiri, **H. Tran**, A. Mosleh, W. Du, J. Liu, B. Li, M. Mortazavi, and S.-Q. Yu, Si-based GeSn Photodetector for Mid-Infrared Integrated Microwave Photonics, International Topical Meeting on Microwave Photonics in Ottawa, Canada, Oct (2019)

[20] Y. Zhou, **H. Tran**, and S. -Q. Yu, W. Du, J. Margetis, J. Tolle, S. Ghetmiri, A. Mosleh, M. Mortazavi, G. Sun, R. Soref, and B. Li, 2019 IEEE BiCMOS and Compound Semiconductor Integrated Circuits and Technology Symposium (BCICTS), Nashville, TN, USA

[19] Y. Zhou, **H. Tran**, and S. -Q. Yu, W. Du, J. Margetis, J. Tolle, S. Ghetmiri, A. Mosleh, and M. Mortazavi, G. Sun, R. Soref, and B. Li, *Development of GeSn Emitters and Detectors towards Integrated Mid-Infrared Photonics Applications*, IEEE Research and Applications of Photonics in Defense (RAPID 2019), Miramar Beach, FL, 8/19-8/21, TuD 1.2.

[18] Y. Zhou, J. Margetis, G. Abernathy, W. Dou, P. C. Grant, B. Alharthi, W. Du, A. Wadsworth, Q. Guo, **H. Tran**, S. Ojo, A. Mosleh, S. A. Ghetmiri, G. B. Thompson, J. Liu, G. Sun, R. Soref, J. Tolle, B. Li, M. Mortazavi, S. -Q. Yu, *Investigation of SiGeSn/GeSn/SiGeSn Quantum Well Structures and Optically Pumped Lasers on Si*, CLEO 2019 (San Jose): Science and Innovations, STu3N. 3

[17] **H. Tran**, T. Pham, J. Margetis, Y. Zhou, W. Dou, P. C. Grant, J. M. Grant, S. Al-Kabi, W. Du, G. Sun, R. A. Soref, J. Tolle, B. Li, M. Mortazavi, S. -Q. Yu, *Study of High-Performance GeSn Photodetectors with Cutoff Wavelength up to 3.7 μm for Low-Cost Infrared Imaging*, CLEO 2019 (San Jose): Science and Innovations, STh4O. 6

[16] Y. Zhou, W. Dou, W. Du, S. Ojo, **H. Tran**, S. Ghetmiri, J. Liu, G. Sun, R. Soref, J. Margetis, J. Tolle, B. Li, Z. Chen, M. Mortazavi, S. -Q. Yu, *Si-based Mid-Infrared GeSn-Edge-Emitting Laser with Operating Temperature up to 260 K*, CLEO 2019 (San Jose): Applications and Technology, AW3P.3

[15] W. Dou, B. Alharthi, P. Grant, J. Grant, **H. Tran**, W. Du, M. Mortazavi, B. Li, H. Naseem, S.-Q. Yu, *Buffer-free GeSn on Si Substrate by Plasma Enhanced Chemical Vapor Deposition*, MIOMD 2018 (Flagstaff, Arizona), WeA9

[14] J. Grant, W. Dou, B. Alharthi, **H. Tran**, A. Mosleh, W. Du, B. Li, M. Mortazavi, H. Naseem, S.-Q. Yu, *Growth and Characterization of GeSn using UHV-CVD System*, MIOMD 2018 (Flagstaff, Arizona), WeA6

[13] S. -Q. Yu, W. Du, W. Dou, Y. Zhou, P. Grant, T. Pham, **H. Tran**, J. Margetis, J. Tolle, S. Ghetmiri, A. Mosleh, M. Mortazavi, J. Liu, G. Sun, R. Soref, and B. Li, *Development of Si-based GeSn Laser*, Compound Semiconductor Week 2018, Th2A6.5

[12] W. Dou, Y. Zhou, **H. Tran**, T. Pham, P. Grant, S. Ghetmiri, A. Mosleh, W. Du, J. Margetis, J. Tolle, M. Mortazavi, G. Sun, R. Soref, B. Li, and S. -Q. Yu, *Development of SiGeSn Technique towards Integrated Mid-Infrared Photonics Applications*, IEEE Summer Topical Meeting 2018 (Waikoloa), IMIP, MA3.2 (Plenary)

[11] **H. Tran**, T. Pham, W. Du, Y. Zhang, A. Ghetmiri, P. C. Grant, J. M. Grant, G. Sun, R. A. Soref, J. Margetis, J. Tolle, B. Li, M. Mortazavi, and S.-Q. Yu, *Systematic Study of $Ge_{0.89}Sn_{0.11}$ Photodiodes for Low-Cost Shortwave Infrared Imaging*, CLEO 2018 (San Jose): Science and Innovations, STh4I. 2

[10] J. Margetis, J. Tolle, S. Al-Kabi, Y. Zhou, **H. Tran**, T. Pham, W. Dou, P. Grant, S.-Q. Yu, W. Du, S. Ghetmiri, M. Mortazavi, G. Sun, R. Soref, B. Li, *GeSn-based Light Sources and Photoconductors towards Integrated Photonics for the Mid-Infrared*, 2017 Summer Topicals Meeting Series (10 – 12 July 2017), San Juan, Puerto Rico

[9] W. Du, S. Ghetmiri, S. Al-Kabi, A. Mosleh, T. Pham, Y. Zhou, **H Tran**, G. Sun, R. Soref, J. Margetis, J. Tolle, B. Li, M. Mortazavi, H. Naseem, S.-Q. Yu, *Silicon-based $Ge_{0.89}Sn_{0.11}$ photodetector and light emitter towards mid-infrared applications*, SPIE Photonics West, No. 10108-38, Jan 30-Feb 1, 2017, San Francisco, CA, USA

[8] **H. Tran**, T. Pham, W. Du, J. Margetis, Y. Zhou, P. C. Grant, G. Sun, R. A. Soref, J. Tolle, B. Li, M. Mortazavi, H. A. Naseem, and S.-Q. Yu, *Study of $Ge_{0.89}Sn_{0.11}$ Photodiodes for Low-Cost Shortwave Infrared Imaging*, CLEO 2017, STu1N. 6

[7] B. Alharthi, A. Mosleh, J. Margetis, S. Al-Kabi, S. A. Ghetmiri, **H. Tran**, W. Du, M. Benamara, M. Mortazavi, J. Tolle, H. Naseem, S.-Q. Yu, *CVD growth of SiGeSn Alloys for Higher Efficiency Multi-Junction Solar Cells*, the 43rd IEEE Photovoltaic Specialists Conference, Portland, OR, USA, June 5-10 (2016)

[6] **H. Tran**, T. Pham, Y. Zhou, S. Ghetmiri, S. Al-Kabi, A. Mosleh, H. Naseem, J. Tolle, J. Margetis, W. Du, M. Mortazavi, R. Soref, G. Sun, B. Li, and S. -Q. Yu, *Investigation of Si-based $Ge_{0.93}Sn_{0.07}$ Photoconductors towards Short-wave Infrared Detection*, IEEE Summer Topicals Meetings, Newport Beach, CA, USA, July 11-13 (2016)

[5] W. Du, S. Al-Kabi, S. Ghetmiri, **H. Tran**, T. Pham, B. Alharthi, A. Mosleh, J. Margetis, J. Tolle, H. Naseem, M. Mortazavi, G. Sun, R. Soref, B. Li, and S. -Q. Yu, *Development of SiGeSn Technique towards Mid-Infrared Devices in Silicon Photonics*, Electrochemical Society Falling Meeting, Honolulu, HI, USA, October 02-07 (2016)

[4] T. Pham, W. Du, **H. Tran**, J. Margetis, J. Tolle, G. Sun, R. A. Soref, H. A. Naseem, B. Li, M. Mortazavi, and S. -Q. Yu, *Systematic study of Si-based $Ge/Ge_{0.9}Sn_{0.1}/Ge$ photodiodes with 2.6 μm detector cutoff*, CLEO 2016, STh1G.7, June 5-10, 2016, San Jose, CA, USA.

[3] A. Mosleh, M. Alher, L. Cousar, H. Abu-safe, W. Dou, P. C. Grant, S. Al- Kabi,, S.A. Ghetmiri, B. Alharthi, **H. Tran**, W. Du, M. Benamara, B. Li ,M. Mortazavi, S.-Q. Yu, and H. Naseem, *Enhancement of Material Quality of (Si)GeSn Films Grown By SnCl4 Precursor*, 2015 ECS Fall (228th meeting), October 11-16, Phoenix, AZ (2015)

[2] S. Al-Kabi, S. A. Ghetmiri, W. Du, **H. Tran**, G. Sun, R. Soref, J. Tolle, J. Margetis, B. Li, H. A. Naseem, and S.-Q. Yu, *Material and Optical Characterizations for Both Bulk and NIP Double Heterostructure of Germanium Tin*, 2015 Electronic Material Conference, June 24~26, Columbus, OH (2015)

[1] T. Pham, B. R. Conley, J. Margetis, **H. Tran**, S. A. Ghetmiri, A. Mosleh, W. Du, G. Sun, R. A Soref, J. Tolle, H. A. Naseem, B. Li, and S.-Q. Yu, *Enhanced responsivity up to 2.85 A/W of Si-based $Ge_{0.89}Sn_{0.11}$ photoconductors by integration of interdigitated electrodes*, CLEO 2015, STh1I.7, May 10-15, 2015, San Jose, CA, USA.